Predictive Models of Metabolite Concentration for Organoid Expansion

Meredith Ellis
St Anne's College
University of Oxford

A thesis submitted for the degree of
Doctor of Philosophy
Trinity 2022

To my family:
My parents, for their unending love and support;
My late Granny, for her shining example of perseverance;
My sister, for being my first friend and lifelong cheerleader;
And to the next generation – I cannot wait to be your Mathematical Aunty.

Acknowledgements

This thesis is a culmination of not only my work, but the support and investment of many others in my research and in me as a person.

First and foremost, I would like to offer my heartfelt thanks to my academic supervisors: Professor Sarah Waters, Professor Helen Byrne, and Dr Mohit Dalwadi. To Sarah, for your encouragement and guidance on this project. To Helen, for your words of wisdom and encouragement, and for your steadfast support from my very first day as a DPhil student. And to Mo, for all your advice, time, patience, and support, and for indulging my love of asymptotics. I am incredibly honoured to be the first in what will undoubtedly become a long line of PhD students – I hope I have done you proud.

I would like to extend my sincere thanks to Cellesce for offering such a mathematically stimulating project, and to Marianne, Kim, Will, and the rest of the team for the informative discussions and for making me feel so welcome in your lab.

I would like to acknowledge all those involved with the Industrially Focused Mathematical Modelling (InFoMM) CDT – I am a better and more well–rounded mathematician for my time on the programme.

Thank you to Oriel, St Anne's, and Trinity, for enabling my studies, facilitating wonderful friendships, and providing opportunities I never thought possible.

I am blessed to have made extraordinary friends who deserve honourable mention and who have filled my time as a DPhil student with many happy memories: Alice – our Friday walkies are stuff of legend and I will be forever grateful for traversing the highs and lows of DPhils and of life with you; Chloé, my fellow cake connoisseur – for being a close and dear companion throughout this process, both in academia and in life; my beloved Juxon St gals – Flavia, Lucy, Yas, Kadi, and Alex – thank you for making our house a home; and to my school friends, Tasmin and Flossie, for reminding and rejoicing in how far we have come.

I would be remiss in not mentioning my family. Simply know, I love you all.

Lastly, a huge amount of thanks and gratitude is owed to Professor Ian Halliday and Dr Xu Xu. Without you both – the wonderful, formative summers of research, and your endless support, encouragement, and belief in me – I would not have learned that the world of mathematical research is a place where I belong.

Predictive Models of Metabolite Concentration for Organoid Expansion

Meredith Ellis

St Anne's College
University of Oxford

A thesis submitted for the degree of
Doctor of Philosophy

Trinity 2022

This thesis is motivated by the culture of organoids, specifically developing mathematical models for metabolite transport and organoid growth within a fed-plate bioreactor. The bioreactor of interest is the proprietary CXP1 bioreactor, invented by biotechnology company Cellesce, which consists of a layer of hydrogel over which culture media is flowed. Organoids are embedded within the hydrogel and flow is thought to enhance nutrient delivery to, and facilitate waste removal from, the organoids. A key priority is ensuring uniformity in organoid size and reproducibility; qualities that depends on bioreactor design and operating conditions. We show how mathematical modelling can be used to improve the yield of organoids grown within CXP1, by predicting metabolite concentrations during culture for different operating conditions.

In this thesis, we develop a series of models focused on different spatial scales and aspects of organoid growth and bioreactor operation, including metabolite transport and fluid flow. We exploit the slender bioreactor geometry and use an asymptotic approach to derive a longwave approximation of the transport problem within a 2D representation of CXP1, where the organoids are modelled via volumetric (bulk) reaction terms. We show these reduced models are excellent approximations to the full 2D model and explore the behaviour of the longwave approximation using both analytical and numerical approaches. We then develop a model for growth of individual organoids embedded within the hydrogel, modelling the organoids as spheres with temporally and spatially varying radii within a cubic lattice. Hence, we derive, via a homogenisation approach, the effective macroscale behaviour across the organoid-hydrogel region while also retaining the relevant organoid-scale information. Next, we consider the corresponding 3D flow problem. We exploit the slow nature of the flow and the geometry of the media domain, and systematically reduce the problem using a lubrication scaling to a 2D streamfunction problem of a circle with a point source and point sink. Finally, we combine the 3D flow model into the model for metabolite transport and organoid growth. We perform an asymptotic analysis on this model to reduce its spatial dimension — this allows us to efficiently predict the metabolic environment and associated organoid size across the CXP1 bioreactor.

Contents

1 Introduction **1**
1.1 Biological motivation 1
1.2 Bioreactor technology overview 4
1.3 Mathematical modelling of bioreactors 6
1.4 Overview of thesis 10
1.4.1 Overview of modelling approach 10
1.4.2 Thesis outline 12
1.5 Statement of originality 14

2 Systematic reduction of a 2D model **15**
2.1 Biological problem 15
2.1.1 Modelling approach 16
2.1.2 Chapter outline 17
2.2 Bioreactor set-up 17
2.2.1 CXP1 experimental set-up and operating protocol 17
2.2.2 Parameter values 19
2.3 Mathematical model 20
2.3.1 Governing equations 20
2.3.2 Typical timescales 23
2.3.3 Non-dimensionalisation 25
2.3.4 Numerical solution of full model 26
2.4 Model reduction 27
2.4.1 Longwave approximation 27
2.4.2 Sublimit of longwave approximation 30
2.5 Results 33
2.5.1 Methods for numerical solution of models 33
2.5.2 Model behaviour and comparison 33
2.5.3 Bioreactor characterisation 39

2.6 Discussion 48

3 Homogenisation of organoid and hydrogel regions 53

3.1 Introduction 53
    3.1.1 Review of mathematical homogenisation 53
    3.1.2 Chapter outline 55
3.2 Model set-up 56
    3.2.1 Governing equations 58
    3.2.2 Non-dimensionalisation of governing equations 64
3.3 Derivation of homogenised metabolite transport equations 67
    3.3.1 Model for dense organoids with volumetric growth 69
    3.3.2 Model for shell organoids with surface growth 78
3.4 Results 87
    3.4.1 Comparison of governing equations for volumetric and surface growth 87
    3.4.2 Numerical solution of the cell problem 89
    3.4.3 Canonical problems 92
3.5 Discussion 102

4 3D media flow problem 106

4.1 Model set-up 106
4.2 Model solution 114
4.3 Analysis of solution 117
    4.3.1 Velocity potential and streamfunction 117
    4.3.2 Information about the streamlines 118
4.4 Discussion 122

5 3D metabolite transport and organoid growth model 123

5.1 Model set-up 124
    5.1.1 Dimensionless transport and organoid growth models 127
    5.1.2 Model reduction 135
    5.1.3 Transforming from Cartesian to streamfunction-arclength formulation 138
5.2 Results 143
    5.2.1 Methods for numerical solution of metabolite transport and organoid growth models 143
    5.2.2 Current operating protocol 145

5.2.3 Changing inlet and outlet position 148
5.2.4 Changing inlet flux 157
5.2.5 Streamfunction-arclength formulation 162
5.3 Discussion 167

6 Conclusions and future work 171
6.1 Summary of work 171
6.2 Future work 176
6.3 Concluding remarks 180

A Derivation of analytic solution to the sublimit approximation 181
A.1 Solution for glucose concentration 181
A.2 Solution for lactate concentration 183

B Derivation of cell problem boundary condition 185

C Derivation of proxy flow boundary condition 186

D Small organoid and strong uptake distinguished limit 191
D.1 Investigating inner problem 192
D.2 Investigating the outer problem 196
D.3 Effective behaviour in thin layer of hydrogel 198

E Another distinguished limit: advection balancing vertical diffusion 201

References 203

List of Figures

1.1 Diagram of CXP1 bioreactor, with an image of a colorectal cancer organoid which has been cultured within CXP1. 3

2.1 Schematic of CXP1 bioreactor and the representative 2D domain . . . 18
2.2 Schematic of the boundary conditions on the two-dimensional representative domain considered 23
2.3 Metabolite concentrations in 2D domain at 1, 3, and 7 days 27
2.4 Characteristic diagram for the system Equations (2.4.10) and (2.4.11). 32
2.5 Comparison of results for the reduced-order models to the full 2D model 34
2.6 Comparison of metrics for the reduced-order and full 2D model 37
2.7 Glucose and lactate concentrations of the longwave approximation for different organoid lines 41
2.8 Bioreactor characterisation metrics for different organoid lines 43
2.9 Bioreactor characterisation metrics for different flow rates 46
2.10 Glucose conversion and turn-off time varying as functions of peak flow velocity 47

3.1 Schematic of a 2D cross-section of CXP1 with the microscale organoid-hydrogel structure 54
3.2 Schematic of organoid types 57
3.3 Two-dimensional projection of the three-dimensional domain we consider. 68
3.4 Diagrams for the reformulated cell problem 89
3.5 Effective diffusivity of organoid-hydrogel region 92
3.6 Boundary conditions for the 3D effective macroscale mass transport model. 93
3.7 3D solutions of glucose and lactate concentrations and organoid radius at $T = 7$ 96
3.8 Lactate concentration at $T = 7$ for different culture conditions 97

3.9 Mean and standard deviation of metabolite concentrations for different culture conditions . . . 98
3.11 Glucose consumption under different culture conditions . . . 99
3.10 Mean and standard deviation of organoid radius under different culture conditions . . . 101
3.12 Objective function for different culture conditions . . . 101

4.1 Diagram of CXP1 bioreactor set-up . . . 107
4.2 Schematic of 3D domain with relevant lengthscales . . . 108
4.3 Schematic of the culture media flow in (X, Y)-plane and depth . . . 114
4.4 Streamfunction and velocity potential for standard operating conditions 118
4.5 Magnitude of velocity and corresponding streamlines . . . 119
4.6 Streamlines in (X, Y)-plane for different positions of inlet and outlet pipes . . . 120
4.7 The position in the (X, Y)-plane and velocity along streamlines for different inlet and outlet positions. . . . 121
4.8 The total length and mean velocity along a streamline as a function of the streamfunction . . . 121

5.1 Diagram of CXP1 bioreactor set-up in 3D . . . 123
5.2 Schematic of the 3D domain considered (culture media and homogenised organoid-hydrogel layers) . . . 129
5.3 2D cross-sections of 3D solutions for metabolite concentration and organoid radius at $T = 7$ . . . 133
5.3 2D cross-sections of 3D solutions for metabolite concentration and organoid radius at $T = 7$ . . . 134
5.4 Change of coordinate system from Cartesian to streamfunction-arclength 139
5.5 Solving along a streamline . . . 142
5.6 Distributions of metabolite concentrations and fold increase in organoid radius for 2D reduced model . . . 147
5.7 Depth-averaged distributions of metabolite concentrations and fold increase in organoid radius for 3D model . . . 147
5.8 Mean fold increase of organoid radius, R/R_c, at $T = 7$, for different inlet and outlet positions. . . . 149
5.9 Mean and standard deviation of fold increase in organoid radius for different inlet and outlet positions . . . 150

5.10 Mean and standard deviation of glucose concentration for different inlet and outlet positions 151
5.11 Profile of mean fold increase in organoid radius for 3 inlets and 1 outlet, for different inlet positions 153
5.12 Mean and standard deviation of fold increase in organoid radius for 3 inlets and 1 outlet for different inlet positions 155
5.13 Mean and standard deviation of glucose concentrations for different inlet and outlet positions 155
5.14 Comparing mean and standard deviation of fold increase in organoid radius for different numbers of inlets 156
5.15 Velocity magnitude profile with streamlines for different inlet/outlet pipe set-ups 156
5.16 Mean fold increase of organoid radius, R/R_c, at $T = 7$, for different inlet fluxes, Q. 158
5.17 Mean and standard deviation of fold increase in organoid radius as inlet flux varies 159
5.18 Mean and standard deviation of glucose concentration as inlet flux varies 160
5.19 Mean and standard deviation of fold increase of organoid radius for piecewise-constant inlet fluxes, $Q_{CE}(T;\tau)$ 161
5.20 Mean and standard deviation of fold increase of organoid radius at $T = 7$ for different piecewise-constant inlet fluxes $Q_{CE}(T;\tau)$, as a function of τ 162
5.21 The behaviour of the 9 streamlines considered in Section 5.2.5.1. 163
5.22 Metabolite concentrations and fold increase in organoid radius along streamlines at $T = 7$ 165
5.23 Position in (X, Y)-plane of and velocity along three streamlines of different lengths. 165
5.24 Metabolite concentrations and fold increase in organoid radius along 3 different streamlines at daily intervals 166
5.25 Metabolite concentrations and fold increase in organoid radius along 3 different streamlines evolving in time 167

Chapter 1

Introduction

This thesis is motivated by the culture of organoids, specifically developing mathematical models for metabolite transport and organoid growth within a fed-plate bioreactor. In this Introduction, we give an overview of organoid technology and its potential for accelerating drug development. We then describe the different types of bioreactor used in organoid culture and highlight the bioreactor developed by our collaborators, Cellesce, that motivates this mathematical study. We review existing mathematical models of perfusion bioreactor systems, and use them to motivate our mathematical modelling approach to studying Cellesce's organoid expansion process. We conclude by summarising the content of this thesis.

1.1 Biological motivation

Organoid technology is becoming increasingly prominent as a biomedical tool, with applications in drug discovery and personalised medicine. In biomedical research, brain, kidney, and liver organoids are used to understand the biological mechanisms underlying tissue development and tissue-drug interactions [4, 24, 47, 86].

Organoids are three-dimensional, multi-cellular structures which are grown *in vitro* and successfully recapitulate *in vivo* tissue-specific structure and function [21]. Organoids contain all of the key cell types of their tissue of origin: stem cells, which allow extended culture studies; and differentiated cells, which retain physiologically relevant functions. For example, organoids cultured from breast cells may produce milk proteins, while those cultured from cancer cells may be invasive. 'Organoid expansion' refers to the growth of multiple organoids from pluripotent stem cells, which are typically derived from patient biopsies or from other organoids [82]. The stem cells are embedded in a supporting extra-cellular matrix (ECM) and cultured in carefully-controlled conditions designed to promote organoid growth. The surrounding ECM provides the biochemical and biomechanical cues needed for the cells to proliferate and differentiate into specialised cells, as happens *in vivo* [24, 42]. Organoids retain many features of the human tissues from which they are derived, such as the tissue structure, pathology, and heterogeneous cellular composition. This makes them a more physiologically representative proxy for *in vivo* tissue than 2D cell line cultures [94].

Current methods for organoid expansion are labour intensive, with organoids typically being produced in small numbers at specialist research laboratories. New technologies are required to manufacture large numbers of organoids with uniform and reproducible characteristics, to meet the demands of applications such as high-throughput screening in drug development. One such technology exploits bioreactors, which aim to deliver sufficient nutrients and growth factors to the cells to promote cell proliferation and differentiation, and to prevent the accumulation of toxins, which can lead to cell death. For a more detailed overview of bioreactor technologies used for 3D cell culture see, for example, Martin et al. [55], Pörtner and Giese [67] and Wendt et al. [91].

The research contained in this thesis is motivated by proprietary organoid expansion bioreactor technology developed by Cellesce [25]. The 'Cellesce Expansion 1 (CXP1)' bioreactor is currently used to expand colorectal cancer organoids, see Figure 1.1. Flow of media through the system is thought to enhance the delivery of nutrients to, and the removal of waste products from, organoids seeded in a hydrogel layer. In this application, oxygen is present at high concentrations, and is not a limiting factor for organoid growth. The key metabolites (substance involved in metabolism) of interest are glucose, which is essential for colorectal cancer organoid growth, and lactate, a byproduct of metabolism. Lactate can have a detrimental effect on cell behaviour, such as metabolism [71], and sufficiently high levels can lead to cell death. Lactate is produced via anaerobic respiration and aerobic glycolysis [51]. We do not focus on the precise mechanisms of lactate production; instead we determine how media flow promotes lactate removal. We note that while colorectal cancer organoids tolerate high lactate concentrations, the intention is to use CXP1 to produce organoids from a range of normal (healthy) and pathological cell types. Since different cell types have distinct requirements (*e.g.* nutrient levels required for cell proliferation and lactate tolerances), understanding the mass transport of glucose and lactate within the bioreactor is important. While we acknowledge that organoid culture is extremely complex, in this thesis attention focuses on the transport of glucose and lactate and their effects on organoid growth within the CXP1 bioreactor. We justify this focus by noting that spatiotemporal knowledge of these two metabolites can provide useful and practical information on the operation of CXP1, and provides the framework for more complex models in the future.

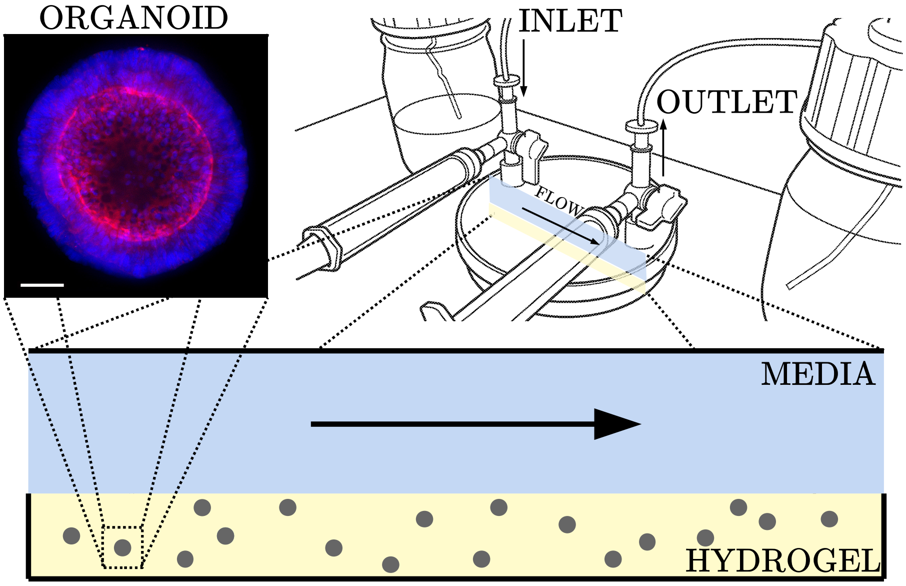

Figure 1.1: (**Top left**) Example of colorectal cancer organoid. Confocal image using 20X objective of Cell Insight Cx7. Organoid stained for nuclear (blue) and cytoskeletal (red) markers for imaging. Scalebar 50µm. Reproduced with permission from Cellesce. (**Top right**) Schematic of 'CXP1' bioreactor (Ellis et al. [25]). (**Bottom**) Two-dimensional cross-section of the bioreactor. Blue is media, yellow is hydrogel, grey is organoid biomass.

Key priorities in the CXP1 bioreactor design and operation are uniformity of organoid size and system reproducibility, to ensure there is minimal variation in organoid characteristics between and within batches grown under the same operating conditions. The main control parameters for the CXP1 bioreactor are the inlet flow rate (controlled via a peristaltic pump) and the initial cell seeding density (the organoids are grown from single cells). Optimisation of these control parameters requires spatiotemporal information about the flow and metabolite (here glucose and lactate) concentrations throughout the bioreactor [29]. Such data are impractical, inefficient, and expensive to collect through experimental means alone, due both to the closed nature of the bioreactor system and also the current limitations in Cellesce's sensing technology.

To complement experimental studies, mathematical models of bioreactor systems can be used to predict media flow profiles and the associated metabolite concentrations that cannot easily be measured *in vitro*, thus providing useful insights to ensure CXP1 operation is maintained within tolerable operating regions of these metabolites.

1.2 Bioreactor technology overview

A bioreactor is a device or system for culturing cells or tissues in a closed, controllable environment which supports biological tissue growth. Bioreactors provide the means to undertake controlled experiments to understand the effects of specific environmental factors, be they biological, chemical or physical [68]. They are, therefore, a valuable biomedical research tool. They should maintain sufficient nutrient for cell proliferation and prevent the accumulation of toxic materials, which could lead to cell death. Bioreactors can also be used in drug screening: efficiently producing a large quantity of tissue constructs for high-throughput screens in a reproducible manner. For a more detailed overview of bioreactor technology for 3D cell culture see Martin et al. [55] and Wendt et al. [91].

The microenviroment surrounding cells, including the mechanical and chemical stimuli they experience, can significantly impact the behaviours the cells display, including their rates of proliferation and differentiation [42]. The cellular response to these external mechanical stimuli is driven via a *mechanotransduction* process [19, 28], where mechanical stimuli are converted into biochemical signals, which, in turn, induce a biological response. To provide appropriate mechanical forces for a specific tissue type, specialised bioreactors are typically required [67]. Many different types of bioreactor have been developed for various biological applications and tissue requirements, in order to reproduce the specific *in vivo* stimuli required. We provide a brief introduction to the bioreactor technology relevant to the CXP1 bioreactor; for a comprehensive overview see Eibl et al. [23], Huang et al. [42], and Pörtner and Giese [67].

Bioreactors can be categorised into static and dynamic bioreactors. Static bioreactors, such as petri dishes or multi-well plates, are typically used for routine cell cultivation and maintenance. One use of static bioreactors is to expand the small number of cells from a patient biopsy to the required number for bioreactor seeding. However, static bioreactors are limited by the cells they can produce (approximately a tenfold increase limit [67]), since the nutrient is delivered by diffusion alone. They also require manual interaction, which means the output can be variable. For larger tissue constructs or larger cell numbers, dynamic bioreactors are often used. Dynamic bioreactors can be driven mechanically (*e.g.* rotating-wall vessel (RWV) bioreactors

[13, 73, 90] and stirred tank bioreactors [18]), hydraulically (*e.g.* perfusion bioreactors [96], such as flat bed (fed-plate) [37] and packed-bed bioreactors [57, 58], fluidised bed bioreactors [32], and hollow fibre bioreactors [9, 77, 80]), or pneumatically (*e.g.* bubble column bioreactor [72, 76]). Dynamic bioreactors can be either batch fed, where discrete amounts of culture medium are replaced periodically, or perfusion, where a continuous flow of culture medium is supplied. (See Placzek et al. [65] for a comparison of the different types of bioreactor and their ideal usage.)

The CXP1 bioreactor is the focus in this thesis and is discussed in more detail in Section 2.2: it can be described as a fed-plate (flat bed) bioreactor, a type of perfusion bioreactor where the flow is tangential to the cell-containing hydrogel. This type of bioreactor has been shown to enable extended culture of cells [89] and has been used to study cell function and differentiation [58]. It has some features in common with other perfusion bioreactors such as packed-bed and hollow fibre bioreactors, which we now review.

A packed-bed bioreactor pumps a nutrient-rich culture medium through the tissue-containing porous scaffold. This method overcomes some of the limitations of static bioreactor systems, mostly those linked to insufficient mass transfer to the entirety of a 3D tissue construct. Perfusion methods have also been used to seed scaffolds with cells, which can then be cultured in a different bioreactor system [75, 96]. For mathematical modelling of packed-bed bioreactors, including some of the challenges, see Yan et al. [93].

Hollow fibre bioreactors (HFB) have been shown to support three-dimensional, high cell-density tissue growth. In a HFB, cells are immobilised in a porous scaffold, also known as the extra-capillary space (ECS), surrounding a hollow tube, or lumen. The culture medium is pumped through the lumen, with an alternative flow route via inlet and outlet ports. The lumen is separated from the ECS by a porous membrane. The membrane allows nutrients and waste products to permeate into/out of the ECS and protects the cells from the direct effects of the high shear stress from the fluid flow within the lumen [80]. Multiple fibres can be used simultaneously to produce larger numbers of cells, but scale-up capabilities are limited. The typical HFB has a culture volume of 2.5µL to 1000µL [23]. Despite this, and other limitations of HFBs (lack of cell environment monitoring and potential mass transfer problems), HFBs are useful because of their low cost and easy handling. Bioreactor systems, including HFBs, lend themselves to mathematical modelling and optimisation, and can streamline experimental testing. Experimentalists design bioreactors to recreate and exploit desired culture conditions, which facilitates understanding of the key mechanisms present within system that influence bioreactor output and operation. The relevant parameter regimes for each bioreactor system are known, as many inputs (such as cell seeding densities and inlet flow rates) are measurable and controllable. This combination of information can be used to create representative mathematical models, which can be calibrated and validated against experimental data. These mathematical models can then be exploited to predict data which can be challenging to obtain empirically.

1.3 Mathematical modelling of bioreactors

To complement experimental studies, mathematical models of bioreactor systems can be used to predict media flow profiles and the associated metabolite concentrations, quantities that cannot easily be measured *in vitro*, thus providing useful insights to ensure CXP1 operation is maintained within tolerable operating regions for these metabolites. A key advantage of such a mathematical modelling approach is the ability to quickly, efficiently, and accurately analyse the system as control parameters are varied.

There are several different approaches regarding modelling of tissue culture within bioreactors; continuum-based models and cell-based models. For a review of cell-based models, where individual cells are resolved, see Macklin et al. [54], Metzcar et al. [56], and Gorochowski [33]. A continuum approach is often used to model bioreactor systems, and can be justified by the typical cell numbers ($\mathcal{O}(10^6)$ cells) and metabolite concentrations (CXP1: 16mM in 15mL of culture media) present. In this thesis, we adopt a continuum modelling approach, in which the dependent variables (cell density, fluid velocity, metabolite concentrations) are assumed to vary continuously in space and time. Our resulting model comprises a system of partial differential equations (PDEs). Henceforth, we focus our attention on continuum-based models and outline their scope by reviewing existing models in the literature. For a more comprehensive review of continuum models for tissue engineering see O'Dea et al. [61].

Most mathematical models of bioreactor systems focuses on predicting metabolite concentrations and/or the mechanical stimuli that cells experience. The metabolites that are most often considered are oxygen, glucose, and lactate. Oxygen has been widely studied [10], because it has been found to be a limiting factor for cell growth, particularly in HFBs [77]. Recent studies have investigated lactate concentration [10, 78, 80]. Lactate can affect cell properties, such as metabolism [71]. Proliferating tumour cells produce lactate even in the presence of oxygen, known as the Warburg effect [88] via a process termed *aerobic glycolysis* [51]. Given that the CXP1 bioreactor cultures cancer cells, it is important to consider lactate concentration here, since tumour cells are sensitive to lactate above a tolerated level. We also consider the glucose concentration, as respiration requires glucose to produce energy, and lactate is produced as a by-product of anaerobic respiration. Glucose can also be a limiting factor in cell growth. Since tumour cells lines will differ in their metabolism rates, it is important, more generally, to be able to map metabolite profiles and how these evolve in time. For examples of models of cell growth kinetics, see Galban and Locke [29, 30].

Mechanical stimuli which can be important in 3D cell culture include tensile and compressive forces, due to *e.g.* elastic deformation, and stresses due to hydrodynamic effects. It is important to consider the behaviour of hydrogels and other ECMs, as these materials play a significant role in determining the local metabolic and mechanical environment experienced by the cells. (See Caccavo et al. [7] and Caccavo [6] for a review of models of hydrogels, and their solute transport and mechanical properties, for drug delivery applications.) The scaffold on which the cells are seeded are often composite materials, to most closely mimic the native ECM [97]. Fibrous networks may be used to reinforce weak hydrogels. For example, Chen et al. [11] derived a mechanistic continuum model for the response of a fibre-reinforced hydrogel scaffold, modelling the fibres and hydrogel as a linear elastic and poroelastic materials, respectively. They used a mathematical homogenisation approach to determine the bulk mechanical properties of the composite construct and compared their results to experimental data. The authors determined how the mechanical properties of the material depend on the fibre spacing and predicted how this affects the local mechanical environment experienced by the cells.

In this thesis, we model fluid flow and metabolite transport problems through bioreactor systems. We focus on PDE-based continuum models, as they can be more easily validated against the experimental data collected by Cellesce. Cellesce are unable to monitor individual organoids, but can measure metabolite levels in the waste culture media. Our continuum approach is also motivated by our requirement to consider large numbers of organoids, which would be too computationally expensive to handle discretely. In this thesis, we neglect the mechanical effects of the hydrogel and any mechanical stimuli on organoid growth. However, we discuss in Section 6.2 how we could develop our models to predict the biomechanical environment within the hydrogel and incorporate its influence on organoid culture.

We now discuss flow and transport models of various bioreactors, which do not include solid mechanics (hydrogel) models.

Tilles et al. [85] consider oxygen transport in a flat plate microchannel bioreactor. They derive an advection-diffusion system for the steady state oxygen concentrations. They then construct analytic solutions for two different set-ups and compare the results to experimental data. Pathi et al. [62] develop an oxygen transport and cell growth model for a perfusion bioreactor consisting of a layer of cells, sandwiched between flow of culture medium. Within the culture media, oxygen is transported via advection and diffusion, and the cell layer is modelled as a two-phase region consisting of cells and fluid. In this fluid, oxygen is transported via diffusion and in the cell colony, oxygen diffuses and is consumed by the cells for metabolism and growth. Pathi et al. use volume averaging to determine how to represent the two-phase cell layer via a single phase mechanistic model. They use the model to investigate the effect of varying the bioreactor operating conditions, such as flow rate and media layer thickness, on the oxygen distribution and cell growth. Hyndman et al. [43] consider fluid flow and solute (drug) transport within a perfusion bioreactor. The bioreactor consists of a chamber through which culture media flows via an inlet and outlet, and the cells are located at the base of this chamber. They model the fluid via the incompressible Navier-Stokes equations and solute transport with an unsteady advection-diffusion system. Within the cell region, the solute is modelled with a reaction-diffusion equation. Hyndman et al. determine the steady state velocity profile within the chamber and the shear stress experienced at the cell region surface for a range of inlet flow rates, and find that the steady-state solute concentrations can be determined *a priori* for nonlinear saturable binding reaction kinetics.

Shipley et al. [78] consider a printed hydrogel scaffold seeded with cells in a perfusion bioreactor, and model the flow of culture media using the Navier-Stokes equations in the media region and assume no flow within the hydrogel scaffold. The cell density within the hydrogel is assumed to be constant and, hence, the cells occupy a fixed volume. The metabolites are transported via advection and diffusion within the media region and diffusion within the scaffold, where reaction (uptake or production) also occurs. The works by Chapman et al. [10] and Shipley and Waters [80] consider a HFB system and use Navier-Stokes for the fluid within the lumen of the HFB and Darcy flow within the ECS. The authors also consider the cell problem as static, an assumption justified by focusing on a timescale shorter than that for cell proliferation. Alternatively, to reduce complexity, one can prescribe the fluid flow and solve for the metabolite concentrations only, *e.g.* Shipley et al. [77]. Shipley et al. consider a HFB and prescribe Poiseuille flow within the lumen and neglect flow across the membrane and within the ECS, applying a common modelling assumption of small pressure drop across the membrane and ECS. The governing equations for the metabolite concentrations in the models discussed are typically advection-diffusion equations in the media regions and advection-reaction-diffusion or reaction-diffusion equations within the hydrogel scaffold [78] or ECS [9, 63, 77, 80]. These results can be used to determine mechanical stimuli, such as shear stress, and account for their impact on cell growth, see *e.g.* [9, 10].

Another approach to modelling tissue culture systems is based on mixture theory, introduced in the context for tissue engineering *in vitro* in the seminal paper by Lemon et al. [50]. In these multiphase models, cells, culture medium, and scaffold are treated as separate phases. The governing equations for volume fraction, velocity, and pressure are obtained via conservation of mass and momentum. It has been noted that cell-cell and cell-scaffold interactions are important determinants of cell behaviour [42], and thus accurate modelling of these interactions is important. The framework introduced by Lemon et al. [50] is applied to a specific tissue engineering application: the dynamics of motile cells and water inside a rigid scaffold. Their model can describe the seeding of a porous rigid scaffold, which is the first step in a bioreactor experiment. O'Dea et al. [60] use a similar framework but concentrate on cell-cell and cell-scaffold interactions, and the impact of *mechanotransduction* mechanisms on construct composition within a perfusion bioreactor. Pearson et al. [63] use mixture theory to model the ECS of a HFB. The authors consider Navier-Stokes for the flow within the lumen and Darcy's law for flow within the membrane. Interactions between cells, scaffold, and culture medium phases are incorporated by including extra pressure, force, and drag terms in the governing equations. Pearson et al. consider several different experimental set-ups for the HFB and use the corresponding models to predict the resulting behaviour and ultimately determine the optimal flow rate for generating spatially uniform cell distributions for each set-up.

Many mathematical techniques have been used to reduce the complexity of the governing equations in bioreactor modelling. Many authors consider a lubrication approximation, motivated by the long thin geometry of the bioreactor, for example, [60, 77, 80] for HFB bioreactors and [13, 14, 49] for RWV bioreactors. Another technique, used in various applications in tissue engineering, is mathematical homogenisation. This is a method to systematically derive a macroscale continuum model from a microscale problem. We introduce mathematical homogenisation in

Section 3.1.1. Sanz-Herrera et al. [74] use homogenisation techniques to characterise the properties of a scaffold for bone tissue growth (*e.g.* the porosity, permeability, and mechanical properties) by averaging the microscale behaviour to obtain macroscale equations. Shipley et al. [78] consider a printed scaffold perfusion bioreactor system, which consists of overlapping cylindrical strands of cell-containing hydrogel. They study the metabolite concentration and flow profiles within the bioreactor for three different scaffold geometries. They derive a set of PDEs via conservation of mass and momentum. They then apply homogenisation techniques to derive the equations governing the effective flow and metabolite transport to determine the dependence of the macroscale problem on the microscale properties of each scaffold, including its geometry. Using dimensional analysis and solutions to the PDE system, they provide recommendations for the optimal bioreactor design; in particular, cell seeding density, mean flow velocity, inlet oxygen concentration, scaffold geometry configuration, and strand diameter and separation.

1.4 Overview of thesis

1.4.1 Overview of modelling approach

Throughout this thesis, we adopt a continuum modelling approach, in which the dependent variables (cell density, fluid velocity, metabolite concentrations) are assumed to vary continuously in space and time. Our mechanistic models comprise systems of partial differential equations (PDEs) for metabolite transport and organoid growth within a specific bioreactor set-up. For our 2D model in Chapter 2, we prescribe the fluid flow in a 2D representative domain. When developing a 3D model, we solve for the flow of culture media within the CXP1 bioreactor.

As discussed in Section 1.3, mathematical models for bioreactor systems in the literature typically focus on predicting either the metabolic or the mechanical environment experienced by the cells, with a few incorporating both. In this thesis, we neglect any mechanistic effects within the bioreactor and the resulting impact of mechanical stimuli on organoid growth, and focus our attention on developing models for metabolite transport coupled to organoid growth. The reasons for this are two-fold. Firstly, since this is an initial step into developing mathematical models for the CXP1 bioreactor, we want to start with simple self-contained models, which can capture sufficient key physics to produce representative and informative results while remaining as tractable as possible. Secondly, we currently have extremely limited knowledge regarding the mechanical forces at play within the CXP1 bioreactor, especially the interaction between the organoids and the hydrogel (it is expected this is highly cell line dependent), and Cellesce do not anticipate obtaining the capability to capture any experimental data to inform parameter values or for model validation. Therefore, modelling mechanics is beyond the scope of this thesis. We also do not track the water phase, for reasons discussed in Chapter 3. However, a significant benefit of the mathematical modelling approach taken in this body of work is that the models developed can be easily extended to include more physics (*e.g.* mechanics) and biology (*e.g.* more physiologically representative organoid growth) as required. We discuss avenues for future model advancements in Section 6.2.

These models generate continuous spatial and temporal data, which is infeasible to obtain experimentally, and yield mechanistic insight into the importance of different physical processes in organoid culture. The model predictions can be utilised to optimise the culture protocol and identify what experimental information should be collected in order to validate and further develop the model.

We will exploit both asymptotic and numerical methods to explore the behaviour of the models we develop. We consider two approaches for systematic model reduction, and explore these methods individually in Chapter 2 and Chapter 3, respectively, and we combine these in Chapter 5 to develop a 3D model for metabolite transport and organoid growth within the CXP1 bioreactor.

The first model reduction technique we employ exploits the slender geometry of the CXP1 bioreactor. In Chapter 2, we derive an advection-diffusion-reaction model for the transport of metabolite within the hydrogel and media layers of the bioreactor and perform a model reduction (via a lubrication scaling), taking an approach similar to that used in [10, 77, 80]. We model the organoids (cell aggregates) as continuous volumetric (bulk) reaction terms over the hydrogel.

The second model reduction technique that we employ is mathematical homogenisation, via the method of multiple scales, in Chapter 3. We consider the behaviour of metabolites and organoids within the organoid-embedded hydrogel and exploit the separation of scales between the size of the organoid and bioreactor. We derive an 'upscaled' macroscale metabolite transport model and formally obtain the appropriate effective (bulk) reaction terms, which depend on the evolving organoid-scale microstructure within the hydrogel.

We combine these techniques to derive a 3D model for metabolite transport and organoid growth within the CXP1 bioreactor in Chapter 5. We show that through careful consideration of coordinate system, we can further reduce the dimensionality of the model. Through a change in coordinate system, we can pose the problem as solving 1D hyperbolic PDEs to determine the temporal evolution of metabolite profiles and organoid size along the streamlines of the flow of culture media.

In utilising these mathematical techniques for model reduction, we highlight two key advantages of deriving reduced models. First, we identify the physical mechanisms that dominate the system behaviour on the timescales of interest. Secondly, reduced models are more tractable than their more detailed model counterparts and, as such, can be solved more rapidly numerically or, in some cases, analytically. This facilitates more detailed exploration of parameter space, which is important for subsequent optimisation of bioreactor operating conditions, and allows more physiologically relevant biological models to be feasibly incorporated.

Some of the key questions we aim to answer in this thesis are:

- "*Are all the organoids across the bioreactor getting sufficient nutrient?*"
  Insufficient nutrient levels would result in cell death. Any variability in nutrient provision to live cells could result in non-homogeneous growth and variability in organoid size.

- "*Are the levels of lactate tolerable everywhere?*"
  The environmental lactic acid levels can modify cell composition [48]. Thus variation in lactate concentration can result in heterogeneity of the organoids across the bioreactor.

- "*Are there operating parameters which give spatially uniform metabolite concentrations?*"
  Cellesce aim to produce organoids with consistent properties and characteristics. Organoid properties are influenced by the metabolite levels they experience throughout the duration of the experiment, so it is optimal for the metabolite concentration profiles to be uniform across the hydrogel layer of the bioreactor.

1.4.2 Thesis outline

In Chapter 2, we present a general model for nutrient and waste metabolite concentrations in a 2D cross-section of the bioreactor. The organoids are modelled via a general smooth volumetric absorption term, which is exponentially increasing in strength in time, within the hydrogel. The flow is assumed to be in the horizontal direction only, where the flow profile in depth is half-Poiseuille flow (due to the bioreactor geometry and slow fluid velocity). We exploit the slender geometry of the domain and use an asymptotic approach to derive a longwave approximation of the system. This reduced-order 1D model accounts for the depth-averaged flow, nutrient uptake, and waste metabolite production, and is more analytically tractable compared to the 2D model. We show that the reduced models are excellent approximations to the full 2D system (which does not exploit the lubrication regime) and explore the behaviour of the longwave approximation and full system using both analytical and numerical approaches.

In Chapter 3, we consider the discrete nature of the organoids in more detail. We develop a model for individual organoids embedded within the hydrogel, modelling the organoids as spheres with temporally and spatially varying radii within a cubic lattice. Since resolving millions of organoids within the hydrogel is computationally infeasible, we employ homogenisation techniques to systematically average the microscale behaviour in a local sense. This allows us to derive the effective macroscale behaviour across the organoid-hydrogel region while also retaining the relevant organoid-scale information. We explore some canonical problems to understand how the culture conditions affect the metabolite concentrations and organoid growth.

In Chapter 4, we turn our attention to the media flow in the CXP1 bioreactor and solve the 3D flow problem. Given the slow nature of the flow and the slender geometry of the media domain, the flow is well-approximated by pressure-driven lubrication flow with a free surface, so the flow profile in depth is half-Poiseuille flow. Due to the decoupling of the depth-dependence, we reformulate our flow problem as a 2D streamfunction problem of a circle with a point source and point sink. We explore the behaviour of the culture media, such as determining the position and length of streamlines of the flow within the domain.

In Chapter 5, we incorporate the flow behaviour into a metabolite transport model for the culture media region, which we couple to the homogenised organoid-hydrogel model via appropriate interfacial conditions. Thus, we obtain a full 3D model for the organoid growth and metabolite transport across the entire bioreactor. We systematically reduce this fully coupled metabolite transport and organoid growth model, by exploiting the separation of timescales of the key transport mechanisms. We also consider a change of coordinate system to a streamfunction-arclength formulation, to further reduce the spatial dimension of the model. We explore how the bioreactor geometry can be changed to improve organoid output and bioreactor efficiency.

We conclude with a summary of the results and outline potential avenues for future work.

1.5 Statement of originality

The modelling, analysis, and numerical results in this thesis are the work of M.A. Ellis under the supervision of S.L. Waters, H.M. Byrne, and M.P. Dalwadi. The work in Chapter 2 has been published in [26]. Two more papers are in preparation, based on Chapter 3 and Chapters 4 and 5, respectively.

Chapter 2

Systematic reduction of a 2D model

2.1 Biological problem

This study is motivated by proprietary organoid expansion bioreactor technology developed by Cellesce [25]. The 'Cellesce Expansion 1 (CXP1)' bioreactor is currently used to expand colorectal cancer organoids (see Figure 2.1). Flow of media through the system enhances the delivery of nutrients to, and the removal of waste products from, organoids seeded in a hydrogel layer. In this application, oxygen is present at high concentrations, and is not a limiting factor for organoid growth. The key metabolites of interest here are glucose, essential for colorectal cancer organoid growth, and lactate. Lactate can have a detrimental effect on cell behaviour, such as metabolism [71], and sufficiently high levels can lead to cell death. Lactate can be produced via anaerobic respiration and aerobic glycolysis [51]. We do not focus on the precise mechanisms of lactate production here, but instead determine how the media flow promotes lactate removal. We note that while colorectal cancer organoids can tolerate high lactate concentrations, the intention is to use CXP1 to expand a range of normal (healthy) and pathological organoids. Since different organoid types have distinct requirements (*e.g.* nutrient levels required for cell proliferation and lactate tolerances), understanding the mass transport of glucose and lactate within the bioreactor is important. While we acknowledge the biological complexity of organoid culture, spatiotemporal knowledge of these two metabolites provide useful and practical information on the operation of CXP1, and provides the framework for more complex models in the future.

Key priorities in the CXP1 bioreactor design and operation are uniformity of organoid size and system reproducibility, to ensure there is minimal variation in organoid characteristics between and within batches grown under the same operating conditions. Two of the main control parameters for the CXP1 bioreactor are the inlet flow rate (controlled via a peristaltic pump) and the initial cell seeding density (the organoids are grown from single cells). In this Chapter, we mainly focus on how metabolite transport is affected by inlet flow rate. Optimisation of these control parameters requires spatiotemporal information about the flow and metabolite (here glucose and lactate) concentrations throughout the bioreactor [29]. Such data are impractical, inefficient, and expensive to collect through experimental means alone.

2.1.1 Modelling approach

We develop a mathematical model of the CXP1 system, with the goal of determining how glucose and lactate levels within the CXP1 bioreactor change as the operating conditions (*e.g.* media inlet flow rate and cell seeding density) and organoid growth characteristics vary. We introduce a reaction-advection-diffusion system for glucose and lactate transport in the CXP1 bioreactor. The hydrogel and media are viewed as two distinct regions, coupled by interfacial conditions.

In this Chapter, we restrict our attention to a two-dimensional representation of the bioreactor, and obtain numerical solutions to the governing equations. Motivated by typical parameter values of the bioreactor, we perform an asymptotic analysis to systematically reduce the model from a two-dimensional geometry to a one-dimensional model, in which vertically-averaged concentration profiles vary with horizontal position along the length of the bioreactor. We validate this reduced model through successful comparisons with numerical solutions of the full system. We exploit the reduced models to explore the parameter space of cell characteristics and bioreactor operating regimes. To assess glucose and lactate levels, we introduce the following quantitative, time-dependent metrics: *glucose conversion* (the ratio between the total amounts of consumed and supplied glucose); *maximum lactate concentration* within the bioreactor; *proportion of domain with intolerable lactate levels* (*i.e.* lactate levels above a tolerated concentration); and *turn-off time* (the time when intolerable lactate levels are first experienced). For a given organoid type, we determine how these metrics change as the inlet flow rate varies. In this way, we aim to show how quantitative insights gained from this modelling approach can inform the selection of experimental bioreactor operating conditions, and ultimately improve the quality and quantity of bioreactor-expanded organoids.

2.1.2 Chapter outline

The structure of this Chapter is as follows. We begin with an outline of the experimental set-up of the CXP1 bioreactor in Section 2.2. In Section 2.3, we introduce the full mathematical model, and then systematically derive two reduced models (referred to as the *longwave approximation* and the *sublimit approximation*) for glucose and lactate transport within the bioreactor. In the Results (Section 2.5), we verify that simulations of the reduced models are in good agreement with solutions of the full model for physiologically relevant parameter regimes. We demonstrate the advantages of the model reductions, highlighting, in particular, the physical insights obtained from systematic derivation of the reduced models from the full system. We then use the longwave approximation model to investigate how the glucose and lactate concentrations within the bioreactor change for different organoid lines. We examine the evolution of the concentration profiles, and demonstrate how our quantitative metrics to assess metabolite behaviour are heavily dependent on organoid line characteristics, such as proliferation and nutrient consumption rates. We then investigate, for a specific organoid line, how the media inlet flow rate affects the metabolite concentrations, and explain how this information can be used to optimise the bioreactor control parameters. This Chapter concludes with a Discussion (Section 2.6) where we summarise and discuss the implications of our results.

2.2 Bioreactor set-up

2.2.1 CXP1 experimental set-up and operating protocol

We consider organoids grown from single cells seeded in a homogeneous thin layer of hydrogel in the bioreactor (lower yellow layer in Figure 2.1). A typical initial seeding density for the CXP1 bioreactor is 4×10^5 cell mL^{-1} $- 6 \times 10^5$ cell mL^{-1}. In reality, only 20% of cells seeded within the bioreactor evolve into organoids. However, for simplicity, we assume that all cells seeded within the hydrogel are viable and become organoids. We further assume that there is negligible settling, given the relative time of the gelation of the well-mixed solution compared to the settling time of the cells. The hydrogel acts as a porous scaffold for the seeded cells, providing the anchorage for cells and the biomechanical and biochemical cues required for cell growth [42]. The bioreactor is placed within an incubator which maintains constant temperature, O_2 (atmospheric levels) and CO_2 concentration. Nutrient-rich culture media, with typical glucose concentration of 16mM, is stored in an upstream reservoir and is fed into the

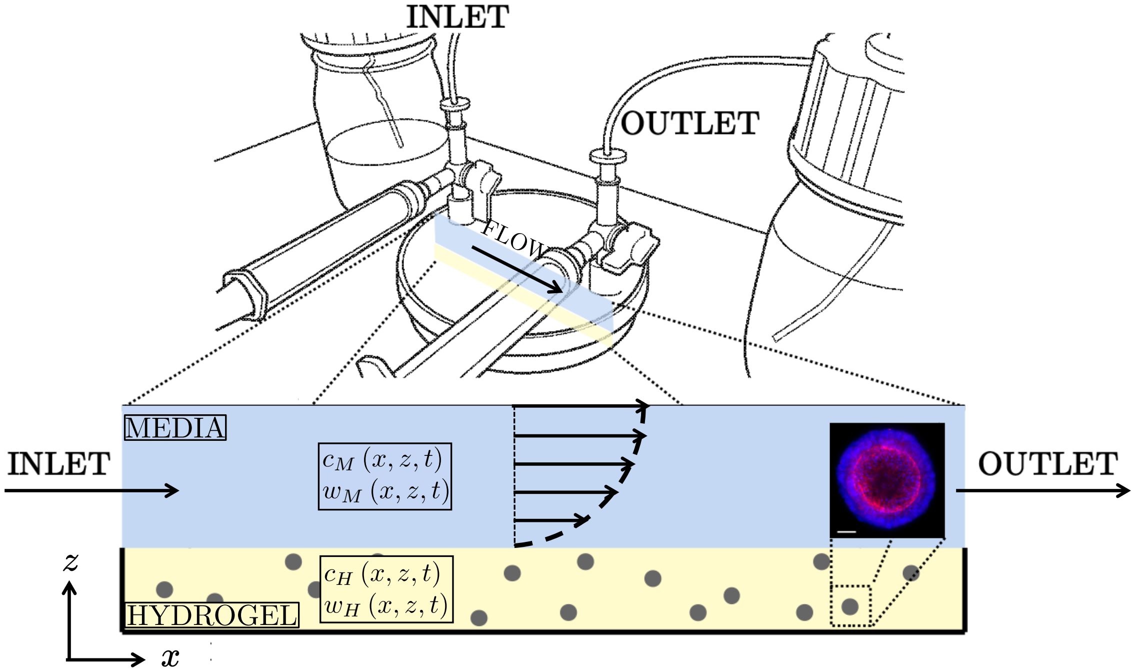

Figure 2.1: (**Top**) Schematic of 'CXP1' bioreactor [25]. (**Bottom**) Two-dimensional cross-section of the bioreactor, with arrows indicating the half-Poiseuille flow profile. Blue is media, yellow is hydrogel, grey is organoid biomass. The glucose concentrations within the media and hydrogel are given by c_M and c_H, respectively. Similarly, the lactate concentrations within hydrogel and media are denoted w_M and w_H, respectively. (**Bottom right**) Example of colorectal cancer organoid. Organoid stained for nuclear (blue) and cytoskeletal (red) markers for imaging. Scalebar 50µm. Reproduced with permission from Cellesce.

system through an inlet pipe, and slowly flows across the bioreactor (upper blue layer in Figure 2.1), with typical flow velocity of $10^{-6}\ \mathrm{m\,s^{-1}}$, controlled via peristaltic pump. The media is then removed from the bioreactor through an outlet pipe at the same rate, to ensure a constant volume of culture media within the bioreactor. The inlet and outlet pipes are held vertically and are partially submerged within the layer of culture media, sufficiently far away from the hydrogel as to not damage or disturb the surface of the hydrogel. The top of the culture media layer is a free surface. We assume no flow within the hydrogel: the hydrogel region is thin and the relatively low lateral pressure gradients suggest that flow in the hydrogel will be negligible. We consider colorectal cancer organoids, which are expanded in the bioreactor for 7 days. The organoids are grown from single stem cells (roughly 10µm in diameter) until they are approximately 40 – 80µm in diameter and comprise approximately 50 cells. The organoids are then extracted from the hydrogel and tested for size, viability, and number of cells per organoid. The total number of organoids per bioreactor is also recorded. Finally, the extracted organoids are frozen and stored for future use in, for example, drug assays.

Cellesce are able to obtain limited experimental data from the CXP1 bioreactor. At the end of the experiment, they can obtain the organoid size distributions and the number of cells per organoid from a representative averaged sample. However, the experiment must end in order to extract the organoids from the hydrogel for measurement. Furthermore, they cannot determine how the organoid size varies spatially, merely quantify the distribution of a small representative sample. Cellesce do not have the sensing technology to measure the metabolite concentrations spatially across the entire bioreactor. In the near future, they anticipate that they shall be able to measure the average metabolite concentrations (including glucose and lactate) entering and leaving CXP1 at the inlet and outlet, respectively, at minute intervals. Unfortunately, due to time and resource constraints, Cellesce were unable to provide sufficient data to validate the models developed within this thesis. We anticipate that when such information becomes available, we shall compare our models to the experimental data, and this is a key area of future work.

We consider the bioreactor design, *e.g.* the hydrogel and media depths, to be fixed, though we note that modelling can provide insights into the role of system geometry on the resulting metabolite concentrations. The glucose concentration in the upstream reservoir is also fixed. The key bioreactor operating parameter with which we are concerned is the media inlet flow rate. The key biological question we seek to answer using mathematical modelling is ‘how do the bioreactor operating conditions and cell characteristics influence the glucose and lactate concentrations within the CXP1 bioreactor’.

2.2.2 Parameter values

The CXP1 geometry and relevant parameter values (*e.g.* bioreactor length, hydrogel and culture media layer depths, maximum culture media flow velocity, and initial cell seeding density) are outlined in [25] and stated in Table 2.1. The hydrogel used in the CXP1 protocol is Corning Matrigel Matrix and the culture media is a modified form of Dulbecco’s modified Eagle medium (DMEM), both of which are described in [25].

The diffusivities of glucose and lactate in hydrogel and culture media used in our model are taken from the literature (see Table 2.1). Our model can be specialised for different cell lines, via characterisation of their rates of proliferation and glucose

Table 2.1: Definitions of dimensional model parameters, together with typical values. Where no citation is given, parameters are taken from the CPX1 set-up. We note that we have a two-dimensional domain, so the concentrations and cell densities are per unit area.

Parameter	Definition	Typical value
D_{CH}	Diffusivity of glucose in hydrogel	$6.0 \times 10^{-10}\mathrm{m}^2\,\mathrm{s}^{-1}$ [84]
D_{CM}	Diffusivity of glucose in media	$6.0 \times 10^{-10}\mathrm{m}^2\,\mathrm{s}^{-1}$ [83]
D_{WH}	Diffusivity of lactate in hydrogel	$1.2 \times 10^{-9}\mathrm{m}^2\,\mathrm{s}^{-1}$ [98]
D_{WM}	Diffusivity of lactate in media	$1.4 \times 10^{-9}\mathrm{m}^2\,\mathrm{s}^{-1}$ [77]
$c_{-\infty}$	Glucose concentration in upstream reservoir	$0.36\ \mathrm{mol}\,\mathrm{m}^{-2}$
$[u]$	Maximum velocity of media flow	$1 \times 10^{-6}\mathrm{m}\,\mathrm{s}^{-1}$
L	Length of bioreactor	$9 \times 10^{-2}\mathrm{m}$
h_H	Height of hydrogel layer	$1 \times 10^{-3}\mathrm{m}$
h_M	Combined height of hydrogel and media	$3 \times 10^{-3}\mathrm{m}$
N_0	Initial cell seeding density	$2.7 \times 10^{10}\mathrm{cell}\,\mathrm{m}^{-2}$ to $4 \times 10^{10}\mathrm{cell}\,\mathrm{m}^{-2}$
p	Cell proliferation rate	$3.9 \times 10^{-6}\mathrm{s}^{-1}$
ν_C	Rate of glucose consumption per unit cell density	$9.4 \times 10^{-17}\mathrm{m}^2\,\mathrm{cell}^{-1}\,\mathrm{s}^{-1}$

consumption. In Table 2.1, we state typical values for rates of cell proliferation and glucose consumption, estimated from CXP1 experimental data of several colorectal cancer organoid cell lines. We were also able to obtain averaged values for lactate concentration in the culture media layer at the end of the experiment empirically, which are similar to the values predicted by the model.

While the current CXP1 operating conditions have been empirically chosen to be specialised for colorectal cancer organoids, a key advantage of mathematical modelling is that it facilitates consideration of metabolite transport within CXP1 for other cell lines (which is the intent of Cellesce). This knowledge will streamline the adaptation of the CXP1 bioreactor to expanding organoids with significantly different behaviour, *e.g.* non-cancerous organoids.

2.3 Mathematical model

2.3.1 Governing equations

To model the system, we use a continuum modelling approach. We consider a two-dimensional representation of the bioreactor, and adopt a Cartesian coordinate system $\boldsymbol{x} = (x, z)$ with origin at the bottom-left corner of the domain (see Figure 2.1). We denote time by t. The hydrogel region of the bioreactor is $(x, z) \in [0,\, L] \times [0,\, h_H]$ (yellow region in Figure 2.1) and the media region is $(x, z) \in [0,\, L] \times [h_H,\, h_M]$ (blue region in Figure 2.1). We denote the glucose concentration by $c = c(x, z, t)$ and the lactate concentration by $w = w(x, z, t)$, with subscripts M and H to denote concentrations in the media and hydrogel, respectively. We define the model parameters introduced below, together with their typical values, in Table 2.1.

In the hydrogel, the glucose and lactate are transported via diffusion, and glucose is consumed by organoids, which subsequently produce lactate. For the organoids (cell aggregates), we model the reaction terms through effective (bulk) sink/source terms over the hydrogel. Such an approach can be mathematically justified through a formal averaging procedure, such as the asymptotic homogenisation carried out for related systems in [16, 18], and in Chapter 3 we perform such a homogenisation for this system (see Equation (3.3.45) and Equation (3.3.72) derived in Section 3.3). The equations governing metabolite transport within the hydrogel, $(x, z) \in [0,\, L] \times [0,\, h_H]$, are then:

$$\frac{\partial c_H}{\partial t} = D_{CH} \nabla^2 c_H - s(t, \boldsymbol{x}, c_H, w_H) n(t), \tag{2.3.1a}$$

$$\frac{\partial w_H}{\partial t} = D_{WH} \nabla^2 w_H + s_W(t, \boldsymbol{x}, c_H, w_H) n(t), \tag{2.3.1b}$$

where s and s_W denote the rates of glucose consumption and lactate production per cell, respectively (units $\mathrm{mol\,cell^{-1}\,s^{-1}}$) and $n(t)$ is the cell density at time t (units $\mathrm{cell\,m^{-2}}$). We assume the cells proliferate at rate p, so that the cell density is

$$n(t) = N_0 e^{pt}, \tag{2.3.2}$$

where N_0 is the spatially uniform initial cell-seeding density. While cell growth is likely to have some dependence on the glucose consumption and local lactate concentration, we assume, as a first approximation, that glucose and lactate concentrations are not growth-rate limiting. Thus, due to the spatially uniform initial cell density, the cell density does not vary in space. We will relax this assumption in later Chapters.

During glycolysis, one glucose molecule produces energy and two lactate molecules [51]. Motivated by this, we impose

$$s_W = 2s. \tag{2.3.3a}$$

In general, we expect the glucose consumption to be a monotonically increasing function of glucose concentration. For simplicity, we assume that

$$s(t, \boldsymbol{x}, c_H, w_H) = \nu_C c_H, \tag{2.3.3b}$$

where ν_C is a constant (units $\mathrm{m}^2\,\mathrm{cell}^{-1}\,\mathrm{s}^{-1}$) representing the rate of glucose consumption per unit cell density.

In the media, $(x, z) \in [0,\, L] \times [h_H,\, h_M]$, the advection-diffusion equations for metabolite transport are:

$$\frac{\partial c_M}{\partial t} + u(z)\frac{\partial c_M}{\partial x} = D_{CM}\nabla^2 c_M, \tag{2.3.4a}$$

$$\frac{\partial w_M}{\partial t} + u(z)\frac{\partial w_M}{\partial x} = D_{WM}\nabla^2 w_M, \tag{2.3.4b}$$

where $u(z)$ is the horizontal media flow, since we are considering a 2D representation of the problem. Given the slow nature of the flow and geometry of the flow domain, the flow is well-approximated by pressure-driven lubrication flow with a flat free surface, so that $u(z)$ is half-Poiseuille flow:

$$u(z) = [u]\frac{(z - h_H)^2}{(h_M - h_H)^2}, \tag{2.3.5}$$

where $[u]$ is the maximum flow velocity.

The governing equations (Equations (2.3.1) and (2.3.4)) require appropriate boundary, initial, and interfacial conditions. The boundaries in the hydrogel are solid walls and we impose zero flux of glucose and lactate at $x = 0, L$:

$$-D_{CH}\frac{\partial c_H}{\partial x} = -D_{WH}\frac{\partial w_H}{\partial x} = 0. \tag{2.3.6a}$$

We assume the concentrations of glucose and lactate in the inlet pipe are maintained at the constant values $c_{-\infty}$ and 0, respectively. Since controlling the media flow rate, and hence controlling the flux of metabolite into and out of the bioreactor, is key to CXP1 operation, we impose conditions on the metabolite flux at the inlet and outlet. We then assume pointwise continuity of metabolite flux at the inlet, $x = 0$:

$$u(z)c_M - D_{CM}\frac{\partial c_M}{\partial x} = u(z)c_{-\infty},\ u(z)w_M - D_{WM}\frac{\partial w_M}{\partial x} = 0; \tag{2.3.6b}$$

and we impose no diffusive flux of metabolites at the outlet, $x = L$:

$$-D_{CM}\frac{\partial c_M}{\partial x} = -D_{WM}\frac{\partial w_M}{\partial x} = 0, \tag{2.3.6c}$$

noting that the metabolites can leave the bioreactor via advection. We impose no-flux conditions for the metabolites at the base of the hydrogel, $z = 0$, and at the top of the media layer, $z = h_M$:

$$-D_{CH}\frac{\partial c_H}{\partial z} = -D_{WH}\frac{\partial w_H}{\partial z} = 0 \quad \text{at } z = 0, \tag{2.3.6d}$$

$$-D_{CM}\frac{\partial c_M}{\partial z} = -D_{WM}\frac{\partial w_M}{\partial z} = 0 \quad \text{at } z = h_M. \tag{2.3.6e}$$

At the media-hydrogel interface, $z = h_H$, we impose continuity of metabolite concentration and flux:

$$c_M = c_H, \quad w_M = w_H, \tag{2.3.6f}$$

$$D_{CM}\frac{\partial c_M}{\partial z} = D_{CH}\frac{\partial c_H}{\partial z}, \quad D_{WM}\frac{\partial w_M}{\partial z} = D_{WH}\frac{\partial w_H}{\partial z}. \tag{2.3.6g}$$

A schematic of these boundary conditions on the domain geometry is given in Figure 2.2.

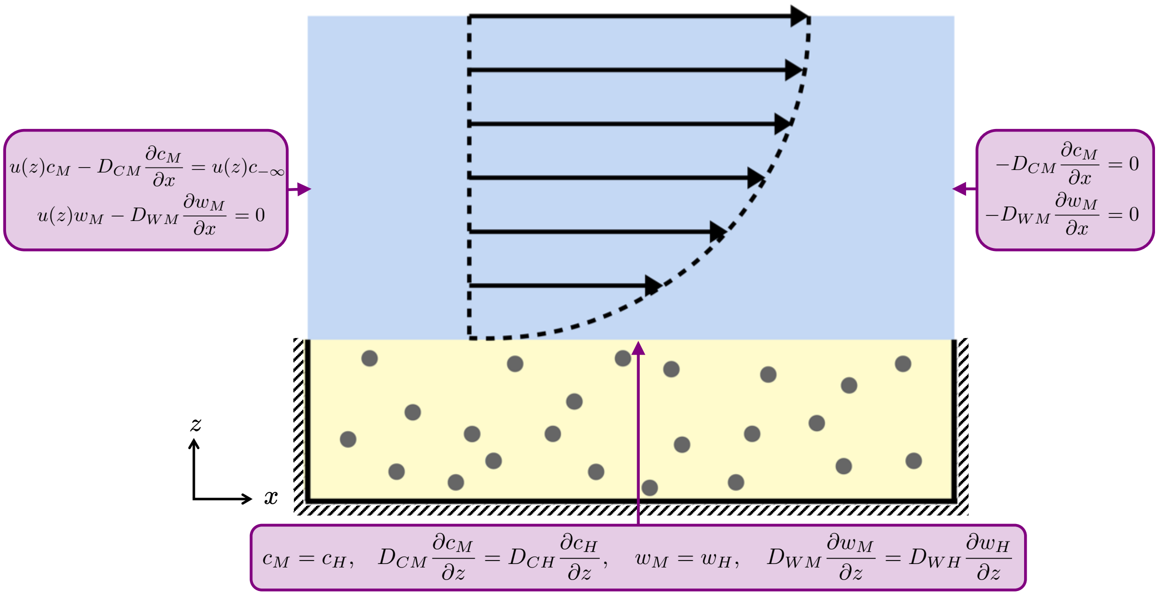

Figure 2.2: Schematic of the boundary conditions (Equation (2.3.6)) for the media (blue) and hydrogel (yellow) layers for Equations (2.3.1) and (2.3.4). At the media-hydrogel interface, we impose continuity of concentration and flux. At the air-media interface and at the impermeable hashed boundaries, we impose no flux. The black arrows indicate the half-Poiseuille flow profile.

As initial conditions, we assume that the glucose concentration in the media equals the glucose concentration in the upstream reservoir, $c = c_{-\infty}$, the glucose concentration in the hydrogel is zero, and that there is no lactate throughout the bioreactor:

$$c_H = 0, \quad c_M = c_{-\infty}, \quad w_H = w_M = 0 \quad \text{at } t = 0. \tag{2.3.7}$$

2.3.2 Typical timescales

The typical parameter values, given in Table 2.1, reveal that the physical processes included in our model broadly act over three different timescales: hours, days, and months, as shown in Table 2.2. Diffusion in the z-direction occurs over the timescale of hours; media flow, glucose consumption, lactate production, and cell proliferation occur over the timescale of a day; and x-diffusion occurs over the timescale of months. This scaling analysis reveals that flow markedly enhances metabolite transport in the x-direction and that, within the media, advection dominates diffusive transport of metabolites in the horizontal direction. The separation of timescales renders the system stiff and, as such, care is needed when implementing numerical methods for its solution. At the same time, it leads naturally to the identification of large and small dimensionless parameters which can be exploited for model reduction (see Section 2.4).

Table 2.2: Timescale groupings of the various physical processes present in the CXP1 bioreactor. We use 'x' and 'z' to denote 'horizontal' and 'vertical', respectively. The timescale for each process is the value such that the each dimensionless parameter grouping, defined in Equation (2.3.11), as the ratio of the timescale of interest to the timescale of the physical process, is equal to one.

	Physical process	Timescale
$\mathcal{O}(\text{hour})$	z-diffusion glucose in hydrogel	$\dfrac{\epsilon^2 L^2}{D_{CH}} = 1.5 \times 10^4\text{s} = 4.2\text{h}$
	z-diffusion glucose in media	$\dfrac{\epsilon^2 L^2}{D_{CM}} = 1.5 \times 10^4\text{s} = 4.2\text{h}$
	z-diffusion lactate in hydrogel	$\dfrac{\epsilon^2 L^2}{D_{WH}} = 7500\text{s} = 2.1\text{h}$
	z-diffusion lactate in media	$\dfrac{\epsilon^2 L^2}{D_{WM}} = 6400\text{s} = 1.8\text{h}$
$\mathcal{O}(\text{day})$	flow	$\dfrac{L}{[u]} = 9 \times 10^4\text{s} = 25\text{h}$
	glucose consumption	$\dfrac{1}{\nu_C N_0} = 2.7 \times 10^5 - 4 \times 10^5\text{s} = 74 - 110\text{h}$
	lactate production	$\dfrac{1}{2\nu_C N_0} = 1.3 \times 10^5 - 2.0 \times 10^5\text{s} = 37 - 55\text{h}$
	cell proliferation	$\dfrac{1}{p} = 2.6 \times 10^5\text{s} = 72\text{h}$
$\mathcal{O}(\text{month})$	x-diffusion glucose in hydrogel	$\dfrac{L^2}{D_{CH}} = 1.4 \times 10^7\text{s} = 3800\text{h}$
	x-diffusion glucose in media	$\dfrac{L^2}{D_{CM}} = 1.4 \times 10^7\text{s} = 3800\text{h}$
	x-diffusion lactate in hydrogel	$\dfrac{L^2}{D_{WH}} = 6.8 \times 10^6\text{s} = 1900\text{h}$
	x-diffusion lactate in media	$\dfrac{L^2}{D_{WM}} = 5.8 \times 10^6\text{s} = 1600\text{h}$

2.3.3 Non-dimensionalisation

We non-dimensionalise the problem to formally identify the relative importance of each transport mechanism. We introduce the following non-dimensional variables, for $i \in \{H, M\}$:

$$X = \frac{x}{L},\ Z = \frac{z}{\epsilon L},\ T = \frac{t}{[t]},\ U(Z) = \frac{u}{[u]},\ C_i = \frac{c_i}{c_{-\infty}},\ W_i = \frac{w_i}{c_{-\infty}}, \tag{2.3.8}$$

where $\boldsymbol{X} = (X, Z)$, $\epsilon = h_M/L \ll 1$ is the ratio between vertical and horizontal lengthscales, $[t]$ is the timescale, and $[u]$ is the maximum flow velocity. The bioreactor domain is then $(X, Z) \in [0, 1] \times [0, 1]$ and the media-hydrogel interface is at dimensionless position $Z = H_H =: h_H/(\epsilon L) = \mathcal{O}(1)$. Metabolite concentrations are non-dimensionalised with the upstream reservoir glucose concentration, $c_{-\infty}$. We fix the timescale of interest to be 1 day, so that we consider the transport on the same timescale as cell growth, and also for ease of interpretation in terms of the experimental run-time being 7 days.

Using the scalings Equation (2.3.8), the governing equations (Equations (2.3.1) and (2.3.4)) become, for $X \in [0, 1]$,

$$\epsilon^2 \frac{\partial C_H}{\partial T} = d_{CH}\left(\epsilon^2 \frac{\partial^2 C_H}{\partial X^2} + \frac{\partial^2 C_H}{\partial Z^2}\right) - \epsilon^2 \sigma C_H e^{PT} \qquad \text{for } Z \in [0, H_H), \tag{2.3.9a}$$

$$\epsilon^2 \frac{\partial W_H}{\partial T} = d_{WH}\left(\epsilon^2 \frac{\partial^2 W_H}{\partial X^2} + \frac{\partial^2 W_H}{\partial Z^2}\right) + 2\epsilon^2 \sigma C_H e^{PT} \qquad \text{for } Z \in [0, H_H), \tag{2.3.9b}$$

$$\epsilon^2 \frac{\partial C_M}{\partial T} + \epsilon^2 \lambda U(Z) \frac{\partial C_M}{\partial X} = d_{CM}\left(\epsilon^2 \frac{\partial^2 C_M}{\partial X^2} + \frac{\partial^2 C_M}{\partial Z^2}\right) \qquad \text{for } Z \in (H_H, 1], \tag{2.3.9c}$$

$$\epsilon^2 \frac{\partial W_M}{\partial T} + \epsilon^2 \lambda U(Z) \frac{\partial W_M}{\partial X} = d_{WM}\left(\epsilon^2 \frac{\partial^2 W_M}{\partial X^2} + \frac{\partial^2 W_M}{\partial Z^2}\right) \qquad \text{for } Z \in (H_H, 1], \tag{2.3.9d}$$

with

$$U(Z) = \frac{(Z - H_H)^2}{(1 - H_H)^2}. \tag{2.3.10}$$

The dimensionless parameters in Equations (2.3.9) and (2.3.10) are:

$$\begin{gathered} \lambda = \frac{[u][t]}{L}, \quad \sigma = [t]\nu_C N_0, \quad P = p[t], \\ (d_{CH}, d_{CM}, d_{WH}, d_{WM}) = \frac{[t]}{L^2}(D_{CH}, D_{CM}, D_{WH}, D_{WM}). \end{gathered} \tag{2.3.11}$$

We provide a physical interpretation of these dimensionless parameters and their typical values in Table 2.3. The boundary and initial conditions, Equations (2.3.6) and (2.3.7), become:

$$-\,d_{CH}\frac{\partial C_H}{\partial X} = 0, \qquad -\,d_{WH}\frac{\partial W_H}{\partial X} = 0 \quad \text{at } X = 0, 1, \tag{2.3.12a}$$

$$\lambda U C_M - d_{CM}\frac{\partial C_M}{\partial X} = \lambda U, \quad \lambda U W_M - d_{WM}\frac{\partial W_M}{\partial X} = 0 \quad \text{at } X = 0, \tag{2.3.12b}$$

$$-d_{CM}\frac{\partial C_M}{\partial X} = -d_{WM}\frac{\partial W_M}{\partial X} = 0 \quad \text{at } X = 1, \tag{2.3.12c}$$

$$-d_{CH}\frac{\partial C_H}{\partial Z} = -d_{WH}\frac{\partial W_H}{\partial Z} = 0 \quad \text{at } Z = 0, \tag{2.3.12d}$$

$$-d_{CM}\frac{\partial C_M}{\partial Z} = -d_{WM}\frac{\partial W_M}{\partial Z} = 0 \quad \text{at } Z = 1, \tag{2.3.12e}$$

$$C_M = C_H, \quad W_M = W_H \quad \text{at } Z = H_H, \tag{2.3.12f}$$

$$d_{CH}\frac{\partial C_H}{\partial Z} = d_{CM}\frac{\partial C_H}{\partial Z}, \quad d_{WH}\frac{\partial W_H}{\partial Z} = d_{WM}\frac{\partial W_M}{\partial Z} \quad \text{at } Z = H_H, \tag{2.3.12g}$$

$$C_H = 0, \quad C_M = 1, \quad W_H = W_M = 0 \quad \text{at } T = 0. \tag{2.3.12h}$$

Table 2.3: Definitions of dimensionless model parameters with their typical values. For the simulations in this Chapter, we take $\sigma = 0.27$ unless otherwise stated. We note that these parameters are all ratios of the relevant transport mechanism compared to one day.

Parameter	Definition	Typical value
ϵ	Ratio of vertical to horizontal lengthscales	1/30
d_{CH}	Dimensionless diffusivity of glucose in hydrogel	6.4×10^{-3}
d_{CM}	Dimensionless diffusivity of glucose in media	6.4×10^{-3}
d_{WH}	Dimensionless diffusivity of lactate in hydrogel	1.28×10^{-2}
d_{WM}	Dimensionless diffusivity of lactate in media	1.49×10^{-2}
λ	Dimensionless maximum media flow velocity	0.96
σ	Dimensionless glucose consumption rate per cell	0.22-0.32
P	Dimensionless cellular proliferation rate	1/3
H_H	Dimensionless position of hydrogel-media interface	1/3
W_{tol}	Dimensionless maximum tolerated lactate concentration	0.7

2.3.4 Numerical solution of full model

We solve the full two-dimensional system, Equations (2.3.9) and (2.3.12), using the parameter values given in Table 2.3, via a finite-element method, using COMSOL Multiphysics® software, with a suitable time-stepper to deal with the stiff nature of the system. The results were shown to be mesh convergent (results not shown). In Figure 2.3 we plot the metabolite concentration profiles at dimensionless times $T = 1, 3, 7$, corresponding to one, three and seven days in dimensional time. Note that we observe very little variation in metabolite concentration in the vertical direction for the parameter values given in Table 2.3.

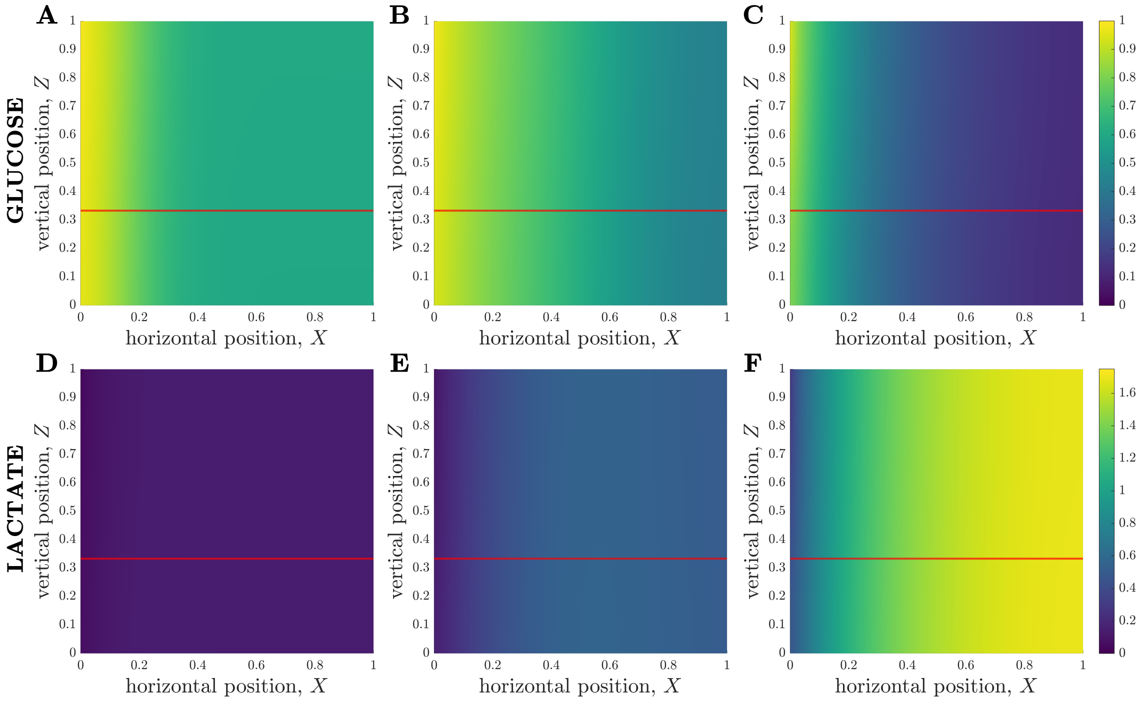

Figure 2.3: Metabolite concentrations at 1, 3, and 7 days into a typical simulation. The horizontal lines at $Z = 1/3$ represents the media-hydrogel interface. (**Top**) Glucose distribution $C(X, Z, T)$ at (**A**) $T = 1$, (**B**) $T = 3$, (**C**) $T = 7$. (**Bottom**) Lactate distribution $W(X, Z, T)$ at (**D**) $T = 1$, (**E**) $T = 3$, (**F**) $T = 7$. Parameter values given in Table 2.3.

2.4 Model reduction

As discussed in Section 2.3.2, the different transport mechanisms in the system have associated timescales that can be broadly grouped into either hours, days, or months. This is made explicit in the dimensionless system through the presence of the small parameter ϵ. We propose a systematic model reduction, with the key advantage of reducing the complexity of the model while retaining the physical processes which dominate over the timescale of interest.

2.4.1 Longwave approximation

Motivated by the long, thin geometry of the bioreactor, characterised by $\epsilon \ll 1$, and the lack of variation in Z compared to X revealed in Figure 2.3, we now systematically average Equations (2.3.9) and (2.3.12) in Z to derive the appropriate reduced lubrication model, referred to as the *longwave approximation*.

In the asymptotic analysis that follows, we consider the limit $\epsilon \to 0$, and assume all other dimensionless parameters remain $\mathcal{O}(1)$ as $\epsilon \to 0$. This distinguished limit is in the same parameter regime as the values of dimensionless parameters given in Table 2.3, and assumes that diffusion in the vertical direction is the dominant transport mechanism for the bioreactor geometry. We note that our choice of time scaling, $[t] = 1$ day, means that we are investigating this system over the timescale of days, which is the flow timescale. We could study the behaviour of this system over shorter timescales, and its transition to the timescale of days, if we systematically considered the timescale $T = \mathcal{O}(\epsilon^2)$. However, this will not be of fundamental physical importance to the problem we study here, so we do not pursue this further.

We consider the following asymptotic expansions for the dependent variables:

$$f \sim f_0 + \epsilon^2 f_1 + \cdots, \text{ as } \epsilon \to 0, \text{ where } f \in \{C_M, C_H, W_M, W_H\}. \tag{2.4.1}$$

We note that the $\mathcal{O}(\epsilon^2)$ size of the first-correction term is standard in lubrication-type models, and arises due to the size of the terms neglected in the leading-order problem. In the standard manner, we substitute Equation (2.4.1) into the governing equations, Equations (2.3.9) and (2.3.12), and equate coefficients of $\mathcal{O}(\epsilon^k)$.

At leading order, the metabolite transport is given by

$$0 = \frac{\partial^2 f_{j0}}{\partial Z^2} \text{ where } f \in \{C, W\} \text{ and } j \in \{H, M\}. \tag{2.4.2}$$

Hence, we see that the leading-order mass transport is driven entirely by vertical diffusion, consistent with our discussion of timescales above.

Integrating Equation (2.4.2) subject to the leading-order versions of the appropriate boundary conditions, Equations (2.3.12d) to (2.3.12g), we deduce that C_{H0}, C_{M0}, W_{H0}, and W_{M0} are independent of vertical position, Z. This is consistent with the numerical solutions seen in Figure 2.3. Given the continuity of concentration condition, Equation (2.3.12f), we deduce that

$$C_{H0}(X,T) = C_{M0}(X,T), \quad W_{H0}(X,T) = W_{M0}(X,T) \quad \text{for all } Z. \tag{2.4.3}$$

However, the correct dependence of the metabolite profiles on T and X is currently undetermined.

To calculate this dependence, we proceed to the next asymptotic order $\mathcal{O}(\epsilon^2)$, and derive an appropriate system. At $\mathcal{O}(\epsilon^2)$, the governing equations are

$$d_{CH}\frac{\partial^2 C_{H1}}{\partial Z^2} = \frac{\partial C_{H0}}{\partial T} - d_{CH}\frac{\partial^2 C_{H0}}{\partial X^2} + \sigma C_{H0}e^{pT} \qquad \text{for } Z \in (0, H_H), \tag{2.4.4a}$$

$$d_{WH}\frac{\partial^2 W_{H1}}{\partial Z^2} = \frac{\partial W_{H0}}{\partial T} - d_{WH}\frac{\partial^2 W_{H0}}{\partial X^2} - 2\sigma C_{H0}e^{pT} \qquad \text{for } Z \in (0, H_H), \tag{2.4.4b}$$

$$d_{CM}\frac{\partial^2 C_{H1}}{\partial Z^2} = \frac{\partial C_{M0}}{\partial T} + \lambda U(Z)\frac{\partial C_{M0}}{\partial X} - d_{CM}\frac{\partial^2 C_{M0}}{\partial X^2} \qquad \text{for } Z \in (H_H, 1), \tag{2.4.4c}$$

$$d_{WM}\frac{\partial^2 W_{H1}}{\partial Z^2} = \frac{\partial W_{M0}}{\partial T} + \lambda U(Z)\frac{\partial W_{M0}}{\partial X} - d_{WM}\frac{\partial^2 W_{M0}}{\partial X^2} \qquad \text{for } Z \in (H_H, 1). \tag{2.4.4d}$$

Integrating each equation over the vertical coordinate and applying the no-flux conditions Equations (2.3.12d) and (2.3.12e) at $\mathcal{O}(\epsilon^2)$ yields:

$$d_{CH}\frac{\partial C_{H1}}{\partial Z}\bigg|_{Z=H_H} = H_H\left(\frac{\partial C_{H0}}{\partial T} - d_{CH}\frac{\partial^2 C_{H0}}{\partial X^2} + \sigma C_{H0}e^{PT}\right), \tag{2.4.5a}$$

$$d_{WH}\frac{\partial W_{H1}}{\partial Z}\bigg|_{Z=H_H} = H_H\left(\frac{\partial W_{H0}}{\partial T} - d_{WH}\frac{\partial^2 W_{H0}}{\partial X^2} - 2\sigma C_{H0}e^{PT}\right), \tag{2.4.5b}$$

$$-d_{CM}\frac{\partial C_{M1}}{\partial Z}\bigg|_{Z=H_H} = (1 - H_H)\left(\frac{\partial C_{M0}}{\partial T} + \lambda\bar{U}\frac{\partial C_{M0}}{\partial X} - d_{CM}\frac{\partial^2 C_{M0}}{\partial X^2}\right), \tag{2.4.5c}$$

$$-d_{WM}\frac{\partial W_{M1}}{\partial Z}\bigg|_{Z=H_H} = (1 - H_H)\left(\frac{\partial W_{M0}}{\partial T} + \lambda\bar{U}\frac{\partial W_{M0}}{\partial X} - d_{WM}\frac{\partial^2 W_{M0}}{\partial X^2}\right), \tag{2.4.5d}$$

where the depth-averaged flow velocity, $\bar{U}$, is found (from Equation (2.3.10)) to be given by:

$$\bar{U} = \frac{1}{1 - H_H}\int_{H_H}^{1} U(Z)\ \mathrm{d}Z = \frac{1}{3}. \tag{2.4.6}$$

Recalling the continuity of flux condition, Equation (2.3.12g), and that $C_{H0} = C_{M0}$ and $W_{H0} = W_{M0}$, we combine the above expressions for the glucose and lactate concentrations in the media and hydrogel to derive the *longwave approximation*:

$$\alpha\frac{\partial C_{M0}}{\partial T} + \beta\frac{\partial C_{M0}}{\partial X} = \delta_C\frac{\partial^2 C_{M0}}{\partial X^2} - \gamma C_{M0}e^{PT}, \tag{2.4.7a}$$

$$\alpha\frac{\partial W_{M0}}{\partial T} + \beta\frac{\partial W_{M0}}{\partial X} = \delta_W\frac{\partial^2 W_{M0}}{\partial X^2} + 2\gamma C_{M0}e^{PT}, \tag{2.4.7b}$$

where we have introduced the following parameters for ease of notation:

$$\begin{gathered}\theta = \frac{H_H}{1 - H_H}, \ \ \alpha = 1 + \theta, \ \ \beta = \lambda\bar{U}, \ \ \gamma = \theta\sigma, \\ \delta_C = d_{CM} + \theta d_{CH}, \ \ \delta_W = d_{WM} + \theta d_{WH}.\end{gathered} \tag{2.4.8}$$

We derive the appropriate boundary and 'initial' conditions for Equation (2.4.7) in a similar manner, by integrating the leading over terms of Equations (2.3.12a) to (2.3.12c) and (2.3.12h) over Z between 0 and 1. We solve Equation (2.4.7) subject to the following boundary and 'initial' conditions:

$$\beta C_{M0} - \delta_C \frac{\partial C_{M0}}{\partial X} = \beta \text{ at } X = 0, \tag{2.4.9a}$$

$$\beta W_{M0} - \delta_W \frac{\partial W_{M0}}{\partial X} = 0 \text{ at } X = 0, \tag{2.4.9b}$$

$$\frac{\partial C_{M0}}{\partial X} = \frac{\partial W_{M0}}{\partial X} = 0 \text{ at } X = 1, \tag{2.4.9c}$$

$$C_{M0} = \frac{1}{\alpha} \quad W_{M0} = 0 \text{ at } T = 0 \text{ for } 0 \leq X \leq 1. \tag{2.4.9d}$$

The reason we refer to Equation (2.4.9d) as 'initial' conditions is because they actually represent asymptotic matching conditions with the earlier timescale problem we mentioned previously. This is the reason why there is a discontinuity in the boundary and 'initial' conditions as $X, T \to 0$. If it were of interest to understand this limit further, one could investigate this region using the scalings $X = \mathcal{O}(\epsilon)$, $T = \mathcal{O}(\epsilon^2)$. However, given that this asymptotic region does not affect any of our subsequent analysis, for brevity we do not pursue it further here.

Equations (2.4.7) and (2.4.9) define the longwave approximation model. We will analyse this reduced system in more detail in Section 2.5. Before this, however, we derive a further reduction of the longwave approximation, by exploiting the separation in scales between horizontal diffusion and the remaining transport mechanisms, namely advection with the media flow, glucose consumption, and lactate production.

2.4.2 Sublimit of longwave approximation

From the typical parameter values given in Table 2.3, we note that the timescale of horizontal diffusion is significantly longer than the remaining transport mechanisms. Given that the longwave approximation derived in Section 2.4.1 is a distinguished asymptotic limit, we can include the separation of scales involved in horizontal diffusion by directly considering the sub-limit d_{CH}, d_{CM}, d_{WH}, $d_{WM} \to 0$, corresponding to δ_C, $\delta_W \to 0$ in Equations (2.4.7) and (2.4.9).

We refer to this as the *sublimit approximation.* This procedure results in the following governing equations for advection-dominated transport:

$$\alpha \frac{\partial C_{M0}}{\partial T} + \beta \frac{\partial C_{M0}}{\partial X} = -\gamma C_{M0} \exp(PT), \tag{2.4.10a}$$

$$\alpha \frac{\partial W_{M0}}{\partial T} + \beta \frac{\partial W_{M0}}{\partial X} = 2\gamma C_{M0} \exp(PT), \tag{2.4.10b}$$

with boundary and initial conditions

$$C_{M0} = 1, \quad W_{M0} = 0 \quad \text{at } X = 0, \tag{2.4.11a}$$

$$C_{M0} = \frac{1}{\alpha}, \quad W_{M0} = 0 \quad \text{at } T = 0. \tag{2.4.11b}$$

We note that the limit we have taken is singular in that the small parameters (diffusivities) pre-multiply the second-order spatial derivatives. As such, we have lost the ability to prescribe two of the four spatial boundary conditions. Given that the information in this system travels with the flow (*i.e.* from left to right), we drop the outlet boundary condition at $X = 1$. We note, however, that this boundary condition could be imposed through the analysis of an appropriate (weak) boundary layer near $X = 1$.

A benefit of this sublimit reduction is that we are able to construct analytic solutions for the glucose and lactate concentrations, using the method of characteristics. We note that the equation governing glucose transport (Equation (2.4.10a)) decouples from the lactate transport model (Equation (2.4.10b)). Therefore, we first solve for glucose concentration, and then solve for the lactate concentration. The method of characteristics involves introducing coordinates in characteristic space, (ξ, τ), where we define

$$\xi = \alpha X - \beta T, \tag{2.4.12}$$

noting that ξ is a constant along each characteristic curve, and τ parameterises the characteristics. The governing equations (Equation (2.4.10)) turn into a system of ODEs, with initial data curve $\Gamma(\xi) = (T(\xi), X(\xi), C_{M0}(\xi))$ at $\tau = 0$. The data consist of the initial condition (Equation (2.4.11b)) for $\xi > 0$ and the boundary condition (Equation (2.4.11a)) for $\xi < 0$. This data curve $\Gamma(\xi)$ has a discontinuity at $\xi = 0$, due to the inconsistent nature of the boundary and initial conditions, Equation (2.4.11). We give a detailed derivation of our application of method of characteristics to solve Equations (2.4.10) and (2.4.11) in Appendix A.

The solution is split into two distinct regions: Region 1, given by $0 < \beta T < \alpha X$; and Region 2, given by $0 < \alpha X < \beta T$:

$$C_{M0} = \begin{cases} \dfrac{1}{\alpha} \exp\left(\dfrac{\gamma}{\alpha P}\left(1 - e^{PT}\right)\right) & \text{for } 0 < \beta T < \alpha X, \quad (2.4.13a) \\ \exp\left(\dfrac{\gamma}{\alpha P}\left(e^{-P\left(\frac{\alpha}{\beta}X - T\right)} - e^{PT}\right)\right) & \text{for } 0 < \alpha X < \beta T. \quad (2.4.13b) \end{cases}$$

The solution Equation (2.4.13) is discontinuous across the boundary separating the two regions, $X = \beta T/\alpha$, which we refer to as the *dividing characteristic*. The reason for this is that Region 1 is forced by the initial conditions whereas Region 2 is forced by the boundary conditions, and there is a discontinuity in these conditions near $T = 0$, $X = 0$ (which could be smoothed through an appropriate asymptotic analysis of the earlier timescale, as mentioned previously). As no information from the boundary condition propagates into Region 1, cells in Region 1 do not feel the effect of any replenishment by the flow. As such, we refer to Region 1 as the *unreplenished region* and Region 2 as the *replenished region*. We show a schematic of the domain split into these regions in Figure 2.4.

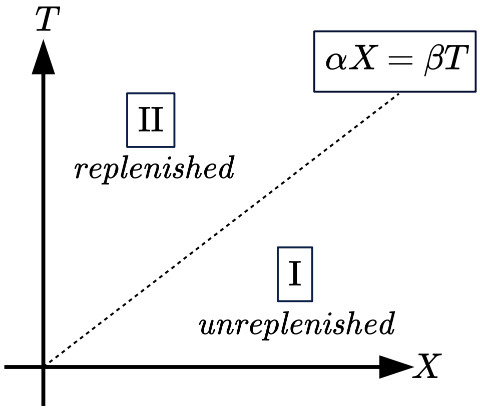

Figure 2.4: Characteristic diagram for the system Equations (2.4.10) and (2.4.11).

Using the method of characteristics, we can write the lactate concentration as a single integral of known functions:

$$W_{M0}(\xi,\tau) = \int_0^\tau 2\gamma C_{M0}(T(\xi,\tau), X(\xi,\tau))e^{PT(\xi,\tau)}\,\mathrm{d}\tau \tag{2.4.14a}$$

with

$$W_{M0} = 0 \quad \text{at } \tau = 0, \tag{2.4.14b}$$

where we define the characteristic variables (ξ, τ) as

$$\xi = \alpha X - \beta T \quad \text{and} \quad \tau = \begin{cases} \dfrac{T}{\alpha} & \text{for } \beta T < \alpha X, & (2.4.15a) \\ \dfrac{X}{\beta} & \text{for } \alpha X < \beta T. & (2.4.15b) \end{cases}$$

As outlined in Appendix A, we can evaluate the integral in Equation (2.4.14) to obtain the solution

$$W_{M0} = \begin{cases} \dfrac{2}{\alpha}\left(1 - \exp\left(\dfrac{\gamma}{P\alpha}\left(1 - e^{PT}\right)\right)\right) & \text{for } 0 < \beta T < \alpha X, & (2.4.16a) \\ 2\left(1 - \exp\left(\dfrac{\gamma}{P\alpha}\left(e^{-P\left(\frac{\alpha}{\beta}X - T\right)} - e^{PT}\right)\right)\right) & \text{for } 0 < \alpha X < \beta T. & (2.4.16b) \end{cases}$$

We note that the quantity $2C_{M0} + W_{M0}$ is conserved along the characteristics defined by $\mathrm{d}X/\mathrm{d}T = \alpha/\beta$ (*i.e.* in the advective frame of reference). This means that the following relationships are satisfied between glucose and lactate concentrations:

$$2C_{M0} + W_{M0} = \frac{2}{\alpha} \quad \text{for } 0 < \beta T < \alpha X, \tag{2.4.17a}$$

$$2C_{M0} + W_{M0} = 2 \quad \text{for } 0 < \alpha X < \beta T, \tag{2.4.17b}$$

where the differing constants are due to the 'initial' information on the characteristics arising from the actual initial conditions for $0 < \beta T < \alpha X$ (Region 1) and the replenishment boundary conditions for $0 < \alpha X < \beta T$ (Region 2).

2.5 Results

2.5.1 Methods for numerical solution of models

The full two-dimensional system, Equations (2.3.9) and (2.3.12), is solved via a finite-element method, using COMSOL Multiphysics® software. The longwave approximation model, Equations (2.4.7) and (2.4.9), is solved numerically using the Chebfun toolbox in MATLAB [20], with a tolerance of 10^{-6}. For the sublimit approximation model, Equations (2.4.10) and (2.4.11), we obtain an analytical expression for the glucose and lactate concentrations. For each numerical approach, the solutions were shown to be mesh convergent (results not shown).

Computationally, there is a significant difference between the models: on a standard desktop, the full problem is solved in $\mathcal{O}(180\text{s})$; the longwave approximation in $\mathcal{O}(20\text{s})$; and the sublimit approximation in $\mathcal{O}(4\text{s})$. That is, there is a nearly ten-fold speed-up in solving the longwave approximation compared to the full model, and the sublimit is five times quicker to solve than the longwave approximation and fifty times quicker than the full model. As we see later (Section 2.5.3), rapid computation of solutions will allow us to perform parameter sensitivity analyses efficiently, and in Section 2.5.2 that it allows us to obtain physical insight into the system.

2.5.2 Model behaviour and comparison

We now discuss and compare results obtained from our reduced models and the full system. This will allow us to understand when each reduced model is a useful systematic reduction. We denote the glucose and lactate concentrations (the leading-order metabolite concentrations in the culture media layer C_{M0} and W_{M0}) as C and W, respectively.

To present the model solutions over space and time, we average solutions of the full 2D model over Z, to facilitate comparison with solutions of the reduced models

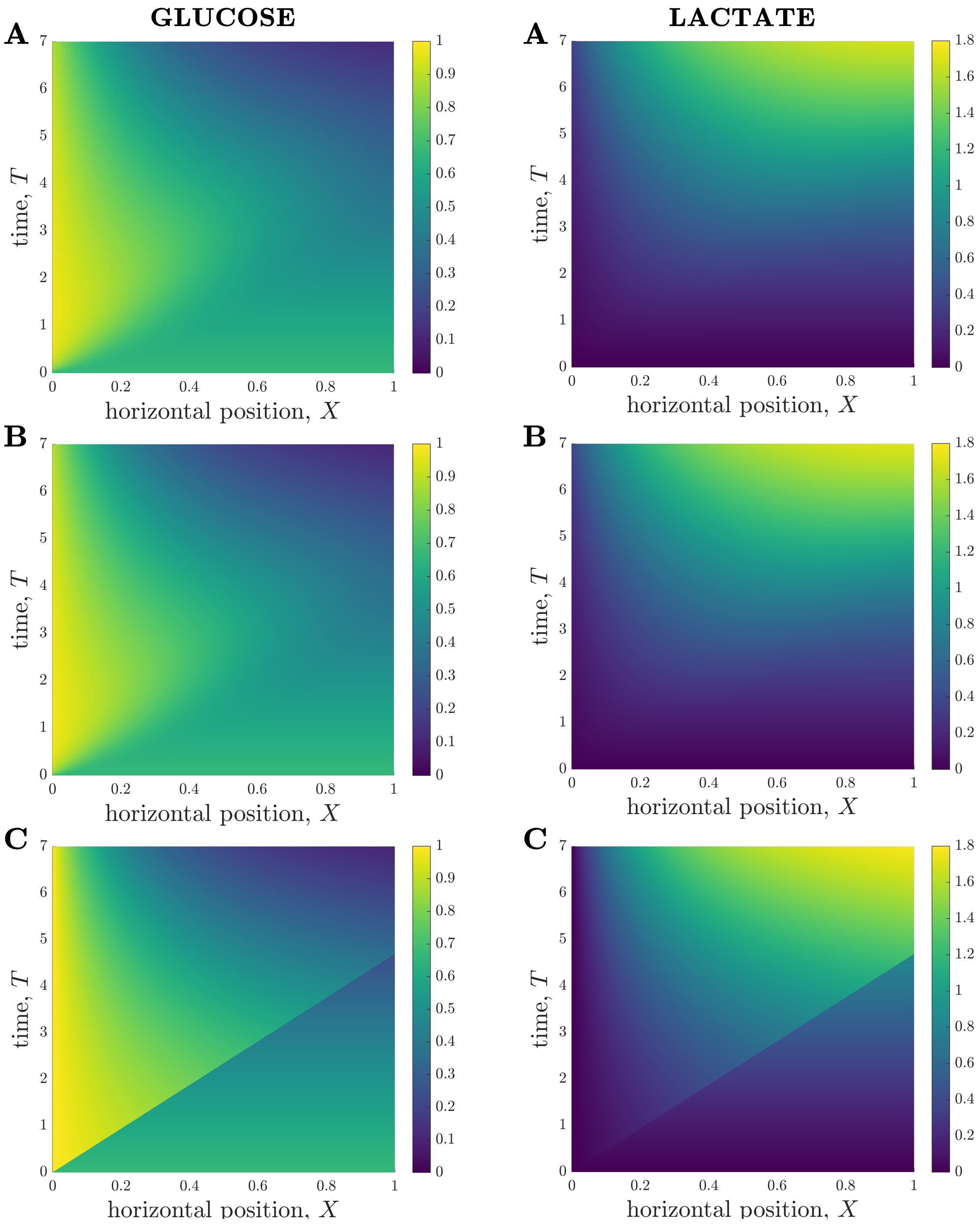

(a) Glucose concentration

(b) Lactate concentration

Figure 2.5: Results showing how the glucose (a) and lactate (b) concentrations change over time during a typical simulation. (**A**) Results from Z-averaged full model. (**B**) Longwave approximation. (**C**) Sublimit of longwave approximation, where the upper-left and lower-right regions are the *replenished* and *unreplenished* regions, respectively. Parameter values: see Table 2.3.

(Figure 2.5). We see that the glucose concentration behaviour appears to be split into two approximate regions, divided by a straight line in (X, T)-space that goes through the origin and reaches the end of the X-domain ($X = 1$) at $T \approx 4$ (Figure 2.5(a)**A**). In the lower-right region, the glucose concentration appears to be approximately constant in space, and to decrease over time. However, in the upper-left region, there is a clear spatial dependence in the glucose concentration, which appears to decrease in X until it reaches the lower-right region. The lactate concentration behaviour appears to be split into the same two approximate regions (Figure 2.5(b)**A**), though the demarcation is less defined than for glucose. In the lower-right region, the lactate concentration also appears to be approximately constant in space, but now increases over time. In the upper-left region, the lactate concentration appears to approximately increase in X until it reaches the lower-right region. To compare these results with the reduced models, we also present solutions for the longwave approximation (Figures 2.5(a,b)**B**) and sublimit approximation (Figures 2.5(a,b)**C**). We see that the longwave approximation is an excellent approximation of the full system through the entire domain. The sublimit is also a good approximation of the full model, except in a small neighbourhood of the dividing characteristic, $\alpha X = \beta T$. Away from this dividing characteristic, the sublimit model exhibits the same qualitative behaviour and predicts very similar spatiotemporal metabolite concentrations to the full model. The sublimit solution is discontinuous across the dividing characteristic because it neglects horizontal diffusion. Appropriate smoothing could be included in the sublimit by investigating a thin boundary layer in the neighbourhood of this discontinuity in which diffusive effects are once again important. We also note that the dividing characteristic is in approximately the same place as the boundary between regions noted in the full model in Figures 2.5(a,b)**A**. We investigate and interpret this observation below.

At this stage, we conclude that when information close to the dividing characteristic is of interest, the longwave approximation should be used instead of the sublimit approximation. If this information is not important, the sublimit approximation should be used since it is faster to solve than both the full model and the longwave approximation, and it admits analytic solutions for metabolite concentrations.

We emphasize that our analytic solutions in the sublimit approximation allow us to understand observations from the full numerical solutions. That is, we can use our analytic solutions from the sublimit model to physically interpret our results and provide insight into the underlying physical system. For example, the dividing characteristic ($\alpha X = \beta T$) in the sublimit model represents the division between information propagated from the initial and the boundary conditions. Physically, this means that the effect of fresh media is only experienced at position X at time $T = \alpha X/\beta$. At earlier times, glucose delivery to organoids at position X is due to the glucose initially present in the system. This allows us to determine the *metabolite transit time*. That is, the average time taken for metabolite within the *fresh* media to traverse the entire bioreactor

$$T^* = \frac{\alpha}{\beta} = \frac{1 + \frac{H_H}{1-H_H}}{\lambda \bar{U}} \approx 4.7 \text{ days.} \tag{2.5.1}$$

The above estimate is in good agreement with our observations of the full solution — that different model solutions arise in the two regions on either side of the straight line through the origin that reaches $X = 1$ at $T \approx 4$. Hence, we now interpret this observation physically; the regions are separate according to whether or not they have experienced fresh media. Since the media does not traverse the bioreactor with a uniform velocity, the *metabolite transit time* is not the same as the timescale associated with the maximum flow velocity of the system, $[t] = 25$ hours. The relevant transport timescale is, therefore, not the one associated with the experimentally imposed flow rate, but rather the metabolite transit timescale, which is associated with the averaged velocity distribution of metabolite across the bioreactor, including the flowless hydrogel region.

Additionally, the analytic solution of our sublimit approximation provides insight into why the glucose and lactate concentration appear to be spatially-independent in the lower-right regions (Figure 2.5). In Region 1 (where $0 < \beta T < \alpha X$), the analytical solutions for metabolite concentrations from the sublimit model are independent of the spatial coordinate. Region 1 is the non-replenished region, *i.e.* it is not replenished from the inlet and subsists on its initial conditions. Therefore, given spatially-uniform initial conditions, spatial effects are not seen in the concentration profiles until the wave of replenishment is experienced; this marks the onset of Region 2.

To quantitatively compare the model predictions, we consider the following time-dependent variables: *minimum glucose concentration*, $C_{\min}(T) = \min_X(C(X,T))$; *maximum lactate concentration*, $W_{\max}(T) = \max_X(W(X,T))$; *spatial position of maximum lactate concentration*, $X_{\max}(T)$, where $W(X_{\max}, T) = W_{\max}(T)$; and the *lactate concentration at outlet*, $W(X = 1, T)$. We emphasize that Equation (2.4.3) allows us to denote the metabolite concentrations $C_{M0} = C_{H0} = C$ and $W_{M0} = W_{H0} = W$ for ease of notation.

In Figure 2.6**A**, we plot the minimum glucose concentration, $C_{\min}(T)$, against time for our two reduced one-dimensional models and the Z-averaged full model and

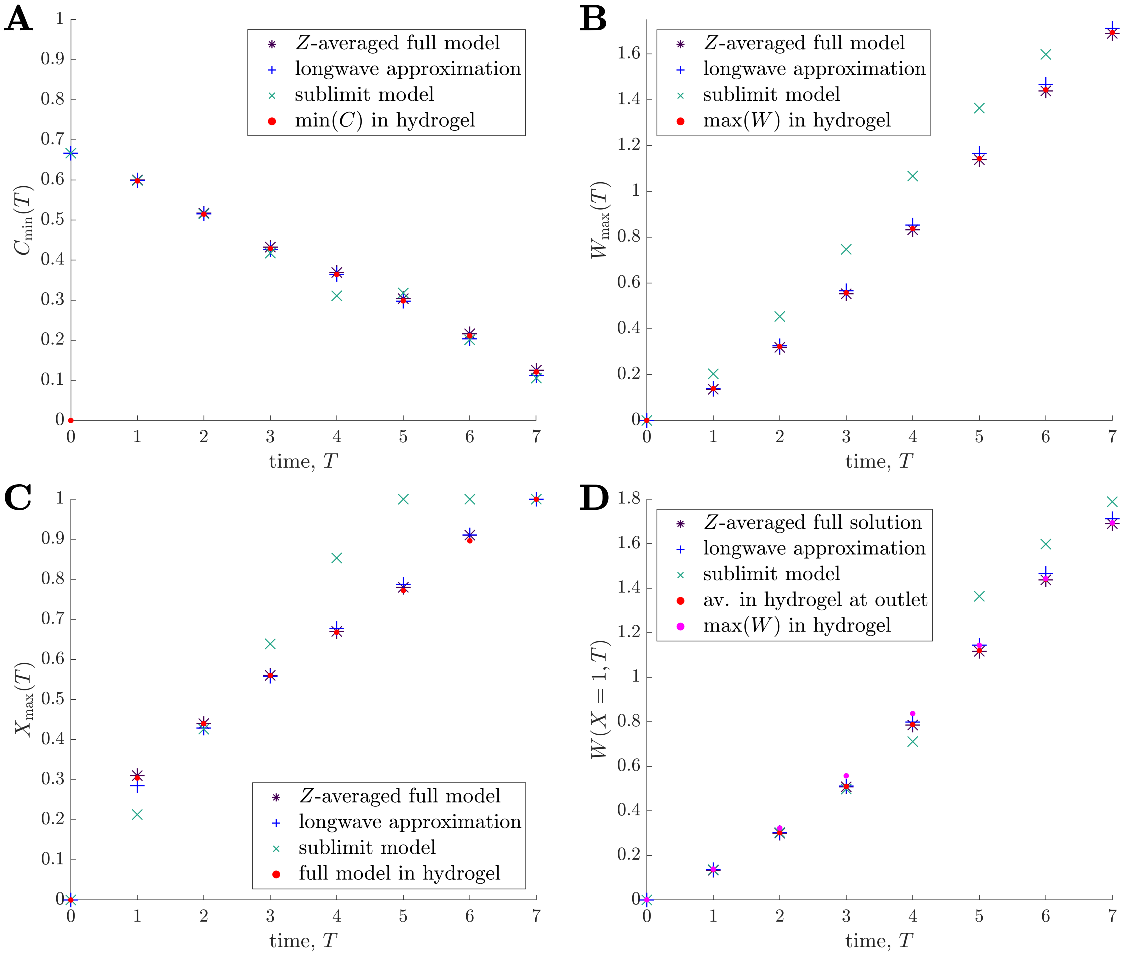

Figure 2.6: Comparison of outputs from the different mathematical models and their evolution in time: (**A**) minimum glucose concentration, $C_{\min}(T)$; (**B**) maximum lactate concentration, $W_{\max}(T)$; (**C**) spatial position of maximum lactate concentration, $X_{\max}(T)$ s.t. $W(X_{\max}, T) = W_{\max}(T)$; (**D**) lactate concentration at outlet of bioreactor, $W(X = 1, T)$. The red points represent the values predicted in the hydrogel region of the full 2D model. Parameter values: see Table 2.3.

compare these values to the predicted minimum glucose concentration in hydrogel, which is found using the full two-dimensional model. We see that the predicted minimum glucose from each model reduction generally agrees well with the minimum glucose within the hydrogel from the full model. The only exceptions to this are around 4–5 days, where the sublimit model disagrees slightly with the other models, and for early times (< 1 day). The first of these is due to the dividing characteristic being important for this metric around 4.7 days, as discussed above. The second is due to our choice of timescale in deriving the reduced model. That is, our reduced models focus over the timescale of days and neglect the initial transient behaviour in the system, as mentioned previously.

Similar plots showing how the maximum lactate concentration, $W_{\max}(T)$, changes over time are presented in Figure 2.6**B**. Again, the Z-averaged full model and the longwave approximation are in good agreement with the predicted value within the hydrogel. Given that there is initially no lactate in the system, this metric avoids the issue with the early-time transient behaviour that occurs for the minimum glucose concentration metric. The sublimit approximation systematically overestimates the lactate concentration, though we note that this is preferable to underestimation, given the detrimental effects of high lactate concentrations. The overestimation arises because the sublimit approximation neglects the removal effect of lactate transport through horizontal diffusion over the dividing characteristic.

We compare the position at which the maximum lactate concentration occurs, $X_{\max}(T)$, in Figure 2.6**C**. We see that $X_{\max}$ is increasing in time, which is consistent with advection being the dominant transport mechanism over the timescale of days (Table 2.2), as the lactate produced is advected towards the outlet by the media. As seen in Figures 2.6**A** and 2.6**B**, the sublimit approximation agrees less well with the full model than the longwave approximation, which has excellent agreement. A notable difference with the sublimit approximation compared to the full model and longwave approximation is the jump in results between times $T = 4$ and $T = 5$ in Figure 2.6. This is due to the discontinuity of the sublimit model at the dividing characteristic, and the appropriate metric value for each given time being taken from the unreplenished region for $T < T^* \approx 4.7$ to the replenished region for $T > T^*$.

It is infeasible to obtain experimental data for maximum lactate concentrations, which we would need to validate our model. Therefore, we consider the lactate concentration at the media outlet, $W(X = 1, T)$, which is measurable empirically, in Figure 2.6**D**. We compare the reduced models to the Z-averaged full solution, the average concentration within the hydrogel at the outlet, and the maximum value in the hydrogel (which are all obtained from numerical solutions to the full 2D system). We find that the lactate concentration at the media outlet is very similar to the maximum lactate concentration within the hydrogel and can, therefore, be used as a proxy for it. The sublimit is a good prediction of the outlet and maximum lactate concentrations at 4 days and earlier, but overestimates the maximum concentration within the hydrogel at 5 days and later. This is again due to the dividing characteristic, and its exit from the domain at 4.7 days.

2.5.3 Bioreactor characterisation

In this Section, we start by exploiting our reduced modelling approach to *characterise* the conditions within the bioreactor. We show how the metabolite concentrations depend on the bioreactor operating parameters such as the inlet flow rate and cell seeding density, and the characteristics of the cells, such as the rates of cell proliferation and glucose consumption. Armed with this insight, we then show how the operating parameters can be selected to ensure the biochemical environment within the bioreactor promotes cell growth.

We investigate and quantify the metabolite behaviour by introducing the following time-dependent metrics. We previously defined the *maximum lactate concentration*, $W_{\text{max}}(T)$, as

$$W_{\text{max}}(T) = \max_X \left(W(X,T) \right). \tag{2.5.2}$$

We now introduce the cumulative *glucose conversion*, $\Upsilon(T)$, as

$$\Upsilon(T) = \frac{\text{glucose consumed}}{\text{glucose supplied}} = \frac{\int_0^T \int_0^1 \gamma C \exp(PT) \, \mathrm{d}X \mathrm{d}T}{\int_0^T (1 - H_H) \lambda \bar{U} \, \mathrm{d}T}. \tag{2.5.3}$$

In general, it is desirable to choose operating parameters that ensure high glucose conversion, so the maximum amount of glucose supplied to the bioreactor is utilised by the cells, and resource wastage is minimised. However, high glucose conversion will also cause high lactate levels, and lactate concentrations above a critical tolerance, W_{tol}, can adversely affect organoid growth. A typical value of W_{tol} for colorectal cancer organoids is 0.7 (this will be lower for benign tissues). To assess this, we define a point X to be *uninhabitable* if $W(X,T) > W_{\text{tol}}$. We use the metric *proportion of domain which is uninhabitable*, $\chi_{\text{U}}(T)$, defined as

$$\chi_{\text{U}}(T) = \int_0^1 H \left[W(T,X) - W_{\text{tol}} \right] \, \mathrm{d}X, \tag{2.5.4}$$

where H is the Heaviside function. In general, it is desirable to choose operating parameters such that χ_{U} is minimised for the duration of the bioreactor run. We define lactate concentrations which are below and above this critical tolerance W_{tol} as *tolerable* and *intolerable*, respectively. In addition to the time-dependent metrics, it is also helpful to quantify the *time at which intolerable lactate levels are first experienced*, which we refer to as the *turn-off time*, and define as

$$T_{\text{off}} = \min(T) \text{ for } T \in \left\{ T : W(X,T) \geq W_{\text{tol}} \right\}. \tag{2.5.5}$$

In general, it is desirable to choose operating parameters such that T_{off} is larger than the duration of the bioreactor run.

There is a trade-off between high glucose conversion and minimising the fraction of the domain which is *uninhabitable*. We show how the mathematical model can be used to identify parameter regimes which strike a balance between promoting glucose conversion and facilitating waste removal in Section 2.5.3.2.

In addition to the metrics we have introduced to assess metabolite distribution, an important cell-specific metric is the *glucose consumption rate per cell*. In our model, the glucose consumption rate per cell is proportional to the glucose concentration and, thus, we can use results such as Figure 2.5**C** to understand the spatial variation in glucose consumption rate per cell. We see that cells nearer the inlet have higher rates of glucose uptake than those closer to the media outlet, and this spatial heterogeneity could lead to spatial variation in cell growth within the physical system.

2.5.3.1 Characterising model behaviour for different organoid lines

Organoid lines differ in many ways including, but not limited to: proliferation rate; glucose consumption rate; the maximum lactate concentration cells can tolerate without affecting cell properties; and minimum glucose level needed for cellular proliferation. To understand the metabolic environment experienced by different organoid lines within the bioreactor, we perform a discrete parameter sensitivity analysis in which we vary the rates of proliferation, P, and glucose consumption per cell, σ, for the bioreactor operating regime specified in Table 2.3. We consider organoid lines whose proliferation rates take the values $P = 1/6$ and $P = 1$, which we refer to as low and high proliferation, respectively, and whose glucose consumption rates take values $\sigma = 0.027$ and $\sigma = 2.7$, referred to as low and high consumption, respectively. We consider five different organoid lines, which we denote as (*i*), (*ii*), (*iii*), (*iv*), and (*v*), with associated proliferation (P) and glucose consumption (σ) rates as defined in Table 2.4. We note that the case (*v*) corresponds to the 'standard' operating practice.

Table 2.4: Proliferation rates P and glucose consumption rates σ for the different organoids considered in Section 2.5.3.1.

Organoid line	Proliferation rate, P	Glucose consumption rate, σ
(*i*)	1/6	0.027
(*ii*)	1/6	2.7
(*iii*)	1	0.027
(*iv*)	1	2.7
(*v*)	1/3	0.27

In Figure 2.7, we plot the metabolite concentration profiles (a) C and (b) W for these four organoid lines, (*i*-*iv*), expanded under an operating regime which does not otherwise differ. The same results for organoid line (*v*) are shown in Figures 2.5(a,b)**B**.

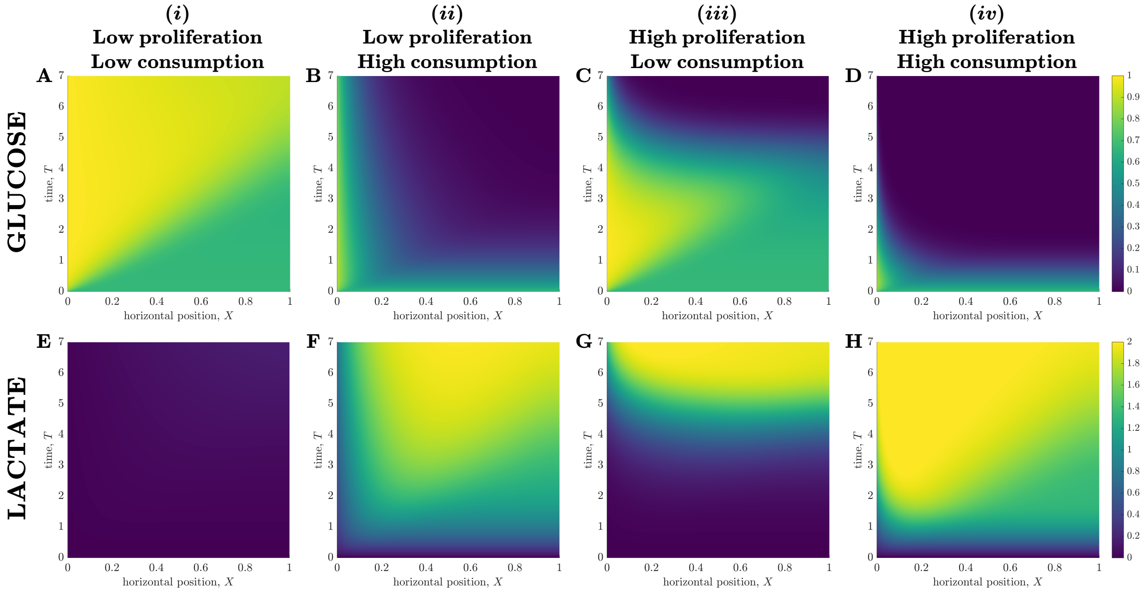

Figure 2.7: Evolution of glucose (**A**, **B**, **C**, **D**) and lactate (**D**, **E**, **F**, **G**) concentration profiles over the duration of a typical experiment for different organoid lines under the same operating conditions. The organoid lines presented are: (**A**, **E**) organoid line (*i*); (**B**, **F**) organoid line (*ii*); (**C**, **G**) organoid line (*iii*); (**D**, **H**) organoid line (*iv*); where the rates of cell proliferation rates and glucose consumption per cell are defined in Table 2.4. Remaining parameter values: see Table 2.3.

In Figures 2.7(**A**, **E**), we show organoid line (*i*), cells with low proliferation and low glucose uptake rates. The lactate levels are very low throughout the bioreactor domain and the domain remains within tolerable lactate concentrations for the entire experiment. The glucose concentration in the replenished region is high and remains close to its inlet value, $C = 1$, so the media flow supplies significantly more glucose into the system than is consumed by the cells. The glucose concentration becomes increasingly homogeneous as time evolves, and consequently the rate of glucose consumption per cell becomes more spatially homogeneous across the bioreactor as time evolves.

We consider organoid line (*ii*), with low proliferation and high glucose uptake rates, in Figures 2.7(**B**, **F**). We see that this larger uptake rate means that the lactate concentration quickly increases and the majority of the region becomes intolerable, even for slowly proliferating cells. While cells close to the inlet still have reasonably high glucose and low lactate levels, resulting in the rate of glucose uptake per cell being high at the inlet, this quickly decreases as one moves into the bioreactor.

For rapidly proliferating cells with a low rate of glucose uptake (organoid line (*iii*)) Figures 2.7(**C**, **G**), we see the environment is tolerable until around day 4 of the experiment. At this point, there are approximately 55 times more cells within the hydrogel than at the start of the experiment. This suggests that the selected operating conditions provide tolerable conditions and allow reasonable rate of glucose consumption per cell up to a critical number of cells, but beyond this critical number, the low glucose concentration means the cells have a very low rate of glucose consumption. The lactate concentration is reasonably spatially homogeneous, which suggests that all cells will be subject to a similar metabolic environment and therefore be affected by lactate to a similar degree.

Finally, we consider cells with high proliferation and high uptake (organoid line (*iv*)), in Figures 2.7(**D**, **G**). The glucose concentration within the bioreactor decays very quickly over the course of a day, and it is never replenished sufficiently by the media flow. As such, the glucose consumption per cell is consistently small away from the inlet region. In the same vein, the lactate concentration quickly increases to above the tolerable level over the course of a day. In contrast to the low proliferation organoid line (*ii*) (Figures 2.7(**B**, **F**)), the maximum lactate concentration for organoid line (*iv*) occurs close to the inlet rather than in the middle of the bioreactor. This is because the rapid expansion of cells means that lactate is produced very quickly throughout the bioreactor, and so is maximised in the location where glucose is mainly consumed. This indicates that the media flow is too slow to facilitate significant waste removal for this organoid line. We note that our cell growth model is not dependent on metabolite concentration, so the cell proliferation rate is unaffected when the metabolic environment is harsh. This limitation is most prominent for the high proliferation and high uptake organoid line, where the cells continue to proliferate exponentially in the presence of no glucose and high lactate levels. In Chapter 3, we consider a model that accounts for this.

Using the metrics we introduced above, we now quantify the behaviour of the bioreactor environment during cell culture for each of the five organoid lines. In Figure 2.8, we plot the total glucose conversion, $\Upsilon(T)$ [Equation (2.5.3)], maximum lactate concentration, $W_{\max}(T)$ [Equation (2.5.2)], and proportion of uninhabitable domain, $\chi_{\mathbf{U}}(T)$ [Equation (2.5.4)] (strongly related to the turn-off time), for each of the five organoid lines. We note that glucose conversion is not simply a metric to determine the amount of glucose consumed by the organoids (which is simply the glucose concentration integrated over time in the models considered in this Chapter), but rather the proportion of glucose consumed by the organoids compared to the amount pumped into the bioreactor. Conversion is an oft-used metric in the field of chemical reaction engineering. Since the experimental set-up does not allow recirculation of 'used' culture media, and given that culture media is expensive, we wish to use this resource as efficiently as possible. This motivates glucose conversion as an informative metric.

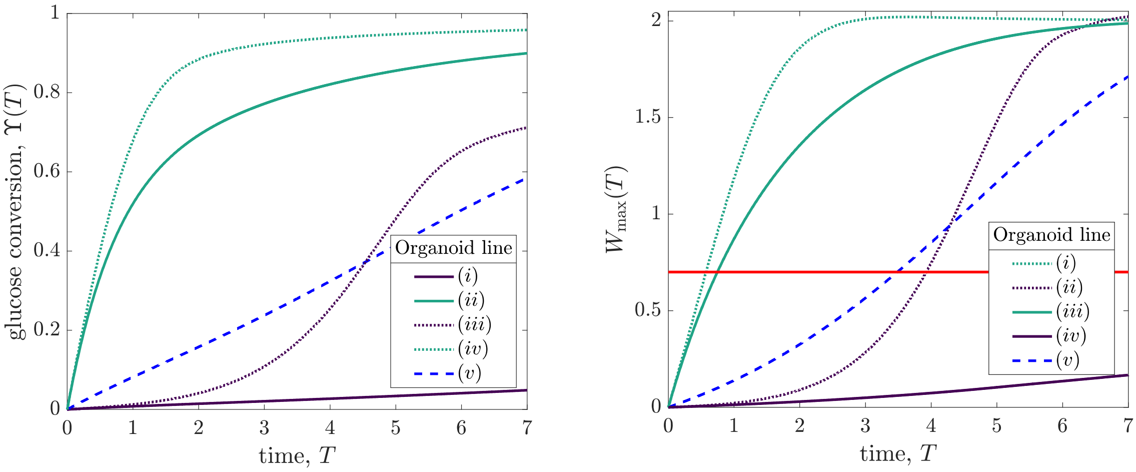

(a) Glucose conversion, Υ, Equation (2.5.3)

(b) Maximum lactate concentration $W_{\max}$, Equation (2.5.2), where the red line represents the maximum tolerated lactate concentration, $W = W_{\text{tol}}$

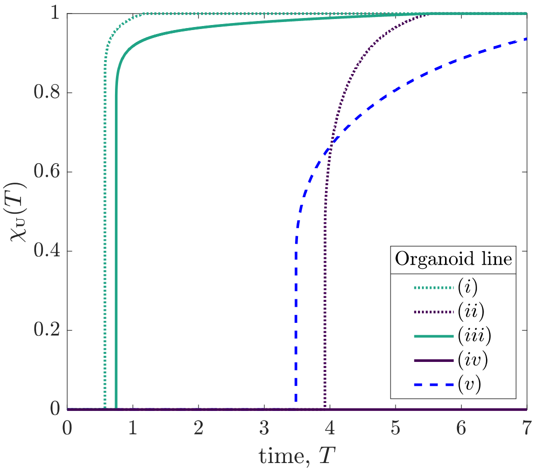

(c) Proportion of domain which is uninhabitable at time T, χ_{U}, Equation (2.5.4)

Figure 2.8: Comparison of bioreactor characterisation metrics for different organoid lines cultured within the bioreactor under the same operating conditions. The line styles correspond to cellular proliferation rate: solid, $P = 1/6$; dashed, $P = 1/3$; dotted, $P = 1$. The line colours correspond to rate of glucose consumption per cell density: purple, $\sigma = 0.027$; blue, $\sigma = 0.27$; green, $\sigma = 2.7$. The proliferation rates and rate of glucose consumption per cell for each organoid line are given in Table 2.4. Remaining parameter values: see Table 2.3.

The glucose conversion generically increases over time, as the cells grow. However, the shape of this increase over time varies significantly between the different organoid lines. While solely considering the standard case [organoid line (*v*)] would suggest that the glucose conversion is approximately linear in time, the additional organoid lines show that this behaviour is not universal. Cells with high rates of glucose consumption [organoid lines (*ii*) and (*iv*)] have a sharp increase in glucose conversion over the first two days before plateauing. For low rates of glucose consumption, the shape of the glucose conversion curve strongly depends on the cell proliferation rate. For low proliferation [organoid line (*i*)], the conversion is low throughout and appears linear. However, for high proliferation [organoid line (*iii*)], the curve has an S-shape. That is, the conversion starts off low, then rapidly increases before plateauing. This rapid increase is linked to the increase in the number of cells in the bioreactor for organoid line (*iii*), and so we would expect organoid line (*i*) to exhibit a similar S-shape if the experiment went on for longer.

We show the maximum lactate concentration in Figure 2.8(b), where the red line represents $W = W_{\text{tol}}$, to understand which of these organoid lines are growing in tolerable environments. This graph is qualitatively very similar to that of the glucose conversion, Figure 2.8(a). For the value of W_{tol} we use, we see that the maximum lactate concentration reaches the tolerated level within 1 day for high uptake cells [organoid lines (*ii*) and (*iv*)]. In comparison, the standard case [organoid line (*v*)] reaches the maximum tolerated level approximately halfway through the experiment. For the low uptake organoid lines, the proliferation rate again makes a significant difference. For high proliferation [organoid line (*iii*)], the maximum tolerated level is again reached approximately halfway through the experiment, whereas for low proliferation [organoid line (*i*)] the lactate never reaches harmful levels.

We examine the time at which the lactate concentration equals the tolerated lactate concentration in Figure 2.8(c), a graph showing the time-dependent proportion of the domain which is uninhabitable, $\chi_{\mathbf{U}}(T)$, for each organoid line. Notably, we see that as soon as some of the domain becomes uninhabitable, the rest of the domain follows over a short timescale. This can be explained through the insight gained from our sublimit approximation. That is, as Region 1 ($0 < \beta T < \alpha X$) has yet to experience replenishment from the inlet, the lactate concentration in this region is approximately spatially homogeneous, and an increase above the tolerable level will quickly be experienced in a large part of the domain. The turn-off time T_{off} (Equation (2.5.5)) can also be determined from Figure 2.8(c) — it is the first time at which $\chi_{\mathbf{U}}(T)$ is non-zero. We see that the high glucose consumption organoid lines [(*ii*) and (*iv*)] have much smaller turn-off times than the other organoid lines. The lactate concentration for organoid line (*i*) does not reach W_{tol} during the experiment, so the turn-off time is larger than the run time of the experiment.

There is a trade-off between promoting: (1) high glucose conversion, to ensure resources are not wasted; (2) high glucose consumption rate per cell, to ensure cells absorb sufficient glucose to proliferate; and (3) increasing the turn-off time, to ensure the lactate concentrations within the bioreactor remain tolerable everywhere throughout the experiment. Our model framework allows for efficient quantification of all these metrics. By determining how these metrics vary with bioreactor operating parameters, we can then identify operating conditions that enhance cell growth. We illustrate this in the next section.

2.5.3.2 Determining operating conditions for a given organoid line

In this subsection, we focus on the standard organoid line (v), with proliferation rate and glucose consumption rate given in Table 2.3. This is the organoid line with a 'medium' rate of glucose consumption per cell, and a doubling time of three days. The current operating conditions lead to lactate concentrations above the tolerated level for half of the experimental run time, suggesting that these operating conditions are sub-optimal.

We now determine how the metrics depend on the inlet flow rate for this organoid line, and show how this leads to the identification of flow rates that enhance cell growth. We focus on flow rate as this is an experimental parameter that is easily varied. We investigate flow rates over two order of magnitudes, $[u] \in [10^{-7}, 10^{-5}]\,\mathrm{m\,s^{-1}}$, all within the range of the peristaltic pump used in the CXP1 protocol.

In Figure 2.9, we show how the metrics vary with inlet flow rate. To illustrate the dependence of the metrics on flow rate, we first present time-dependent results for five different flow rates. The glucose conversion monotonically increases in time (Figure 2.9(a)), due to the increasing number of cells causing an increased glucose consumption. The effect of increasing flow rate is to decrease the glucose conversion. This is because stronger flows correspond to feeding more glucose into the system over a given time period as well as the media spending less time within the bioreactor, so there is less time for the glucose to be consumed by the cells. However, we also note that the conversion is relatively insensitive to flow rate: increasing the flow by two orders of magnitude only decreases the conversion by a factor of around six.

While the time-dependent maximum lactate concentration within the domain monotonically increases for a given flow rate, the effect of varying the flow rate is non-monotonic (Figure 2.9(b)). For a given run time of the experiment, there is a flow rate that maximises the maximal lactate concentration. We emphasize that this flow rate will depend on the experimental run time. The reason for there being a

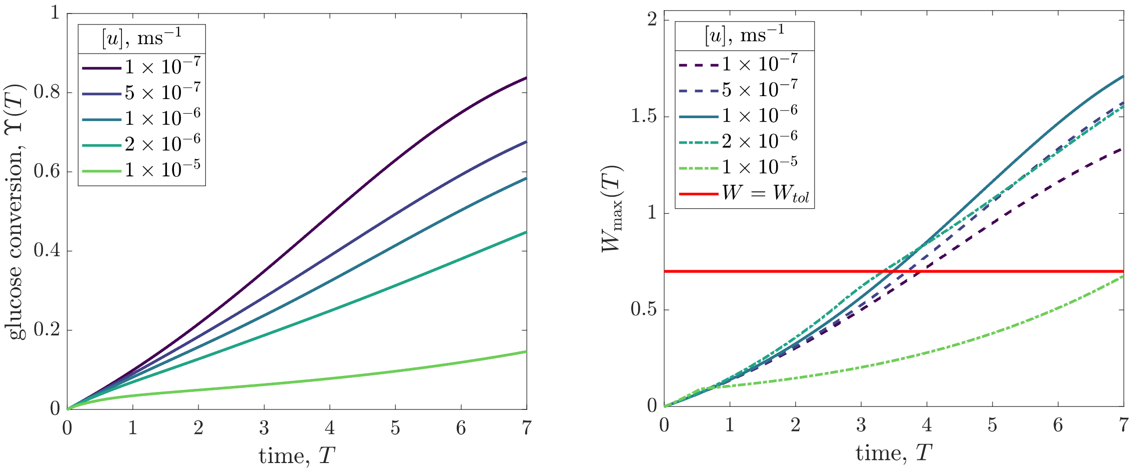

(a) Glucose conversion, Υ, Equation (2.5.3)

(b) Maximum lactate concentration $W_{\max}$, Equation (2.5.2), where the red line represents the maximum tolerated lactate concentration, $W = W_{\text{tol}}$

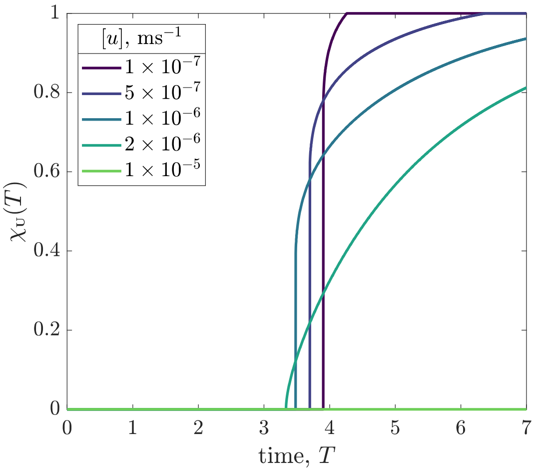

(c) Proportion of domain which is uninhabitable at time T, $\chi_{\mathbf{U}}$, Equation (2.5.4)

Figure 2.9: Comparison of bioreactor characterisation metrics for a specific organoid line (v) against time for five different flow rates. For $[u] = 10^{-5}\text{m s}^{-1}$, the value of $\chi_{\mathbf{U}}$ is zero. The peak flow velocities $[u] \in \{10^{-7}, 5 \times 10^{-7}, 10^{-6}, 2 \times 10^{-6}, 10^{-5}\}\text{m s}^{-1}$ used correspond to the dimensionless flow velocity parameter $\lambda \in \{0.096, 0.48, 0.96, 1.92, 9.6\}$, respectively. Remaining parameter values: see Table 2.3.

flow rate which maximises the maximal lactate concentration (the ‘worst’ flow rate, in some sense) is due to two competing factors. Firstly, the rate of glucose consumption per cell, and therefore the rate of lactate production, increases with increasing flow rate. Secondly, for slower flow rates the media is not able to advect sufficient quantities of lactate out of the bioreactor to maintain a tolerable lactate level. These two factors combine to produce a worst possible flow rate for a given experimental run time. We also note that up until approximately one day ($T = 1$), the maximum lactate concentration is the same for all the flow rates considered. This reflects the fact that there is a lag in the production of lactate, and that the lactate production is initially set by the initial conditions rather than the operating regime of the bioreactor.

In Figure 2.9(c), we plot the proportion of the domain which is uninhabitable against time, for the five different flow rates considered. In general, a lower flow rate corresponds to a sharper increase in the uninhabitable proportion once initially triggered. This is because more of the domain is in the non-replenished Region 1 for lower flow rates, and the metabolite concentrations are approximately spatially independent in Region 1, for reasons discussed above. In addition, we note that a large enough flow rate can ensure that none of the domain becomes uninhabitable for the duration of the experimental run, as we see for a flow rate of 1×10^{-5} $\mathrm{m\,s^{-1}}$. However, we also note that increasing the flow rate can have an unwanted effect on the turn-off time. From Figure 2.9(c), we see that increasing the flow rate slightly decreases the turn-off time, up to a point. As noted above, for large enough flow rates the system never exhibits intolerable lactate concentrations.

We now consider a more finely refined investigation of the effect of flow rate of the system metrics. In Figure 2.10, we consider the effect of flow rate both on the glucose conversion at day 7 (Figure 2.10(a)) and on the turn-off time (Figure 2.10(b)).

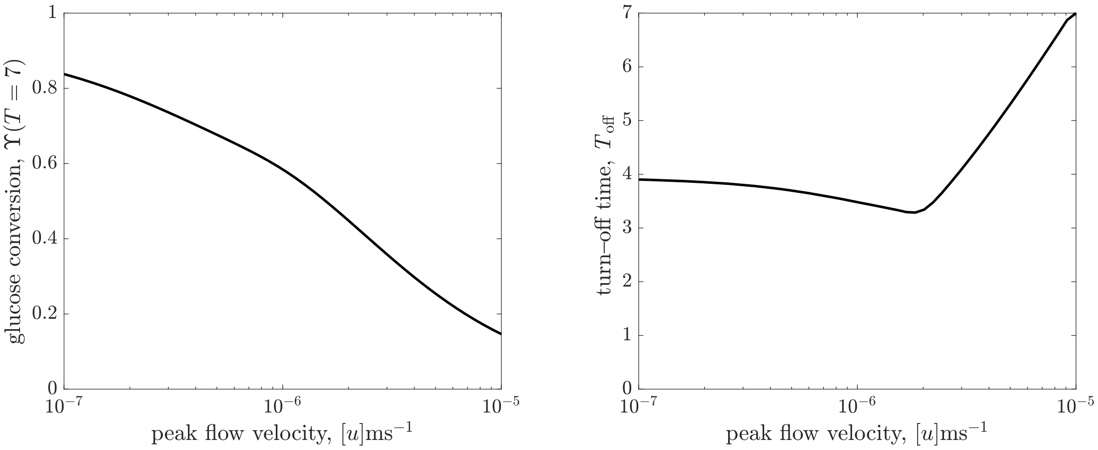

(a) Glucose conversion

(b) Turn-off time

Figure 2.10: Plots of the metrics (a) glucose conversion Υ, Equation (2.5.3), at time $T = 7$ and (b) turn-off time T_{off} (the time when intolerable lactate levels first experienced, Equation (2.5.5)) for the CXP1 bioreactor varying with flow rate, for a given organoid line. Peak flow velocities $[u] \in [10^{-7}, 10^{-5}]\,\mathrm{m\,s^{-1}}$ correspond to dimensionless flow rate, λ, in the range $\lambda \in [0.096, 9.6]$. Remaining parameter values: see Table 2.3.

We see that the relationship between glucose conversion at 7 days and media flow velocity is monotonically decreasing, and the rate of decrease is larger for flows faster than $[u] = 10^{-6}\,\mathrm{m\,s^{-1}}$ (Figure 2.10(a)). However, as noted above, the turn-off time (Figure 2.10(b)) is not monotonic in the flow rate (see also Figure 2.9(c)). We see that there is a minimal turn-off time when the flow is approximately $2 \times 10^{-6}\ \mathrm{m\,s^{-1}}$. This is the *worst* possible flow rate from the point of view of ensuring the domain remains tolerable for as long as possible. For flow rates below this, the bioreactor is *transport-limited*, either by insufficient glucose delivery to cells or by insufficient waste removal from the bioreactor. For flow rates above this, the turn-off time is *proliferation-limited*, where the rate at which the cell population is growing sets the timescale at which lactate is produced.

An advantage of our mathematical modelling framework is that we have been able to easily explore a wide range of parameter values, in this case the flow rate, and explore the nonlinear effects of varying experimental parameters. For example, an experimentalist may start with a slow flow rate of $10^{-7}\ \mathrm{m\,s^{-1}}$ and conduct a set of experiments over which they increased the flow. Over an order of magnitude increase in flow, they would see no improvement in turn-off time, and therefore might be discouraged from increasing the flow any further. In such a scenario, they would miss finding the flow rate values required for turn-off times greater than 4 days.

The ‘optimal’ operating conditions for the bioreactor will determine glucose and lactate concentrations which (1) yield a specified value for glucose conversion; (2) maintain a glucose consumption rate per cell which is sufficient for cellular proliferation; and (3) predict a turn-off time which is greater than the run time of the experiment. The specific values and relative importance of each of these requirements will depend on the user. Our model reduction facilitates rapid calculation of each metric. Hence, our work could be combined with an optimisation algorithm, with user-specified cost functions, to produce an efficient framework that can identify the bioreactor operating conditions that optimise for growth of organoids.

2.6 Discussion

We have presented an unsteady, two-dimensional model of metabolite transport that predicts metabolite concentrations within the CXP1 bioreactor system. We used an asymptotic analysis to systematically derive two reduced models which exploit the extreme spatial and temporal parameter ratios in the system. Our model predicts the spatiotemporal distribution of the metabolic environment within the bioreactor, information which is challenging to obtain experimentally. Both reduced models are one-dimensional in space; the *longwave approximation* comprises two coupled reaction-advection-diffusion equations (second-order in space), whereas the *sublimit approximation* comprises two coupled reaction-advection equations (first-order in space). Our systematic analysis allows us to relate parameters in the reduced models to geometric and operating parameters of the CXP1 system, such as the ratio between the depth of the hydrogel and media layers, and the fluid flux over the hydrogel. We have shown that both reduced models provide good approximations of the full model for most physically relevant parameter regimes. The longwave approximation appears to be an excellent representation throughout the entire domain, whereas the sublimit approximation appears good everywhere apart from a specific dividing line in space-time that we are able to calculate.

Although the above may appear to suggest that the sublimit approximation is not useful, it does have additional benefits over the longwave approximation. A notable benefit is that it admits analytic solutions in the entire domain. Interpreting these analytic results and understanding why they are discontinuous across the specific line in space-time provides insight into the underlying physical system. We find that the specific line in space-time is a dividing characteristic in the (hyperbolic) sublimit approximation we derive. We are able to infer that this line divides the domain into two regions, depending on whether or not the effect of replenishment from the inlet has been experienced.

The flow of media through the bioreactor has the dual function of delivering nutrients to, and removing waste from, the growing organoids. As such, the inlet flow rate needs to be chosen carefully. The systematic reduction we have performed yields models that are easier to solve numerically than the full model. More importantly, they provide insight into the behaviour of the full model, particularly the dominant transport mechanisms. This systematic reduction has enabled us to efficiently characterise the experimental parameter space for given cell characteristics. One key outcome from this analysis is our prediction of a ‘worst-case’ flow rate that minimises the turn-off time (the time when intolerable lactate concentrations first occur), Equation (2.5.5). Our model reduction has allowed us to understand why this minimum arises: for higher flow rates, the lactate is washed away more quickly (the bioreactor is in a proliferation-limited regime), for lower flow rates the lactate is produced more slowly since glucose is not delivered quickly enough (the bioreactor is in a transport-limited regime).

To understand how outcomes change as the control parameters are varied, we introduced the following time-dependent metrics which characterise bioreactor performance:

- ***Glucose conversion*** — the ratio between the total amounts of consumed and supplied glucose. It is desirable to minimise the amount of resources, *e.g.* glucose, required for bioreactor operation, which corresponds to maximising glucose consumption.

- ***Maximum lactate concentration*** within the bioreactor — the worst metabolic environment experienced by the cells. High lactate concentrations have a detrimental effect on cells [71], and therefore an ideal bioreactor operating regime would have low maximum lactate concentrations.

- ***Proportion of uninhabitable domain*** — the fraction of the domain where the lactate concentrations exceeds the maximum tolerated level for the specific organoid line. An operating regime is improved if the proportion of the domain which is uninhabitable decreases, and an 'ideal' operating regime would maintain lactate levels below the maximum tolerable level for the entire experiment.

- ***Turn-off time*** — the time at which lactate concentration first reaches levels which are intolerable for the cells. To optimise operating conditions, the turn-off time should be increased. Ideally, the turn-off time should exceed the run time of the experiment.

Different bioreactor operating conditions will yield different values of these metrics. The relative importance of each metric will depend on the particular organoid line being investigated and the specific user requirements. Our work provides a framework for efficiently determining desirable bioreactor operating conditions for given cell properties.

In this Chapter, we performed a systematic model reduction to study metabolite transport within the CXP1 bioreactor, whose geometry differs significantly from other bioreactors, such as hollow fibre or perfusion bioreactors. An important insight gained from our model reduction is the identification of the transport mechanisms that are dominant on our timescale of interest. We performed model reductions in two ways: (1) we exploited the slender geometry of the system to obtain the *longwave approximation*; and (2) we exploited the separation of timescales of the physical processes in play to derive the *sublimit approximation.* By systematically reducing our original model (Equations (2.3.9) and (2.3.12)), we have simplified a two-dimensional parabolic PDE system first to a one-dimensional parabolic PDE system (the *longwave approximation*), and then to a one-dimensional hyperbolic PDE system (the *sublimit* *approximation*). A significant advantage of this approach is the analytical tractability of the *sublimit approximation*. As a result, we can construct explicit expressions for the metabolite concentrations across the entire bioreactor that reveal both the spatiotemporal-dependence and the dependence on the control parameters, *e.g.* flow rate, of the metabolite concentrations in the bioreactor. We have shown that the reduced models serve as excellent approximations of the full system and are much easier to solve numerically. We have also identified the small region of space-time where the assumptions required for the validity of sublimit model break down.

The mathematical modelling approach developed in this Chapter provides a framework for establishing how organoid viability can be improved by varying bioreactor operating conditions. The framework has the flexibility to consider different organoid lines, via characterisation of their proliferation and nutrient consumption rates and their tolerance to the presence of waste metabolite. Although the model developed in this Chapter has provided valuable insight, we note that there are several limitations: it is 2D, whereas the CXP1 bioreactor is 3D; the proliferation rate is constant (independent of local metabolic environment) with a spatially constant cell density, meaning that we cannot predict the spatial variation in organoid size across the bioreactor; there is no feedback of the inhibitory effect of lactate; and we do not solve for the true media flow within the bioreactor. We explore extensions to the work, which overcome the limitations discussed, throughout the rest of this thesis.

Namely, in Chapter 3, we will represent individual organoids as small, localised regions within a 3D hydrogel where glucose consumption and lactate production occur (at rates dependent on local metabolite concentration), and regulate organoid growth. We will use a mathematical homogenisation approach (see *e.g.* [16, 18, 74, 78]) to systematically average the behaviour over the microscale to obtain a macroscale governing equation for the hydrogel layer with effective *glucose consumption*, *lactate production*, and *organoid growth* terms. One can take into account the sensitivity of the organoids to lactate via the organoid growth model. This in turn will increase our understanding of the relationship between the bioreactor operating parameters and the mean and variation in organoid size, ultimately facilitating optimisation of the bioreactor operating conditions to minimise organoid size variation.

In Chapter 4, we consider the flow of culture media within the CXP1 bioreactor. We model the culture media as an incompressible fluid using the Navier-Stokes equations and derive an analytic expression for the velocity of the media. The flow profile in depth is shown to be half-Poiseuille, as imposed in this Chapter, and we determine the direction of the flow in the (X, Y)-plane and the associated streamlines. This gives insight into how the positions of the inlet and outlet pipes within the domain affect the flow profile.

In Chapter 5, we derive a 3D model for the metabolite transport and organoid growth in the bioreactor. This model can predict for spatial variation in organoid size across the bioreactor, and consists of the homogenised organoid-hydrogel model we derive in Chapter 3 coupled to an advection-diffusion model in the culture media (analogous to the 2D version considered in this Chapter), with the 3D culture media flow as explicitly determined in Chapter 4.

Chapter 3

Homogenisation of organoid and hydrogel regions

3.1 Introduction

In this Chapter, we focus on accurately capturing the microscale behaviour of the organoids within the hydrogel. The system derived in Chapter 2 modelled the effect of the organoids on the metabolite concentrations presented via a general (smooth) volumetric absorption term representing glucose consumption within the hydrogel. We now consider the discrete nature of the organoids in more detail. We develop a model for individual organoids suspended within the hydrogel, and employ homogenisation techniques to systematically average the microscale behaviour in a local sense. This allows us to derive the governing equations which describe the *effective macroscale behaviour* across the organoid-hydrogel region, see Figure 3.1.

3.1.1 Review of mathematical homogenisation

Here, we give a brief overview of some applications of mathematical homogenisation. For an introduction to homogenisation, we refer the reader to Hornung [38]. Broadly, the idea of homogenisation is to 'upscale' a microscale problem (in our case, on the scale of organoids) to understand its behaviour on the macroscale (*e.g.* on the laboratory scale). This requires a sufficient separation of scales, where the ratio between the microscale and macroscale lengthscales is small. We focus on the method of multiple scales [35] (as opposed to *e.g.* volume averaging [92]), specifically deterministic approaches. For an example of a stochastic approach, see *e.g.* Chernyavsky et al. [12], who consider solute transport in a disordered domain with randomly distributed point sinks. For a comparison of the deterministic method of multiple scale to stochastic realisations, see Bruna and Chapman [5]. Classic homogenisation requires a strictly

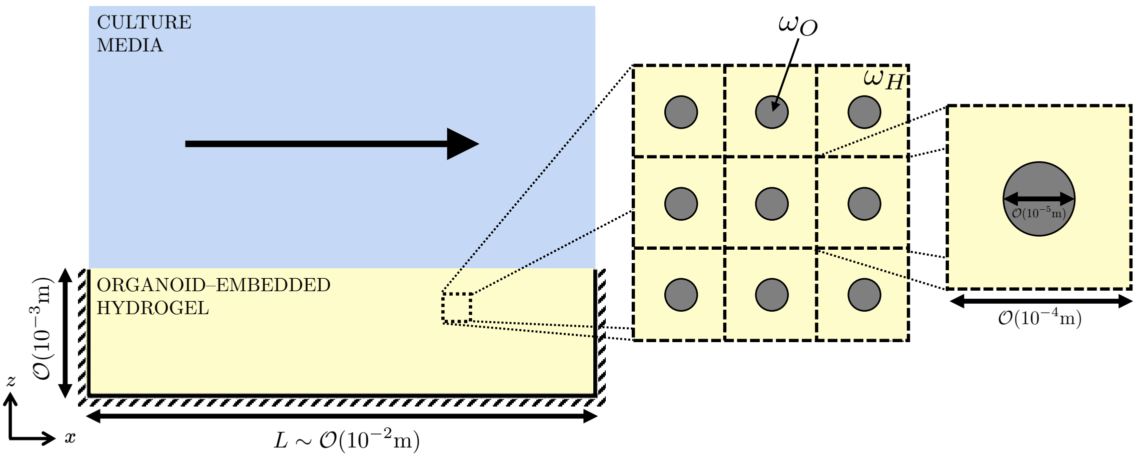

Figure 3.1: (**Left**) Schematic of a 2D cross-section of the CXP1 bioreactor, where the arrow denotes direction of culture media flow. Blue is nutrient-rich culture media. Yellow is a layer of hydrogel in which organoids are embedded. (**Centre**) 2D cross-section of microscale domain for the ‘hydrogel’ layer. Yellow is hydrogel, grey is organoid. (**Right**) 2D cross-section of a microscale periodically-repeating ‘cell’, which is centred around a spherical organoid. The typical lengthscales of the problem are indicated on the relevant macro- and microscale schematics.

periodic microstructure. However, more recently the framework has been developed to relax this assumption and allow locally periodic domains [5, 59]. The method of multiple scales has been well-studied, particularly for reaction-advection-diffusion models, and work has been done to prove uniqueness and convergence [39, 40].

There are a broad range of applications for homogenisation, and these range from contamination modelling (*e.g.* filters [14, 15] and decontamination [52]), soil mechanics [22, 27], lithium-ion batteries [70], to biological applications, such as tissue engineering, drug delivery in tumours [45, 79], cell growth [36, 44], and biofilms [18]. Homogenisation allows understanding of the effective properties of composite materials [41, 78]. Chen et al. [11] develop a homogenised model for a fibre-reinforced hydrogel, consisting of linear elastic fibres embedded within a poroelastic hydrogel. They derive the bulk mechanical properties of this composite construct, and their dependence on the fibre spacing, and compare their model to experimental data. Through their analysis, they can predict the local mechanical environment experienced by the cells.

Multiple-scale homogenisation approaches have also been taken in multiphase models, such as [36]. Holden et al. [36] consider a layer of growing tissue on a rigid (periodic) scaffold. The upscaled system they obtain consists of Darcy flow for the culture medium, a reaction-advection model for the nutrient, and a PDE for the cell fraction. Importantly, they find that the macroscale system is coupled to the microscale structure and dynamics, and they derive the appropriate relationship to impose.

Dalwadi et al. [15] consider a contaminant transport through a filter with a locally periodic time-dependent microstructure. The contaminant is transported via advection, diffusion, and sorption to the filter, and the filter structure evolves due to this deposition. The homogenised system derived by the authors consists of an advection-diffusion-reaction equation for the solute transport and a modified Darcy law for the fluid flow, and an evolution model for the underlying effective porosity of the filter. Dalwadi and King [16] consider diffusive chemical transport through a colony of bacterium contained within an extracellular matrix. The microscale domain consists of a locally periodic array of spherical bacteria acting as (nonlinear) volumetric sinks. Dalwadi and King derive an effective macroscale reaction-diffusion system by identifying and exploring the different distinguished limits of the model.

In the model we develop in this Chapter, we consider a local microstructure which varies both in macroscale space and in time, evolving due to organoid growth. We model the transport of a nutrient and a waste metabolite within the hydrogel and organoid regions, considering the distinct cases of volumetric and surface uptake, and couple this to a model for organoid growth. We derive a closed macroscale model consisting of an organoid growth model and effective reaction-diffusion equation for metabolite transport, which depends on the local microstructure. This is an extension to the model derived in [17], as we allow our microstructure to depend on time, and also to [15], as we track the metabolite concentrations across the whole microscale domain (including within our microscale obstacle).

3.1.2 Chapter outline

The CXP1 bioreactor is initially seeded with $\mathcal{O}(10^6)$ cells of diameter 10 µm in a hydrogel. CXP1 typically cultures organoids expanded from single cells until they are approximately $40 - 85$µm in diameter. The lengthscale of the hydrogel is $\mathcal{O}(10^{-2}\text{m})$. A schematic showing the different lengthscales in the problem is shown in Figure 3.1. Resolving for all the individual organoid regions within the hydrogel is, therefore, a formidable and computationally expensive task. We take a mathematical homogenisation approach to understand how the behaviour of the organoids on the *microscale* influences the *macroscale* metabolite behaviour in the hydrogel layer. To this end, we systematically derive *effective* macroscale governing equations for metabolite transport.

We take a similar approach to [16], who consider mass transport within a hydrogel layer containing spherical metabolite sink regions, which can vary in size spatially. We model individual organoids embedded within the hydrogel as time-varying spherical regions within a cubic lattice. We allow the organoid radii to be temporally dependent as we consider the growth of the organoids, and for the organoids to have slightly different radii to their neighbours. The temporal dependence of organoid radii is prescribed through a growth model, which is dependent on local metabolite concentrations. Since the local metabolite concentrations are spatially dependent, this induces (macroscale) spatial variation in the organoid radii. We consider two different types of organoid structure: *dense* organoids which are dense spherical clusters of cells, Figure 3.2 (**left**), and *shell* organoids, comprising of a single layer of cells forming a spherical shell with a central lumen devoid of cells, Figure 3.2 (**centre**). For dense organoids, we impose volumetric growth and assume that glucose is consumed and lactate is produced across the entire organoid. For shell organoids, we impose surface growth and assume that glucose is consumed and lactate is produced at the organoid-hydrogel boundary. We model the individual cells within an organoid as incompressible rigid spheres, all of which have the same radius, and assume the packing density of cells within an organoid is constant. We introduce models for glucose consumption and organoid growth in Section 3.2.1.2. We present the detailed derivation of homogenised equations for volumetric growth of a dense organoid, and we highlight how this would differ for surface growth in Section 3.3.2. In Section 3.4.1, we discuss the similarities of, and differences between, the models for volumetric and surface growth. In Section 3.4.2, we explain how we numerically solve the microscale *cell problem* (see Section 3.3.1), which allows us to compute the effective diffusivities of glucose and lactate as functions of organoid radius. In Section 3.4.3, we consider the model behaviour for a cube of hydrogel under different culture conditions. We investigate the effect of increasing flow rate on the metabolite concentrations and the mean and variation in organoid radius, and compare this data to that obtained for static culture conditions. In Section 3.5, we discuss our results and highlight avenues of model development and potential future work.

3.2 Model set-up

We consider the diffusive transport of glucose and lactate through an array of organoids embedded within a hydrogel. We account for the uptake and production of glucose

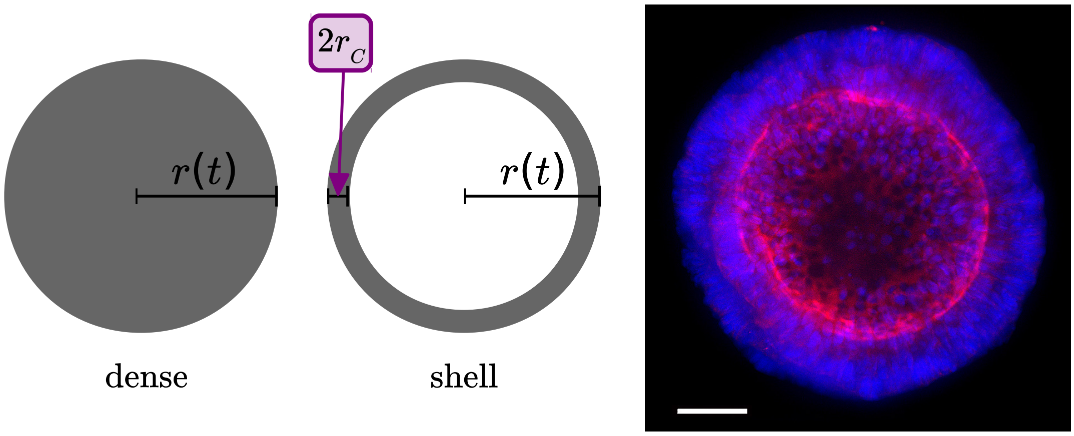

Figure 3.2: (**Left, centre**) Two-dimensional schematics of the organoid structures considered, dense (**left**) and shell (**centre**), where $r(t)$ denotes the organoid radius and r_c is the radius of a single cell. (**Right**) Example of colorectal organoid, stained for nuclear (blue) and cytoskeletal (red) markers for imaging. Scale 50µm.

and lactate, respectively, within the organoids. The organoids are modelled as a collection of spheres that grow in time and through which the metabolites can diffuse. We denote the glucose and lactate concentrations as $c(\boldsymbol{x}, t)$ and $w(\boldsymbol{x}, t)$ respectively, and use subscripts H and O to denote the hydrogel and organoid domains, respectively. Here $\boldsymbol{x}$ is the macroscale spatial coordinate (we adopt a Cartesian coordinate system $\boldsymbol{x} = (x, y, z)$) and t is time. The hydrogel phase of the domain is defined as ω_H and the organoid phase is defined as ω_O. There are no voids in the domain. The entire domain is, therefore, $\omega := \omega_H \cup \omega_O$. We impose that the volume of the entire domain does not change with time. We do not track water in the system, as we require the total volume of the organoid and hydrogel domains to remain constant. Therefore, any water displaced from the hydrogel domain due to organoid growth must enter the organoid domain. We do not model any mechanical effects of the hydrogel or organoid regions.

The organoid phase is modelled by a collection of non-overlapping spheres whose centres are located on a cubic lattice at a distance of δL apart, where δ is a small dimensionless parameter and L is the characteristic bioreactor lengthscale. Thus, $\delta \ll 1$ is the ratio of organoid centre separation to bioreactor length. We allow the radii of the spheres to vary in both space and time, and a sphere with centre at $\boldsymbol{x}$ has radius $r(\boldsymbol{x}, t)$, where $2r \leq \delta L$. We note that, strictly speaking, this is piecewise constant, rather than continuously varying, however we find that it is okay to treat it as continuous at the macroscale. A schematic of this set-up is shown in Figure 3.1. We define the model parameters introduced below, together with typical values, in Table 3.1.

3.2.1 Governing equations

We consider metabolite transport within hydrogel and organoid regions, denoted ω_H and ω_O. respectively, as shown in Figure 3.1. We make the following assumptions about the transport mechanisms:

- Glucose and lactate are transported via diffusion in the hydrogel and organoid regions.
- Since the hydrogel and organoid regions are time-dependent, the metabolites are also transported via dilution.
- For dense organoids, glucose and lactate are consumed and produced, respectively, across the entire organoid region, since it is closely packed with living cells.
- For shell organoids, glucose and lactate are consumed and produced, respectively, at the organoid-hydrogel interface where the cells are located.
- Lactate is produced at twice the rate glucose is consumed, due to the reaction stoichiometry [51].
- Glucose consumption is dependent on the local metabolite concentrations.
- Cellular proliferation is dependent on the local metabolite concentrations [23].

We model the transport of metabolite as a system of partial differential equations, where glucose and lactate concentrations are c_i and w_i, respectively, where $i \in \{H, O\}$ denote the hydrogel and organoid regions, respectively. The hydrogel and organoids domains are denoted $\omega_H(t)$ and $\omega_O(t)$, respectively. We impose that the total volume of organoid and hydrogel regions (that is, the total domain ω) remains constant and there are no voids within the domain. We denote the organoid-hydrogel boundary as $\partial\omega_O$. The velocity of the hydrogel and organoid regions are $\boldsymbol{u}_H$ and $\boldsymbol{u}_O$, respectively, and the velocity of the organoid-hydrogel boundary is denoted $\boldsymbol{u}_{\partial\omega_O}$. For dense organoids undergoing volumetric growth, these governing equations are:

$$\frac{\partial c_H}{\partial t} + \nabla \cdot (\boldsymbol{u}_H c_H) = D_{CH} \nabla^2 c_H \qquad \text{for } \boldsymbol{x} \in \omega_H, \tag{3.2.1a}$$

$$\frac{\partial c_O}{\partial t} + \nabla \cdot (\boldsymbol{u}_O c_O) = D_{CO} \nabla^2 c_O - s(c_O, w_O) \qquad \text{for } \boldsymbol{x} \in \omega_O, \tag{3.2.1b}$$

$$\frac{\partial w_H}{\partial t} + \nabla \cdot (\boldsymbol{u}_H w_H) = D_{WH} \nabla^2 w_H \qquad \text{for } \boldsymbol{x} \in \omega_H, \tag{3.2.1c}$$

$$\frac{\partial w_O}{\partial t} + \nabla \cdot (\boldsymbol{u}_O w_O) = D_{WO} \nabla^2 w_O + 2s(c_O, w_O) \qquad \text{for } \boldsymbol{x} \in \omega_O. \tag{3.2.1d}$$

The parameters $\{D_{CH}, D_{CO}, D_{WH}, D_{WO}\}$ are the diffusivities of glucose and lactate within the hydrogel and organoid regions, respectively, with units $\mathrm{m}^2\,\mathrm{s}^{-1}$. The term s is the rate of glucose consumption per unit volume per second, with units $\mathrm{mol}\,\mathrm{m}^{-3}\,\mathrm{s}^{-1}$. Although we prescribe a constitutive model for glucose consumption in Section 3.2.1.1, we proceed in the following analysis with a general form for the glucose consumption rate and note that, physically, we would expect this to be a monotonically increasing with glucose concentration. Lactate production occurs at rate $2s$ due to the reaction stoichiometry.

At the interface between the organoid and the hydrogel, $\partial\omega_O$, we impose a partition condition and continuity of flux at the *moving* hydrogel-organoid interface, $\boldsymbol{x} \in \partial\omega_O(t)$:

$$K_C c_O = c_H, \quad K_W w_O = w_H, \tag{3.2.2a}$$

$$\mathbf{n} \cdot (c_H (\boldsymbol{u}_H - \boldsymbol{u}_{\partial\omega_O}) - D_{CH}\nabla c_H) = \mathbf{n} \cdot (c_O (\boldsymbol{u}_O - \boldsymbol{u}_{\partial\omega_O}) - D_{CO}\nabla c_O), \tag{3.2.2b}$$

$$\mathbf{n} \cdot (w_H (\boldsymbol{u}_H - \boldsymbol{u}_{\partial\omega_O}) - D_{WH}\nabla w_H) = \mathbf{n} \cdot (w_O (\boldsymbol{u}_O - \boldsymbol{u}_{\partial\omega_O}) - D_{WO}\nabla w_O), \tag{3.2.2c}$$

where $\mathbf{n}$ is the outward-pointing unit normal on the organoid-hydrogel boundary in the radial direction, pointing from the organoid region into the hydrogel region. This latter condition captures the mass transfer across the organoid-hydrogel interface, *i.e.* when the organoid-hydrogel interface moves and a representative volume changes from *e.g.* hydrogel to organoid, any metabolite which was previously contained within the hydrogel is now absorbed within the organoid region. The partition condition governs the distribution of a solute between two immiscible solvents: the ratio between solute concentrations in each solvent is a constant, known as the *partition coefficient.* Non-unitary partition coefficients allow our model to capture physical systems where the properties of the hydrogel and organoid tissue are sufficiently different and have different solubilities to metabolites. We note that the organoid-hydrogel boundary velocity, $\boldsymbol{u}_{\partial\omega_O}$, is related to the rate of organoid growth via:

$$\mathbf{n} \cdot \boldsymbol{u}_{\partial\omega_O} = \frac{\partial r}{\partial t}. \tag{3.2.3}$$

We impose the initial glucose and lactate concentrations at $t = 0$,

$$c_H = c_{H\mathrm{init}}, \quad w_H = w_{H\mathrm{init}} \quad \text{for } \boldsymbol{x} \in \omega_H, \tag{3.2.4a}$$

$$c_O = c_{O\mathrm{init}}, \quad w_O = w_{O\mathrm{init}} \quad \text{for } \boldsymbol{x} \in \omega_O. \tag{3.2.4b}$$

There are two special cases we could consider to describe different interactions between the organoid and hydrogel:

(1) the hydrogel **compresses** as the organoid regions grow, with continuity of velocity at the organoid-hydrogel interface, *i.e.*

$$\boldsymbol{u}_O \cdot \mathbf{n} = \boldsymbol{u}_H \cdot \mathbf{n} = \boldsymbol{u}_{\partial\omega_O} \cdot \mathbf{n} = \frac{\partial r}{\partial t} \quad \text{at } \boldsymbol{x} \in \partial\omega_O, \tag{3.2.5}$$

which means the boundary conditions, Equations (3.2.2b) and (3.2.2c), become

$$\mathbf{n} \cdot (D_{CH} \nabla c_H) = \mathbf{n} \cdot (D_{CO} \nabla c_O), \tag{3.2.6a}$$

$$\mathbf{n} \cdot (D_{WH} \nabla w_H) = \mathbf{n} \cdot (D_{WO} \nabla w_O); \tag{3.2.6b}$$

(2) the hydrogel is static but **degrades** at the same rate as the organoid growth, *i.e.*

$$\boldsymbol{u}_H \equiv \mathbf{0} \quad \text{for } \boldsymbol{x} \in \omega_H \quad \text{and} \quad \boldsymbol{u}_O \cdot \mathbf{n} = \boldsymbol{u}_{\partial\omega_O} \cdot \mathbf{n} = \frac{\partial r}{\partial t} \quad \text{at } \boldsymbol{x} \in \partial\omega_O, \tag{3.2.7}$$

which means the boundary conditions, Equations (3.2.2b) and (3.2.2c), become

$$\mathbf{n} \cdot (D_{CH} \nabla c_H) + \mathbf{n} \cdot (\boldsymbol{u}_{\partial\omega_O} c_H) = \mathbf{n} \cdot (D_{CO} \nabla c_O), \tag{3.2.8a}$$

$$\mathbf{n} \cdot (D_{WH} \nabla w_H) + \mathbf{n} \cdot (\boldsymbol{u}_{\partial\omega_O} w_H) = \mathbf{n} \cdot (D_{WO} \nabla w_O), \tag{3.2.8b}$$

which can also be written, using Equation (3.2.3), as

$$\mathbf{n} \cdot (D_{CH} \nabla c_H) + \frac{\partial r}{\partial t} c_H = \mathbf{n} \cdot (D_{CO} \nabla c_O), \tag{3.2.9a}$$

$$\mathbf{n} \cdot (D_{WH} \nabla w_H) + \frac{\partial r}{\partial t} w_H = \mathbf{n} \cdot (D_{WO} \nabla w_O). \tag{3.2.9b}$$

Although we mention these special cases for hydrogel behaviour for specificity, we note that the following non-dimensionalisation and homogenisation analysis holds for the general continuity of flux boundary condition (Equations (3.2.2b) and (3.2.2c)), so long as the velocities within the hydrogel and the organoid regions are of the same asymptotic order as the organoid-hydrogel boundary (*i.e.* the same timescale as organoid growth), which we could expect physically. We also note that we do not include any model for the mechanics of the hydrogel or organoid regions, and hence neglect any potential mechanical effects (*e.g.* compression) on the hydrogel or organoid properties. We discuss potential avenues to incorporate this in Section 6.2.

We now discuss how we model the glucose consumption and the growth of the organoids within the hydrogel layer.

3.2.1.1 Glucose consumption model

We pose a constitutive model for the reaction kinetics for glucose consumption, $s(c_O, w_O, t)$:

$$s(c_O, w_O, t) = s_V \phi \frac{c_O}{\nu_W w_O + c_O}, \tag{3.2.10}$$

where s_V is the rate of glucose consumption per unit volume of organoid biomass, with units $\mathrm{mol\,m^{-3}\,s^{-1}}$, ϕ is the packing density of the cells within the uptake region of organoid, *i.e.* the volume fraction of cells in an organoid, and ν_W is a dimensionless constant prescribing the (inhibitory) sensitivity of the organoids to lactate. This is a difficult parameter to quantify. Since we find that the results for different ν_W are not qualitatively different, we set $\nu_W = 0.5$ for the simulations in Section 3.4. This glucose consumption function, s, is saturating increasing in glucose concentration and is inhibited by increasing levels of lactate.

3.2.1.2 Organoid growth model

We require a constitutive relation for the evolution of organoid radius over time in order to close the system. We assume that organoids are spherical and that all cells within the organoid proliferate exponentially. Since the organoids are very small ($\mathcal{O}(10^{-5} - 10^{-4}\mathrm{m})$ in diameter), there is no necrotic core at the centre of the organoids. We model the individual cells within the organoids as rigid spheres of radius r_c, which do not deform or overlap, and they have an associated (constant) packing density ϕ within the organoid. We denote the organoid biomass volume, which is the volume of cells plus their packing space within an organoid, as v. Therefore, the organoid biomass volume, v, evolves as:

$$\frac{\partial v}{\partial t} = pv, \tag{3.2.11}$$

where p is the proliferation rate. We note that although the packing space within the organoid does not explicitly proliferate, the new cells created through proliferation of existing cells have an associated packing space.

For dense organoids, the entire volume is densely packed with cells (with constant packing density ϕ) and, therefore, the relationship between organoid biomass volume, v, and radius, r, is

$$v = \frac{4\pi}{3} r^3, \tag{3.2.12}$$

which means the rate of change in organoid radius in time is:

$$\frac{\partial r}{\partial t} = \frac{p}{3} r. \tag{3.2.13}$$

For shell organoids, the organoid consists of a single layer of proliferating cells (with thickness $2r_c$, the diameter of a single cell) around a central lumen, which does not proliferate or consume glucose. We assume the diffusivity in the cell and lumen regions are the same. The relationship between organoid biomass volume, v, and the organoid radius, r, is

$$v = \frac{4}{3}\pi\left(r^3 - (r-2r_c)^3\right) = 8\pi r_c\left((r-r_c)^2 + \frac{r_c^2}{3}\right), \tag{3.2.14}$$

since the proliferating cells are located only within one cell diameter, $2r_c$, from the outer boundary of the organoid, which gives the rate of change of organoid radius in time:

$$(r-r_c)\frac{\mathrm{d}r}{\mathrm{d}t} = \frac{p}{2}\left((r-r_c)^2 + \frac{r_c^2}{3}\right). \tag{3.2.15}$$

Depending on the nature of the experimental data, it may be helpful to relate the organoid radius to the number of cells within the organoid. For dense organoids, the entire volume is densely packed with cells with packing density ϕ, so the organoid biomass volume is related to number of cells via

$$\phi v(\boldsymbol{x},t) = \phi\frac{4}{3}\pi r^3(\boldsymbol{x},t) = v_C n(\boldsymbol{x},t), \tag{3.2.16}$$

where v_C is the volume of a single cell, $v_C = 4\pi r_C^3/3$, and $n(\boldsymbol{x},t)$ is the number of cells within an organoid. This simplifies to

$$n = \frac{\phi r^3}{r_C^3} \iff r = \phi^{-\frac{1}{3}} r_c n^{\frac{1}{3}}, \tag{3.2.17}$$

which shows that the number of cells scales with r^3, as expected. We choose the packing density, ϕ, to be $\pi/3\sqrt{2}$, the optimal packing density for spheres in an infinite domain [34, 81].

For shell organoids of radius r, the total organoid volume is $4\pi r^3/3$ and, since the cells are in a single layer around a central lumen, the organoid biomass volume is related to number of cells via

$$\phi v(\boldsymbol{x},t) = \phi\frac{4}{3}\pi\left(r^3 - (r-2r_c)^3\right) = v_C n(\boldsymbol{x},t), \tag{3.2.18}$$

which simplifies to

$$n = \frac{6\phi}{r_c^2}\left((r-r_c)^2 + \frac{r_c^2}{3}\right) \iff r = r_c + \frac{r_c}{\sqrt{6}}\left(\frac{n}{\phi} - 2\right)^{\frac{1}{2}}. \tag{3.2.19}$$

This gives that the number of cells, n, within a shell organoid scales with r^2 for large n, as expected.

3.2.1.3 Model for cellular proliferation

We now introduce a functional form for the rate of cellular proliferation, informed by experimental data. Cellular proliferation is dependent on the local metabolite concentrations [23], and we allow the proliferation rate to depend on glucose and lactate concentrations within the organoid regions and write $p = p(c_O, w_O)$.

The cellular proliferation responds positively to increasing glucose concentrations and negatively to increasing lactate concentrations. We model the inhibitory effect of lactate on cell proliferation via an inhibition term in the proliferation rate. We pose the following constitutive model for proliferation rate:

$$p(c_O, w_O) = f\frac{g_b}{\phi}s(c_O, w_O), \tag{3.2.20}$$

where s is the glucose consumption rate discussed in Section 3.2.1.1. We have assumed that a fraction, f, of the glucose consumed is synthesised into organoid biomass, where g_b is the volume of cells produced per mole of glucose consumed, units $\mathrm{m}^3\,\mathrm{mol}^{-1}$. This parameter depends on the type of respiration the cells undergo, *anaerobic* or *aerobic*. Cancerous cells are known to utilise anaerobic respiration in the presence of the sufficient oxygen, known as the Warburg effect [51]. The factor of $1/\phi$ is incorporated to relate how the new cells increase the organoid biomass volume. Typical parameter values for the system Equations (3.2.1) to (3.2.4) are given in Table 3.1.

Table 3.1: Definitions of dimensional model parameters, together with typical values. Where no citation is given, parameters are taken from the CPX1 set-up.

Parameter	Definition	Typical value
D_{CH}	Diffusivity of glucose in hydrogel	$6.0 \times 10^{-10}\ \mathrm{m}^2\,\mathrm{s}^{-1}$ [84]
D_{CO}	Diffusivity of glucose in organoid	$1 \times 10^{-10}\ \mathrm{m}^2\,\mathrm{s}^{-1}$ [95]
D_{WH}	Diffusivity of lactate in hydrogel	$1.2 \times 10^{-9}\ \mathrm{m}^2\,\mathrm{s}^{-1}$ [98]
D_{WO}	Diffusivity of lactate in organoid	$2.1 \times 10^{-10}\ \mathrm{m}^2\,\mathrm{s}^{-1}$ [31]
$c_{-\infty}$	Glucose concentration in upstream reservoir	$16\ \mathrm{mol}\,\mathrm{m}^{-3}$
L	Typical lengthscale of bioreactor	$9 \times 10^{-2}\ \mathrm{m}$
s_V	Glucose consumption rate per volume of cell	$1.9 \times 10^{-1}\ \mathrm{mol}\,\mathrm{m}^{-3}\,\mathrm{s}^{-1}$
r_c	Radius of single cell	$5 \times 10^{-6}\ \mathrm{m}$
ϕ	Packing fraction of cells within an organoid	$\pi/3\sqrt{2} \approx 0.74$ [34]
g_b	Volume of cells produced per glucose consumed	7×10^{-5} (anaerobic) to $10^{-3}\ \mathrm{m}^3\,\mathrm{mol}^{-1}$ (aerobic) [46]

To obtain a value for g_b, the volume of cells produced per glucose consumed, we must consider how the glucose consumed by the organoids is converted into ATP (adenosine triphosphate) and consequently used in cell synthesis. The amount of ATP produced depends on the type of respiration [88]: for *anaerobic respiration*, 1 mol of glucose produces 2 mol of ATP; and for *aerobic respiration* 1 mol of glucose produces up to 32 mol ATP. Kilburn et al. [46] find that the mean energy required to synthesise a single cell is 1.6×10^{-11} moles of ATP per cell. Therefore,

$$\begin{aligned}&\text{volume of cells produced per glucose consumed}\\ &\quad= \frac{\text{ATP produced per mole of glucose consumed}}{\text{ATP required to synthesise a cell}} \times \text{volume of a cell},\end{aligned}$$

and we determine g_b to be

$$\begin{aligned} g_b &= \frac{(2-32)[\text{mol ATP}]/[\text{mol glucose}]}{1.6\times 10^{-11}[\text{mol ATP}]/\text{cell}} \times \left(\frac{4}{3}\pi r_c^3 \text{ m}^3\,\text{cell}^{-1}\right),\\ \Rightarrow\quad g_b &= 7\times 10^{-5}[\text{anaerobic}] - 1\times 10^{-3}[\text{aerobic}]\ \text{m}^3\,\text{mol}^{-1}. \end{aligned} \tag{3.2.21}$$

In Section 3.4, we take the average of this, $g_b = 5.4 \times 10^{-4}\ \text{m}^3\,\text{mol}^{-1}$, so that this represents an equal proportion of the organoids respiring aerobically and anaerobically.

3.2.2 Non-dimensionalisation of governing equations

We non-dimensionalise via the scalings:

$$\begin{gathered} \boldsymbol{x} = L\boldsymbol{X}, \quad t = \frac{L^2}{D_{CH}}T, \quad n = n_0 N, \quad (r, r_c) = \delta L(R, R_c), \quad p = f g_b s_V P,\\ s(c_O, w_O) = s_V \phi S(C_O, W_O), \quad (\boldsymbol{u}_O, \boldsymbol{u}_H, \boldsymbol{u}_{\partial\omega_O}) = \frac{\delta D_{CH}}{L}(\boldsymbol{U}_O, \boldsymbol{U}_H, \boldsymbol{U}_{\partial\Omega_O}),\\ (c_H, c_O, c_{H\text{init}}, c_{O\text{init}}) = c_{-\infty}(C_H, C_O, C_{H\text{init}}, C_{O\text{init}}),\\ (w_H, w_O, w_{H\text{init}}, w_{O\text{init}}) = c_{-\infty}(W_H, W_O, W_{H\text{init}}, W_{O\text{init}}), \end{gathered} \tag{3.2.22}$$

where δ is the ratio of organoid centre separation and bioreactor lengthscales, n_0 is the initial number of cells within an organoid (in our case, 1 cell), and the metabolite concentrations are scaled with $c_{-\infty}$, the glucose concentration within the culture media stored in the upstream reservoir of the CXP1 bioreactor. We have chosen to scale the organoid-hydrogel interface velocity with $\delta D_{CH}/L$ to balance the relationship Equation (3.2.3), and we assume that the velocities of the hydrogel and the organoid are of the same order (that is, $\mathcal{O}(\delta D_{CH}/L)$).

The governing equations for dense organoids undergoing volumetric growth (Equation (3.2.1)) become:

$$\frac{\partial C_H}{\partial T} + \delta\nabla \cdot (\boldsymbol{U}_H C_H) = \nabla^2 C_H, \qquad \text{for } \boldsymbol{X} \in \Omega_H, \tag{3.2.23a}$$

$$\frac{\partial C_O}{\partial T} + \delta\nabla \cdot (\boldsymbol{U}_O C_O) = d_{CO}\nabla^2 C_O - \sigma_V S, \qquad \text{for } \boldsymbol{X} \in \Omega_O, \tag{3.2.23b}$$

$$\frac{\partial W_H}{\partial T} + \delta\nabla \cdot (\boldsymbol{U}_H W_H) = d_{WH}\nabla^2 W_H \qquad \text{for } \boldsymbol{X} \in \Omega_H, \tag{3.2.23c}$$

$$\frac{\partial W_O}{\partial T} + \delta\nabla \cdot (\boldsymbol{U}_O W_O) = d_{WO}\nabla^2 W_O + 2\sigma_V S \qquad \text{for } \boldsymbol{X} \in \Omega_O, \tag{3.2.23d}$$

where the hydrogel and organoid domains are denoted Ω_H and Ω_O, respectively. We define the dimensionless parameter groupings:

$$\sigma_V = \frac{s_V \phi L^2}{c_{-\infty} D_{CH}}, \quad (d_{CO}, d_{WH}, d_{WO}) = \frac{1}{D_{CH}}(D_{CO}, D_{WH}, D_{WO}), \tag{3.2.24}$$

where σ_V is the ratio of the timescale of glucose consumption to diffusion of glucose in hydrogel (Damköhler number) and d_{ij} is the ratio of diffusivity of metabolite i ($i \in \{C, W\}$) in domain j ($j \in \{H, O\}$) to the diffusivity of glucose in hydrogel. The definitions of the dimensionless parameters in this model and their typical values are given in Table 3.2.

The boundary conditions at the hydrogel-organoid interface, $\boldsymbol{X} \in \partial\Omega_O$, are:

$$K_C C_O = C_H, \quad K_W W_O = W_H, \tag{3.2.25a}$$

$$\mathbf{n} \cdot (\nabla C_H + \delta (\boldsymbol{U}_{\partial\Omega_O} - \boldsymbol{U}_H) C_H) = \mathbf{n} \cdot (d_{CO}\nabla C_O + \delta (\boldsymbol{U}_{\partial\Omega_O} - \boldsymbol{U}_O) C_O), \tag{3.2.25b}$$

$$\mathbf{n} \cdot (d_{WH}\nabla W_H + \delta (\boldsymbol{U}_{\partial\Omega_O} - \boldsymbol{U}_H) W_H) = \mathbf{n} \cdot (d_{WO}\nabla W_O + \delta (\boldsymbol{U}_{\partial\Omega_O} - \boldsymbol{U}_O) W_O); \tag{3.2.25c}$$

with

$$\boldsymbol{U}_{\partial\Omega_O} \cdot \mathbf{n} = \frac{\partial R}{\partial T}. \tag{3.2.25d}$$

We note that the boundary conditions (Equations (3.2.25b) and (3.2.25c)) at the hydrogel-organoid interface, $\boldsymbol{X} \in \partial\Omega_O$, for **compression** of hydrogel would reduce to:

$$\mathbf{n} \cdot (\nabla C_H) = \mathbf{n} \cdot (d_{CO}\nabla C_O), \tag{3.2.26a}$$

$$\mathbf{n} \cdot (d_{WH}\nabla W_H) = \mathbf{n} \cdot (d_{WO}\nabla W_O); \tag{3.2.26b}$$

with continuity of velocity,

$$\boldsymbol{U}_O = \boldsymbol{U}_H = \boldsymbol{U}_{\partial\Omega_O} \quad \text{with} \quad \mathbf{n} \cdot \boldsymbol{U}_{\partial\Omega_O} = \frac{\partial R}{\partial T}. \tag{3.2.26c}$$

Similarly, for **degradation** of hydrogel, they would to become:

$$\mathbf{n} \cdot (\nabla C_H + \delta \boldsymbol{U}_{\partial\Omega_O} C_H) = \mathbf{n} \cdot (d_{CO} \nabla C_O), \tag{3.2.27a}$$

$$\mathbf{n} \cdot (d_{WH} \nabla W_H) = \mathbf{n} \cdot (d_{WO} \nabla W_O); \tag{3.2.27b}$$

with continuity of velocity,

$$\boldsymbol{U}_O = \boldsymbol{U}_{\partial\Omega_O} \quad \text{with} \quad \mathbf{n} \cdot \boldsymbol{U}_{\partial\Omega_O} = \frac{\partial R}{\partial T}. \tag{3.2.27c}$$

The glucose and lactate concentrations at $T = 0$ are:

$$C_H = C_{H\text{init}}, \quad W_H = W_{H\text{init}} \quad \text{for } \boldsymbol{X} \in \Omega_H, \tag{3.2.28a}$$

$$C_O = C_{O\text{init}}, \quad W_O = W_{O\text{init}} \quad \text{for } \boldsymbol{X} \in \Omega_O. \tag{3.2.28b}$$

We non-dimensionalise the glucose consumption (Equation (3.2.10)) and proliferation rates (Equation (3.2.20)) using Equation (3.2.24) to obtain

$$S(C_O, W_O) = \frac{C_O}{\nu_W W_O + C_O}, \tag{3.2.29a}$$

$$P(C_O, W_O) = \frac{C_O}{\nu_W W_O + C_O}. \tag{3.2.29b}$$

We obtain the following dimensionless governing equations for organoid growth and relationships between dimensionless organoid radius R and dimensionless number of cells N:

dense organoids:
$$\begin{cases} \dfrac{\partial R}{\partial T} = \dfrac{\rho}{3} P(C_O, W_O) R, & (3.2.30a) \\ R = \phi^{-\frac{1}{3}} R_c N^{\frac{1}{3}}; & (3.2.30b) \end{cases}$$

shell organoids:
$$\begin{cases} (R - R_c) \dfrac{\mathrm{d}R}{\mathrm{d}T} = \dfrac{\rho}{2} P(C_O, W_O) \left((R - R_c)^2 + \dfrac{R_c^2}{3} \right), & (3.2.31a) \\ R = R_c + \dfrac{R_c}{\sqrt{6}} \left(\dfrac{N}{\phi} - 2 \right)^{\frac{1}{2}}; & (3.2.31b) \end{cases}$$

where we define the dimensionless parameter grouping ρ,

$$\rho = [p][t] = \frac{f g_b s_V L^2}{D_{CH}}. \tag{3.2.32}$$

We highlight that, since the proliferation rate, Equation (3.2.29b), depends on the local metabolite concentrations, R can evolve spatially even for an initially uniform organoid radius.

We give typical values for the dimensionless parameters in our model for metabolite transport and organoid growth in Table 3.2. In this table, we take $L = 1.9 \times 10^{-2}$ m, as this is the value of L used in Section 3.4. This value of L is the length of a cube which has the same volume as the hydrogel in CXP1.

Table 3.2: Definitions of dimensionless model parameters, together with typical values. The typical lengthscale L has been taken to be 1.9×10^{-2} m.

Parameter	Definition	Typical value
δ	Ratio of microscale 'cell' lengthscale to bioreactor lengthscale	10^{-2}
d_{CO}	Ratio of diffusivity of glucose in organoid to diffusivity of glucose in hydrogel	1/6
d_{WH}	Ratio of diffusivity of lactate in hydrogel to diffusivity of glucose in hydrogel	2
d_{WO}	Ratio of diffusivity of lactate in organoid to diffusivity of glucose in hydrogel	0.35
σ_V	Ratio of rate of glucose consumption per organoid volume to glucose diffusion in hydrogel	5.3×10^3
σ_S	Ratio of rate of glucose consumption per surface area of organoid-hydrogel boundary to glucose diffusion in hydrogel	280
R_c	Dimensionless radius of single cell	2.6×10^{-2}
ρ	Ratio of timescale of cell proliferation to timescale of glucose diffusion in hydrogel	$2 - 29$
ϕ	Dimensionless packing density of spheres within spheres	$\pi/3\sqrt{2}$ [34]
ν_W	Sensitivity of cell line to lactate	0.5
f	Fraction of glucose consumed utilised for cell synthesis	0.25
K_C	Organoid-hydrogel partition coefficient for glucose	1
K_W	Organoid-hydrogel partition coefficient for lactate	1

3.3 Derivation of homogenised metabolite transport equations

We now derive the homogenised governing equations for metabolite transport within the organoid-hydrogel region. We consider the case of general hydrogel deformation, but note that the homogenised governing equations for both the compression of hydrogel (Equation (3.2.26)) and the degradation of hydrogel (Equation (3.2.27)) models are the same as for the general model (Equation (3.2.25)).

We proceed by introducing a microscale spatial variable, $\boldsymbol{Y}$, defined as

$$\boldsymbol{Y} = \frac{\boldsymbol{X} - \lfloor \boldsymbol{X} \rfloor}{\delta} - \boldsymbol{b}, \tag{3.3.1}$$

where $\boldsymbol{b}$ is a translation vector, $\boldsymbol{b} = (1/2, 1/2, 1/2)^T$, and $\lfloor \cdot \rfloor$ is the floor function, so $\boldsymbol{Y} \in [-1/2, 1/2]^3$, defined in unit cell $\Omega(\boldsymbol{X}, T)$, centred around one organoid. Equation (3.3.1) is a mapping from macroscale space, $\boldsymbol{X} \in \Omega_H \cup \Omega_O$, to the microscale periodic cell, $\boldsymbol{Y} \in [-1/2, 1/2]^3$. We treat all variables as functions of $\boldsymbol{X}$ and $\boldsymbol{Y}$, and we remove the extra degree of freedom this gives by imposing periodicity in each component of $\boldsymbol{Y}$. This unit cell is dependent on the macroscale spatial variable $\boldsymbol{X}$, as we allow there to be variation in metabolite concentration and organoid size over a long macroscale lengthscale. The parameter δ is the ratio between organoid centre separation and bioreactor lengthscales and can be equivalently thought of as the lengthscale of the microscale unit cell. A schematic of this is shown in Figure 3.3.

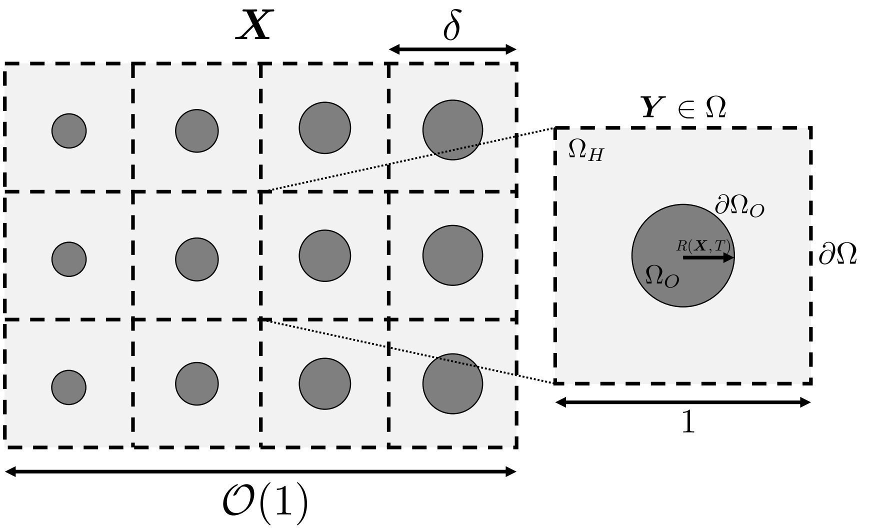

Figure 3.3: Two-dimensional projection of the three-dimensional domain we consider.

We note that spatial derivatives transform as:

$$\nabla \to \nabla_{\boldsymbol{X}} + \frac{1}{\delta}\nabla_{\boldsymbol{Y}}. \tag{3.3.2}$$

Due to this, the unit normal to the boundary $\partial\Omega_O(\boldsymbol{X}, T)$ also transforms. To understand how it depends on both spatial variables, we define $\chi(\boldsymbol{X}, \boldsymbol{Y}) = \|\boldsymbol{Y}\| - R(\boldsymbol{X}, T)$, so $\chi = 0$ gives $\partial\Omega_O(\boldsymbol{X}, T)$. Since the normal to the boundary is proportional to the gradient of the surface $\nabla\chi$, we use Equation (3.3.2) and find

$$\mathbf{n} = \frac{\nabla\chi}{\|\nabla\chi\|} \;\Rightarrow\; \mathbf{n} = \frac{\mathbf{n}_{\boldsymbol{Y}} - \delta\nabla_{\boldsymbol{X}} R}{\|\mathbf{n}_{\boldsymbol{Y}} - \delta\nabla_{\boldsymbol{X}} R\|}, \tag{3.3.3}$$

where we define

$$\mathbf{n}_{\boldsymbol{Y}} = \frac{\boldsymbol{Y}}{\|\boldsymbol{Y}\|}, \tag{3.3.4}$$

as the geometric unit normal to the organoid-hydrogel boundary $\partial\Omega_O$ pointing from the organoid region into the hydrogel region, where $\|\cdot\|$ is the L^2-norm. Equation (3.3.3) relates how to interpret the macroscale unit normal on the microscale, due to the macroscale-evolving microstructure.

3.3.1 Model for dense organoids with volumetric growth

In this Section, we derive the homogenised governing equations for metabolite concentration within the 'hydrogel layer' for dense organoids undergoing volumetric growth.

Using Equation (3.3.2), the governing equations, Equation (3.2.23), become:

$$\begin{aligned}
\delta^2\frac{\partial C_H}{\partial T} &+ \delta^2\left(\nabla_{\boldsymbol{Y}} + \delta\nabla_{\boldsymbol{X}}\right)\cdot\left(\boldsymbol{U}_H C_H\right) \\
&= \left(\nabla_{\boldsymbol{Y}} + \delta\nabla_{\boldsymbol{X}}\right)\cdot\left(\nabla_{\boldsymbol{Y}} + \delta\nabla_{\boldsymbol{X}}\right)C_H \text{ for } \boldsymbol{Y}\in\Omega_H(\boldsymbol{X},T), \qquad (3.3.5\text{a})\\
\delta^2\frac{\partial C_O}{\partial T} &+ \delta^2\left(\nabla_{\boldsymbol{Y}} + \delta\nabla_{\boldsymbol{X}}\right)\cdot\left(\boldsymbol{U}_O C_O\right) = d_{CO}\left(\nabla_{\boldsymbol{Y}} + \delta\nabla_{\boldsymbol{X}}\right)\cdot\left(\nabla_{\boldsymbol{Y}} + \delta\nabla_{\boldsymbol{X}}\right)C_O \\
&\qquad - \delta^2\sigma_V S(C_O, W_O) \text{ for } \boldsymbol{Y}\in\Omega_O(\boldsymbol{X},T), \qquad (3.3.5\text{b})\\
\delta^2\frac{\partial W_H}{\partial T} &+ \delta^2\left(\nabla_{\boldsymbol{Y}} + \delta\nabla_{\boldsymbol{X}}\right)\cdot\left(\boldsymbol{U}_H W_H\right) \\
&= d_{WH}\left(\nabla_{\boldsymbol{Y}} + \delta\nabla_{\boldsymbol{X}}\right)\cdot\left(\nabla_{\boldsymbol{Y}} + \delta\nabla_{\boldsymbol{X}}\right)W_H \text{ for } \boldsymbol{Y}\in\Omega_H(\boldsymbol{X},T), \qquad (3.3.5\text{c})\\
\delta^2\frac{\partial W_O}{\partial T} &+ \delta^2\left(\nabla_{\boldsymbol{Y}} + \delta\nabla_{\boldsymbol{X}}\right)\cdot\left(\boldsymbol{U}_O W_O\right) = d_{WO}\left(\nabla_{\boldsymbol{Y}} + \delta\nabla_{\boldsymbol{X}}\right)\cdot\left(\nabla_{\boldsymbol{Y}} + \delta\nabla_{\boldsymbol{X}}\right)W_O \\
&\qquad + 2\delta^2\sigma_V S(C_O, W_O) \text{ for } \boldsymbol{Y}\in\Omega_O(\boldsymbol{X},T), \qquad (3.3.5\text{d})
\end{aligned}$$

with boundary conditions (Equation (3.2.25)) on $\boldsymbol{Y}\in\partial\Omega_O(\boldsymbol{X},T)$ transforming to:

$$K_C C_O = C_H, \qquad K_W W_O = W_H, \qquad (3.3.6\text{a})$$

$$\begin{aligned}
&\left(\mathbf{n}_{\boldsymbol{Y}} - \delta\nabla_{\boldsymbol{X}}R\right)\cdot\left(\left(\nabla_{\boldsymbol{Y}} + \delta\nabla_{\boldsymbol{X}}\right)C_H + \delta^2 C_H\left(\boldsymbol{U}_{\partial\Omega_O} - \boldsymbol{U}_H\right) + \mathcal{O}(\delta^3)\right) \\
&= \left(\mathbf{n}_{\boldsymbol{Y}} - \delta\nabla_{\boldsymbol{X}}R\right)\cdot\left(d_{CO}\left(\nabla_{\boldsymbol{Y}} + \delta\nabla_{\boldsymbol{X}}\right)C_O + \delta^2 C_O\left(\boldsymbol{U}_{\partial\Omega_O} - \boldsymbol{U}_O\right) + \mathcal{O}(\delta^3)\right), \qquad (3.3.6\text{b})\\
&\left(\mathbf{n}_{\boldsymbol{Y}} - \delta\nabla_{\boldsymbol{X}}R\right)\cdot\left(d_{WH}\left(\nabla_{\boldsymbol{Y}} + \delta\nabla_{\boldsymbol{X}}\right)W_H + \delta^2 W_H\left(\boldsymbol{U}_{\partial\Omega_O} - \boldsymbol{U}_H\right) + \mathcal{O}(\delta^3)\right) \\
&= \left(\mathbf{n}_{\boldsymbol{Y}} - \delta\nabla_{\boldsymbol{X}}R\right)\cdot\left(d_{WO}\left(\nabla_{\boldsymbol{Y}} + \delta\nabla_{\boldsymbol{X}}\right)W_O + \delta^2 W_O\left(\boldsymbol{U}_{\partial\Omega_O} - \boldsymbol{U}_O\right) + \mathcal{O}(\delta^3)\right), \qquad (3.3.6\text{c})
\end{aligned}$$

and periodicity of C_H and W_H in $\boldsymbol{Y}$ on the unit cell boundary, $\boldsymbol{Y}\in\partial\Omega$.

In order to retain as many transport mechanisms in our homogenised equations as possible, we consider the distinguished limit

$$\begin{gathered}
d_{CO}\sim d_{WO}\sim d_{WH}\sim\mathcal{O}(1), \quad \sigma_V\sim\mathcal{O}(1), \quad R\sim\mathcal{O}(1), \\
\boldsymbol{U}_O\sim\boldsymbol{U}_H\sim\boldsymbol{U}_{\partial\Omega_O}\sim\mathcal{O}(1),
\end{gathered} \qquad (3.3.7)$$

and pose an asymptotic expansion in the limit $\delta\to 0$:

$$f\sim f_0 + \delta f_1 + \delta^2 f_2 + \ldots, \quad \text{where } f\in\{C_H, C_O, W_H, W_O\}. \qquad (3.3.8)$$

We note that there are other distinguished limits which pose interesting mathematical results. We discuss such a limit, where the organoids are very small with very strong uptake, in Appendix D.

$\mathcal{O}(1)$ problem:
At leading order in δ, Equations (3.3.5) and (3.3.6) yield

$$0 = \nabla_{\boldsymbol{Y}}^2 C_{H0}, \qquad 0 = d_{WH}\nabla_{\boldsymbol{Y}}^2 W_{H0} \quad \text{for } \boldsymbol{Y} \in \Omega_H(\boldsymbol{X},T), \tag{3.3.9a}$$

$$0 = d_{CO}\nabla_{\boldsymbol{Y}}^2 C_{O0}, \qquad 0 = d_{WO}\nabla_{\boldsymbol{Y}}^2 W_{O0} \quad \text{for } \boldsymbol{Y} \in \Omega_O(\boldsymbol{X},T), \tag{3.3.9b}$$

with boundary conditions on $\partial\Omega_O(\boldsymbol{X},T)$:

$$K_C C_{O0} = C_{H0}, \qquad \mathbf{n}_{\boldsymbol{Y}} \cdot \nabla_{\boldsymbol{Y}} C_{H0} = \mathbf{n}_{\boldsymbol{Y}} \cdot d_{CO}\nabla_{\boldsymbol{Y}} C_{M0}, \tag{3.3.10a}$$

$$K_W W_{O0} = W_{H0}, \qquad \mathbf{n}_{\boldsymbol{Y}} \cdot d_{WH}\nabla_{\boldsymbol{Y}} W_{H0} = \mathbf{n}_{\boldsymbol{Y}} \cdot d_{WO}\nabla_{\boldsymbol{Y}} W_{M0}; \tag{3.3.10b}$$

and C_{H0} and W_{H0} periodic on $\partial\Omega$. Thus, C_{H0}, C_{O0}, W_{H0}, W_{O0} are independent of $\boldsymbol{Y}$ at leading order, *i.e.*

$$C_{H0} = C_{H0}(\boldsymbol{X},T),\ C_{O0} = C_{O0}(\boldsymbol{X},T),\ W_{H0} = W_{H0}(\boldsymbol{X},T),\ W_{O0} = W_{O0}(\boldsymbol{X},T). \tag{3.3.11}$$

This states that the metabolite concentration within each organoid is spatially uniform. Since the leading-order metabolite concentrations are independent of $\boldsymbol{Y}$, the partition condition, which is prescribed on the boundary $\boldsymbol{Y} \in \partial\Omega_O$, holds for all $\boldsymbol{Y}$ and, therefore,

$$C_{H0}(\boldsymbol{X},T) = K_C C_{O0}(\boldsymbol{X},T) \quad \text{and} \quad W_{H0}(\boldsymbol{X},T) = K_W W_{O0}(\boldsymbol{X},T). \tag{3.3.12}$$

We use these relationships to simplify the analysis going forward.

Our remaining goal is to determine the governing equations for C_{O0} and W_{O0}. To determine the dependence of the metabolite concentrations on $\boldsymbol{X}$ and T, we now proceed to the $\mathcal{O}(\delta)$ problem.

$\mathcal{O}(\delta)$ problem:
The $\mathcal{O}(\delta)$ terms of the system Equations (3.3.5) and (3.3.6) are

$$0 = \nabla_{\boldsymbol{Y}} \cdot (\nabla_{\boldsymbol{Y}} C_{H1} + \nabla_{\boldsymbol{X}} C_{H0}) + \nabla_{\boldsymbol{X}} \cdot (\nabla_{\boldsymbol{Y}} C_{H0}) \quad \text{for } \boldsymbol{Y} \in \Omega_H(\boldsymbol{X},T), \tag{3.3.13a}$$

$$0 = d_{CO}\left[\nabla_{\boldsymbol{Y}} \cdot (\nabla_{\boldsymbol{Y}} C_{O1} + \nabla_{\boldsymbol{X}} C_{O0}) + \nabla_{\boldsymbol{X}} \cdot (\nabla_{\boldsymbol{Y}} C_{O0})\right] \quad \text{for } \boldsymbol{Y} \in \Omega_O(\boldsymbol{X},T), \tag{3.3.13b}$$

$$0 = d_{WH}\left[\nabla_{\boldsymbol{Y}} \cdot (\nabla_{\boldsymbol{Y}} W_{H1} + \nabla_{\boldsymbol{X}} W_{H0}) + \nabla_{\boldsymbol{X}} \cdot (\nabla_{\boldsymbol{Y}} W_{H0})\right] \quad \text{for } \boldsymbol{Y} \in \Omega_H(\boldsymbol{X},T), \tag{3.3.13c}$$

$$0 = d_{WO}\left[\nabla_{\boldsymbol{Y}} \cdot (\nabla_{\boldsymbol{Y}} W_{O1} + \nabla_{\boldsymbol{X}} W_{O0}) + \nabla_{\boldsymbol{X}} \cdot (\nabla_{\boldsymbol{Y}} W_{O0})\right] \quad \text{for } \boldsymbol{Y} \in \Omega_O(\boldsymbol{X},T), \tag{3.3.13d}$$

with boundary conditions on $\boldsymbol{Y} \in \partial\Omega_O(\boldsymbol{X}, T)$:

$$K_C C_{O1} = C_{H1}, \quad K_W W_{O1} = W_{H1}, \tag{3.3.14a}$$

$$\begin{aligned}&\left[\mathbf{n}_{\boldsymbol{Y}} \cdot (\nabla_{\boldsymbol{Y}} C_{H1} + \nabla_{\boldsymbol{X}} C_{H0}) - (\nabla_{\boldsymbol{X}} R) \cdot (\nabla_{\boldsymbol{Y}} C_{H0})\right] \\ &\qquad = d_{CO}\left[\mathbf{n}_{\boldsymbol{Y}} \cdot (\nabla_{\boldsymbol{Y}} C_{O1} + \nabla_{\boldsymbol{X}} C_{O0}) - (\nabla_{\boldsymbol{X}} R) \cdot (\nabla_{\boldsymbol{Y}} C_{O0})\right],\end{aligned} \tag{3.3.14b}$$

$$\begin{aligned}&d_{WH}\left[\mathbf{n}_{\boldsymbol{Y}} \cdot (\nabla_{\boldsymbol{Y}} W_{H1} + \nabla_{\boldsymbol{X}} W_{H0}) - (\nabla_{\boldsymbol{X}} R) \cdot (\nabla_{\boldsymbol{Y}} W_{H0})\right] \\ &\qquad = d_{WO}\left[\mathbf{n}_{\boldsymbol{Y}} \cdot (\nabla_{\boldsymbol{Y}} W_{O1} + \nabla_{\boldsymbol{X}} W_{O0}) - (\nabla_{\boldsymbol{X}} R) \cdot (\nabla_{\boldsymbol{Y}} W_{O0})\right].\end{aligned} \tag{3.3.14c}$$

Since $\{C_{H0}, C_{O0}, W_{H0}, W_{O0}\}$ are independent of $\boldsymbol{Y}$, the governing equations reduce to:

$$0 = \nabla^2_{\boldsymbol{Y}} C_{H1}, \qquad 0 = d_{WH}\nabla^2_{\boldsymbol{Y}} W_{H1} \quad \text{for } \boldsymbol{Y} \in \Omega_H(\boldsymbol{X}, T), \tag{3.3.15a}$$

$$0 = d_{CO}\nabla^2_{\boldsymbol{Y}} C_{O1}, \qquad 0 = d_{WO}\nabla^2_{\boldsymbol{Y}} W_{O1} \quad \text{for } \boldsymbol{Y} \in \Omega_O(\boldsymbol{X}, T), \tag{3.3.15b}$$

with boundary conditions on $\boldsymbol{Y} \in \partial\Omega_O(\boldsymbol{X}, T)$:

$$K_C C_{O1} = C_{H1}, \quad \mathbf{n}_{\boldsymbol{Y}} \cdot (\nabla_{\boldsymbol{Y}} C_{H1} + \nabla_{\boldsymbol{X}} C_{H0}) = d_{CO}\mathbf{n}_{\boldsymbol{Y}} \cdot (\nabla_{\boldsymbol{Y}} C_{O1} + \nabla_{\boldsymbol{X}} C_{O0}), \tag{3.3.16a}$$

$$\begin{aligned}&K_W W_{O1} = W_{H1}, \\ &\qquad d_{WH}\mathbf{n}_{\boldsymbol{Y}} \cdot (\nabla_{\boldsymbol{Y}} W_{H1} + \nabla_{\boldsymbol{X}} W_{H0}) = d_{WO}\mathbf{n}_{\boldsymbol{Y}} \cdot (\nabla_{\boldsymbol{Y}} W_{O1} + \nabla_{\boldsymbol{X}} W_{O0}).\end{aligned} \tag{3.3.16b}$$

We also have C_{H1} and W_{H1} are periodic on $\partial\Omega$, due to their 1-periodicity in $\boldsymbol{Y}$.

To reduce the parameter dependence of this problem, we exploit the linearity of the system, and seek solutions of the form:

$$C_{H1}(\boldsymbol{X}, \boldsymbol{Y}, T) = -\boldsymbol{\psi}(\boldsymbol{X}, \boldsymbol{Y}, T) \cdot \nabla_{\boldsymbol{X}} C_{H0} + \check{C}_{H1}(\boldsymbol{X}, T), \tag{3.3.17a}$$

$$C_{O1}(\boldsymbol{X}, \boldsymbol{Y}, T) = -\boldsymbol{\Psi}(\boldsymbol{X}, \boldsymbol{Y}, T) \cdot \nabla_{\boldsymbol{X}} C_{O0} + \check{C}_{O1}(\boldsymbol{X}, T), \tag{3.3.17b}$$

$$W_{H1}(\boldsymbol{X}, \boldsymbol{Y}, T) = -\boldsymbol{\gamma}(\boldsymbol{X}, \boldsymbol{Y}, T) \cdot \nabla_{\boldsymbol{X}} W_{H0} + \check{W}_{H1}(\boldsymbol{X}, T), \tag{3.3.17c}$$

$$W_{O1}(\boldsymbol{X}, \boldsymbol{Y}, T) = -\boldsymbol{\Gamma}(\boldsymbol{X}, \boldsymbol{Y}, T) \cdot \nabla_{\boldsymbol{X}} W_{O0} + \check{W}_{O1}(\boldsymbol{X}, T), \tag{3.3.17d}$$

where $\boldsymbol{\psi}$, $\boldsymbol{\Psi}$, $\boldsymbol{\gamma}$, $\boldsymbol{\Gamma}$ are vectors with components $i = 1, 2, 3$. We note that we do not determine the functions $\check{C}_{H1}$, $\check{C}_{O1}$, $\check{W}_{H1}$, $\check{W}_{O1}$, since we only require the derivatives of C_{H1}, C_{O1}, W_{H1}, and W_{O1} with respect to $\boldsymbol{Y}$ in the later analysis. We would only require these terms if we wished to compute the $\mathcal{O}(\delta)$ correction to the leading-order solutions $\{C_{H0}, C_{O0}, W_{H0}, W_{O0}\}$.

Our 'cell problem', in component form, becomes:

$$0 = \nabla^2_{\boldsymbol{Y}} \psi_i \quad \text{for } \boldsymbol{Y} \in \Omega_H, \tag{3.3.18a}$$

$$0 = \nabla^2_{\boldsymbol{Y}} \Psi_i \quad \text{for } \boldsymbol{Y} \in \Omega_O, \tag{3.3.18b}$$

$$0 = \nabla^2_{\boldsymbol{Y}} \gamma_i \quad \text{for } \boldsymbol{Y} \in \Omega_H, \tag{3.3.18c}$$

$$0 = \nabla^2_{\boldsymbol{Y}} \Gamma_i \quad \text{for } \boldsymbol{Y} \in \Omega_O, \tag{3.3.18d}$$

with boundary conditions for $\boldsymbol{Y} \in \partial\Omega_O(\boldsymbol{X}, T)$,

$$\psi_i = K_C\Psi_i, \qquad \mathbf{n}_{\boldsymbol{Y}} \cdot (K_C\nabla_{\boldsymbol{Y}}\psi_i - d_{CO}\nabla_{\boldsymbol{Y}}\Psi_i) = (K_C - d_{CO})\,\mathbf{n}_{\boldsymbol{Y}} \cdot \boldsymbol{e}_i, \tag{3.3.19a}$$

$$\gamma_i = K_W\Gamma_i, \qquad \mathbf{n}_{\boldsymbol{Y}} \cdot \left(K_W\nabla_{\boldsymbol{Y}}\gamma_i - \frac{d_{WO}}{d_{WH}}\nabla_{\boldsymbol{Y}}\Gamma_i\right) = \left(K_W - \frac{d_{WO}}{d_{WH}}\right)\mathbf{n}_{\boldsymbol{Y}} \cdot \boldsymbol{e}_i, \tag{3.3.19b}$$

with ψ_i and γ_i periodic for $\boldsymbol{Y} \in \partial\Omega$, and where $\boldsymbol{e}_i$ is the unit vector in the Y_i-direction. We provide details on the derivation of the boundary conditions in B.

$\mathcal{O}(\delta^2)$ problem:
We proceed to $\mathcal{O}(\delta^2)$ in order to determine the dependence of $\{C_{H0}, C_{O0}, W_{H0}, W_{O0}\}$ on the macroscale spatial variable, $\boldsymbol{X}$, and time, T. The $\mathcal{O}(\delta^2)$ governing equations, Equation (3.3.5), are:

$$\frac{\partial C_{H0}}{\partial T} + \nabla_{\boldsymbol{Y}} \cdot (\boldsymbol{U}_H C_{H0}) = \nabla_{\boldsymbol{Y}} \cdot (\nabla_{\boldsymbol{Y}} C_{H2} + \nabla_{\boldsymbol{X}} C_{H1}) + \nabla_{\boldsymbol{X}} \cdot (\nabla_{\boldsymbol{Y}} C_{H1} + \nabla_{\boldsymbol{X}} C_{H0}) \quad \text{for } \boldsymbol{Y} \in \Omega_H, \tag{3.3.20a}$$

$$\frac{\partial C_{O0}}{\partial T} + \nabla_{\boldsymbol{Y}} \cdot (\boldsymbol{U}_O C_{O0}) = d_{CO}\left(\nabla_{\boldsymbol{Y}} \cdot (\nabla_{\boldsymbol{Y}} C_{O2} + \nabla_{\boldsymbol{X}} C_{O1}) + \nabla_{\boldsymbol{X}} \cdot (\nabla_{\boldsymbol{Y}} C_{O1} + \nabla_{\boldsymbol{X}} C_{O0})\right) - \sigma_V S(C_{O0}, W_{O0}) \quad \text{for } \boldsymbol{Y} \in \Omega_O, \tag{3.3.20b}$$

$$\frac{\partial W_{H0}}{\partial T} + \nabla_{\boldsymbol{Y}} \cdot (\boldsymbol{U}_H W_{H0}) = d_{WH}\left(\nabla_{\boldsymbol{Y}} \cdot (\nabla_{\boldsymbol{Y}} W_{H2} + \nabla_{\boldsymbol{X}} W_{H1}) + \nabla_{\boldsymbol{X}} \cdot (\nabla_{\boldsymbol{Y}} W_{H1} + \nabla_{\boldsymbol{X}} W_{H0})\right) \quad \text{for } \boldsymbol{Y} \in \Omega_H, \tag{3.3.20c}$$

$$\frac{\partial W_{O0}}{\partial T} + \nabla_{\boldsymbol{Y}} \cdot (\boldsymbol{U}_O W_{O0}) = d_{WO}\left(\nabla_{\boldsymbol{Y}} \cdot (\nabla_{\boldsymbol{Y}} W_{O2} + \nabla_{\boldsymbol{X}} W_{O1}) + \nabla_{\boldsymbol{X}} \cdot (\nabla_{\boldsymbol{Y}} W_{O1} + \nabla_{\boldsymbol{X}} W_{O0})\right) + 2\sigma_V S(C_{O0}, W_{O0}) \quad \text{for } \boldsymbol{Y} \in \Omega_O, \tag{3.3.20d}$$

where we have taken the leading-order term of a Taylor expansion of S about (C_{O0}, W_{O0}) for the consumption/production terms. The boundary conditions on $\boldsymbol{Y} \in \partial\Omega_O(\boldsymbol{X}, T)$ are:

$$K_C C_{O2} = C_{H2}, \qquad K_W W_{O2} = W_{H2}, \tag{3.3.21a}$$

$$\begin{aligned}\mathbf{n}_{\boldsymbol{Y}} \cdot (\nabla_{\boldsymbol{Y}} C_{H2} + \nabla_{\boldsymbol{X}} C_{H1} + (\boldsymbol{U}_{\partial\Omega_O} - \boldsymbol{U}_H)\,C_{H0}) - \nabla_{\boldsymbol{X}} R \cdot (\nabla_{\boldsymbol{Y}} C_{H1} + \nabla_{\boldsymbol{X}} C_{H0})\\ = \mathbf{n}_{\boldsymbol{Y}} \cdot (d_{CO}(\nabla_{\boldsymbol{Y}} C_{O2} + \nabla_{\boldsymbol{X}} C_{O1}) + (\boldsymbol{U}_{\partial\Omega_O} - \boldsymbol{U}_O)\,C_{O0})\\ - d_{CO}\nabla_{\boldsymbol{X}} R \cdot (\nabla_{\boldsymbol{Y}} C_{O1} + \nabla_{\boldsymbol{X}} C_{O0}),\end{aligned} \tag{3.3.21b}$$

$$\begin{aligned}\mathbf{n}_{\boldsymbol{Y}} \cdot (d_{WH}(\nabla_{\boldsymbol{Y}} W_{H2} + \nabla_{\boldsymbol{X}} W_{H1}) + (\boldsymbol{U}_{\partial\Omega_O} - \boldsymbol{U}_H)\,W_{H0}) - d_{WH}\nabla_{\boldsymbol{X}} R \cdot (\nabla_{\boldsymbol{Y}} W_{H1} + \nabla_{\boldsymbol{X}} W_{H0})\\ = \mathbf{n}_{\boldsymbol{Y}} \cdot (d_{WO}(\nabla_{\boldsymbol{Y}} W_{O2} + \nabla_{\boldsymbol{X}} W_{O1}) + (\boldsymbol{U}_{\partial\Omega_O} - \boldsymbol{U}_O)\,W_{O0})\\ - d_{WO}\nabla_{\boldsymbol{X}} R \cdot (\nabla_{\boldsymbol{Y}} W_{O1} + \nabla_{\boldsymbol{X}} W_{O0}),\end{aligned} \tag{3.3.21c}$$

and C_{H2} and W_{H2} are periodic on $\partial\Omega$.

Since we are trying to determine the governing equations for C_{H0} and W_{H0} which give the dependence of the metabolite concentrations on $\boldsymbol{X}$ and T, we now derive an appropriate system, which results in a closed model for C_{H0} and W_{H0}. This is obtained from the $\mathcal{O}(\delta^2)$ problem, Equations (3.3.20) and (3.3.21), where the dependence on microscale spatial variable $\boldsymbol{Y}$ has been removed. We do this by integrating the governing equations Equations (3.3.20a) and (3.3.20c) over Ω_H and Equations (3.3.20b) and (3.3.20d) over Ω_O to remove the dependence of the system on $\boldsymbol{Y}$, and then sum the resulting integrals for glucose and lactate, respectively. We present the derivation for the glucose concentration here, noting that the lactate derivation is analogous. The initial integration yields:

$$
\begin{aligned}
\int_{\Omega_H} \frac{\partial C_{H0}}{\partial T} + \underbrace{\nabla_{\boldsymbol{Y}} \cdot (\boldsymbol{U}_H C_{H0})}_{\textcircled{\dagger_1}} \, \mathrm{d}\boldsymbol{Y} + \int_{\Omega_O} \frac{\partial C_{O0}}{\partial T} + \underbrace{\nabla_{\boldsymbol{Y}} \cdot (\boldsymbol{U}_O C_{O0})}_{\textcircled{\dagger_1}} \, \mathrm{d}\boldsymbol{Y} \\
= \underbrace{\int_{\Omega_H} \nabla_{\boldsymbol{Y}} \cdot (\nabla_{\boldsymbol{Y}} C_{H2} + \nabla_{\boldsymbol{X}} C_{H1}) \, \mathrm{d}\boldsymbol{Y}}_{\textcircled{\dagger_1}} + \int_{\Omega_H} \nabla_{\boldsymbol{X}} \cdot (\nabla_{\boldsymbol{Y}} C_{H1} + \nabla_{\boldsymbol{X}} C_{H0}) \, \mathrm{d}\boldsymbol{Y} \\
+ \underbrace{\int_{\Omega_O} d_{CO} \nabla_{\boldsymbol{Y}} \cdot (\nabla_{\boldsymbol{Y}} C_{O2} + \nabla_{\boldsymbol{X}} C_{O1}) \, \mathrm{d}\boldsymbol{Y}}_{\textcircled{\dagger_1}} \\
+ \int_{\Omega_O} d_{CO} \nabla_{\boldsymbol{X}} \cdot (\nabla_{\boldsymbol{Y}} C_{O1} + \nabla_{\boldsymbol{X}} C_{O0}) - \sigma_V S(C_{O0}, W_{O0}) \, \mathrm{d}\boldsymbol{Y}. \quad (3.3.22)
\end{aligned}
$$

We apply the divergence theorem on the $\textcircled{\dagger_1}$ terms in Equation (3.3.22) to get surface integrals over the organoid-hydrogel boundary $\partial\Omega_O(\boldsymbol{X}, T)$,

$$
\begin{aligned}
\underbrace{\int_{\Omega_H} \frac{\partial C_{H0}}{\partial T} \, \mathrm{d}\boldsymbol{Y}}_{\textcircled{\dagger_2}} + \underbrace{\int_{\Omega_O} \frac{\partial C_{O0}}{\partial T} \, \mathrm{d}\boldsymbol{Y}}_{\textcircled{\dagger_2}} + \int_{\partial\Omega_O} (\boldsymbol{U}_O \cdot \mathbf{n}_{\boldsymbol{Y}}) C_{O0} + (\boldsymbol{U}_H \cdot (-\mathbf{n}_{\boldsymbol{Y}})) C_{H0} \, \mathrm{d}A \\
= \int_{\Omega_H} \nabla_{\boldsymbol{X}} \cdot (\nabla_{\boldsymbol{Y}} C_{H1} + \nabla_{\boldsymbol{X}} C_{H0}) \, \mathrm{d}\boldsymbol{Y} \\
+ \int_{\Omega_O} d_{CO} \nabla_{\boldsymbol{X}} \cdot (\nabla_{\boldsymbol{Y}} C_{O1} + \nabla_{\boldsymbol{X}} C_{O0}) - \sigma_V S(C_{O0}, W_{O0}) \, \mathrm{d}\boldsymbol{Y} \\
+ \int_{\partial\Omega_O} \mathbf{n}_{\boldsymbol{Y}} \cdot \left(- \left(\nabla_{\boldsymbol{Y}} C_{H2} + \nabla_{\boldsymbol{X}} C_{H1} \right) + d_{CO} \left(\nabla_{\boldsymbol{Y}} C_{O2} + \nabla_{\boldsymbol{X}} C_{O1} \right) \right) \, \mathrm{d}A. \quad (3.3.23)
\end{aligned}
$$

Next, we use Reynolds transport theorem on the volume integrals $\textcircled{\dagger_2}$ on the left-hand side of Equation (3.3.23), noting that $\Omega_H(\boldsymbol{X}, T)$ and $\Omega_O(\boldsymbol{X}, T)$ are time-dependent with outward-pointing normals $-\mathbf{n}_{\boldsymbol{Y}}$ and $\mathbf{n}_{\boldsymbol{Y}}$, respectively, so we gain a contribution of a surface integral,

$$\begin{aligned}
&\underbrace{\frac{\partial}{\partial T}\left(\int_{\Omega_H} C_{H0}\,\mathrm{d}\boldsymbol{Y} + \int_{\Omega_O} C_{O0}\,\mathrm{d}\boldsymbol{Y}\right) - \int_{\partial\Omega_O} (\boldsymbol{U}_{\partial\Omega_O}\cdot\mathbf{n}_{\boldsymbol{Y}})C_{O0} + (\boldsymbol{U}_{\partial\Omega_O}\cdot(-\mathbf{n}_{\boldsymbol{Y}}))C_{H0}\,\mathrm{d}A}_{\textcircled{\dagger_2}} \\
&+ \int_{\partial\Omega_O}(\boldsymbol{U}_O\cdot\mathbf{n}_{\boldsymbol{Y}})C_{O0} + (\boldsymbol{U}_H\cdot(-\mathbf{n}_{\boldsymbol{Y}}))C_{H0}\,\mathrm{d}A = \underbrace{\int_{\Omega_H}\nabla_{\boldsymbol{X}}\cdot\left(\nabla_{\boldsymbol{Y}}C_{H1}+\nabla_{\boldsymbol{X}}C_{H0}\right)\,\mathrm{d}\boldsymbol{Y}}_{\textcircled{\dagger_3}} \\
&\qquad + \underbrace{\int_{\Omega_O} d_{CO}\nabla_{\boldsymbol{X}}\cdot\left(\nabla_{\boldsymbol{Y}}C_{O1}+\nabla_{\boldsymbol{X}}C_{O1}\right)}_{\textcircled{\dagger_3}} - \sigma_V S(C_{O0}, W_{O0})\,\mathrm{d}\boldsymbol{Y} \\
&\quad + \int_{\partial\Omega_O}\mathbf{n}_{\boldsymbol{Y}}\cdot\left(-\left(\nabla_{\boldsymbol{Y}}C_{H2}+\nabla_{\boldsymbol{X}}C_{H1}\right) + d_{CO}\left(\nabla_{\boldsymbol{Y}}C_{O2}+\nabla_{\boldsymbol{X}}C_{O1}\right)\right)\,\mathrm{d}A.
\end{aligned} \tag{3.3.24}$$

Now, we consider the volume integrals $\textcircled{\dagger_3}$. We want to obtain terms of the form $\nabla_{\boldsymbol{X}}\cdot\int_{\Omega_i}$, and in a similar way to the $\textcircled{\dagger_2}$ terms, we can apply Reynolds transport theorem. Typically, we think of Reynolds transport theorem in terms of time T for arbitrary vector field $\boldsymbol{f}(T)$

$$\frac{\partial}{\partial T}\int_{V(T)}\boldsymbol{f}\,\mathrm{d}V = \int_{V(T)}\frac{\partial\boldsymbol{f}}{\partial T}\,\mathrm{d}V + \int_{\partial V(T)}\left(\frac{\partial}{\partial T}(\boldsymbol{Y}^{\mathrm{bdy}})\cdot\mathbf{n}_{\boldsymbol{Y}}\right)\boldsymbol{f}\,\mathrm{d}A, \tag{3.3.25}$$

where $\boldsymbol{Y}^{\mathrm{bdy}}(\boldsymbol{X},T)$ denotes the position of points on the surface $\partial V(T)$ with outward normal $\mathbf{n}_{\boldsymbol{Y}}$ and we understand $\partial\boldsymbol{Y}^{\mathrm{bdy}}/\partial T$ as the local velocity of the boundary. However, as discussed in Appendix A of Auton et al. [2], T is an arbitrary parameter in this formulation and therefore we can write Equation (3.3.25) in terms of arbitrary general independent variable X_i for arbitrary vector field $\boldsymbol{f}(\boldsymbol{X})$ as

$$\frac{\partial}{\partial X_i}\int_{V(\boldsymbol{X})}\boldsymbol{f}\,\mathrm{d}V = \int_{V(\boldsymbol{X})}\frac{\partial\boldsymbol{f}}{\partial X_i}\,\mathrm{d}V + \int_{\partial V(\boldsymbol{X})}\left(\frac{\partial}{\partial X_i}(\boldsymbol{Y}^{\mathrm{bdy}})\cdot\mathbf{n}_{\boldsymbol{Y}}\right)\boldsymbol{f}\,\mathrm{d}A, \tag{3.3.26}$$

where $\boldsymbol{Y}^{\mathrm{bdy}}(\boldsymbol{X})$ denotes the position of points on the surface $\partial V(\boldsymbol{X})$. We can impose Equation (3.3.26) component-wise for

$$\boldsymbol{X} = \sum_{i=1}^{3}\boldsymbol{e}_i X_i, \tag{3.3.27}$$

where $V(\boldsymbol{X}) = \Omega_{H,O}(\boldsymbol{X})$ to the volume integrals $\textcircled{\dagger_3}$ over Ω_H and Ω_O on the right-hand side of Equation (3.3.24).

In our case, we take the volume integrals over the hydrogel and organoid domains, Ω_H and Ω_O, respectively, and denote the position of the points on the organoid-hydrogel boundary by $\boldsymbol{Y}^{\partial\Omega_O}$, which is dependent on $\boldsymbol{X}$ and T. We note that this term is

$$\frac{\partial}{\partial X_i}\left(\boldsymbol{Y}^{\partial\Omega_O}(\boldsymbol{X},T)\right)\cdot\mathbf{n}_{\boldsymbol{Y}}=\frac{\partial R}{\partial X_i}, \tag{3.3.28}$$

where $\mathbf{n}_{\boldsymbol{Y}}$ is the unit normal pointing into the hydrogel from the organoid region.

Therefore, the following relationships can be derived:

$$\begin{aligned}\int_{\Omega_H}\nabla_{\boldsymbol{X}}\cdot\left(\nabla_{\boldsymbol{Y}}C_{H1}+\nabla_{\boldsymbol{X}}C_{H0}\right)\,\mathrm{d}\boldsymbol{Y}=&\nabla_{\boldsymbol{X}}\cdot\left(\int_{\Omega_H(\boldsymbol{X},T)}\nabla_{\boldsymbol{Y}}C_{H1}+\nabla_{\boldsymbol{X}}C_{H0}\,\mathrm{d}\boldsymbol{Y}\right)\\&+\int_{\partial\Omega_O(\boldsymbol{X},T)}\nabla_{\boldsymbol{X}}R\cdot\left(\nabla_{\boldsymbol{Y}}C_{H1}+\nabla_{\boldsymbol{X}}C_{H0}\right)\,\mathrm{d}A,\end{aligned} \tag{3.3.29a}$$

$$\begin{aligned}\int_{\Omega_O}d_{CO}\nabla_{\boldsymbol{X}}\cdot\left(\nabla_{\boldsymbol{Y}}C_{O1}+\nabla_{\boldsymbol{X}}C_{O0}\right)\,\mathrm{d}\boldsymbol{Y}=&d_{CO}\nabla_{\boldsymbol{X}}\cdot\left(\int_{\Omega_O(\boldsymbol{X},T)}\nabla_{\boldsymbol{Y}}C_{O1}+\nabla_{\boldsymbol{X}}C_{O0}\,\mathrm{d}\boldsymbol{Y}\right)\\&-\int_{\partial\Omega_O(\boldsymbol{X},T)}d_{CO}\nabla_{\boldsymbol{X}}R\cdot\left(\nabla_{\boldsymbol{Y}}C_{O1}+\nabla_{\boldsymbol{X}}C_{O0}\right)\,\mathrm{d}A.\end{aligned} \tag{3.3.29b}$$

Using Equation (3.3.29), the governing equation Equation (3.3.24) becomes:

$$\begin{aligned}&\frac{\partial}{\partial T}\left(\int_{\Omega_H}C_{H0}\,\mathrm{d}\boldsymbol{Y}+\int_{\Omega_O}C_{O0}\,\mathrm{d}\boldsymbol{Y}\right)\\&\qquad+\underbrace{\int_{\partial\Omega_O}((\boldsymbol{U}_{\partial\Omega_O}-\boldsymbol{U}_H)\cdot\mathbf{n}_{\boldsymbol{Y}})C_{H0}-((\boldsymbol{U}_{\partial\Omega_O}-\boldsymbol{U}_O)\cdot\mathbf{n}_{\boldsymbol{Y}})C_{O0}\,\mathrm{d}A}_{\textcircled{\dagger_4}}\\&=\nabla_{\boldsymbol{X}}\cdot\left(\int_{\Omega_H}\nabla_{\boldsymbol{Y}}C_{H1}+\nabla_{\boldsymbol{X}}C_{H0}\,\mathrm{d}\boldsymbol{Y}\right)+d_{CO}\nabla_{\boldsymbol{X}}\cdot\left(\int_{\Omega_O}\nabla_{\boldsymbol{Y}}C_{O1}+\nabla_{\boldsymbol{X}}C_{O0}\,\mathrm{d}\boldsymbol{Y}\right)\\&+\underbrace{\int_{\partial\Omega_O}\nabla_{\boldsymbol{X}}R\cdot\left(\nabla_{\boldsymbol{Y}}C_{H1}+\nabla_{\boldsymbol{X}}C_{H0}\right)\,\mathrm{d}A}_{\textcircled{\dagger_4}}-\underbrace{\int_{\partial\Omega_O}d_{CO}\nabla_{\boldsymbol{X}}R\cdot\left(\nabla_{\boldsymbol{Y}}C_{O1}+\nabla_{\boldsymbol{X}}C_{O0}\right)\,\mathrm{d}A}_{\textcircled{\dagger_4}}\\&\qquad-\int_{\Omega_O}\sigma_V S(C_{O0},W_{O0})\,\mathrm{d}\boldsymbol{Y}\\&\qquad+\underbrace{\int_{\partial\Omega_O}\mathbf{n}_{\boldsymbol{Y}}\cdot\left(-\left(\nabla_{\boldsymbol{Y}}C_{H2}+\nabla_{\boldsymbol{X}}C_{H1}\right)+d_{CO}\left(\nabla_{\boldsymbol{Y}}C_{O2}+\nabla_{\boldsymbol{X}}C_{O1}\right)\right)\,\mathrm{d}A}_{\textcircled{\dagger_4}}.\end{aligned} \tag{3.3.30}$$

Applying the continuity of flux condition Equation (3.3.21b) on $\partial\Omega_O$ means that the surface integrals ($\dagger_4$) cancel out, reducing Equation (3.3.30) to:

$$\begin{aligned}
&\frac{\partial}{\partial T}\left(\int_{\Omega_H} C_{H0}\,\mathrm{d}\boldsymbol{Y} + \int_{\Omega_O} C_{O0}\,\mathrm{d}\boldsymbol{Y}\right)\\
&=\nabla_{\boldsymbol{X}}\cdot\left(\left(\int_{\Omega_H} \nabla_{\boldsymbol{Y}} C_{H1} + \nabla_{\boldsymbol{X}} C_{H0}\,\mathrm{d}\boldsymbol{Y}\right) + d_{CO}\left(\int_{\Omega_O} \nabla_{\boldsymbol{Y}} C_{O1} + \nabla_{\boldsymbol{X}} C_{O0}\,\mathrm{d}\boldsymbol{Y}\right)\right)\\
&\quad-\int_{\Omega_O} \sigma_V S(C_{O0}, W_{O0})\,\mathrm{d}\boldsymbol{Y}. \qquad (3.3.31)
\end{aligned}$$

Noting that C_{H0} and C_{O0} are independent of $\boldsymbol{Y}$, Equation (3.3.31) becomes:

$$\begin{aligned}
&\frac{\partial}{\partial T}\left(\|\Omega_H\|\, C_{H0} + \|\Omega_O\|\, C_{O0}\right)\\
&=\nabla_{\boldsymbol{X}}\cdot\left(\left(\int_{\Omega_H} \nabla_{\boldsymbol{Y}} C_{H1} + \nabla_{\boldsymbol{X}} C_{H0}\,\mathrm{d}\boldsymbol{Y}\right) + d_{CO}\left(\int_{\Omega_O} \nabla_{\boldsymbol{Y}} C_{O1} + \nabla_{\boldsymbol{X}} C_{O0}\,\mathrm{d}\boldsymbol{Y}\right)\right)\\
&\quad-\sigma_V\,\|\Omega_O\|\, S(C_{O0}, W_{O0}), \qquad (3.3.32)
\end{aligned}$$

where we define the volume of domain Ω_i as

$$\|\Omega_i\| = \int_{\Omega_i} \mathrm{d}V, \qquad (3.3.33)$$

and, since we have assumed spherical organoids,

$$\|\Omega_O\| = \frac{4}{3}\pi R^3 \quad \text{and} \quad \|\Omega_H\| = 1 - \frac{4}{3}\pi R^3. \qquad (3.3.34)$$

We now write the $\nabla_{\boldsymbol{Y}} C_{H1}$ and $\nabla_{\boldsymbol{Y}} C_{O1}$ terms in terms of C_{H0} and C_{O0} using the cell problem, Equations (3.3.18) and (3.3.19). This is so that we only need to solve for the leading-order behaviour of C_H and C_O, *i.e.* C_{H0} and C_{O0}. Recalling the ansatz for C_{H1}, Equation (3.3.17a), we find

$$\begin{aligned}
\nabla_{\boldsymbol{Y}} C_{H1} &= \begin{pmatrix}\partial_{Y_1}\\ \partial_{Y_2}\\ \partial_{Y_3}\end{pmatrix}\left(-\psi_1\partial_{X1}C_{H0} - \psi_2\partial_{X2}C_{H0} - \psi_3\partial_{X3}C_{H0}\right), &(3.3.35)\\
&= -\begin{pmatrix}\partial_{Y_1}\psi_1 & \partial_{Y_1}\psi_2 & \partial_{Y_1}\psi_3\\ \partial_{Y_2}\psi_1 & \partial_{Y_2}\psi_2 & \partial_{Y_2}\psi_3\\ \partial_{Y_3}\psi_1 & \partial_{Y_3}\psi_2 & \partial_{Y_3}\psi_3\end{pmatrix}\nabla_{\boldsymbol{X}} C_{H0}, &(3.3.36)\\
&= -\frac{\partial \psi_j}{\partial Y_i}\nabla_{\boldsymbol{X}} C_{H0} = -\left(\boldsymbol{J}_{\boldsymbol{\psi}}^{\mathsf{T}}\right)\nabla_{\boldsymbol{X}} C_{H0}. &(3.3.37)
\end{aligned}$$

Similarly, using the ansatz for C_{O1}, Equation (3.3.17b), we deduce that

$$\nabla_{\boldsymbol{Y}} C_{O1} = -\left(\boldsymbol{J}_{\boldsymbol{\Psi}}^{\mathsf{T}}\right)\nabla_{\boldsymbol{X}} C_{O0}, \qquad (3.3.38)$$

where

$$\left(\boldsymbol{J}_{\boldsymbol{\psi}}^{\mathsf{T}}\right)_{ij} = \frac{\partial \psi_j}{\partial Y_i}, \quad \left(\boldsymbol{J}_{\boldsymbol{\Psi}}^{\mathsf{T}}\right)_{ij} = \frac{\partial \Psi_j}{\partial Y_i}, \tag{3.3.39}$$

are the transposes of the Jacobian matrices of $\boldsymbol{\psi}$ and $\boldsymbol{\Psi}$, respectively, which are solutions to the cell problem, Equations (3.3.18a), (3.3.18b) and (3.3.19a).

We can now write the governing equation, Equation (3.3.32), in terms of $\bar{C} = C_{O0} = C_{H0}/K_C$ and $\bar{W} = W_{O0} = W_{H0}/K_W$ as

$$\frac{\partial}{\partial T}\left(\left(\left\|\Omega_H\right\| K_C + \left\|\Omega_O\right\|\right)\bar{C}\right) = \nabla_{\boldsymbol{X}} \cdot \left(\bar{\boldsymbol{d}}_C(\boldsymbol{X},T)\nabla_{\boldsymbol{X}}\bar{C}\right) - \sigma_V \left\|\Omega_O\right\| S(\bar{C},\bar{W}), \tag{3.3.40}$$

where the *effective diffusivity* tensor of glucose, $\bar{\boldsymbol{d}}_C$, is defined to be

$$\bar{\boldsymbol{d}}_C(\boldsymbol{X},T) = K_C \int_{\Omega_H} \left(\boldsymbol{I} - \boldsymbol{J}_{\boldsymbol{\psi}}^{\mathsf{T}}\right)\, \mathrm{d}\boldsymbol{Y} + \int_{\Omega_O} d_{CO} \left(\boldsymbol{I} - \boldsymbol{J}_{\boldsymbol{\Psi}}^{\mathsf{T}}\right)\, \mathrm{d}\boldsymbol{Y}, \tag{3.3.41}$$

and is obtained by solving the cell problem, Equations (3.3.18a) and (3.3.18b) subject to the boundary conditions in Equation (3.3.19a). Similarly, for lactate, the governing equation is

$$\frac{\partial}{\partial T}\left(\left(\left\|\Omega_H\right\| K_W + \left\|\Omega_O\right\|\right)\bar{W}\right) = \nabla_{\boldsymbol{X}} \cdot \left(\bar{\boldsymbol{d}}_W(\boldsymbol{X},T)\nabla_{\boldsymbol{X}}\bar{W}\right) + 2\sigma_V \left\|\Omega_O\right\| S(\bar{C},\bar{W}), \tag{3.3.42}$$

where the *effective diffusivity* tensor of lactate, $\bar{\boldsymbol{d}}_W$, is defined to be

$$\bar{\boldsymbol{d}}_W(\boldsymbol{X},T) = K_W \int_{\Omega_H} d_{WH} \left(\boldsymbol{I} - \boldsymbol{J}_{\boldsymbol{\gamma}}^{\mathsf{T}}\right)\, \mathrm{d}\boldsymbol{Y} + \int_{\Omega_O} d_{WO} \left(\boldsymbol{I} - \boldsymbol{J}_{\boldsymbol{\Gamma}}^{\mathsf{T}}\right)\, \mathrm{d}\boldsymbol{Y}, \tag{3.3.43}$$

obtained by solving the cell problem, Equations (3.3.18c) and (3.3.18d) subject to the boundary conditions in Equation (3.3.19b). In the case of spherical organoids, the following terms in $\bar{\boldsymbol{d}}_C$ and $\bar{\boldsymbol{d}}_W$ simplify to become

$$\int_{\Omega_H} \left(\boldsymbol{J}_{\boldsymbol{\psi}}^{\mathsf{T}}\right)\, \mathrm{d}\boldsymbol{Y} = \left(\int_{\Omega_H} \frac{\partial \psi_i}{\partial Y_i}\, \mathrm{d}\boldsymbol{Y}\right)\boldsymbol{I}, \quad \int_{\Omega_O} \left(\boldsymbol{J}_{\boldsymbol{\Psi}}^{\mathsf{T}}\right)\, \mathrm{d}\boldsymbol{Y} = \left(\int_{\Omega_O} \frac{\partial \Psi_i}{\partial Y_i}\, \mathrm{d}\boldsymbol{Y}\right)\boldsymbol{I}, \tag{3.3.44a}$$

$$\int_{\Omega_H} \left(\boldsymbol{J}_{\boldsymbol{\gamma}}^{\mathsf{T}}\right)\, \mathrm{d}\boldsymbol{Y} = \left(\int_{\Omega_H} \frac{\partial \gamma_i}{\partial Y_i}\, \mathrm{d}\boldsymbol{Y}\right)\boldsymbol{I}, \quad \int_{\Omega_O} \left(\boldsymbol{J}_{\boldsymbol{\Gamma}}^{\mathsf{T}}\right)\, \mathrm{d}\boldsymbol{Y} = \left(\int_{\Omega_O} \frac{\partial \Gamma_i}{\partial Y_i}\, \mathrm{d}\boldsymbol{Y}\right)\boldsymbol{I}, \tag{3.3.44b}$$

for $i \in \{1, 2, 3\}$, due to the (rotational) symmetry of the cell problem.

Therefore, the governing equations for metabolite transport within a hydrogel embedded with spherical dense organoids exhibiting volumetric growth are:

$$\frac{\partial}{\partial T}\left(\left(\left\|\Omega_H\right\| K_C + \left\|\Omega_O\right\|\right)\bar{C}\right) = \nabla_{\boldsymbol{X}} \cdot \left(\bar{d}_C(\boldsymbol{X},T)\nabla_{\boldsymbol{X}}\bar{C}\right) - \left\|\Omega_O\right\| \sigma_V S(\bar{C},\bar{W}), \tag{3.3.45a}$$

$$\frac{\partial}{\partial T}\left(\left(\left\|\Omega_H\right\| K_W + \left\|\Omega_O\right\|\right)\bar{W}\right) = \nabla_{\boldsymbol{X}} \cdot \left(\bar{d}_W(\boldsymbol{X},T)\nabla_{\boldsymbol{X}}\bar{W}\right) + 2\left\|\Omega_O\right\| \sigma_V S(\bar{C},\bar{W}), \tag{3.3.45b}$$

where the sizes of the hydrogel and organoid domains, $\|\Omega_H\|$ and $\|\Omega_O\|$, respectively, are given by

$$\|\Omega_O\| = \frac{4}{3}\pi R^3 \quad \text{and} \quad \|\Omega_H\| = 1 - \frac{4}{3}\pi R^3, \tag{3.3.46}$$

noting that $\|\Omega_H\|$ and $\|\Omega_O\|$ are dependent on $\boldsymbol{X}$ and T via their dependence on the organoid radius, $R = R(\boldsymbol{X}, T)$. The diffusivity tensors $\bar{\boldsymbol{d}}_C = \bar{d}_C \boldsymbol{I}$ and $\bar{\boldsymbol{d}}_W = \bar{d}_W \boldsymbol{I}$ are isotropic and, therefore, the *effective diffusivities* of glucose and lactate in the hydrogel, $\bar{d}_C$ and $\bar{d}_W$, respectively, are:

$$\bar{d}_C(\boldsymbol{X}, T) = K_C \left[\|\Omega_H\| - \int_{\Omega_H} \frac{\partial \psi_1}{\partial Y_1} \, \mathrm{d}\boldsymbol{Y} \right] + d_{CO} \left[\|\Omega_O\| - \int_{\Omega_O} \frac{\partial \Psi_1}{\partial Y_1} \, \mathrm{d}\boldsymbol{Y} \right], \tag{3.3.47a}$$

$$\bar{d}_W(\boldsymbol{X}, T) = K_W d_{WH} \left[\|\Omega_H\| - \int_{\Omega_H} \frac{\partial \gamma_1}{\partial Y_1} \, \mathrm{d}\boldsymbol{Y} \right] + d_{WO} \left[\|\Omega_O\| - \int_{\Omega_O} \frac{\partial \Gamma_1}{\partial Y_1} \, \mathrm{d}\boldsymbol{Y} \right]. \tag{3.3.47b}$$

The *effective consumption/production* terms are of the form $\|\Omega_O\| \, \sigma_V S(\bar{C}, \bar{W})$. Therefore, the *effective* glucose consumption and *effective* lactate production terms are dependent on the microscale problem (volume integrals of the organoid region), and scale with the volume of the organoid region. This is as we might expect given the uptake within the organoid region is volumetric. We note that these governing equations are valid for general glucose consumption/lactate production terms, $S(C_O, W_O)$.

In the case of time-independent organoid radii, $R = R(\boldsymbol{X})$ (which is specified), we have a closed system for metabolite transport within the media and hydrogel layers. However, to close the system for temporally-dependent organoid radii, we must couple these equations for the effective macroscale metabolite transport within the hydrogel to a model for the evolution of the organoid radius. We discussed this in Section 3.2.1.2.

3.3.2 Model for shell organoids with surface growth

In the case of shell organoids, the cells are all located at the organoid-hydrogel boundary and we assume uptake occurs at this interface rather than throughout the organoid region. We capture metabolite consumption/production via boundary conditions rather than source/sinks in PDEs. The governing equations, Equations (3.2.1b) and (3.2.1d) in the case of dense organoids, are instead:

$$\frac{\partial c_O}{\partial t} + \nabla \cdot (\boldsymbol{u}_O c_O) = D_{CO} \nabla^2 c_O \qquad \text{for } \boldsymbol{x} \in \omega_O, \tag{3.3.48a}$$

$$\frac{\partial w_O}{\partial t} + \nabla \cdot (\boldsymbol{u}_O w_O) = D_{WO} \nabla^2 w_O \qquad \text{for } \boldsymbol{x} \in \omega_O, \tag{3.3.48b}$$

and the continuity of flux boundary condition at the organoid-hydrogel interface, $\boldsymbol{x} \in \partial\omega_O$, Equations (3.2.2b) and (3.2.2c), would include a sink or source term, respectively:

$$\begin{aligned}
&\mathbf{n} \cdot (c_H(\boldsymbol{u}_H - \boldsymbol{u}_{\partial\omega_O}) - D_{CH}\nabla c_H) \\
&\qquad = \mathbf{n} \cdot (c_O(\boldsymbol{u}_O - \boldsymbol{u}_{\partial\omega_O}) - D_{CO}\nabla c_O) - 2r_c s(c_O, w_O), \qquad (3.3.49a) \\
&\mathbf{n} \cdot (w_H(\boldsymbol{u}_H - \boldsymbol{u}_{\partial\omega_O}) - D_{WH}\nabla w_H) \\
&\qquad = \mathbf{n} \cdot (w_O(\boldsymbol{u}_O - \boldsymbol{u}_{\partial\omega_O}) - D_{WO}\nabla w_O) + 4r_c s(c_O, w_O), \qquad (3.3.49b)
\end{aligned}$$

which can be thought of as 'the jump in glucose/lactate flux from the hydrogel region to the organoid region is equal to the glucose consumed/lactate produced, respectively'. The sink term s is the same as for the dense organoid case. The volume of uptake region is related to the organoid surface area via the relationship *volume = surface area × thickness of organoid shell.* Since the shell organoids are assumed to be one cell in thickness, the rate of glucose consumption per unit surface area per second (units $\mathrm{mol\,m^{-2}\,s^{-1}}$) is $2r_c s$, where r_c is the radius of a single cell.

We note that the model for shell organoids is not valid for small organoids, that is for organoids of radius less than the diameter of a single cell, $\|r - 2r_c\| \ll 1$. Biologically, we would expect organoids that start off as single cells to initially be dense and then transition to shell organoids at some later time, once they consist of a sufficient number of cells.

For the case of compressing hydrogel, Equation (3.3.49) reduces to

$$\mathbf{n} \cdot (D_{CH}\nabla c_H) - 2r_c s(c_O, w_O) = \mathbf{n} \cdot (D_{CO}\nabla c_O), \qquad (3.3.50a)$$

$$\mathbf{n} \cdot (D_{WH}\nabla w_H) + 4r_c s(c_O, w_O) = \mathbf{n} \cdot (D_{WO}\nabla w_O); \qquad (3.3.50b)$$

whereas, for the case of degrading hydrogel, Equation (3.3.49) reduces to

$$\mathbf{n} \cdot (\boldsymbol{u}_{\partial\omega_O} c_H + D_{CH}\nabla c_H) - 2r_c s(c_O, w_O) = \mathbf{n} \cdot (D_{CO}\nabla c_O), \qquad (3.3.51a)$$

$$\mathbf{n} \cdot (\boldsymbol{u}_{\partial\omega_O} w_H + D_{WH}\nabla w_H) + 4r_c s(c_O, w_O) = \mathbf{n} \cdot (D_{WO}\nabla w_O). \qquad (3.3.51b)$$

Similarly to the model for dense organoids undergoing volumetric growth, we will show that the homogenised governing equations for shell organoids undergoing surface growth are the same regardless of whether the hydrogel compresses or degrades.

Non-dimensionalising the governing equations, Equation (3.3.48), using Equation (3.2.24), we obtain:

$$\frac{\partial C_H}{\partial T} + \delta\nabla\cdot(\boldsymbol{U}_H C_H) = \nabla^2 C_H, \qquad \text{for } \boldsymbol{X}\in\Omega_H, \tag{3.3.52a}$$

$$\frac{\partial C_O}{\partial T} + \delta\nabla\cdot(\boldsymbol{U}_O C_O) = d_{CO}\nabla^2 C_O, \qquad \text{for } \boldsymbol{X}\in\Omega_O, \tag{3.3.52b}$$

$$\frac{\partial W_H}{\partial T} + \delta\nabla\cdot(\boldsymbol{U}_H W_H) = d_{WH}\nabla^2 W_H \qquad \text{for } \boldsymbol{X}\in\Omega_H, \tag{3.3.52c}$$

$$\frac{\partial W_O}{\partial T} + \delta\nabla\cdot(\boldsymbol{U}_O W_O) = d_{WO}\nabla^2 W_O \qquad \text{for } \boldsymbol{X}\in\Omega_O, \tag{3.3.52d}$$

where the dimensionless parameter groupings $\{d_{CO}, d_{WH}, d_{WO}\}$ are defined as in Equation (3.2.24).

The boundary conditions at the hydrogel-organoid interface, $\boldsymbol{X}\in\partial\Omega_O$, are:

$$K_C C_O = C_H, \quad K_W W_O = W_H, \tag{3.3.53a}$$

$$\begin{aligned}\mathbf{n}\cdot(\nabla C_H + \delta\left(\boldsymbol{U}_{\partial\Omega_O} - \boldsymbol{U}_H\right)C_H) - \delta\sigma_S S(C_O, W_O) \\ = \mathbf{n}\cdot(d_{CO}\nabla C_O + \delta\left(\boldsymbol{U}_{\partial\Omega_O} - \boldsymbol{U}_O\right)C_O),\end{aligned} \tag{3.3.53b}$$

$$\begin{aligned}\mathbf{n}\cdot(d_{WH}\nabla W_H + \delta\left(\boldsymbol{U}_{\partial\Omega_O} - \boldsymbol{U}_H\right)W_H) + 2\delta\sigma_S S(C_O, W_O) \\ = \mathbf{n}\cdot(d_{WO}\nabla W_O + \delta\left(\boldsymbol{U}_{\partial\Omega_O} - \boldsymbol{U}_O\right)W_O);\end{aligned} \tag{3.3.53c}$$

with

$$\mathbf{n}\cdot\boldsymbol{U}_{\partial\Omega_O} = \frac{\partial R}{\partial T}, \tag{3.3.53d}$$

where the dimensionless parameter grouping σ_S is defined as

$$\sigma_S = \frac{2R_c s_V \phi L^2}{c_{-\infty} D_{CH}}. \tag{3.3.54}$$

The boundary conditions at the hydrogel-organoid interface, $\boldsymbol{X}\in\partial\Omega_O$, for **compression** of hydrogel reduce to:

$$\mathbf{n}\cdot(\nabla C_H) - \delta\sigma_S S(C_O, W_O) = \mathbf{n}\cdot(d_{CO}\nabla C_O), \tag{3.3.55a}$$

$$\mathbf{n}\cdot(d_{WH}\nabla W_H) + 2\delta\sigma_S S(C_O, W_O) = \mathbf{n}\cdot(d_{WO}\nabla W_O), \tag{3.3.55b}$$

with continuity of velocity,

$$\boldsymbol{U}_O = \boldsymbol{U}_H = \boldsymbol{U}_{\partial\Omega_O} \quad \text{with} \quad \mathbf{n}\cdot\boldsymbol{U}_{\partial\Omega_O} = \frac{\partial R}{\partial T}; \tag{3.3.55c}$$

whereas the boundary conditions at the hydrogel-organoid interface, $\boldsymbol{X}\in\partial\Omega_O$, for **degradation** of hydrogel reduce to:

$$\mathbf{n}\cdot(\nabla C_H + \delta\boldsymbol{U}_{\partial\Omega_O} C_H) - \delta\sigma_S S(C_O, W_O) = \mathbf{n}\cdot(d_{CO}\nabla C_O), \tag{3.3.56a}$$

$$\mathbf{n}\cdot(d_{WH}\nabla W_H) + 2\delta\sigma_S S(C_O, W_O) = \mathbf{n}\cdot(d_{WO}\nabla W_O), \tag{3.3.56b}$$

with continuity of velocity,

$$\boldsymbol{U}_O = \boldsymbol{U}_{\partial\Omega_O} \quad \text{with} \quad \mathbf{n}\cdot\boldsymbol{U}_{\partial\Omega_O} = \frac{\partial R}{\partial T}. \tag{3.3.56c}$$

In a similar manner to Section 3.3.1, we can perform a homogenisation on the model for shell organoids undergoing surface growth. We consider the case of compressing hydrogel, and note that the homogenised governing equations for metabolite transport are the same as for the case of degradation of hydrogel. Introducing microscale variable $\boldsymbol{Y}$, Equation (3.3.1), and writing Equations (3.3.52) and (3.3.53) using the definitions of spatial derivatives and normal to the organoid-hydrogel, Equations (3.3.2) and (3.3.3), we obtain:

$$\begin{aligned}
&\delta^2\frac{\partial C_H}{\partial T} + \delta^2\left(\nabla_{\boldsymbol{Y}} + \delta\nabla_{\boldsymbol{X}}\right)\cdot\left(\boldsymbol{U}_H C_H\right)\\
&\qquad = \left(\nabla_{\boldsymbol{Y}} + \delta\nabla_{\boldsymbol{X}}\right)\cdot\left(\nabla_{\boldsymbol{Y}} + \delta\nabla_{\boldsymbol{X}}\right)C_H \qquad \text{for } \boldsymbol{Y}\in\Omega_H(\boldsymbol{X},T), && (3.3.57a)\\
&\delta^2\frac{\partial C_O}{\partial T} + \delta^2\left(\nabla_{\boldsymbol{Y}} + \delta\nabla_{\boldsymbol{X}}\right)\cdot\left(\boldsymbol{U}_O C_O\right)\\
&\qquad = d_{CO}\left(\nabla_{\boldsymbol{Y}} + \delta\nabla_{\boldsymbol{X}}\right)\cdot\left(\nabla_{\boldsymbol{Y}} + \delta\nabla_{\boldsymbol{X}}\right)C_O \qquad \text{for } \boldsymbol{Y}\in\Omega_O(\boldsymbol{X},T), && (3.3.57b)\\
&\delta^2\frac{\partial W_H}{\partial T} + \delta^2\left(\nabla_{\boldsymbol{Y}} + \delta\nabla_{\boldsymbol{X}}\right)\cdot\left(\boldsymbol{U}_H W_H\right)\\
&\qquad = d_{WH}\left(\nabla_{\boldsymbol{Y}} + \delta\nabla_{\boldsymbol{X}}\right)\cdot\left(\nabla_{\boldsymbol{Y}} + \delta\nabla_{\boldsymbol{X}}\right)W_H \qquad \text{for } \boldsymbol{Y}\in\Omega_H(\boldsymbol{X},T), && (3.3.57c)\\
&\delta^2\frac{\partial W_O}{\partial T} + \delta^2\left(\nabla_{\boldsymbol{Y}} + \delta\nabla_{\boldsymbol{X}}\right)\cdot\left(\boldsymbol{U}_O W_O\right)\\
&\qquad = d_{WO}\left(\nabla_{\boldsymbol{Y}} + \delta\nabla_{\boldsymbol{X}}\right)\cdot\left(\nabla_{\boldsymbol{Y}} + \delta\nabla_{\boldsymbol{X}}\right)W_O \qquad \text{for } \boldsymbol{Y}\in\Omega_O(\boldsymbol{X},T), && (3.3.57d)
\end{aligned}$$

with boundary conditions on $\boldsymbol{Y}\in\partial\Omega_O(\boldsymbol{X},T)$:

$$\begin{aligned}
&K_C C_O = C_H, \quad K_W W_O = W_H, && (3.3.58a)\\
&\left(\mathbf{n}_{\boldsymbol{Y}} - \delta\nabla_{\boldsymbol{X}}R\right)\cdot\big(\left(\nabla_{\boldsymbol{Y}} + \delta\nabla_{\boldsymbol{X}}\right)C_H + \delta^2 C_H\left(\boldsymbol{U}_{\partial\Omega_O} - \boldsymbol{U}_H\right)\big) - \delta^2\sigma_S S\\
&\quad = \left(\mathbf{n}_{\boldsymbol{Y}} - \delta\nabla_{\boldsymbol{X}}R\right)\cdot\big(d_{CO}\left(\nabla_{\boldsymbol{Y}} + \delta\nabla_{\boldsymbol{X}}\right)C_O + \delta^2 C_O\left(\boldsymbol{U}_{\partial\Omega_O} - \boldsymbol{U}_O\right)\big) + \mathcal{O}(\delta^3), && (3.3.58b)\\
&\left(\mathbf{n}_{\boldsymbol{Y}} - \delta\nabla_{\boldsymbol{X}}R\right)\cdot\big(d_{WH}\left(\nabla_{\boldsymbol{Y}} + \delta\nabla_{\boldsymbol{X}}\right)W_H + \delta^2 W_H\left(\boldsymbol{U}_{\partial\Omega_O} - \boldsymbol{U}_H\right)\big) + 2\delta\sigma_S S\\
&\quad = \left(\mathbf{n}_{\boldsymbol{Y}} - \delta\nabla_{\boldsymbol{X}}R\right)\cdot\big(d_{WO}\left(\nabla_{\boldsymbol{Y}} + \delta\nabla_{\boldsymbol{X}}\right)W_O + \delta^2 W_O\left(\boldsymbol{U}_{\partial\Omega_O} - \boldsymbol{U}_O\right)\big) + \mathcal{O}(\delta^3), && (3.3.58c)
\end{aligned}$$

and periodicity of C_H and W_H in $\boldsymbol{Y}$ on the unit cell boundary, $\boldsymbol{Y}\in\partial\Omega$.

Since large parts of the analysis are the same as in Section 3.3.1, we largely focus on the new aspects here.

We again consider the distinguished limit $d_{CO}\sim d_{WO}\sim d_{WH}\sim\mathcal{O}(1)$, $\sigma_S\sim\mathcal{O}(1)$, and $R\sim\mathcal{O}(1)$, and pose an asymptotic expansion in the limit $\delta\to 0$:

$$f \sim f_0 + \delta f_1 + \delta^2 f_2 + \ldots, \quad \text{where } f\in\{C_H, C_O, W_H, W_O\}. \tag{3.3.59}$$

The $\mathcal{O}(1)$ problem is the same as for volumetric growth, Equations (3.3.9) and (3.3.10). Therefore, we still have that the leading-order metabolite concentrations are independent of the microscale variable $\boldsymbol{Y}$ and satisfy $C_{H0} = K_C C_{O0}$ and $W_{H0} = K_W W_{O0}$.

The $\mathcal{O}(\delta)$ problem is also the same as for volumetric growth, Equations (3.3.15) and (3.3.16). Therefore, we pose the same ansatz for solution, Equation (3.3.17) to obtain the same cell problem for $\boldsymbol{\psi}$, $\boldsymbol{\Psi}$, $\boldsymbol{\gamma}$, and $\boldsymbol{\Gamma}$ as in the volumetric growth case, Equations (3.3.18) and (3.3.19).

$\boldsymbol{\mathcal{O}(\delta^2)}$ problem:
The governing equations for $\{C_{H2}, C_{O2}, W_{H2}, W_{O2}\}$ in the case of shell organoids are:

$$\begin{aligned}
&\frac{\partial C_{H0}}{\partial T} + \nabla_{\boldsymbol{Y}} \cdot (\boldsymbol{U}_H C_{H0}) \\
&= (\nabla_{\boldsymbol{Y}} \cdot (\nabla_{\boldsymbol{Y}} C_{H2} + \nabla_{\boldsymbol{X}} C_{H1}) + \nabla_{\boldsymbol{X}} \cdot (\nabla_{\boldsymbol{Y}} C_{H1} + \nabla_{\boldsymbol{X}} C_{H0})) \quad \text{for } \boldsymbol{Y} \in \Omega_H, \quad (3.3.60\text{a})\\
&\frac{\partial C_{O0}}{\partial T} + \nabla_{\boldsymbol{Y}} \cdot (\boldsymbol{U}_O C_{O0}) \\
&= d_{CO} (\nabla_{\boldsymbol{Y}} \cdot (\nabla_{\boldsymbol{Y}} C_{O2} + \nabla_{\boldsymbol{X}} C_{O1}) + \nabla_{\boldsymbol{X}} \cdot (\nabla_{\boldsymbol{Y}} C_{O1} + \nabla_{\boldsymbol{X}} C_{O0})) \text{ for } \boldsymbol{Y} \in \Omega_O, \quad (3.3.60\text{b})\\
&\frac{\partial W_{H0}}{\partial T} + \nabla_{\boldsymbol{Y}} \cdot (\boldsymbol{U}_H W_{H0}) \\
&= d_{WH} (\nabla_{\boldsymbol{Y}} \cdot (\nabla_{\boldsymbol{Y}} W_{H2} + \nabla_{\boldsymbol{X}} W_{H1}) + \nabla_{\boldsymbol{X}} \cdot (\nabla_{\boldsymbol{Y}} W_{H1} + \nabla_{\boldsymbol{X}} W_{H0})) \text{ for } \boldsymbol{Y} \in \Omega_H, \quad (3.3.60\text{c})\\
&\frac{\partial W_{O0}}{\partial T} + \nabla_{\boldsymbol{Y}} \cdot (\boldsymbol{U}_O W_{O0}) \\
&= d_{WO} (\nabla_{\boldsymbol{Y}} \cdot (\nabla_{\boldsymbol{Y}} W_{O2} + \nabla_{\boldsymbol{X}} W_{O1}) + \nabla_{\boldsymbol{X}} \cdot (\nabla_{\boldsymbol{Y}} W_{O1} + \nabla_{\boldsymbol{X}} W_{O0})) \text{ for } \boldsymbol{Y} \in \Omega_O. \quad (3.3.60\text{d})
\end{aligned}$$

The boundary conditions on $\boldsymbol{Y} \in \partial\Omega_O(\boldsymbol{X}, T)$ are:

$$\begin{aligned}
K_C C_{O2} = C_{H2} \quad &\text{and} \quad K_W W_{O2} = W_{H2}, \quad (3.3.61\text{a})\\
\mathbf{n}_{\boldsymbol{Y}} \cdot (\nabla_{\boldsymbol{Y}} C_{H2} + \nabla_{\boldsymbol{X}} C_{H1}) - \nabla_{\boldsymbol{X}} R \cdot (\nabla_{\boldsymbol{Y}} C_{H1} + \nabla_{\boldsymbol{X}} C_{H0}) - \sigma_S S(C_{O0}, W_{O0})&\\
= d_{CO} \left[\mathbf{n}_{\boldsymbol{Y}} \cdot (\nabla_{\boldsymbol{Y}} C_{O2} + \nabla_{\boldsymbol{X}} C_{O1}) - \nabla_{\boldsymbol{X}} R \cdot (\nabla_{\boldsymbol{Y}} C_{O1} + \nabla_{\boldsymbol{X}} C_{O0})\right],& \quad (3.3.61\text{b})\\
d_{WH} \left[\mathbf{n}_{\boldsymbol{Y}} \cdot (\nabla_{\boldsymbol{Y}} W_{H2} + \nabla_{\boldsymbol{X}} W_{H1}) - \nabla_{\boldsymbol{X}} R \cdot (\nabla_{\boldsymbol{Y}} W_{H1} + \nabla_{\boldsymbol{X}} W_{H0})\right] + 2\sigma_S S(C_{O0}, W_{O0})&\\
= d_{WO} \left[\mathbf{n}_{\boldsymbol{Y}} \cdot (\nabla_{\boldsymbol{Y}} W_{O2} + \nabla_{\boldsymbol{X}} W_{O1}) - \nabla_{\boldsymbol{X}} R \cdot (\nabla_{\boldsymbol{Y}} W_{O1} + \nabla_{\boldsymbol{X}} W_{O0})\right],& \quad (3.3.61\text{c})
\end{aligned}$$

where we have taken the leading-order term of a Taylor expansion of S about (C_{O0}, W_{O0}) for the consumption/production terms. We also have that C_{H2} and W_{H2} are periodic on $\partial\Omega$.

We proceed, as in Section 3.3.1, by integrating the governing equations Equations (3.3.60a) and (3.3.60c) over Ω_H and Equations (3.3.60b) and (3.3.60d) over Ω_O, to remove the dependence of the system on $\boldsymbol{Y}$. We then sum the integrated governing equations for glucose and lactate, respectively. The following derivation is similar to that for volumetric growth, however there is a subtle difference in the analysis, as the consumption and production terms now appear via the application of the boundary condition on a surface integral over the organoid-hydrogel boundary. We present the derivation for the glucose concentration, and note that the derivation for lactate is analogous.

The sum of the initial integrated governing equations, Equations (3.3.60a) and (3.3.60b), is

$$\begin{aligned}
&\int_{\Omega_H} \frac{\partial C_{H0}}{\partial T} + \underbrace{\nabla_{\boldsymbol{Y}} \cdot (\boldsymbol{U}_H C_{H0})}_{\textcircled{\dagger_1}} \, \mathrm{d}\boldsymbol{Y} + \int_{\Omega_O} \frac{\partial C_{O0}}{\partial T} + \underbrace{\nabla_{\boldsymbol{Y}} \cdot (\boldsymbol{U}_O C_{O0})}_{\textcircled{\dagger_1}} \, \mathrm{d}\boldsymbol{Y} \\
&\quad = \underbrace{\int_{\Omega_H} \nabla_{\boldsymbol{Y}} \cdot (\nabla_{\boldsymbol{Y}} C_{H2} + \nabla_{\boldsymbol{X}} C_{H1}) \, \mathrm{d}\boldsymbol{Y}}_{\textcircled{\dagger_1}} + \int_{\Omega_H} \nabla_{\boldsymbol{X}} \cdot (\nabla_{\boldsymbol{Y}} C_{H1} + \nabla_{\boldsymbol{X}} C_{H0}) \, \mathrm{d}\boldsymbol{Y} \\
&\qquad + \underbrace{\int_{\Omega_O} d_{CO} \nabla_{\boldsymbol{Y}} \cdot (\nabla_{\boldsymbol{Y}} C_{O2} + \nabla_{\boldsymbol{X}} C_{O1}) \, \mathrm{d}\boldsymbol{Y}}_{\textcircled{\dagger_1}} \\
&\qquad + \int_{\Omega_O} d_{CO} \nabla_{\boldsymbol{X}} \cdot (\nabla_{\boldsymbol{Y}} C_{O1} + \nabla_{\boldsymbol{X}} C_{O0}) \, \mathrm{d}\boldsymbol{Y}. \qquad (3.3.62)
\end{aligned}$$

We, again, apply the divergence theorem on the $\textcircled{\dagger_1}$ terms in Equation (3.3.62) to get a surface integral over the organoid-hydrogel boundary $\partial\Omega_O$,

$$\begin{aligned}
&\underbrace{\int_{\Omega_H} \frac{\partial C_{H0}}{\partial T} \, \mathrm{d}\boldsymbol{Y}}_{\textcircled{\dagger_2}} + \underbrace{\int_{\Omega_O} \frac{\partial C_{O0}}{\partial T} \, \mathrm{d}\boldsymbol{Y}}_{\textcircled{\dagger_2}} + \int_{\partial\Omega_O} (\boldsymbol{U}_O \cdot \mathbf{n}_{\boldsymbol{Y}}) C_{O0} + (\boldsymbol{U}_H \cdot (-\mathbf{n}_{\boldsymbol{Y}})) C_{H0} \, \mathrm{d}A \\
&\quad = \int_{\partial\Omega_O} \mathbf{n}_{\boldsymbol{Y}} \cdot \left(- (\nabla_{\boldsymbol{Y}} C_{H2} + \nabla_{\boldsymbol{X}} C_{H1}) + d_{CO} (\nabla_{\boldsymbol{Y}} C_{O2} + \nabla_{\boldsymbol{X}} C_{O1}) \right) \, \mathrm{d}A \\
&\quad + \int_{\Omega_H} \nabla_{\boldsymbol{X}} \cdot (\nabla_{\boldsymbol{Y}} C_{H1} + \nabla_{\boldsymbol{X}} C_{H0}) \, \mathrm{d}\boldsymbol{Y} \\
&\quad + \int_{\Omega_O} d_{CO} \nabla_{\boldsymbol{X}} \cdot (\nabla_{\boldsymbol{Y}} C_{O1} + \nabla_{\boldsymbol{X}} C_{O0}) \, \mathrm{d}\boldsymbol{Y}. \qquad (3.3.63)
\end{aligned}$$

Next, we use Reynolds transport theorem on the volume integrals $\textcircled{\dagger_2}$ on the left-hand side of Equation (3.3.63) (see Equation (3.3.26) and Appendix A of [2]), noting that $\Omega_H(\boldsymbol{X}, T)$ and $\Omega_O(\boldsymbol{X}, T)$ are time-dependent, so we gain a contribution of a surface integral,

$$\begin{aligned}
&\frac{\partial}{\partial T}\left(\int_{\Omega_H} C_{H0}\ \mathrm{d}\boldsymbol{Y} + \int_{\Omega_O} C_{O0}\ \mathrm{d}\boldsymbol{Y}\right) - \int_{\partial\Omega_O} (\boldsymbol{U}_{\partial\Omega_O}\cdot\mathbf{n}_{\boldsymbol{Y}})C_{O0} + (\boldsymbol{U}_{\partial\Omega_O}\cdot(-\mathbf{n}_{\boldsymbol{Y}}))C_{H0}\ \mathrm{d}A \\
&\quad + \int_{\partial\Omega_O} (\boldsymbol{U}_O\cdot\mathbf{n}_{\boldsymbol{Y}})C_{O0} + (\boldsymbol{U}_H\cdot(-\mathbf{n}_{\boldsymbol{Y}}))C_{H0}\ \mathrm{d}A \\
&= \int_{\Omega_H} \nabla_{\boldsymbol{X}}\cdot\left(\nabla_{\boldsymbol{Y}}C_{H1} + \nabla_{\boldsymbol{X}}C_{H0}\right)\ \mathrm{d}\boldsymbol{Y} + \int_{\Omega_O} d_{CO}\nabla_{\boldsymbol{X}}\cdot\left(\nabla_{\boldsymbol{Y}}C_{O1} + \nabla_{\boldsymbol{X}}C_{O1}\right)\ \mathrm{d}\boldsymbol{Y} \\
&\quad + \int_{\partial\Omega_O} \mathbf{n}_{\boldsymbol{Y}}\cdot\left(-\left(\nabla_{\boldsymbol{Y}}C_{H2} + \nabla_{\boldsymbol{X}}C_{H1}\right) + d_{CO}\left(\nabla_{\boldsymbol{Y}}C_{O2} + \nabla_{\boldsymbol{X}}C_{O1}\right)\right)\ \mathrm{d}A. \qquad (3.3.64)
\end{aligned}$$

In a similar manner to the dense organoid case (see Equation (3.3.26) in Section 3.3.1), we wish to obtain terms of the form $\nabla_{\boldsymbol{X}}\cdot\int_{\Omega_i}$, so we apply Reynolds transport theorem, Equation (3.3.26), component-wise to the volume integrals over $\Omega_H(\boldsymbol{X},T)$ and $\Omega_O(\boldsymbol{X},T)$ on the right-hand side of Equation (3.3.64), and therefore, we can derive the following relationships:

$$\begin{aligned}
\int_{\Omega_H} \nabla_{\boldsymbol{X}}\cdot\left(\nabla_{\boldsymbol{Y}}C_{H1} + \nabla_{\boldsymbol{X}}C_{H0}\right)\ \mathrm{d}\boldsymbol{Y} =& \nabla_{\boldsymbol{X}}\cdot\left(\int_{\Omega_H} \nabla_{\boldsymbol{Y}}C_{H1} + \nabla_{\boldsymbol{X}}C_{H0}\ \mathrm{d}\boldsymbol{Y}\right) \\
&+ \int_{\partial\Omega_O} \nabla_{\boldsymbol{X}}R\cdot\left(\nabla_{\boldsymbol{Y}}C_{H1} + \nabla_{\boldsymbol{X}}C_{H0}\right)\ \mathrm{d}A, \qquad (3.3.65\mathrm{a}) \\
\int_{\Omega_O} d_{CO}\nabla_{\boldsymbol{X}}\cdot\left(\nabla_{\boldsymbol{Y}}C_{O1} + \nabla_{\boldsymbol{X}}C_{O0}\right)\ \mathrm{d}\boldsymbol{Y} =& d_{CO}\nabla_{\boldsymbol{X}}\cdot\left(\int_{\Omega_O} \nabla_{\boldsymbol{Y}}C_{O1} + \nabla_{\boldsymbol{X}}C_{O0}\ \mathrm{d}\boldsymbol{Y}\right) \\
&- \int_{\partial\Omega_O} d_{CO}\nabla_{\boldsymbol{X}}R\cdot\left(\nabla_{\boldsymbol{Y}}C_{O1} + \nabla_{\boldsymbol{X}}C_{O0}\right)\ \mathrm{d}A. \qquad (3.3.65\mathrm{b})
\end{aligned}$$

Using Equation (3.3.65), our governing equation, Equation (3.3.64), becomes:

$$\begin{aligned}
&\frac{\partial}{\partial T}\left(\int_{\Omega_H} C_{H0}\,\mathrm{d}\boldsymbol{Y} + \int_{\Omega_O} C_{O0}\,\mathrm{d}\boldsymbol{Y}\right) \\
&\qquad + \underbrace{\int_{\partial\Omega_O} ((\boldsymbol{U}_{\partial\Omega_O} - \boldsymbol{U}_H)\cdot\mathbf{n}_{\boldsymbol{Y}})C_{H0} - ((\boldsymbol{U}_{\partial\Omega_O} - \boldsymbol{U}_O)\cdot\mathbf{n}_{\boldsymbol{Y}})C_{O0}\,\mathrm{d}A}_{\textcircled{\dagger_3}} \\
&= \nabla_{\boldsymbol{X}}\cdot\left(\int_{\Omega_H} \nabla_{\boldsymbol{Y}}C_{H1} + \nabla_{\boldsymbol{X}}C_{H0}\,\mathrm{d}\boldsymbol{Y}\right) + \underbrace{\int_{\partial\Omega_O} \nabla_{\boldsymbol{X}}R\cdot\left(\nabla_{\boldsymbol{Y}}C_{H1} + \nabla_{\boldsymbol{X}}C_{H0}\right)\,\mathrm{d}A}_{\textcircled{\dagger_3}} \\
&+ d_{CO}\nabla_{\boldsymbol{X}}\cdot\left(\int_{\Omega_O} \nabla_{\boldsymbol{Y}}C_{O1} + \nabla_{\boldsymbol{X}}C_{O0}\,\mathrm{d}\boldsymbol{Y}\right) \underbrace{- \int_{\partial\Omega_O} d_{CO}\nabla_{\boldsymbol{X}}R\cdot\left(\nabla_{\boldsymbol{Y}}C_{O1} + \nabla_{\boldsymbol{X}}C_{O0}\right)\,\mathrm{d}A}_{\textcircled{\dagger_3}} \\
&\qquad + \underbrace{\int_{\partial\Omega_O} \mathbf{n}_{\boldsymbol{Y}}\cdot\left(-\left(\nabla_{\boldsymbol{Y}}C_{H2} + \nabla_{\boldsymbol{X}}C_{H1}\right) + d_{CO}\left(\nabla_{\boldsymbol{Y}}C_{O2} + \nabla_{\boldsymbol{X}}C_{O1}\right)\right)\,\mathrm{d}A}_{\textcircled{\dagger_3}}. \qquad (3.3.66)
\end{aligned}$$

Applying the continuity of flux condition, Equation (3.3.61b), to the surface integrals on the RHS of Equation (3.3.66), $\textcircled{\dagger_3}$, we find that these terms can be written in terms of the rate of glucose consumption. We find that Equation (3.3.66) becomes:

$$\begin{aligned}
\frac{\partial}{\partial T}\left(\int_{\Omega_H} C_{H0}\,\mathrm{d}\boldsymbol{Y} + \int_{\Omega_O} C_{O0}\,\mathrm{d}\boldsymbol{Y}\right) &= \nabla_{\boldsymbol{X}}\cdot\left(\int_{\Omega_H} \nabla_{\boldsymbol{Y}}C_{H1} + \nabla_{\boldsymbol{X}}C_{H0}\,\mathrm{d}\boldsymbol{Y}\right) \\
&+ d_{CO}\nabla_{\boldsymbol{X}}\cdot\left(\int_{\Omega_O} \nabla_{\boldsymbol{Y}}C_{O1} + \nabla_{\boldsymbol{X}}C_{O0}\,\mathrm{d}\boldsymbol{Y}\right) - \int_{\partial\Omega_O} \sigma_S S(C_{O0}, W_{O0})\,\mathrm{d}A. \qquad (3.3.67)
\end{aligned}$$

Similarly to the case of volumetric growth, Equation (3.3.67) can be simplified and rewritten in terms of $\bar{C} = C_{O0} = C_{H0}/K_C$ and $\bar{W} = W_{O0} = W_{H0}/K_W$ as:

$$\frac{\partial}{\partial T}\left(\left(\|\Omega_H\|\,K_C + \|\Omega_O\|\right)\bar{C}\right) = \nabla_{\boldsymbol{X}}\cdot\left(\bar{\boldsymbol{d}}_C(\boldsymbol{X},T)\nabla_{\boldsymbol{X}}\bar{C}\right) - \sigma_S\,\|\partial\Omega_O\|\,S(\bar{C},\bar{W}), \qquad (3.3.68)$$

where we define the surface area of boundary $\partial\Omega_i$ as

$$\|\partial\Omega_i\| = \int_{\partial\Omega_i} \mathrm{d}A. \qquad (3.3.69)$$

Since we have spherical organoids, the volumes of the organoid and hydrogel domains and the surface area of the organoid-hydrogel boundary are:

$$\|\Omega_O\| = \frac{4}{3}\pi R^3, \quad \|\Omega_H\| = 1 - \frac{4}{3}\pi R^3, \quad \|\partial\Omega_O\| = 4\pi R^2, \qquad (3.3.70)$$

respectively. The *effective diffusivity* tensor for glucose, $\bar{\boldsymbol{d}}_C$, is defined as

$$\bar{\boldsymbol{d}}_C(\boldsymbol{X},T) = K_C \int_{\Omega_H} \left(\boldsymbol{I} - \boldsymbol{J}_{\boldsymbol{\psi}}^{\top}\right) \, \mathrm{d}\boldsymbol{Y} + \int_{\Omega_O} d_{CO} \left(\boldsymbol{I} - \boldsymbol{J}_{\boldsymbol{\Psi}}^{\top}\right) \, \mathrm{d}\boldsymbol{Y}, \tag{3.3.71}$$

where $\boldsymbol{J}_{\boldsymbol{\psi}}^{\top}$ and $\boldsymbol{J}_{\boldsymbol{\Psi}}^{\top}$ are the transposes of the Jacobian matrices of $\boldsymbol{\psi}$ and $\boldsymbol{\Psi}$, respectively, which are solutions to the cell problem, Equations (3.3.18a) and (3.3.18b) subject to Equation (3.3.19a). A similar equation can be derived for effective macroscale behaviour for lactate concentration.

Using the simplification of terms in the isotropic diffusivity tensors $\bar{\boldsymbol{d}}_C = \bar{d}_C \boldsymbol{I}$ and $\bar{\boldsymbol{d}}_W = \bar{d}_W \boldsymbol{I}$ for spherical organoids, Equation (3.3.44), we obtain the following governing equations for metabolite transport within a hydrogel embedded with spherical shell organoids exhibiting surface growth:

$$\frac{\partial}{\partial T}\left[\left(\|\Omega_H\| \, K_C + \|\Omega_O\|\right) \bar{C}\right] = \nabla_{\boldsymbol{X}} \cdot \left(\bar{d}_C(\boldsymbol{X},T) \nabla_{\boldsymbol{X}} \bar{C}\right) - \|\partial\Omega_O\| \, \sigma_S S(\bar{C},\bar{W}), \tag{3.3.72a}$$

$$\frac{\partial}{\partial T}\left[\left(\|\Omega_H\| \, K_W + \|\Omega_O\|\right) \bar{W}\right] = \nabla_{\boldsymbol{X}} \cdot \left(\bar{d}_W(\boldsymbol{X},T) \nabla_{\boldsymbol{X}} \bar{W}\right) + 2 \, \|\partial\Omega_O\| \, \sigma_S S(\bar{C},\bar{W}), \tag{3.3.72b}$$

where the *effective diffusivities* of glucose and lactate in the hydrogel, $\bar{d}_C$ and $\bar{d}_W$ respectively, are:

$$\bar{d}_C(\boldsymbol{X},T) = K_C \left[\|\Omega_H\| - \int_{\Omega_H} \frac{\partial \psi_1}{\partial Y_1} \, \mathrm{d}\boldsymbol{Y}\right] + d_{CO}\left[\|\Omega_O\| - \int_{\Omega_O} \frac{\partial \psi_1}{\partial Y_1} \, \mathrm{d}\boldsymbol{Y}\right], \tag{3.3.73a}$$

$$\bar{d}_W(\boldsymbol{X},T) = K_W d_{WH}\left[\|\Omega_H\| - \int_{\Omega_H} \frac{\partial \gamma_1}{\partial Y_1} \, \mathrm{d}\boldsymbol{Y}\right] + d_{WO}\left[\|\Omega_O\| - \int_{\Omega_O} \frac{\partial \Gamma_1}{\partial Y_1} \, \mathrm{d}\boldsymbol{Y}\right], \tag{3.3.73b}$$

which are obtained by solving the cell problem, Equations (3.3.18) and (3.3.19).

We note that the volumes of the hydrogel and organoid domains, $\|\Omega_H\|$ and $\|\Omega_O\|$, and the surface area of the boundary $\|\partial\Omega_O\|$, are dependent on $\boldsymbol{X}$ and T via their dependence on the organoid radius, $R = R(\boldsymbol{X},T)$. To close the system, we require a constitutive relationship for glucose consumption and organoid growth. We introduced these models in Section 3.2.1.1 and Sections 3.2.1.2 and 3.2.1.3, respectively.

3.4 Results

In this Section, we examine the similarities and differences between the dense and shell organoid models. We solve the model numerically, using COMSOL Multiphysics® (a finite-element solver). A key component is solving the *cell problem*, Equations (3.3.18) and (3.3.19), in order to compute the *effective diffusivities*, $\bar{d}_C(\boldsymbol{X}, T)$ and $\bar{d}_W(\boldsymbol{X}, T)$. We then consider two canonical cases, representing two different culture conditions for expansion of dense organoids. We discuss the influence the culture conditions have on the metabolite concentrations and the resulting effect on organoid growth within the hydrogel.

3.4.1 Comparison of governing equations for volumetric and surface growth

In Sections 3.3.1 and 3.3.2, we derived the effective macroscale equations governing metabolite transport and organoid growth within the hydrogel layer. We now examine and compare the models for volumetric and surface growth of the organoids.

The homogenised model for metabolite transport and organoid growth for volumetric growth of dense organoids is:

$$\frac{\partial}{\partial T}\left(\left[\left(1-\frac{4}{3}\pi R^3\right)K_C+\frac{4}{3}\pi R^3\right]\bar{C}\right)=\nabla_{\boldsymbol{X}}\cdot\left(\bar{d}_C(\boldsymbol{X},T)\nabla_{\boldsymbol{X}}\bar{C}\right)-\frac{4}{3}\pi R^3\sigma_V S(\bar{C},\bar{W}), \tag{3.4.1a}$$

$$\frac{\partial}{\partial T}\left(\left[\left(1-\frac{4}{3}\pi R^3\right)K_W+\frac{4}{3}\pi R^3\right]\bar{W}\right)=\nabla_{\boldsymbol{X}}\cdot\left(\bar{d}_W(\boldsymbol{X},T)\nabla_{\boldsymbol{X}}\bar{W}\right)+\frac{8}{3}\pi R^3\sigma_V S(\bar{C},\bar{W}), \tag{3.4.1b}$$

$$\frac{\partial R}{\partial T}=\frac{\rho}{3}P(\bar{C},\bar{W})R. \tag{3.4.1c}$$

The homogenised model for metabolite transport and organoid growth for surface growth of spherical shell organoids is:

$$\frac{\partial}{\partial T}\left(\left[\left(1-\frac{4}{3}\pi R^3\right)K_C+\frac{4}{3}\pi R^3\right]\bar{C}\right)=\nabla_{\boldsymbol{X}}\cdot\left(\bar{d}_C(\boldsymbol{X},T)\nabla_{\boldsymbol{X}}\bar{C}\right)-4\pi R^2\sigma_S S(\bar{C},\bar{W}), \tag{3.4.2a}$$

$$\frac{\partial}{\partial T}\left(\left[\left(1-\frac{4}{3}\pi R^3\right)K_W+\frac{4}{3}\pi R^3\right]\bar{W}\right)=\nabla_{\boldsymbol{X}}\cdot\left(\bar{d}_W(\boldsymbol{X},T)\nabla_{\boldsymbol{X}}\bar{W}\right)+8\pi R^2\sigma_S S(\bar{C},\bar{W}), \tag{3.4.2b}$$

$$(R-R_c)\frac{\partial R}{\partial T}=\frac{\rho}{2}P(\bar{C},\bar{W})\left((R-R_c)^2+\frac{R_c^2}{3}\right). \tag{3.4.2c}$$

Comparing the homogenised equations for metabolite transport within the hydrogel layer for volumetric growth of dense organoids, Equation (3.4.1), to those for surface growth of shell organoids, Equation (3.4.2), we see that they are both reaction-diffusion equations. Notably, the *effective diffusivities*, $\bar{d}_C(\boldsymbol{X}, T)$ and $\bar{d}_W(\boldsymbol{X}, T)$ defined in Equations (3.3.73a) and (3.3.73b), are identical. In both cases, a partition coefficient causes effective quickening ($K_i < 1$)/slowing ($K_i > 1$) of metabolite transport in the system, as can be observed by the coefficient in front of the time derivative, $[(1 - 4\pi R^3/3)\, K_i + 4\pi R^3/3]$. We note that the spatial variation of organoid radius R appears implicitly via spatial variation in the metabolite concentrations within the organoid regions.

There are two key differences between the homogenised models for volumetric and surface growth. For volumetric growth, the glucose consumption and lactate production terms are proportional to the organoid volume within the periodic cell, $\|\Omega_O\| = 4\pi R^3/3$; for surface growth, this factor is instead the surface area of the organoid-hydrogel interface within the periodic cell, $\|\partial\Omega_O\| = 4\pi R^2$. The relationship between the dimensionless scaling σ_V and σ_S is $\sigma_S = 2R_c\sigma_V = 2r_c\sigma_V/(\delta L)$. This scaling describes how we related the volume of the glucose-consuming cells within the shell organoid to the organoid surface area, *volume of uptake region* $=$ *surface area* $\times$ *thickness of organoid shell.*

The second important difference between the two models is in the organoid growth model. For dense organoids, the entire volume consists of proliferating organoid biomass, the evolution of organoid radius is given by Equation (3.4.1c), and the number of cells within an organoid, N, scales as $N \propto R^3$. For shell organoids, the proliferating organoid biomass is localised in a layer of cells at the organoid boundary, the evolution of organoid radius is given by Equation (3.4.2c), and the number of cells within a shell organoid, N, scales as $N \propto R^2$.

In the case where the organoid-hydrogel partition coefficients, K_C and K_W, are both equal to one, the metabolite transport model simplifies. For example, for dense organoids undergoing volumetric growth we have:

$$\frac{\partial \bar{C}}{\partial T} = \nabla_{\boldsymbol{X}} \cdot \left(\bar{d}_C(\boldsymbol{X}, T)\nabla_{\boldsymbol{X}}\bar{C}\right) - \frac{4}{3}\pi R^3\sigma_V S(\bar{C}, \bar{W}), \tag{3.4.3a}$$

$$\frac{\partial \bar{W}}{\partial T} = \nabla_{\boldsymbol{X}} \cdot \left(\bar{d}_W(\boldsymbol{X}, T)\nabla_{\boldsymbol{X}}\bar{W}\right) + \frac{8}{3}\pi R^3\sigma_V S(\bar{C}, \bar{W}), \tag{3.4.3b}$$

$$\frac{\partial R}{\partial T} = \frac{\rho}{3}P(\bar{C}, \bar{W})R, \tag{3.4.3c}$$

subject to boundary and initial conditions. This is an reaction-diffusion system of the same form as the one considered in Chapter 2, where the diffusive and reaction terms now account for the evolving organoid structure within the hydrogel.

3.4.2 Numerical solution of the cell problem

In order to solve the homogenised metabolite transport models, we require knowledge of the effective diffusivity for all $\boldsymbol{X}$ for all times $T \geq 0$. Computing the effective diffusivities of glucose and lactate, $\bar{d}_C$ and $\bar{d}_W$, requires the solution of the *cell problem*, Equations (3.3.18) and (3.3.19). We do this numerically using COMSOL Multiphysics®, similarly to *e.g.* [16, 18, 2]. A schematic of the three-dimensional domain of the cell problem is shown in Figure 3.4(a). The cell problem is quasi-static, in the sense that the governing equations are temporally independent. However, the domains $\Omega_O(\boldsymbol{X}, T)$ and $\Omega_H(\boldsymbol{X}, T)$ depend on time and the macroscale spatial variable, $\boldsymbol{X}$. One option would be to solve the macroscale problem numerically, where each point in space is coupled to a different cell problem that varies quasi-statically over time. However, this is very computationally expensive and entirely unnecessary if we can pre-compute the effective diffusivity over enough points in parameter space to interpolate it accurately.

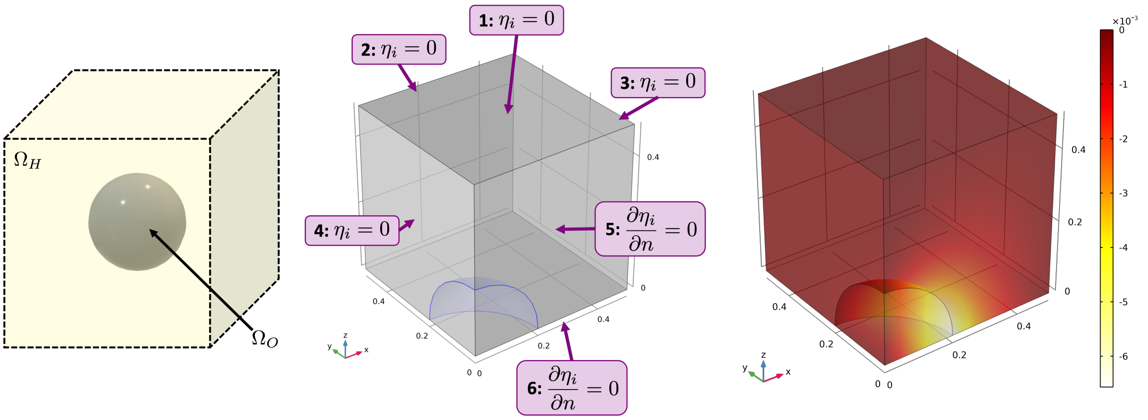

(a) Schematic of the 3D domain.

(b) Schematic of the domain for numerically solving the cell problem with boundary conditions labelled for i being the X component ($i = 1$) of $\boldsymbol{\eta}$.

(c) Solution of the X-component, η_1, of the 3D cell problem, Equations (3.4.5) and (3.4.6), for $d_{CO} = 0.9$, $K_C = 1$ and $R = 0.2$.

Figure 3.4: Schematics of the domains and a numerical solution to the reformulated cell problem, Equations (3.4.5) and (3.4.6).

We consider the cell problem for the variables $\boldsymbol{\psi}$ and $\boldsymbol{\Psi}$, which are given componentwise in Equations (3.3.18a), (3.3.18b) and (3.3.19a). We restate these here for convenience:

$$0 = \nabla^2_{\boldsymbol{Y}} \psi_i \quad \text{for } \boldsymbol{Y} \in \Omega_H, \tag{3.4.4a}$$

$$0 = \nabla^2_{\boldsymbol{Y}} \Psi_i \quad \text{for } \boldsymbol{Y} \in \Omega_O, \tag{3.4.4b}$$

with boundary conditions for $\boldsymbol{Y} \in \partial\Omega_O(\boldsymbol{X}, T)$,

$$\psi_i = K_C \Psi_i, \qquad \mathbf{n}_{\boldsymbol{Y}} \cdot (K_C \nabla_{\boldsymbol{Y}} \psi_i - d_{CO} \nabla_{\boldsymbol{Y}} \Psi_i) = (K_C - d_{CO})\, \mathbf{n}_{\boldsymbol{Y}} \cdot \boldsymbol{e}_i, \tag{3.4.4c}$$

with ψ_i and γ_i periodic for $\boldsymbol{Y} \in \partial\Omega$, and where $\boldsymbol{e}_i$ is the unit vector in the Y_i-direction. We provide details on the derivation of the boundary conditions in B. Since COMSOL Multiphysics® is more amenable to solving PDEs posed in 'standard' formats, we must introduce some scalings before solving. Specifically, this allows us to pose continuity of our dependent variables at the interface. To this end, we introduce $\eta_i = \psi_i / K_C$, and reformulate the cell problem as

$$0 = \nabla^2_{\boldsymbol{Y}} \eta_i \qquad \text{for } \boldsymbol{Y} \in \Omega_H, \tag{3.4.5a}$$

$$0 = \frac{d_{CO}}{{K_C}^2} \nabla^2_{\boldsymbol{Y}} \Psi_i \qquad \text{for } \boldsymbol{Y} \in \Omega_O, \tag{3.4.5b}$$

with continuity of concentration and a discontinuous flux condition on the boundary $\partial\Omega_O$,

$$\eta_i = \Psi_i \qquad \text{for } \boldsymbol{Y} \in \partial\Omega_O, \tag{3.4.6a}$$

$$\mathbf{n}_{\boldsymbol{Y}} \cdot \left(\nabla_{\boldsymbol{Y}} \eta_i - \frac{d_{CO}}{{K_C}^2} \nabla_{\boldsymbol{Y}} \Psi_i \right) = \frac{1}{{K_C}^2} (K_C - d_{CO}) \mathbf{n}_{\boldsymbol{Y}} \cdot \boldsymbol{e}_i \qquad \text{for } \boldsymbol{Y} \in \partial\Omega_O. \tag{3.4.6b}$$

We also impose periodicity of η_i on the boundary $\partial\Omega$. The system Equations (3.4.5) and (3.4.6) remains characterised by three parameter groupings — in this case: $1/K_C$, $d_{CO}/{K_C}^2$, and R.

The cell problem for $\boldsymbol{\gamma}$ and $\boldsymbol{\Gamma}$ is formulated in the same way: with $\eta_i = \gamma_i / K_W$, we have

$$0 = \nabla^2_{\boldsymbol{Y}} \eta_i \qquad \text{for } \boldsymbol{Y} \in \Omega_H, \tag{3.4.7a}$$

$$0 = \frac{1}{{K_W}^2} \frac{d_{WO}}{d_{WH}} \nabla^2_{\boldsymbol{Y}} \Gamma_i \qquad \text{for } \boldsymbol{Y} \in \Omega_O, \tag{3.4.7b}$$

with periodicity of η_i on the boundary $\partial\Omega$ and with continuity of concentration and a discontinuous flux condition on the boundary $\boldsymbol{Y} \in \partial\Omega_O$,

$$\eta_i = \Gamma_i \qquad \text{for } \boldsymbol{Y} \in \partial\Omega_O, \tag{3.4.8a}$$

$$\mathbf{n}_{\boldsymbol{Y}} \cdot \left(\nabla_{\boldsymbol{Y}} \eta_i - \frac{1}{{K_W}^2} \frac{d_{WO}}{d_{WH}} \nabla_{\boldsymbol{Y}} \Gamma_i \right) = \frac{1}{{K_W}^2} \left(K_W - \frac{d_{WO}}{d_{WH}} \right) \mathbf{n}_{\boldsymbol{Y}} \cdot \boldsymbol{e}_i \quad \text{for } \boldsymbol{Y} \in \partial\Omega_O. \tag{3.4.8b}$$

Equations (3.4.7) and (3.4.8) have the same form as Equations (3.4.5) and (3.4.6), with the equivalent parameter groupings: $1/K_W$, $d_{WO}/d_{WH}{K_W}^2$, and R.

We may also reduce the complexity of the system by exploiting the symmetry of the problem, and considering an eighth of the domain, the octant $\boldsymbol{Y} \in [0, 0.5]^3$ (see Figure 3.4(b)). Due to the symmetry of the problem, we have that $\bar{\boldsymbol{d}}_C$ is isotropic, *i.e.* $\bar{\boldsymbol{d}}_C = \bar{d}_C\boldsymbol{I}$, and, therefore, we only need to solve for one of the components of $\boldsymbol{\eta}$. Without loss of generality, we consider the problem for the η_1 component of the cell problem. On the boundaries which are part of $\partial\Omega$ (*i.e.* faces 1, 2, and 3 in Figure 3.4(b)), we impose $\eta_1 = 0$ to ensure periodicity. On face 4, we also impose $\eta_1 = 0$ due to the anti-symmetry of the problem in Y_1. On faces 5 and 6, we impose $\partial\eta_1/\partial n = 0$ to enforce reflectional symmetry in Y_2 and Y_3, respectively.

A numerical solution to the cell problem defined by Equations (3.4.5) and (3.4.6) in $\boldsymbol{Y} \in [0, 0.5]^3$ is computed in COMSOL Multiphysics® and shown in Figure 3.4(c).

We solve the cell problem for a range of $1/K_C$, $d_{CO}/{K_C}^2$, and R. We compute the effective diffusivity for each set of parameters $\{R, d_{CO}, K_C\}$ considered, where $\bar{d}_C$ is defined as follows

$$\bar{d}_C = 8\left(K_C\int_{\Omega_H} 1 - K_C\frac{\partial\eta_1}{\partial Y_1}\,\mathrm{d}\boldsymbol{Y} + d_{CO}\int_{\Omega_O} 1 - \frac{\partial\Psi_1}{\partial Y_1}\,\mathrm{d}\boldsymbol{Y}\right), \tag{3.4.9}$$

where the integrals are over the domains Ω_H and Ω_O in the octant $\boldsymbol{Y} \in [0, 0.5]^3$. Varying organoid radius R changes the domains Ω_O and Ω_H over which we solve the cell problem.

We can then interpolate this data to create an interpolative 'look-up' table for the effective diffusivity as a function of organoid radius, R, ratio of diffusivities, d_{CO}, and partition coefficient, K_C, using *e.g.* `interp3` in MATLAB. In Section 3.4.3 we only consider $K_C = K_W = 1$. Therefore, we solve the cell problem Equations (3.4.5) and (3.4.6) for a range of R and d_{CO} and generate data for the corresponding values of $\bar{d}_C$. We use the curve fitting toolbox in MATLAB to fit a polynomial (`poly55`) surface to $\bar{d}_C(R, d_{CO})$. To solve our metabolite transport model (Equation (3.4.1)) numerically in COMSOL Multiphysics®, we define the effective diffusivity $\bar{d}_C = \bar{d}_C(R, d_{CO})$ as a two-dimensional polynomial function of degree 5,

$$\bar{d}_C(R, d_{CO}) = \sum_{\substack{i\leq 5, j\leq 5\\ i+j\leq 5}} \alpha_{ij}(R)^i(d_{CO})^j, \tag{3.4.10}$$

with coefficients α_{ij} obtained from the `'poly55'` surface fitting in MATLAB.

Since we only need to solve the cell problem once for a finite number of parameter sets, we can do this *a priori*, significantly reducing the complexity of numerically solving the homogenised metabolite transport problem. We have therefore de-coupled the dependence of the cell problem (and, hence, effective diffusivity) on the transport model and, as a result, do not have to solve the cell problem and transport model simultaneously.

In Figure 3.5(**A**,**B**) we plot the effective diffusivity, $\bar{d}_C = \bar{d}_C(R, d_{CO}, K_C)$, as an (interpolated) function of organoid radius R and d_{CO}, the ratio of the glucose diffusivity in the organoid to that in the hydrogel, with $K_C = 1$. We find that the effect of varying d_{CO} becomes more prominent for larger R, as we expect from the form of Equation (3.4.9). In Figure 3.5**C**, we plot the effective diffusivities $\bar{d}_C$ as a function of organoid radius R (from a 'look-up' table) for the parameters given in Table 3.2, that is $K_C = K_W = 1$ and $d_{CO} = 1/6$ and $d_{WO}/d_{WH} = 0.175$. The first is the effective diffusivity of glucose within the organoid-hydrogel region, $\bar{d}_C = \bar{d}_C(R, d_{CO} = 1/6, K_C = 1)$, and the second is proportional to the effective diffusivity of lactate within the organoid-hydrogel region, $\bar{d}_W = d_{WH}\bar{d}_C(R, d_{WO}/d_{WH} = 0.175, K_W = 1)$. We compare these to the case where $d_{CO} = 1$ and $K_C = 1$, where we can explicitly see from Equation (3.3.47) that the effective diffusivity would relax to $\bar{d}_C = d_{CO} = 1$.

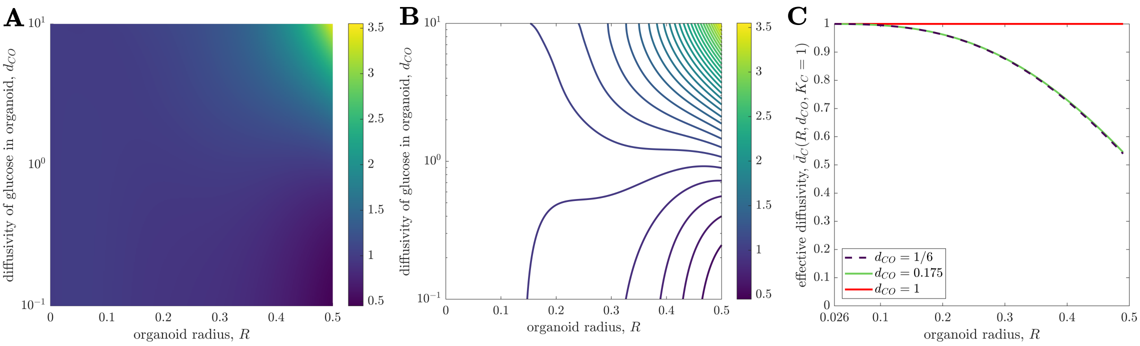

Figure 3.5: Surface (**A**) and contour plots (**B**) of the effective diffusivity $\bar{d}_C$ for $K_C = 1$. (**C**) Plot of the effective diffusivity $\bar{d}_C$ as a function of organoid radius R (where the radius of a single cell $R_c = 0.026$) for the values of d_{CO} and $K_C = 1$ used in Table 3.2, where $\bar{d}_C = \bar{d}_C(R, d_{CO}, K_C = 1)$ defined by Equation (3.4.9).

3.4.3 Canonical problems

In this Section, we investigate the behaviour of the homogenised metabolite transport and organoid growth models introduced in Sections 3.2.1.2 and 3.3, in particular for dense organoids undergoing volumetric growth (Equation (3.4.1)). Since Cellesce have determined empirically that flow of culture media is necessary for their bioreactor protocol, we interrogate our mathematical model to understand this finding. We consider canonical toy problems which replicate culture conditions that might arise within the CXP1 bioreactor. This mathematical modelling approach can help inform different hydrogel and flow geometries that Cellesce could use in future bioreactor protocols.

We consider a cube of hydrogel consisting of the same volume and seeding density used in the CXP1 bioreactor. We take the 'typical lengthscale', on which we non-dimensionalise the macroscale spatial variable, as the side length of the hydrogel cube, so that we are solving the system on the unit cube. We mimic the CXP1 bioreactor set-up of having no-flux conditions on all boundaries except at a single face, which we term the 'hydrogel-media interface'. Without any loss of generality, this is on the 'top' surface (Figure 3.6), defined by $Z = 1$.

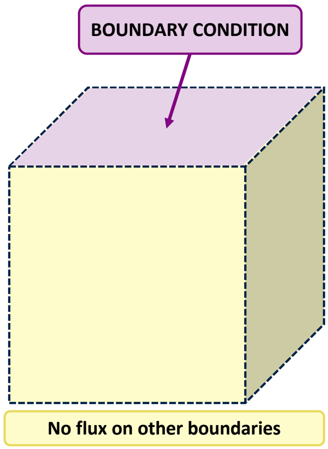

Figure 3.6: Boundary conditions for the 3D effective macroscale mass transport model.

The boundary conditions we impose at the 'hydrogel-media' interface depend on the bioreactor operating conditions. We consider the following two cases of initial and boundary conditions at the 'hydrogel-media' interface:

(1) **Static culture**

In this case, we assume that, initially, a fixed amount of glucose is added to the bioreactor and that it contains no lactate. We assume further that no metabolite enters or leaves the domain, modelled via a no-flux boundary condition. We write these initial and boundary conditions mathematically as:

$$\bar{C} = 1,\ \bar{W} = 0 \ \text{ at } T = 0, \tag{3.4.11a}$$

$$\frac{\partial \bar{C}}{\partial n} = 0 = \frac{\partial \bar{W}}{\partial n} \text{ on the 'hydrogel-media' interface, } Z = 1. \tag{3.4.11b}$$

(2) **Proxy flow**

In this case, we assume that, initially, a fixed amount of glucose is added to the bioreactor and that it contains no lactate. We approximate the effect of a flow of culture media in the X-direction along the 'hydrogel-media' interface, $Z = 1$, by imposing the following *proxy* flow boundary condition:

$$\bar{C} = 1,\ \bar{W} = 0 \quad \text{at } T = 0, \tag{3.4.12a}$$

$$\bar{C} + \frac{X^{\frac{1}{3}}}{\alpha_C}\bar{d}_C(\boldsymbol{X}, T)\frac{\partial \bar{C}}{\partial Z} = 1 \quad \text{on } Z = 1, \tag{3.4.12b}$$

$$\bar{W} + \frac{X^{\frac{1}{3}}}{\alpha_W}\bar{d}_W(\boldsymbol{X}, T)\frac{\partial \bar{W}}{\partial Z} = 0 \quad \text{on } Z = 1, \tag{3.4.12c}$$

where we have used that $\partial/\partial n = \partial/\partial Z$. Equations (3.4.12b) and (3.4.12c) are effective Robin boundary conditions, where α_C and α_W are effective Péclet numbers, describing the local ratio of advective to diffusive transport. Increasing α_C and α_W corresponds to higher flow rates of culture media. A derivation of these *proxy* flow boundary conditions is given in Appendix C. The factor of $X^{\frac{1}{3}}$ arises because the analysis exploits the presence of a mass transfer boundary layer.

As shown in Appendix C, the relationship between α_C and α_W is given by

$$\alpha_W = \left(\frac{D_{CM}}{D_{WM}}\right)^{\frac{2}{3}} \alpha_C \approx 0.57\alpha_C, \tag{3.4.13}$$

where $D_{CM} = 6 \times 10^{-10}\mathrm{m}^2\,\mathrm{s}^{-1}$ [83] and $D_{WM} = 1.4 \times 10^{-9}\mathrm{m}^2\,\mathrm{s}^{-1}$ [77] are the diffusivities of glucose and lactate, respectively, in the culture media.

We now present numerical solutions to the mass transport model for dense organoids undergoing volumetric growth, Equation (3.3.45), subject to static, Equation (3.4.11), and proxy flow, Equation (3.4.12), culture conditions. We consider three different flows, characterised by $\alpha_C \in \{0.1, 1, 10\}$. Since the organoids are seeded as single cells within the hydrogel, the initial condition for organoid radius R is

$$R(\boldsymbol{X}, T = 0) = R_c. \tag{3.4.14}$$

We solve the system in 3D, partly as proof of concept and partly to gain experience of solving 3D reaction-diffusion equations in COMSOL Multiphysics®. However, we note that there is no spatial variation in the macroscale Y-direction (width) due to the symmetry of the governing equations and the independence of the boundary conditions on Y. We obtain similar results for shell organoids undergoing surface growth and, as such, do not present these results here. Unless otherwise stated, the parameter values used are: $L = 1.9 \times 10^{-2}$ m, $d_{CO} = 1/6$, $d_{WH} = 2$, $d_{WO} = 0.35$, $\sigma_V = 5200$, $\rho = 15$, $K_C = K_W = 1$, $\phi = 0.74$, $\delta = 10^{-2}$, $f = 0.25$, $\nu_W = 0.5$.

In Figure 3.7, we present the three-dimensional glucose and lactate concentrations and organoid radius at the end of the experiment (7 days) under proxy flow culture conditions for $\alpha_C = 10$. Qualitatively similar results are observed for $\alpha_C = \{0.1, 1\}$, and therefore we do not present them here. Under static culture conditions, the metabolite concentrations and organoid radius are spatially homogeneous (results not shown). This is expected since the boundary and initial conditions are uniform and the governing equations do not induce spatial variation. In the static culture case, all the glucose is consumed by the end of the experiment and, in fact, 90% of the glucose is consumed by 4.7 days (Figure 3.11). The organoid radius increases, by a factor of 2.7, from $R_c = 0.026$ to $R = 0.07$. Incorporating flow induces variation in X and Z, as seen in Figure 3.7. The Z-variation is due to glucose being supplied at only one surface, $Z = 1$, and the X-variation is due to the boundary condition on $Z = 1$ having X-dependence (due to flow in the X-direction inducing a mass transfer boundary layer). Faster flows increase the glucose concentration near the hydrogel-media interface (see Figure 3.7**A**). This leads to larger organoid radii near the hydrogel-media interface (Figure 3.7**C**). Since uptake dominates vertical diffusion, increasing the flow rate increases the spatial variation in glucose concentration and organoid radii. Since there is minimal glucose transport in the Z-direction (depth), the organoids within the bulk of the hydrogel (away from $Z = 1$) only consume glucose which is initially in the hydrogel. Consequently, even with flow, organoids away from the hydrogel-media interface only attain size similar to those for static culture conditions. This suggests that this protocol and hydrogel geometry is not optimal to produce organoids with little size variation. However, since the hydrogel geometry in the CXP1 bioreactor is long and thin, the slow diffusive transport is less of an issue in the CXP1 bioreactor than in this canonical cuboid domain case, as shown in Chapter 2.

The organoid radius R, Figure 3.7**C**, behaves in a similar manner to $\bar{C}$; regions with higher glucose concentrations have larger organoid radii. This suggests that the glucose concentration can be used as a proxy for predicting organoid size, meaning that real-time monitoring of metabolite concentrations in the bioreactor culture media could be used to predict organoid size.

We plot the lactate distribution at the end of the experiment (7 days) in Figure 3.8, noting there is no variation of $\bar{C}$, $\bar{W}$, or R in Y due to the symmetry of the governing equations and independence of the initial data on Y. We plot the lactate concentrations along the bottom ($Z = 0$) and top ($Z = 1$) of the domain at 7 days in

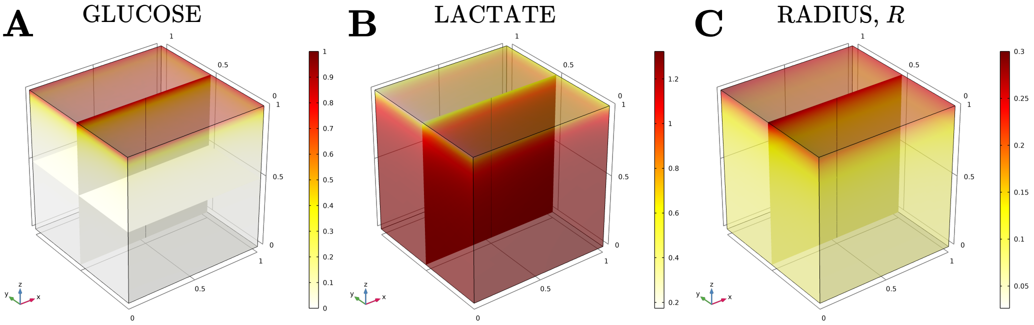

Figure 3.7: Glucose, $\bar{C}$, and lactate, $\bar{W}$, concentration and organoids radius, R, profiles within a cube of hydrogel at the end of an experiment (7 days) for proxy flow culture conditions with $\alpha_C = 10$. Parameter values used are: $L = 1.9 \times 10^{-2}$m, $d_{CO} = 1/6$, $d_{WH} = 2$, $d_{WO} = 0.35$, $R_c = 0.026$, $\sigma_V = 5200$, $\rho = 15$, $K_C = K_W = 1$, $\phi = 0.74$, $\delta = 10^{-2}$, $f = 0.25$, $\nu_W = 0.5$.

the left and right plots of Figure 3.8, respectively, and plot the 2D lactate concentration profile in the X-Z plane at 7 days for the proxy flow boundary condition with $\alpha_C = 10$ in the central plot. The lactate concentration under static culture conditions is spatially uniform (results not shown). Since, for static culture, the initial glucose concentration within the homogenised hydrogel is $\bar{C} = 1$ everywhere and all glucose has been consumed, the reaction stoichiometry of one glucose molecule producing two lactate molecules means that the lactate concentration is $\bar{W} = 2$ everywhere. As well as its role in enhancing nutrient delivery, the flow of culture media facilitates waste removal. For weak flows, *e.g.* $\alpha_C = 0.1$, lactate removal is unable to compensate for the increased rate of lactate production, which occurs due to the increased presence of glucose and associated glucose consumption. This is seen in Figure 3.8(**A**,**C**), where lactate concentrations are higher than for the static culture case, except in a small region near the inlet at the hydrogel-media interface. For stronger flows (increasing α_C by an order of magnitude from 0.1 to 1), the lactate concentration is lower than for the static culture case. Increasing the flow further ($\alpha_C = 10$), leads to a significant reduction in lactate concentrations, reducing the average lactate concentration by 37% compared to the static culture case. The larger the flow rate, the more prominent the spatial variation in both the X- and Z-directions. Understanding that increasing flow rates (above a certain minimum flow rate) decreases lactate concentrations is important when culturing cells that are highly sensitive to the toxicity of lactate. In all of the flow cases, the largest horizontal variation of lactate is at the hydrogel-media interface and the largest vertical variation of lactate is near the 'media inlet', at $X = 0$. This is expected, since for small X, Equation (3.4.12) is approximately $\bar{C} = 1$, $\bar{W} = 0$, meaning glucose and lactate enter and leave the hydrogel, respectively, at faster rates for small X. This is where the boundary layer at the hydrogel-media interface is the thinnest.

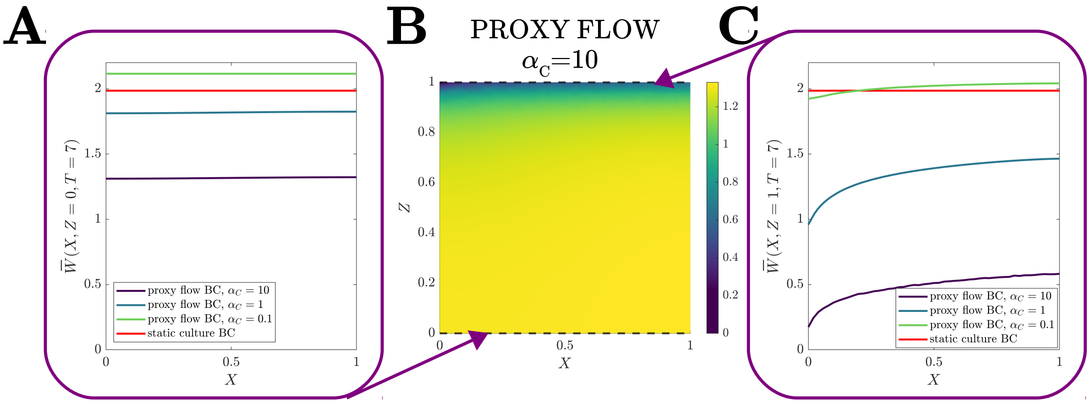

Figure 3.8: (**A**, **C**) Lactate concentration profiles at $Z = 0$ (**A**) and $Z = 1$ (**C**) at end of experiment (7 days) for different culture conditions. (**B**) Two-dimensional cross-section of lactate concentration for proxy flow boundary conditions with $\alpha_C = 10$ at end of the experiment (7 days).

We investigate the time evolution of the glucose and lactate concentrations in Figure 3.9. The mean lactate concentration is monotonically increasing in time. We see that the lactate concentration for the static culture case saturates at $\bar{W} = 2$, as expected. The slower flow rate (corresponding to $\alpha_C = 0.1$) has a similar average lactate concentration to the static culture case during the experiment, and is larger than the static case after day 5. For flow rates corresponding to $\alpha_C = 1$ and $\alpha_C = 10$, lactate concentrations are lower than for the static culture case and decrease as the flow rate increases. This is because the fresh culture media arriving at $X = 0$ contains no lactate, so any lactate within the media layer must have diffused from the hydrogel. For higher flow rates, a larger volume of culture media is exposed to the hydrogel, so there is a larger concentration gradient between the media and the hydrogel, and thus more lactate diffuses into the culture media, and is then advected away.

The mean glucose concentration is monotonically decreasing in time. Flow increases the glucose concentration compared to the static culture case. However, the mean glucose concentration is not significantly different for the flow cases $\alpha_C = 1$ and $\alpha_C = 10$. Although we might expect the mean glucose concentration to be higher for stronger flows, higher rates of glucose influx facilitate increased rates of glucose consumption. This effect, coupled with reduced lactate concentrations, means that

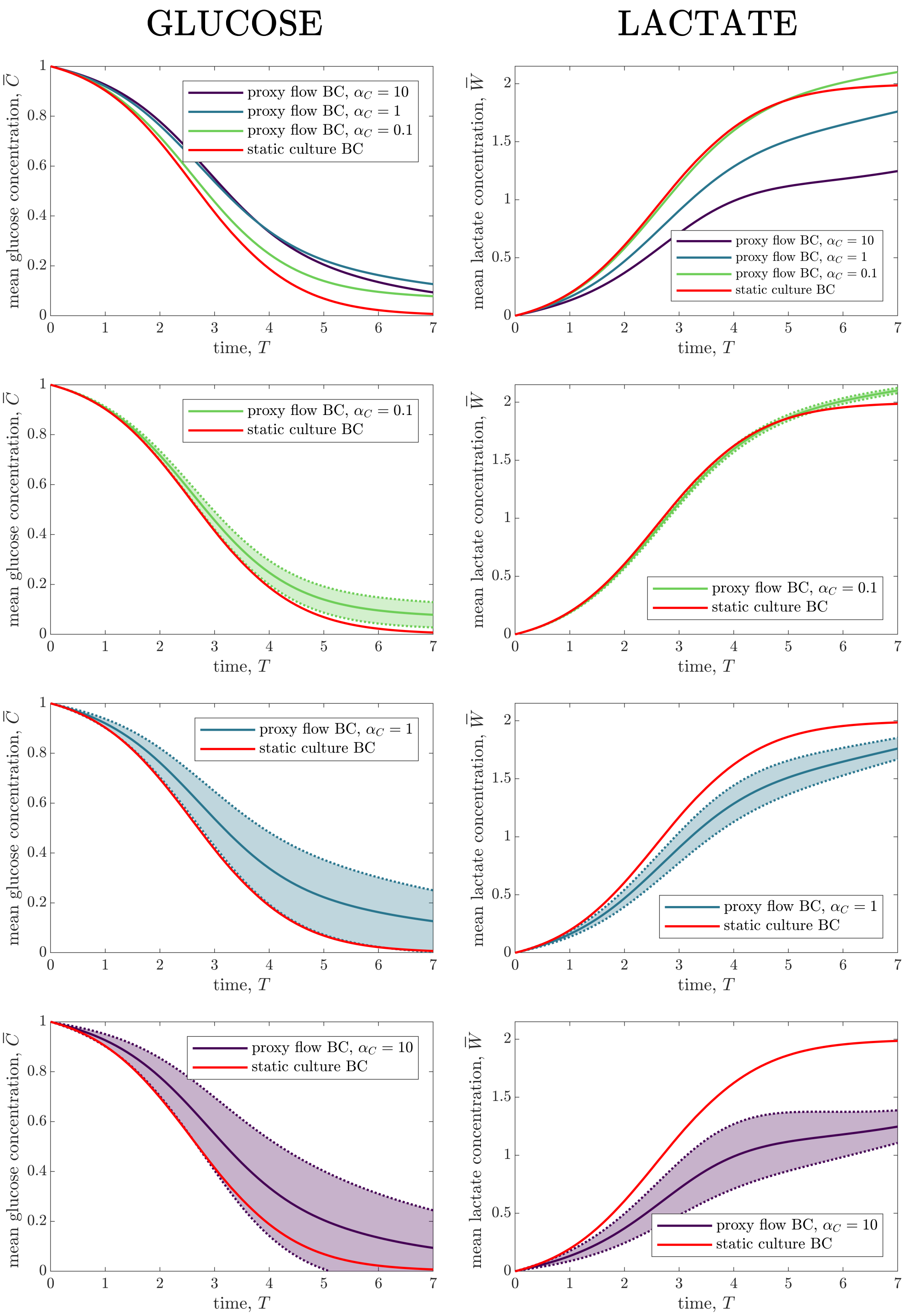

Figure 3.9: Series of plots of the mean and standard deviation of glucose and lactate concentrations, $\bar{C}$ and $\bar{W}$, under different culture conditions evolving in time. (We have rescaled in time such that $T = 1$ represents 1 day.)

glucose concentrations for $\alpha_C = 1$ and $\alpha_C = 10$ are similar. We also see in Figure 3.9 that increasing the flow increases the spatial variation in metabolite concentrations.

We plot the mean and standard deviation of the organoid radii, $R(\boldsymbol{X}, T)$, over 7 days for the four different culture conditions in Figure 3.10. Increasing the flow rate increases the mean organoid radius. Under static culture conditions, R increases by a factor of 2.7 during the experiment. For flows with $\alpha_C = 0.1$, $\alpha_C = 1$, and $\alpha_C = 10$, the increases are 3 fold, 3.5 fold, and 4 fold, respectively. It is interesting to note that there is an initial transient period of approximately two days, during which the mean organoid radius is the same under all culture conditions considered. During this time period, the organoids consume glucose initially contained within the hydrogel; glucose supplied by the culture media has not penetrated sufficiently far into the hydrogel to have a significant effect on glucose levels, and hence glucose consumption and organoid growth. For the static culture case, there is no spatial variation across the hydrogel, and, therefore, the standard deviation in R is zero. By contrast, increasing the flow rate increases the standard deviation in organoid radius. Similar results have been observed by Cellesce. We find that increasing flow increases both the mean and variation of R. We conclude that there is an optimal flow rate, which balances maximising the organoid radius R, by improving glucose delivery and lactate removal (increasing flow), with minimising the variation in R (decreasing flow).

In Figure 3.11, we plot the cumulative glucose consumption, which is defined by

$$K(T) = \int_0^T \int_{\Omega_{HO}} \frac{4}{3}\pi R^3 \sigma_V S(\bar{C}, \bar{W}) \, \mathrm{d}\boldsymbol{X} \mathrm{d}T, \tag{3.4.15}$$

where Ω_{HO} is the homogenised organoid-hydrogel domain. The glucose consumption, $K(T)$, is increasing in flow strength, α_C. This is expected, given that organoid growth is proportional to glucose consumption and the mean organoid radius increases with increasing flow rate (Figure 3.10).

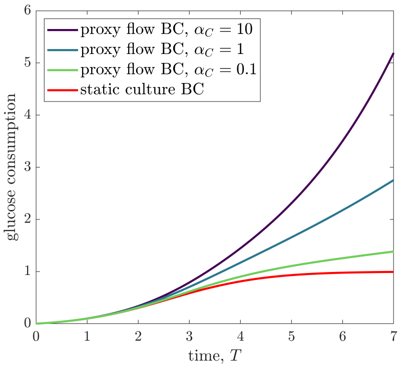

Figure 3.11: Glucose consumption, $K(T)$, under different culture conditions evolving in time. (Rescaled so $T = 1$ is 1 day.)

As a brief case study and illustration of how we can use our results, we seek to understand the 'best' flow regime of the ones considered ($\alpha_C \in \{0.1, 1, 10\}$). We introduce an objective function, F, which we wish to maximise and we choose F such that increasing the mean organoid radius

R increases F, and increasing the standard deviation of R penalises the objective function. A simple, dimensionless function that satisfies these properties is:

$$F(R) = \frac{\text{mean}(R) - \text{mean}(R_{\text{static}})}{\text{mean}(R_{\text{static}})} - \varphi \frac{\sigma(R)}{\text{mean}(R_{\text{static}})} \tag{3.4.16}$$

where mean(R) and $\sigma(R)$ represents the mean average and standard deviation of $R(\boldsymbol{X}, T)$, respectively, R_{static} denotes the organoid radius for the static culture condition case, and φ is a tunable constant, representing the relevant importance of maximising the mean of R to minimising standard deviation of R. We consider the value of this objective function $F(R;\varphi)$ for the different culture cases for two different values of φ ($\varphi \in \{0.5, 0.75\}$) over time in Figure 3.12. For the case $\varphi = 0.5$, the objective function F is monotonically increasing in time for all flow rates. The flow regime $\alpha_C = 10$ corresponds to the largest F for all time — this suggests that $\alpha_C = 10$ is the best flow regime out of the cases considered. For the case $\varphi = 0.75$, where increasing standard deviations of R are penalised more than for the case $\varphi = 0.5$, F is no longer monotonically increasing for the $\alpha_C = 10$ case. At time ~ 5.5 days, the curves for F for cases $\alpha_C = 10$ and $\alpha_C = 1$ intersect. This tells us that for experiments of duration less than 5.5 days, we should use the flow regime corresponding to $\alpha_C = 10$, but for experiments of duration greater than 5.5 days we should use the flow regime corresponding to $\alpha_C = 1$. It may be better to use the flow rate corresponding to $\alpha_C = 10$ and stop at $T \approx 4.5$ unless running the experiment for $\alpha_C = 1$ for $T \geq 6$. Therefore, depending on the stopping time, the optimal flow regime will be different. Perhaps more importantly, this suggests that the implications of our results will be sensitive to the specific choice of φ, and our objective function more generally. We note that the behaviour of $R(\boldsymbol{X}, T)$ is cell line dependent, and therefore the optimal flow rate for maximising $F(R)$ would have to be determined for each individual cell line.

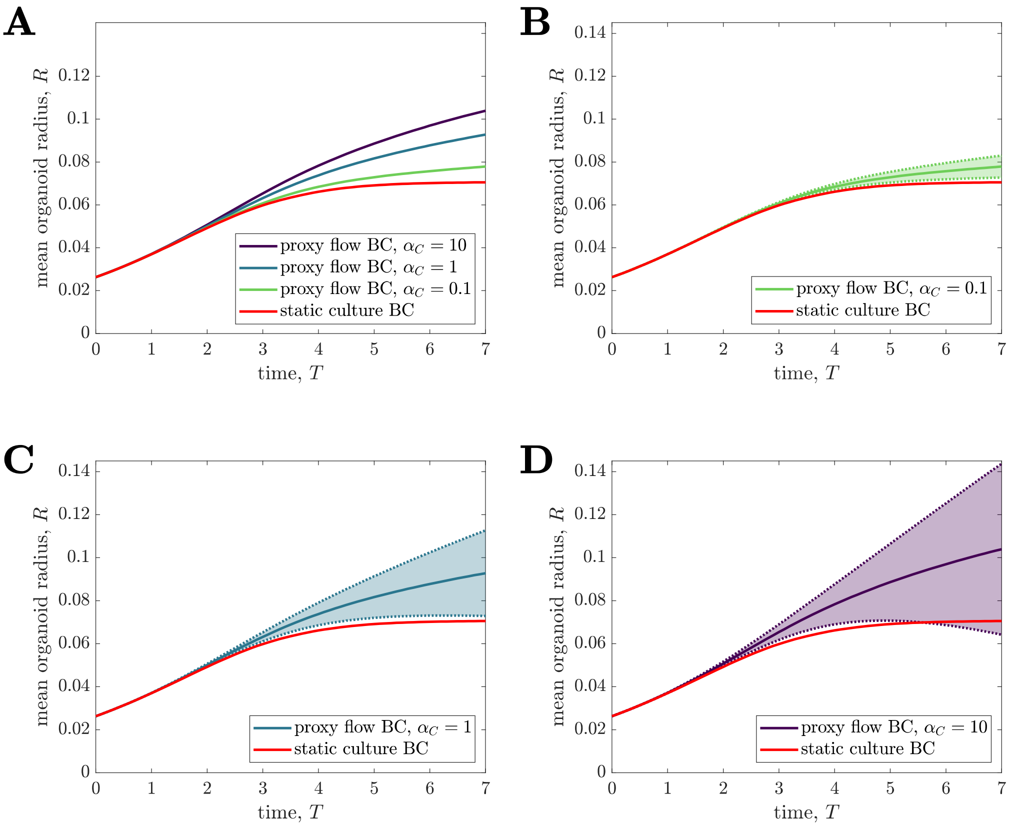

Figure 3.10: Series of plots of the mean and standard deviation of organoid radius, R, under different culture conditions evolving in time. (We have rescaled in time such that $T = 1$ represents 1 day.)

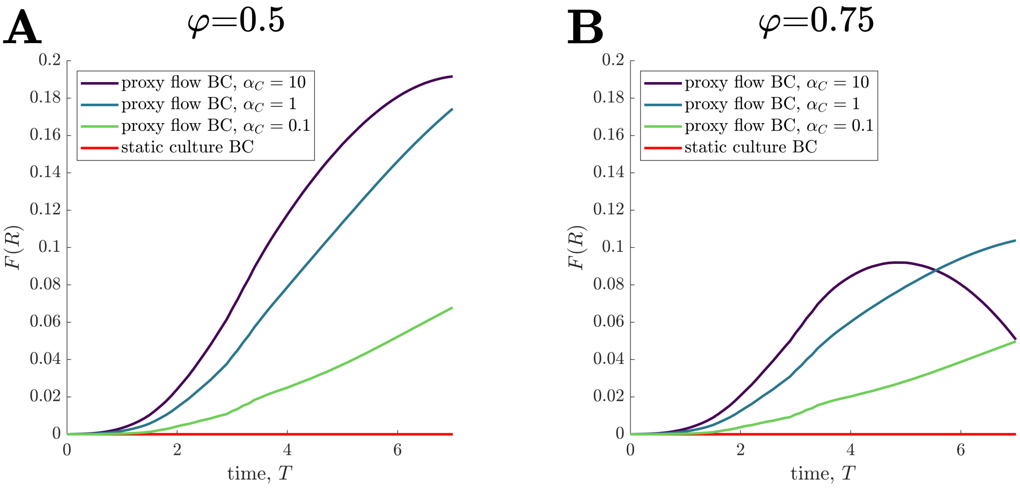

Figure 3.12: Objective function, F, evolving in time for different culture conditions. (We have rescaled in time such that $T = 1$ represents 1 day.)

3.5 Discussion

In this Chapter, we have presented a 3D model for glucose and lactate transport and organoid growth within a hydrogel. We modelled the organoids as time-varying spherical regions, in which metabolite diffuses, glucose is consumed and lactate is produced. Within the hydrogel, there is diffusive transport of metabolite. The full problem within the full hydrogel and organoid regions is computationally challenging, due to the multiply connected three-dimensional domain involving millions of moving boundaries between organoid and hydrogel regions. The separation of scales within the problem motivates an asymptotic (multiscale) approach to systematically derive the *effective macroscale behaviour* across the organoid-hydrogel region. We used mathematical homogenisation (using the method of multiple scales) to derive effective equations that govern the macroscale mass transport, determining how the microscale behaviour of the organoids influences the macroscale 'organoid-hydrogel' region. The result is a coupled reaction-diffusion system for metabolite transport. We determined that the metabolite concentrations are independent of the microscale at leading order, meaning that the concentrations are spatially uniform within each organoid and, therefore, there are no mass transport aspects of organoid growth. We obtained expressions for the effective diffusivities of glucose and lactate and their effective rates of consumption/production. We investigated how the organoid structure affects the effective macroscale system, comparing the behaviour of dense organoids undergoing volumetric growth to shell organoids undergoing surface growth. We found that the strength of the reaction term (uptake/production) is dependent on the organoid volume for dense organoids, whereas for shell organoids, it is dependent on the organoid surface area, as might be expected on physical grounds. However, we note that different distinguished limits and different effective results could be obtained for, *e.g.* sparse organoids with high uptake [16, 18].

We introduced constitutive models for glucose consumption and organoid growth. We assumed that the rate of cell proliferation is proportional to the rate of glucose consumption. We incorporated the inhibitory effect of lactate on cell growth by employing a functional form of glucose consumption which is inversely proportional to the lactate concentration.

We discussed an approach to the numerical solution of the 3D 'cell problem', a system from the first-order correction mass transport problem on which the effective macroscale diffusivities depend. We reformulated the problem as Laplace's equation in 3D with continuity of concentration and a flux discontinuity at the organoid-hydrogel interface. We are able to solve the cell problem *a priori* and use the results to inform numerical solution of the coupled homogenised metabolite transport and organoid growth models. We solved the cell problems for a range of organoid radii, ratios of diffusivities in organoid and hydrogel, and partition coefficients, and computed the effective diffusivities for each parameter regime. We then interpolated this data to obtain the effective diffusivities of glucose and lactate as functions of R, d_{ij} and K_i,

$$\bar{d}_C = \bar{d}_C(R, d_{CO}, K_C) \quad \text{and} \quad \bar{d}_W = \bar{d}_W\left(R, \frac{d_{WO}}{d_{WH}}, K_W\right), \tag{3.5.1}$$

which we incorporated into our numerical solver for $\bar{C}$ and $\bar{W}$.

We then introduced different toy problems on a cube of hydrogel to represent different culture conditions: *static culture* and *proxy flow culture*, which includes the influence of a *flow* of media along one surface of the hydrogel domain. We presented numerical results for the solutions of $\bar{C}$, $\bar{W}$, and R for static culture and proxy flow for three different flow strengths. The results for static culture indicate that this method is insufficient for expanding organoids to the required size within CXP1. We showed that flow generally enhances nutrient delivery. For culture conditions with flow, there is an increased rate of lactate production due to the higher levels of glucose within the hydrogel. For the slowest flow case considered, $\alpha_C = 0.1$, the rate of waste removal is very low and lactate builds up within the domain. For sufficiently strong flows ($\alpha_C = 1$, $\alpha_C = 10$), the flow facilitates lactate removal and the lactate concentrations are lower than for the static culture case, in spite of the larger glucose consumption/lactate production. Hence nutrient delivery and waste removal is promoted by flow.

However, we also found that the variation in metabolite concentrations and organoid radius increases with increasing flow rate. Since Cellesce wish to minimise the variation in organoid size within each expansion of CXP1, this suggests that Cellesce should minimise the flow to reduce variation. This generates two opposing requirements and indicates that there is an optimal flow rate for the system that depends on the relative priorities of Cellesce.

Increasing flow increases the glucose concentration, reduces the lactate levels, and increases the mean organoid radius within the hydrogel. Decreasing the flow rate decreases the variation in organoid radius. The optimal flow rate would balance the requirements of maximising organoid size and minimising variation in organoid size. Since the organoid size depends on the cell line characteristics, such as sensitivity to lactate, glucose requirements for proliferation, and organoid structure, this optimal flow rate is unique to each cell line, and must be found for each hydrogel geometry and cell line. Since we have derived homogenised governing equations for metabolite transport within the hydrogel, we can see how the microscale organoid behaviour directly influences the macroscale behaviour and finding this optimal flow rate is now feasible. We conducted a small case study, comparing the static culture case to the three different flow rates considered. We considered a simple objective function, which promoted increase in organoid size and penalised increase in standard deviation of organoid radius. We found that, for the given cell line and hydrogel geometry, the optimal flow rate depended on the relative importance of each metric and the run-time of the experiment.

There are several avenues for future work, and these can be split into two groups: (1) developing the model to make it more biologically representative; and (2) incorporating this homogenised hydrogel model to a 3D model for bioreactors. In experiments, Cellesce have found that there is an initial time period (2 days) during which the organoids proliferate slower than normally expected, while they adapt to the bioreactor environment following the bioreactor set-up protocol. We could include this effect in our constitutive model for proliferation rate:

$$p(c_O, w_O) = \begin{cases} p_{\text{initial}} & \text{for } 0 < t < t_p, \quad (3.5.2) \\ f\dfrac{g_b}{\phi} s(c_O, w_O) & \text{for } t_p < t < t_{\text{end}}, \quad (3.5.3) \end{cases}$$

where t_p is the length of the transient period and t_{end} is the length of the experiment. Cellesce also want to culture non-cancerous cell lines, which are notoriously sensitive to lactate, with high levels of lactate inducing cell necrosis. This could be incorporated by a death term in the organoid growth model,

$$\frac{\mathrm{d}v}{\mathrm{d}t} = \underbrace{p(c_O, w_O)v}_{\text{cell proliferation}} - \underbrace{a(w_O)v}_{\text{cell death}}, \tag{3.5.4}$$

where cell death occurs if lactate concentrations increase above a threshold value, w_{tol}, via, *e.g.*

$$a(w_O) = a_n(w_O - w_{\text{tol}})H(w_O - w_{\text{tol}}), \tag{3.5.5}$$

where a_n is a constant and H is the Heaviside function, and we have assumed that death rate increases linearly with w_O if $w_O > w_{\text{tol}}$.

Future work could consider how to more realistically capture the behaviour of cells within an individual organoid, since cells are not necessarily always spherical, nor rigid, but can deform. This would require further input from Cellesce, regarding the relevant biology and the typical behaviour of cells they observe during culture.

Since the homogenisation approach is independent of hydrogel geometry, we could use our effective macroscale model to consider different hydrogel geometries, *e.g.* spheroids. This will give initial insight into the metabolite transport and inform future bioreactor design.

The area of future work we focus on in the next chapter of this thesis is coupling the 3D homogenised metabolite transport and organoid growth models to the 3D media flow problem within the CXP1 bioreactor geometry. This will yield a tractable 3D macroscale model for predicting metabolite concentrations and organoid size within the CXP1 bioreactor. We consider the 3D flow problem in Chapter 4 and the 3D metabolite transport problem in Chapter 5. We will use these models to study the relationship between the media flow and the microscale organoid behaviour. This mathematical model could be used to inform the future design of bioreactors, such as investigating the impact of changing positions of media inlet and outlet ports, and different flow protocols to improve organoid viability and uniformity.

Chapter 4

3D media flow problem

We now turn our attention to the layer of culture media within the CXP1 bioreactor (Figure 4.1). We develop a mathematical model for the flow within the 3D media layer. Our main motivation for wanting to understand the flow is that metabolite transport within the culture media is advection-dominated.

As indicated in Figure 4.1, fresh culture media enters the bioreactor through an inlet pipe, at a prescribed volumetric flow rate. Culture media is pumped out of the bioreactor with the same volumetric flow rate, so the total volume of culture media within the bioreactor remains constant. The flow is slow (in a manner to be made precise later), so as to not damage the surface of the hydrogel layer.

Flow within the media layer is modelled by the incompressible Navier-Stokes equations. We show that the culture media flow can be formulated as a two-dimensional problem, with a point source and a point sink. The key control parameter for CXP1 operation is the volumetric flow rate through the inlet pipe and this can be controlled throughout the experiment. Cellesce can also alter where the inlet and outlet pipes are positioned within the domain (these remain fixed during a given experiment). We explore how the fluid velocity depends on the volumetric inlet flow rate and inlet and outlet pipe positions. We also analyse the behaviour of the flow and how it changes as the number and position of inlet and outlet pipes vary. We are then in a position to incorporate this information into the metabolite transport problem, which we explore in Chapter 5.

4.1 Model set-up

We model the culture media as an incompressible viscous fluid with constant viscosity μ and constant density ρ_M. The CXP1 bioreactor is kept at a constant temperature of 37°C and, therefore, we neglect any temperature-dependence of system parameters.

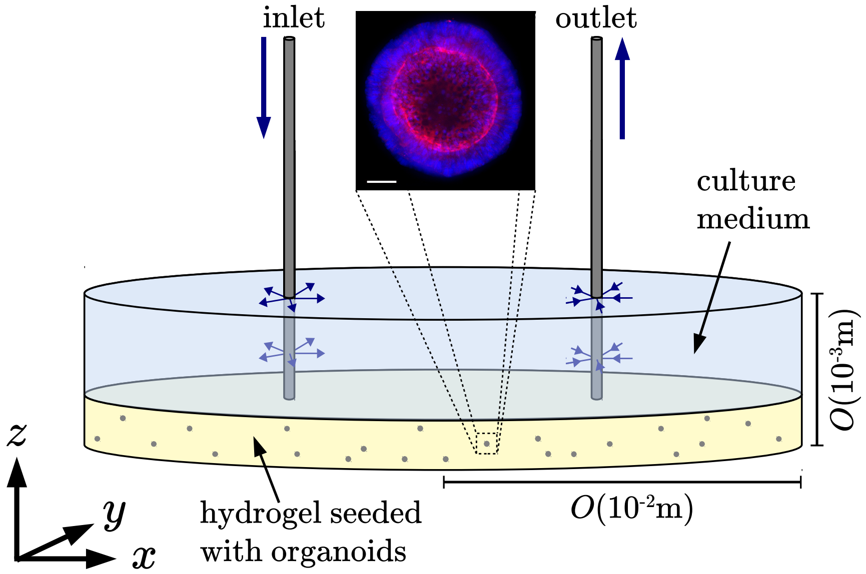

Figure 4.1: Diagram of CXP1 bioreactor set-up. The blue region represents the culture media; the yellow region represents the hydrogel; and the grey regions represent the organoids suspended within the hydrogel. **(Zoomed in region)** Example of colorectal organoid. Organoid stained for nuclear (blue) and cytoskeletal (red) markers for imaging. Scalebar 50µm. Reproduced with permission from Cellesce.

The culture media in the CXP1 bioreactor is on top of the hydrogel layer. A peristaltic pump is used to slowly pump culture media at a prescribed rate into, and out, of the bioreactor through an inlet and an outlet pipe, respectively. The inlet and outlet pipes are held vertically and are partially submerged within the layer of culture media.

The flow domain is modelled as a circular cylinder with diameter L and height $h_M - h_H$ (where h_H is the height of the hydrogel layer and h_M is the total combined height of the hydrogel and media layers). We denote the fluid domain as ω_M. The aspect ratio of the media layer depth to diameter is small, $(h_M - h_H)/L \ll 1$. We denote the bioreactor radius as $b = L/2$ and the inlet/outlet pipe radii as a (a small parameter). We use the Cartesian coordinate system $\boldsymbol{x} = (x, y, z)$, with the cylindrical domain centred about the z-axis, as shown in Figure 4.2. Time is denoted t.

The equations governing incompressible Newtonian viscous flow are

$$\rho_M \left(\frac{\partial \boldsymbol{u}_M}{\partial t} + (\boldsymbol{u}_M \cdot \nabla)\, \boldsymbol{u}_M \right) = -\nabla p + \mu \nabla^2 \boldsymbol{u}_M, \tag{4.1.1a}$$

$$\nabla \cdot \boldsymbol{u}_M = 0, \tag{4.1.1b}$$

where $\boldsymbol{u}_M(\boldsymbol{x}, t)$, $p(\boldsymbol{x}, t)$, ρ_M, and μ are the velocity, pressure, density, and viscosity

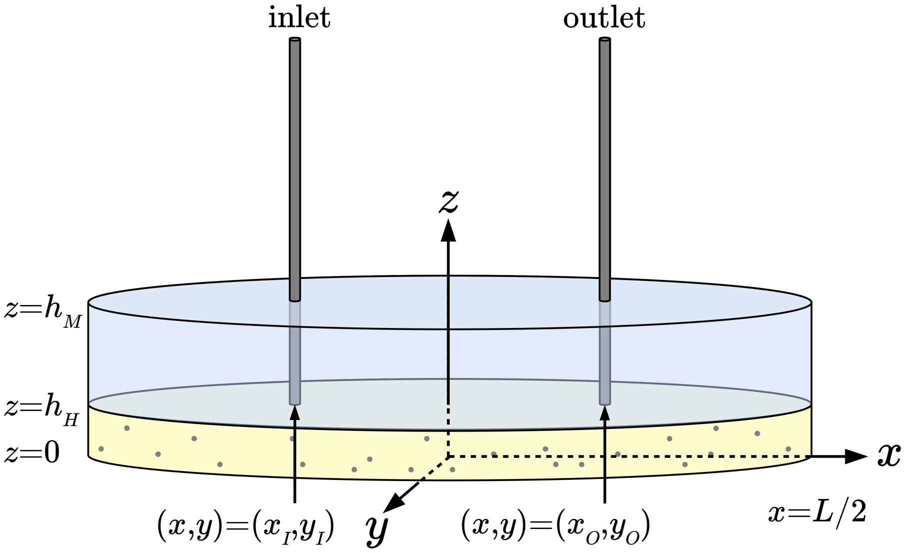

Figure 4.2: Schematic of the three-dimensional domain considered in this Chapter, depicting the axes and relevant lengths of the CXP1 geometry.

of the culture media, respectively. The boundary conditions are: no slip and no flux at the hydrogel-media interface $z = h_H$, and on the bioreactor walls $\partial\omega_{\text{wall}}$, mathematically defined as

$$\boldsymbol{u}_M = \mathbf{0} \quad \text{for } \boldsymbol{x} \in \{\boldsymbol{x} : \boldsymbol{x} \in \omega_M,\ z = h_H\}, \quad \text{and} \quad \boldsymbol{x} \in \partial\omega_{\text{wall}}; \tag{4.1.2}$$

where $\partial\omega_{\text{wall}} := \{(x, y, z) : x^2 + y^2 = b^2,\ z \in [h_H, h_M]\}$. Strictly speaking, there is a free boundary at the top of the media layer, between the culture media and the air. However, in practice, the surface tension is sufficiently large that the interface is flat. Motivated by this, we skip the derivation of a flat interface solution and impose that the air-media interface is flat. We impose no flux (equivalent to a kinematic condition) and no shear stress at the media-air interface, $z = h_M$, given by

$$\boldsymbol{u}_M \cdot \mathbf{e}_z = 0, \tag{4.1.3a}$$

$$\hat{\mathbf{t}} \cdot \boldsymbol{\sigma} \cdot \hat{\mathbf{n}} = 0, \tag{4.1.3b}$$

where $\hat{\mathbf{t}}$ is the unit tangent and $\hat{\mathbf{n}}$ is the (outward-pointing) unit normal to the surface of the culture media. Culture media is pumped into and out of the domain via an inlet pipe centred at (x, y)-position $\boldsymbol{x}_I = (x_I, y_I)$ and outlet pipe centred at (x, y)-position $\boldsymbol{x}_O = (x_O, y_O)$, respectively, both of radius, a, which is small compared to the bioreactor diameter. The media flows into the domain through the inlet pipe with flux q, and therefore we write the conditions at the inlet and outlet as

$$\lim_{z\to\infty}\int_{\omega_{\text{in}}} (-\boldsymbol{u}_M\cdot\mathbf{e}_z)\,\mathrm{d}A = q, \tag{4.1.4a}$$

$$\lim_{z\to\infty}\int_{\omega_{\text{out}}} (-\boldsymbol{u}_M\cdot\mathbf{e}_z)\,\mathrm{d}A = -q, \tag{4.1.4b}$$

where ω_{in} and ω_{out} are the cross-sectional areas of the inlet and outlet pipes, respectively. The parameter values of the media flow model are given in Table 4.1.

Table 4.1: Definitions of dimensional media flow model parameters, together with typical values. Where no citation is given, parameters are taken from the CPX1 set-up.

Parameter	Definition	Typical value
L	Diameter of bioreactor	9×10^{-2} m
h_M	Depth of bioreactor	3×10^{-3} m
h_H	Depth of organoid-hydrogel layer	1×10^{-3} m
b	Typical bioreactor radius	4.5×10^{-2} m
a	Typical inlet/outlet pipe radius	2×10^{-3} m
q_{ref}	Volumetric flow rate of culture media through inlet pipe	1.74×10^{-10} m^3 s^{-1}
$[u_M]$	Typical velocity of culture media in bulk	6.43×10^{-7} m s^{-1}
μ	Viscosity of culture media	1×10^{-3} Pa s [66]
ρ_M	Density of culture media	1×10^{3} kg m^{-3} [66]

We define the ratio between the bioreactor diameter and height as $\epsilon := h_M/L \ll 1$. We non-dimensionalise using standard lubrication scalings, exploiting the slender geometry of the domain:

$$\begin{gathered}(x,y,z) = L(X,Y,\epsilon Z), \quad (u_M,v_M,w_M) = [u_M](U_M,V_M,\epsilon W_M),\\ p = \frac{\mu[u_M]}{\epsilon^2 L}P + p_{\text{atm}}, \quad t = [t]T = \frac{L}{[u_M]}T, \quad \boldsymbol{t} = \frac{\mu[u_M]}{\epsilon^2 L}\hat{\boldsymbol{t}}.\end{gathered} \tag{4.1.5}$$

We denote the dimensionless media flow region as Ω_M. The dimensionless height of the hydrogel layer is $H_H := h_H/\epsilon L$ and we denote the dimensionless radii of the bioreactor and inlet/outlet pipes as B and A, respectively.

The dimensionless governing equations for the media flow are

$$\begin{aligned}
\epsilon^2\mathrm{Re}\left(\frac{\partial U_M}{\partial T}+\left(U_M\frac{\partial}{\partial X}+V_M\frac{\partial}{\partial Y}+W_M\frac{\partial}{\partial Z}\right)U_M\right)&\\
=-\frac{\partial P}{\partial X}+\left(\epsilon^2\left(\frac{\partial^2}{\partial X^2}+\frac{\partial^2}{\partial Y^2}\right)+\frac{\partial^2}{\partial Z^2}\right)U_M,&\qquad(4.1.6\text{a})\\
\epsilon^2\mathrm{Re}\left(\frac{\partial V_M}{\partial T}+\left(U_M\frac{\partial}{\partial X}+V_M\frac{\partial}{\partial Y}+W_M\frac{\partial}{\partial Z}\right)V_M\right)&\\
=-\frac{\partial P}{\partial Y}+\left(\epsilon^2\left(\frac{\partial^2}{\partial X^2}+\frac{\partial^2}{\partial Y^2}\right)+\frac{\partial^2}{\partial Z^2}\right)V_M,&\qquad(4.1.6\text{b})\\
\epsilon^4\mathrm{Re}\left(\frac{\partial W_M}{\partial T}+\left(U_M\frac{\partial}{\partial X}+V_M\frac{\partial}{\partial Y}+W_M\frac{\partial}{\partial Z}\right)W_M\right)&\\
=-\frac{\partial P}{\partial Z}+\left(\epsilon^4\left(\frac{\partial^2}{\partial X^2}+\frac{\partial^2}{\partial Y^2}\right)+\epsilon^2\frac{\partial^2}{\partial Z^2}\right)W_M,&\qquad(4.1.6\text{c})\\
0=\frac{\partial U_M}{\partial X}+\frac{\partial V_M}{\partial Y}+\frac{\partial W_M}{\partial Z},&\qquad(4.1.6\text{d})
\end{aligned}$$

where we define the Reynolds number, $\mathrm{Re}=\rho_M L[u_M]/\mu$, which characterises the ratio of inertial to viscous forces within the culture media. The dimensionless boundary conditions are:

$$\boldsymbol{U}_M=\boldsymbol{0}\quad\text{for } \boldsymbol{X}\in\{\boldsymbol{X}:\boldsymbol{X}\in\Omega_M,\ Z=H_H\}\text{ and }\boldsymbol{X}\in\partial\Omega_{\text{wall}},\qquad(4.1.7)$$

where $\partial\Omega_{\text{wall}}:=\{(X,Y,Z):X^2+Y^2=B^2,Z\in[H_H,1]\}$, with B denoting the dimensionless radius of the CXP1 bioreactor. The kinematic boundary condition and no-stress condition can be written

$$W_M=0\text{ at }Z=1,\qquad(4.1.8\text{a})$$

$$\frac{\partial U_M}{\partial Z}+\epsilon^2\frac{\partial W_M}{\partial X}=0,\quad\frac{\partial V_M}{\partial Z}+\epsilon^2\frac{\partial W_M}{\partial Y}=0\text{ at }Z=1.\qquad(4.1.8\text{b})$$

The dimensionless inlet and outlet pipes $\partial\Omega_{\text{in}}$ and $\partial\Omega_{\text{out}}$ are defined as

$$\begin{aligned}
\partial\Omega_{\text{in}}&:=\left\{(X,Y,Z):(X-X_I)^2+(Y-Y_I)^2=A^2,\ H_H<Z\le 1\right\},\\
\partial\Omega_{\text{out}}&:=\left\{(X,Y,Z):(X-X_O)^2+(Y-Y_O)^2=A^2,\ H_H<Z\le 1\right\}
\end{aligned}\qquad(4.1.9)$$

respectively. We will discuss the appropriate inlet/outlet conditions shortly, after taking appropriate asymptotic limits.

As the reduced Reynolds number is small ($\epsilon^2\mathrm{Re}\ll 1$). We now obtain the systematic asymptotic reduction of the system Equations (4.1.6) to (4.1.8) and (4.1.13), by exploiting the limits $\epsilon\ll 1$ and $\epsilon^2\mathrm{Re}\ll 1$.

Therefore, the leading order behaviour of the media flow model, Equation (4.1.6), (neglecting $\mathcal{O}(\epsilon^2)$ and $\mathcal{O}(\epsilon^2\mathrm{Re})$ terms) is

$$\begin{aligned}
0 &= -\frac{\partial P}{\partial X} + \frac{\partial^2 U_M}{\partial Z^2}, && (4.1.10\text{a})\\
0 &= -\frac{\partial P}{\partial Y} + \frac{\partial^2 V_M}{\partial Z^2}, && (4.1.10\text{b})\\
0 &= -\frac{\partial P}{\partial Z}, && (4.1.10\text{c})\\
0 &= \frac{\partial U_M}{\partial X} + \frac{\partial V_M}{\partial Y} + \frac{\partial W_M}{\partial Z}. && (4.1.10\text{d})
\end{aligned}$$

We note that there is an $\mathcal{O}(\epsilon)$ inner region around the inlet and the outlet in the culture medium, where the velocity relaxes from consisting only of a vertical component as $z \to \infty$ to the lubrication region we work with (where we will later find there is no vertical component of flow). One could solve for this inner problem in practise. However, the only information we require for the outer lubrication problem is the flux of fluid coming out of this $\mathcal{O}(\epsilon)$ inner region. (We can interpret this as treating the inlet and outlet pipes as perforated pipes which extend the full depth of the culture media region.) Therefore, instead of Equation (4.1.4), we impose the matching condition for the lubrication region as our boundary conditions at the inlet and outlet, where we prescribe the total flux, q, through the walls of the inlet, $\partial\omega_{\text{in}}$, and outlet, $\partial\omega_{\text{out}}$, pipes:

$$\int_{h_H}^{h_M}\int_0^{2\pi} (\hat{\mathbf{n}}\cdot\boldsymbol{u}_M)\ \tilde{r}_I\ \mathrm{d}\theta\mathrm{d}z = +q \quad \text{on } \tilde{r}_I := \sqrt{(x-x_I)^2+(y-y_I)^2} = a, \qquad (4.1.11\text{a})$$

$$\int_{h_H}^{h_M}\int_0^{2\pi} (\hat{\mathbf{n}}\cdot\boldsymbol{u}_M)\ \tilde{r}_O\ \mathrm{d}\theta\mathrm{d}z = -q \quad \text{on } \tilde{r}_O := \sqrt{(x-x_O)^2+(y-y_O)^2} = a, \qquad (4.1.11\text{b})$$

introducing local coordinate systems — $(\tilde{r}_I, \theta, Z)$ and $(\tilde{r}_O, \theta, Z)$ (cylindrical polar coordinates) — centred around the inlet and outlet pipe, respectively, where $\partial\omega_{\text{in}}$ and $\partial\omega_{\text{out}}$ are defined as

$$\begin{aligned}
\partial\omega_{\text{in}} &:= \left\{(x,y,z) : (x-x_I)^2 + (y-y_I)^2 = a^2,\ h_H < z < h_M\right\},\\
\partial\omega_{\text{out}} &:= \left\{(x,y,z) : (x-x_O)^2 + (y-y_O)^2 = a^2,\ h_H < z < h_M\right\}.
\end{aligned} \qquad (4.1.12)$$

The total flux condition becomes

$$\int_{H_H}^{1}\int_0^{2\pi} (\hat{\mathbf{n}}\cdot\boldsymbol{U}_M)\ \tilde{R}_I\ \mathrm{d}\theta\mathrm{d}Z = +Q \quad \text{on } \tilde{R}_I := \sqrt{(X-X_I)^2+(Y-Y_I)^2} = A, \qquad (4.1.13\text{a})$$

$$\int_{H_H}^{1}\int_0^{2\pi} (\hat{\mathbf{n}}\cdot\boldsymbol{U}_M)\ \tilde{R}_O\ \mathrm{d}\theta\mathrm{d}Z = -Q \quad \text{on } \tilde{R}_O := \sqrt{(X-X_O)^2+(Y-Y_O)^2} = A, \qquad (4.1.13\text{b})$$

where the dimensionless total flux, $Q = q/(\epsilon[u_M]L^2)$. We choose $[u_M]$ such that $Q = 1$ for the typical volumetric flow rate q in Table 4.1, that is $[u_M] = q_{\text{ref}}/\epsilon L^2$.

The leading-order boundary conditions, Equations (4.1.7), (4.1.8) and (4.1.13), become:

$$\boldsymbol{U}_M = \mathbf{0} \quad \text{for } \boldsymbol{X} \in \{\boldsymbol{X} : \boldsymbol{X} \in \Omega_M,\ Z = H_H\}, \tag{4.1.14a}$$

$$\boldsymbol{U}_M \cdot \hat{\mathbf{n}} = \mathbf{0} \quad \text{on } \partial\Omega_{\text{wall}} := \left\{(X, Y, Z) : X^2 + Y^2 = B^2,\ Z \in [H_H, 1]\right\}, \tag{4.1.14b}$$

$$W_M = 0, \quad \frac{\partial U_M}{\partial Z} = 0, \quad \frac{\partial V_M}{\partial Z} = 0 \quad \text{at } Z = 1. \tag{4.1.14c}$$

$$\int_{H_H}^{1} \int_0^{2\pi} (\hat{\mathbf{n}} \cdot \boldsymbol{U}_M)\ \tilde{R}_I\ \mathrm{d}\theta\mathrm{d}Z = +Q \quad \text{on } \lim_{A\to 0} \tilde{R}_I = A, \tag{4.1.14d}$$

$$\int_{H_H}^{1} \int_0^{2\pi} (\hat{\mathbf{n}} \cdot \boldsymbol{U}_M)\ \tilde{R}_O\ \mathrm{d}\theta\mathrm{d}Z = -Q \quad \text{on } \lim_{A\to 0} \tilde{R}_O = A. \tag{4.1.14e}$$

We note that we can only impose zero normal flux through the bioreactor wall, since, in this lubrication scaling, we have neglected second-order derivatives in the X- and Y-directions and therefore can only impose one boundary condition.

From Equation (4.1.10c), we see that the pressure is independent of Z, *i.e.* $P = P(X, Y, T)$. We solve Equations (4.1.10a) and (4.1.10b), subject to Equations (4.1.7) and (4.1.14c), to find

$$U_M = -\frac{1}{2}\frac{\partial P}{\partial X}\left((1 - H_H)^2 - (Z - 1)^2\right), \tag{4.1.15a}$$

$$V_M = -\frac{1}{2}\frac{\partial P}{\partial Y}\left((1 - H_H)^2 - (Z - 1)^2\right). \tag{4.1.15b}$$

We integrate Equation (4.1.10d) with respect to Z, to give

$$0 = \int_{H_H}^{1} \frac{\partial U_M}{\partial X} + \frac{\partial V_M}{\partial Y} + \frac{\partial W_M}{\partial Z}\ \mathrm{d}Z = \frac{\partial}{\partial X}\left(\int_{H_H}^{1} U_M\ \mathrm{d}Z\right) + \frac{\partial}{\partial Y}\left(\int_{H_H}^{1} V_M\ \mathrm{d}Z\right) + [W_M]_{Z=H_H}^{Z=1}. \tag{4.1.16}$$

We express the integrated velocities appearing in Equation (4.1.16) in terms of pressure using Equation (4.1.15),

$$\int_{H_H}^{1} U_M\ \mathrm{d}Z = -\frac{1}{3}\frac{\partial P}{\partial X}(1 - H_H)^3, \quad \int_{H_H}^{1} V_M\ \mathrm{d}Z = -\frac{1}{3}\frac{\partial P}{\partial Y}(1 - H_H)^3, \tag{4.1.17}$$

and use the boundary conditions on W_M (Equations (4.1.14a) and (4.1.14c)) to find that P solves

$$0 = \frac{\partial^2 P}{\partial X^2} + \frac{\partial^2 P}{\partial Y^2}, \tag{4.1.18a}$$

subject to

$$\hat{\mathbf{n}} \cdot \nabla P = 0 \quad \text{on } \partial\Omega_{\text{wall}}, \tag{4.1.18b}$$

$$\lim_{r\to 0} \int_0^{2\pi} (\hat{\mathbf{n}} \cdot \nabla P) r \, \mathrm{d}\theta = \lim_{r\to 0} \int_0^{2\pi} \frac{\partial P}{\partial r} r \, \mathrm{d}\theta = \mp Q_P, \tag{4.1.18c}$$

where $r = |(X, Y) - (X_i, Y_i)|$ for $i = I, O$, for inlet/outlet respectively. Here, Q_P is unknown and which we must relate to the total flux Q.

We see from Equations (4.1.6) and (4.1.14) that the Z-component of velocity vanishes, $W_M = 0$. We note that we can write the media velocity in terms of the pressure gradient,

$$\boldsymbol{U}_M = -G(Z)\nabla P, \tag{4.1.19a}$$

where

$$G(Z) = \frac{1}{2}\left((1 - H_H)^2 - (Z - 1)^2\right). \tag{4.1.19b}$$

Therefore, noting that $\hat{\mathbf{n}} = \mathbf{e}_{\tilde{R}_I}$, the total influx condition on $\tilde{R}_I = A$ becomes

$$\int_{H_H}^1 \int_0^{2\pi} (\hat{\mathbf{n}} \cdot \boldsymbol{U}_M) \, \tilde{R}_I \, \mathrm{d}\theta \mathrm{d}Z = Q, \tag{4.1.20a}$$

$$\Rightarrow \quad \int_{H_H}^1 \int_0^{2\pi} (\hat{\mathbf{n}} \cdot (-G(Z)\nabla P)) \, \tilde{R}_I \, \mathrm{d}\theta \mathrm{d}Z = Q, \tag{4.1.20b}$$

$$\Rightarrow \quad \int_{H_H}^1 \int_0^{2\pi} \hat{\mathbf{n}} \cdot \left(-\frac{1}{2}\left((1 - H_H)^2 - (Z - 1)^2\right)\nabla P\right) \, \tilde{R}_I \, \mathrm{d}\theta \mathrm{d}Z = +Q \tag{4.1.20c}$$

$$\Rightarrow \quad \int_0^{2\pi} \frac{1}{3}(1 - H_H)^3 \, (-\hat{\mathbf{n}} \cdot \nabla P) \, \tilde{R}_I \, \mathrm{d}\theta = Q, \tag{4.1.20d}$$

and, using Equation (4.1.18c), we find that,

$$Q_P = \frac{3Q}{(1 - H_H)^3}. \tag{4.1.21}$$

Similarly, from the total outflux condition on $\tilde{R}_O = A$ we obtain

$$Q_P = \frac{3Q}{(1 - H_H)^3}. \tag{4.1.22}$$

Thus, we have a point source/sink with strength $Q_P = 3Q/(1 - H_H)^3$ at $\tilde{R}_I = 0$ and $\tilde{R}_O = 0$, respectively. We note that this determines the normal velocity at the pipe boundaries, $\tilde{R}_I = \tilde{R}_O = A$ (in the limit $A \to 0$), to be

$$\hat{\mathbf{n}} \cdot \boldsymbol{U}_M = \hat{\mathbf{n}} \cdot (-G(Z)\nabla P) = \pm \frac{3Q\left((1 - H_H)^2 - (Z - 1)^2\right)}{4\pi A (1 - H_H)^3}, \tag{4.1.23}$$

under the assumption the flow around the pipes is uniform. This assumption is valid, except when the pipes are placed close to the bioreactor walls.

We write the velocity field $\boldsymbol{U}_M = (U_M, V_M, 0)$ as

$$\boldsymbol{U}_M = (U(X,Y)G(Z), V(X,Y)G(Z), 0), \tag{4.1.24}$$

where $\boldsymbol{U} = (U, V)$ is related to the pressure via $\boldsymbol{U} = -\nabla P$ and $G(Z)$ is as defined in Equation (4.1.19b).

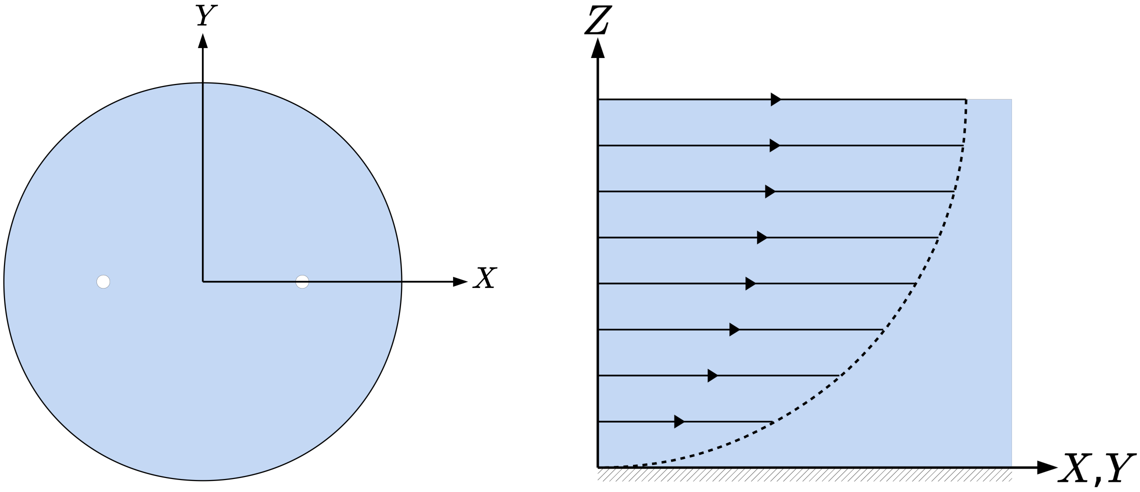

(a) domain for solving (U, V) (b) velocity profile in depth, $G(Z)$

Figure 4.3: Schematic of: (a) the 2D domain in the (X, Y)-plane in which we consider the behaviour of $\boldsymbol{U}$; and (b) the velocity profile in the Z-direction across the whole media layer.

4.2 Model solution

Given that the pressure satisfies 2D Laplace's equation, we proceed by utilising fluid dynamics theory for two-dimensional incompressible, irrotational flow [1]. We introduce the velocity potential, ϕ, defined by

$$\boldsymbol{U} = \nabla\phi, \tag{4.2.1}$$

where the velocity potential and the pressure are related via $\phi = -P$. We are, therefore, solving

$$\nabla^2\phi = 0, \tag{4.2.2}$$

with a point source at the inlet, (X_I, Y_I), and a point sink at the outlet, (X_O, Y_O), both of strength $3Q/(1 - H_H)^3$. We view the (X,Y)-plane as the complex plane, via $\zeta = X + iY$. Since $\nabla^2\phi = 0$, we can write $\phi = \text{Re}(W(\zeta))$, where W is the complex potential, a holomorphic function. Then

$$W = \phi + i\psi, \tag{4.2.3}$$

where ϕ and ψ are real, and ψ is the streamfunction. The streamfunction, ψ, is related to the flow velocity components via

$$U = \frac{\partial \psi}{\partial Y}, \quad V = -\frac{\partial \psi}{\partial X}. \tag{4.2.4}$$

The complex potential, $f(\zeta)$, for a point source and point sink of strength Q_P (where $Q_P = 3Q/(1-H_H)^3$, Equation (4.1.21)) at $\zeta_I = X_I + iY_I$ and $\zeta_O = X_O + iY_O$, respectively, in an unbounded domain is given by

$$f(\zeta) = \frac{3Q}{2\pi(1 - H_H)^3}\log(\zeta - \zeta_I) - \frac{3Q}{2\pi(1 - H_H)^3}\log(\zeta - \zeta_O). \tag{4.2.5}$$

However, our domain is bounded by a circle. The condition of no flux through the boundary wall is equivalent to the boundary $|\zeta| = B$ being a streamline of the flow. Using the Milne-Thomson circle theorem [3], the appropriate complex potential solution is

$$W(\zeta) = f(\zeta) + \overline{f\left(\frac{B^2}{\bar{\zeta}}\right)}, \tag{4.2.6a}$$

$$= \frac{3Q}{2\pi(1 - H_H)^3}\left(\log(\zeta - \zeta_I) - \log(\zeta - \zeta_O) + \log\left(\frac{B^2}{\zeta} - \bar{\zeta}_I\right) - \log\left(\frac{B^2}{\zeta} - \bar{\zeta}_O\right)\right), \tag{4.2.6b}$$

where $\bar{\cdot}$ denotes the complex conjugate. We note that

$$\log\left(\frac{B^2}{\zeta} - \bar{\zeta}_I\right) = \log\left(\zeta - \frac{B^2}{\bar{\zeta}_I}\right) - \log\left(\zeta\right) + \log(-\bar{\zeta}_I), \tag{4.2.6c}$$

and, therefore, the complex potential, $W(\zeta)$, can be written as

$$W = \frac{3Q}{2\pi(1 - H_H)^3}\left(\log(\zeta - \zeta_I) - \log(\zeta - \zeta_O) + \log\left(\zeta - \frac{B^2}{\bar{\zeta}_I}\right) - \log\left(\zeta - \frac{B^2}{\bar{\zeta}_O}\right) + \log\left(\frac{\bar{\zeta}_I}{\bar{\zeta}_O}\right)\right), \tag{4.2.6d}$$

for later convenience when plotting and when using in numerical solvers (*e.g.* to avoid any divisions by zero).

Since the complex potential, Equation (4.2.6d), consists of complex logarithms, we need to define the branch cut. We define W as

$$\begin{aligned} W(\zeta) =& \frac{3Q}{2\pi(1-H_H)^3}\left(\log(r_I) - \log(r_O) + \log(r_{IM}) - \log(r_{OM}) + \alpha\right) \\ &+ i\frac{3Q}{2\pi(1-H_H)^3}\left((\theta_I - \theta_O + \theta_{IM} - \theta_{OM}) + \beta\right), \end{aligned} \tag{4.2.7a}$$

where we denote the angle between the inlet and outlet positions in the complex plane as $\theta^* = \arg(\zeta_I - \zeta_O)$, and the variables

$$\rho_I = |\zeta - \zeta_I|, \qquad \theta_I = \arg(\zeta - \zeta_I) \quad \text{where } \theta_I \in [-\pi - \theta^*, \pi - \theta^*) \tag{4.2.7b}$$

$$\rho_O = |\zeta - \zeta_O|, \qquad \theta_O = \arg(\zeta - \zeta_O) \quad \text{where } \theta_O \in [-\pi - \theta^*, \pi - \theta^*) \tag{4.2.7c}$$

$$\rho_{IM} = \left|\zeta - \frac{B^2}{\bar{\zeta}_I}\right|, \qquad \theta_{IM} = \arg\left(\zeta - \frac{B^2}{\bar{\zeta}_I}\right), \tag{4.2.7d}$$

$$\rho_{OM} = \left|\zeta - \frac{B^2}{\bar{\zeta}_O}\right|, \qquad \theta_{OM} = \arg\left(\zeta - \frac{B^2}{\bar{\zeta}_O}\right), \tag{4.2.7e}$$

$$\alpha = \left|\frac{\bar{\zeta}_I}{\bar{\zeta}_O}\right|, \qquad \beta = \arg\left(\frac{\bar{\zeta}_I}{\bar{\zeta}_O}\right), \tag{4.2.7f}$$

and $\theta_{IM}, \theta_{OM} \in (-\pi, \pi]$ if $\mathrm{Re}(\zeta_{IM}, \zeta_{OM}) < 0$, respectively, and else $\theta_{IM}, \theta_{OM} \in [0, 2\pi)$. Our choice of range for θ_I and θ_O is to place the branch cut of the complex logarithms $\log(\zeta - \zeta_I)$ and $\log(\zeta - \zeta_O)$ on the straight line connecting ζ_I and ζ_O. With this notation, the velocity potential ϕ and streamfunction ψ can be written as

$$\phi = \mathrm{Re}(W) = \frac{3Q}{2\pi(1-H_H)^3}\left(\log(\rho_I) - \log(\rho_O) + \log(\rho_{IM}) - \log(\rho_{OM}) + \log(\alpha)\right), \tag{4.2.8a}$$

$$\psi = \mathrm{Im}(W) = \frac{3Q}{2\pi(1-H_H)^3}\left(\theta_I - \theta_O + \theta_{IM} - \theta_{OM} + \beta\right). \tag{4.2.8b}$$

We determine the X- and Y-components of velocity, (U, V), via:

$$\frac{\mathrm{d}W}{\mathrm{d}\zeta} = U - iV; \tag{4.2.9a}$$

that is

$$U = \mathrm{Re}\left(\frac{\mathrm{d}W}{\mathrm{d}\zeta}\right), \quad V = -\mathrm{Im}\left(\frac{\mathrm{d}W}{\mathrm{d}\zeta}\right), \tag{4.2.9b}$$

where

$$\frac{\mathrm{d}W}{\mathrm{d}\zeta} = \frac{3Q}{2\pi(1-H_H)^3}\left(\frac{1}{\zeta - \zeta_I} - \frac{1}{\zeta - \zeta_O} + \frac{1}{\zeta - (B^2/\bar{\zeta}_I)} - \frac{1}{\zeta - (B^2/\bar{\zeta}_O)}\right). \tag{4.2.9c}$$

4.3 Analysis of solution

Now, we consider the behaviour of the velocity potential ϕ and streamfunction ψ (Equation (4.2.8)), derived in Section 4.2.

4.3.1 Velocity potential and streamfunction

In Figure 4.4, to understand how the velocity potential and streamfunction behave within the CXP1 geometry, we plot ϕ and ψ with inlet and outlet pipes located at $(X, Y) = (-0.25, 0)$ and $(X, Y) = (0.25, 0)$, respectively. We see that ψ is in the range $\psi \in [-(3Q)/(2(1 - H_H)^3), +(3Q)/(2(1 - H_H)^3)]$, as is expected by definition of the streamfunction: the change in value of the streamfunction from one streamline to another is equal to the net flux between them. Therefore, since the total flux of fluid entering the system is $3Q/(1 - H_H)^3$, the range of ψ must be equal to this. We plot the contours of ψ in Figure 4.4(c), and these lines of constant streamfunction represent the streamlines of the culture media — the lines along which the fluid flows. We find that the velocity potential is in the range $\phi \in (-\infty, \infty)$, reaching $\mp\infty$ at the point source/sink singularities, however we plot with a finite colourmap. The plot in Figure 4.4(d) shows that the contours of ϕ are very close together near the inlet and outlet pipes.

We plot the magnitude of the culture media velocity $|\boldsymbol{U}_M|$ at the top of the media layer, $Z = 1$, and the associated streamlines under the standard operating protocol in Figure 4.5. The velocity near the inlet and outlet is high, while the velocity away from the pipes is significantly lower and is $\mathcal{O}(1)$. The fastest flow is along the straight line connecting the inlet and outlet pipes. There are two stagnation points which occur at $(\pm B, 0)$.

We consider how the streamlines change if the inlet and outlet ports are located in different positions within the domain in Figure 4.6. For inlet and outlet ports close together (Figure 4.6(a)), there is a greater range of streamline length. The shortest streamline is ~ 0.1, whereas the longest streamline needs to travel nearly twice the radius plus half the circumference of the bioreactor, $2B + \pi$. For inlet and outlet ports far apart (Figure 4.6(b)), the shortest streamline is longer than for the standard operating protocol, around 90% of the diameter of the bioreactor. However, the longest streamline is shorter than for the standard operating protocol, and therefore the range in streamline length is smaller. If the inlet and outlet ports are not placed symmetrically in the domain (Figure 4.6(c)), then the streamlines are not symmetric. We can also consider the effect of having multiple inlets in the

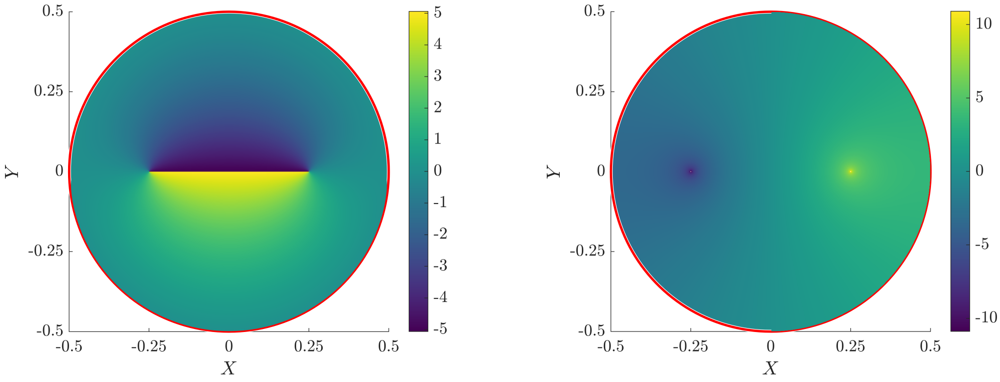

(a) streamfunction, ψ

(b) velocity potential, ϕ

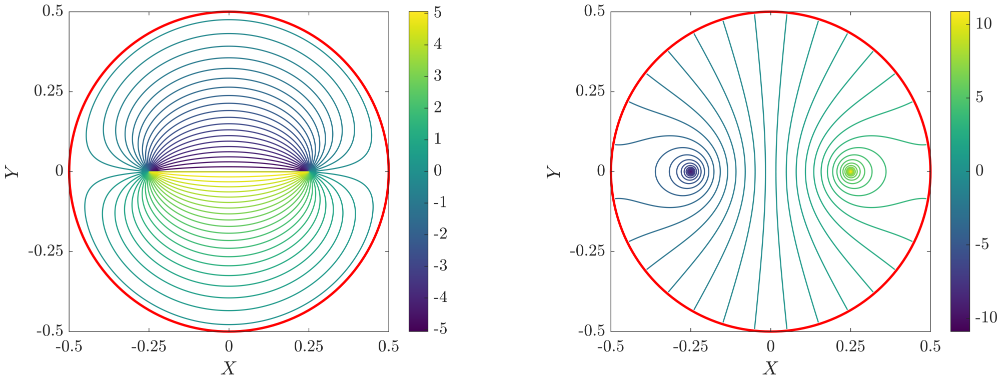

(c) contours of streamfunction, ψ

(d) contours of velocity potential, ϕ

Figure 4.4: Profiles in the (X, Y)-plane of the streamfunction, ψ, and the velocity potential, ϕ, defined in Equation (4.2.8). The inlet and outlet are at $(X, Y) = (\mp 0.25, 0)$. The parameter values used are $B = 1/2$, $H_H = 1/3$, and $Q = 1$.

bioreactor (Figure 4.6(d)). In this set-up, there are three inlets, which are equally spaced from each other and the same distance from the outlet, which is at the origin. We see that the typical streamline length is shorter than for the standard operating protocol, however there are six stagnation points.

4.3.2 Information about the streamlines

We consider the streamfunction, ψ, and the velocity along a streamline for different inlet and outlet pipe positions. We use the depth-averaged velocity field $\bar{\boldsymbol{U}}_M$, defined by

$$\bar{\boldsymbol{U}}_M = \frac{1}{1 - H_H} \int_{H_H}^{1} \boldsymbol{U}_M(X, Y, Z)\, \mathrm{d}Z. \tag{4.3.1}$$

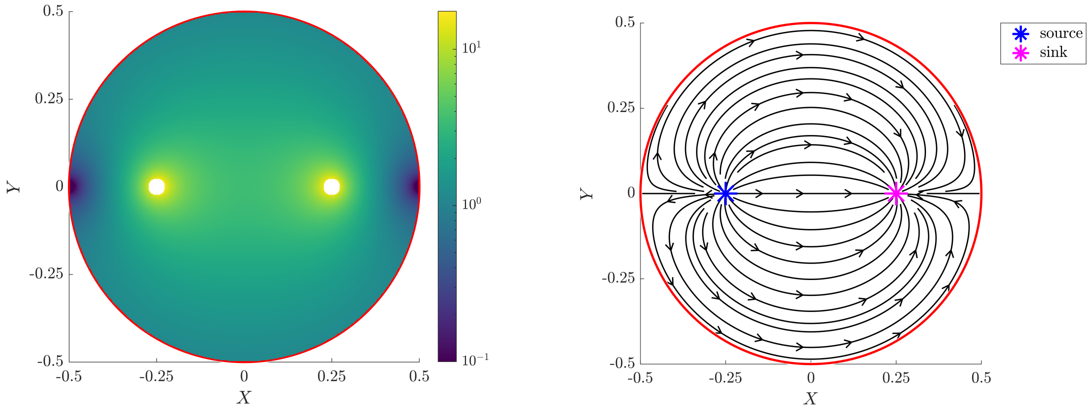

(a) magnitude of velocity at top of media layer, $|\boldsymbol{U}|G(Z=1)$

(b) streamlines of velocity

Figure 4.5: Behaviour of the flow of culture media within the CXP1 bioreactor in the (X, Y)-plane. The inlet and outlet are at $(X, Y) = (\mp 0.25, 0)$. The parameter values used are $B = 1/2$, $A = 2/90$, $H_H = 1/3$, and $Q = 1$.

By definition, $\bar{\boldsymbol{U}}_M = \tilde{U}_M(\psi, s)\mathbf{e}_s$, where $s \in [0, 1]$ parameterises the streamline. We go into further detail about this in Section 5.1.3.

We consider 9 set-ups (and explore these further in Section 5.2.3 in the context of metabolite transport), where the inlets and outlets are positioned at $(\mp X_O, 0)$ for $X_O \in \{0.05, 0.1, \ldots, 0.45\}$. Since the model is symmetric about the X-axis, without loss of generality, we restrict attention to the domain with $Y \geq 0$. The streamfunction in $Y \geq 0$ is non-positive, and is odd in the Y variable, that is

$$\psi(X, Y) = -\psi(X, -Y). \tag{4.3.2}$$

Hence, we will discuss our observations in terms of $|\psi|$, as the results are analogous for $Y \leq 0$ (with a non-negative streamfunction).

In Figure 4.7, we plot 21 uniformly spaced streamlines (for $Q = 1$ and $H_H = 1/3$) within the range $\psi \in [-0.5Q/((1 - H_H)), -0.005Q/(1 - H_H)]$, which correspond to $\psi \in [-0.75, -0.0075]$. For $X_O = 0.05$, these streamlines are far from uniformly spaced within the domain (the majority of the domain has low $|\psi|$), whereas for $X_O = 0.45$ the streamlines are more uniformly spaced and with less steep gradients of ψ across the domain. The flow is fastest at the inlet and outlet, as expected. The culture media typically slows down until the midpoint of the streamline ($s = 0.5$) and then speeds up towards the outlet pipe. The media velocity is symmetric about $s = 0.5$, due to the symmetry of the pipe placement.

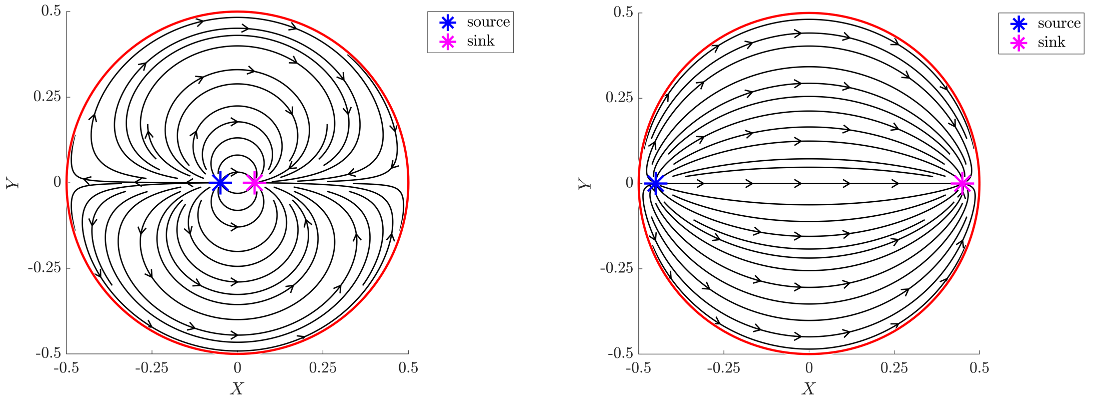

(a) 1 inlet and 1 outlet at $(X, Y) = (\mp 0.05, 0)$

(b) 1 inlet and 1 outlet at $(X, Y) = (\mp 0.45, 0)$

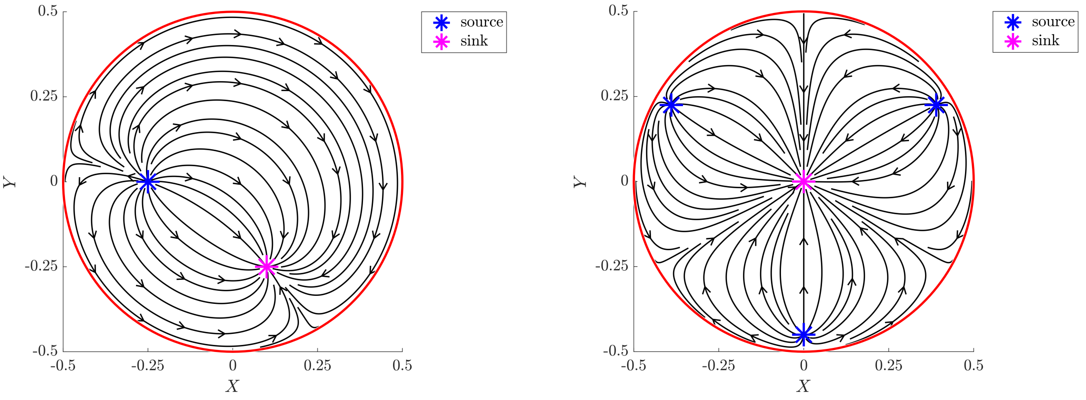

(c) non-symmetric inlet and outlet

(d) 3 inlets, 1 outlet

Figure 4.6: Streamlines in the (X, Y)-plane of the flow of culture media of the CXP1 bioreactor for different inlet and outlet pipe positions.

The media velocity along streamlines which are close to the X-axis (larger $|\psi|$) — that being the shortest path from inlet to outlet pipe — is faster than for longer streamlines (smaller $|\psi|$). For example, for $X_O = 0.05$ (Figure 4.7(a)), the velocity along the shortest streamline is approximately 10 and is about an order of magnitude larger than on the longest streamline considered, where it is approximately 0.2. For $X_O = 0.25$ (Figure 4.7(b)), the velocity in the bulk ($s \in (0.2, 0.8)$) along the shortest streamline is $\tilde{U}_M(\psi = -0.75, s) \approx 3$, whereas on the longest streamline $\tilde{U}_M(\psi = -0.0075, s) \approx 1$. When the inlet and outlet are far apart ($X_O = 0.45$; Figure 4.7(c)), media travelling along streamlines in the negative X-direction has to decelerate rapidly due to the bioreactor wall and switch to flow in the positive X-direction. We observe this in the plot of $\tilde{U}_M$, where the velocity falls rapidly close to $s = 0$ and $s = 1$. The media velocity along the shortest streamline is 1.9, approximately double that on the longest streamline (0.96). We note that there may be some asymptotic breakdown as $X_O \to B$.

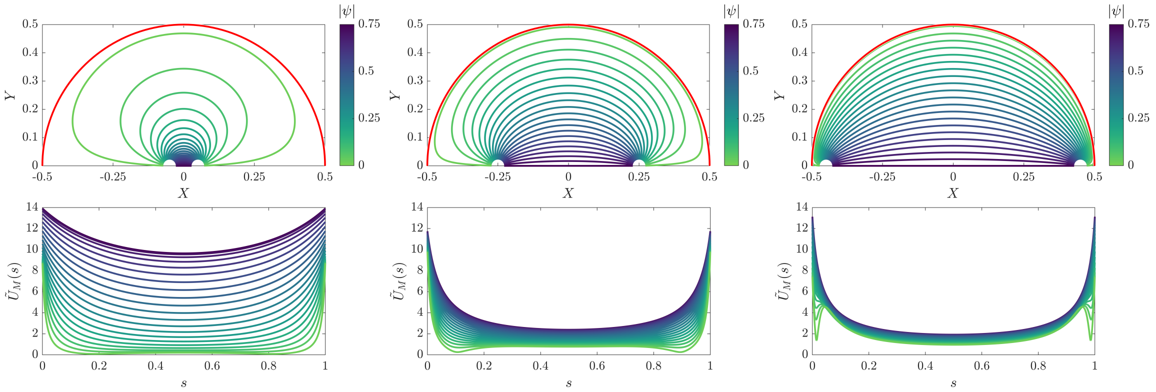

(a) $X_O = 0.05$ (b) $X_O = 0.25$ (c) $X_O = 0.45$

Figure 4.7: The position in the (X, Y)-plane and velocity along streamlines for different inlet and outlet positions.

We also wish to know the total length of the streamline with streamfunction ψ, $\mathcal{L}^{\text{total}}(\psi)$. In Figure 4.8(a) we show how the total length of a given streamline, $\mathcal{L}^{\text{total}}(\psi)$, varies with ψ for the 9 cases of inlet and outlet positions. As $|\psi|$ increases (that is, as the streamline lies further away from the bioreactor wall), the length of the streamline decreases. As X_O increases, the range of $\mathcal{L}^{\text{total}}$ decreases. For $X_O = 0.05$, the streamlines vary in length from 0.056 to 2.36, whereas for $X_O = 0.45$, they range from 0.86 to 1.62.

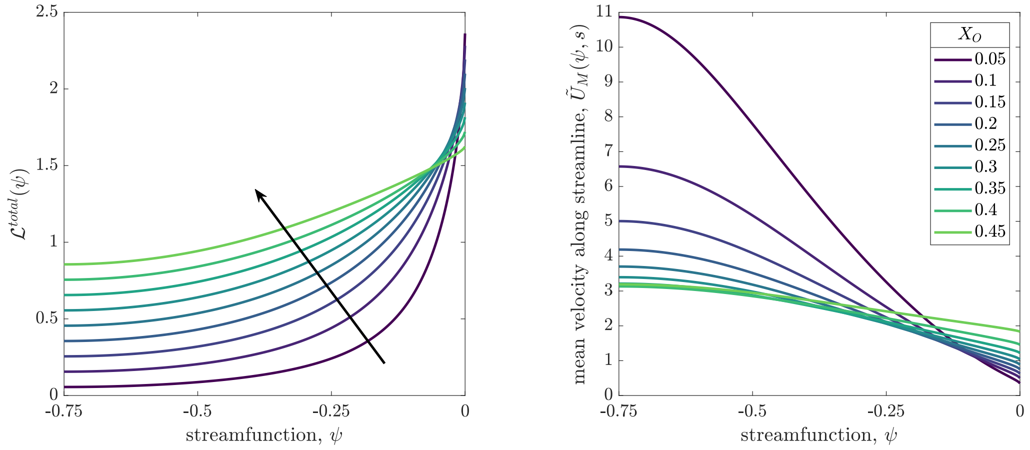

(a) length of streamline, $\mathcal{L}^{\text{total}}(\psi)$ (b) mean velocity along streamline

Figure 4.8: The length of streamline and mean velocity against streamfunction, ψ, for different inlet and outlet positions. Inlet and outlet are at $(-X_O,\ 0)$ and $(X_O, 0)$, respectively, where $X_O \in \{0.05, 0.1, 0.15, 0.2, 0.25, 0.3, 0.35, 0.4, 0.45\}$. Arrow direction indicates increasing X_O.

It is interesting to compare the streamline length to the mean velocity along a streamline. As observed in Figure 4.7, Figure 4.8(b) shows that as $|\psi|$ increases (decreasing ψ in Figure 4.8(b), since the streamfunction is negative), the mean velocity along the streamline increases. The set-up with $X_O = 0.05$ has the largest range of mean velocities on streamlines.

4.4 Discussion

We have presented a model for the culture media flow within the CXP1 bioreactor. We showed that the media flow can be formulated as a 2D problem in the (X, Y)-plane, with a point source at the inlet pipe and a point sink at the outlet pipe, and the flow profile in the Z-direction represented by half-Poiseuille flow. We derived an analytic expression for the velocity field within the current CXP1 bioreactor operating protocol and discussed how this changes for multiple sources and/or sinks. We explored how the positions of the inlet and outlet pipes affect the flow within the domain.

We determined analytic expressions for the velocity potential and streamfunction, and related this to the 3D velocity within the culture media layer of the CXP1 bioreactor. We found that the velocity field across the bioreactor is highly dependent on the position and number of inlet and outlet ports. The velocity not only varies in depth, but also varies between streamlines and along a given streamline. The culture media has the greatest velocity at the inlet and outlet pipes and the circular geometry has the potential to exhibit stagnation points, dependent on the positions of the inlet and outlet pipes. This variety of behaviour suggests that there is a large scope for altering inlet and outlet pipe positions to significantly influence glucose delivery, lactate removal, and overall organoid growth. We couple the 3D flow of culture media to the metabolite transport and organoid growth problem in Chapter 5.

Chapter 5

3D metabolite transport and organoid growth model

In this Chapter, we consider the entire CXP1 bioreactor (Figure 5.1), combining the derived models and mathematical techniques used in earlier chapters. Our goal is to understand how the bioreactor operating conditions, *e.g.* inlet flux and pipe positions, influence metabolite transport and, consequently, organoid growth.

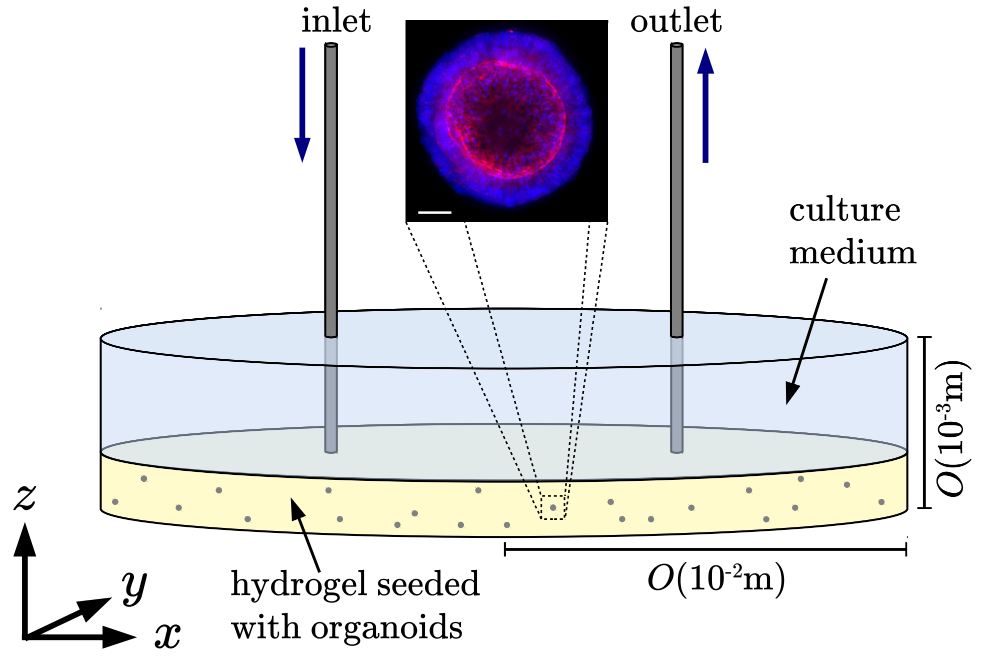

Figure 5.1: Diagram of CXP1 bioreactor set-up. The blue region represents the culture media; the yellow region represents the hydrogel; and the grey regions represent the organoids suspended within the hydrogel. (**Zoomed in region**) Example of colorectal organoid. Organoid stained for nuclear (blue) and cytoskeletal (red) markers for imaging. Scalebar 50µm. Reproduced with permission from Cellesce.

In Chapter 2, we presented a general model for glucose and lactate transport in a simplified 2D representation for the media and hydrogel layers within the CXP1 bioreactor. We showed that we can perform asymptotic analysis to systematically reduce the model, by exploiting the bioreactor geometry and separation of timescales. In Chapter 3, we developed a model for the effective macroscale transport of metabolites within the organoid-hydrogel layer of the bioreactor. We explored its behaviour for several canonical problems. Experimental observation of the bioreactor together with results generated from these canonical problems indicated that advection, due to the flow of culture media, is vitally important for efficient nutrient delivery to, and waste removal from, the bioreactor. In Chapter 4, we developed a mathematical model for the culture media flow within the CXP1 bioreactor.

We derive our full 3D model for metabolite transport within the bioreactor by coupling an advection-diffusion model for the media layer (similar to the 2D model in Chapter 2), with 3D media velocity determined in Chapter 4, to the homogenised organoid-hydrogel and organoid growth models derived in Chapter 3, subject to suitable coupling and boundary conditions. We perform a systematic model reduction, deriving a 2D model (in the X-Y plane) by averaging in depth — analogous to that considered in Chapter 2, but now accurately accounting for how advective strength varies across the bioreactor. We solve the reduced model for the glucose and lactate concentrations and organoid radius. We use our model to gain insight into how the operating protocol — specifically, the position of the inlet and outlet pipes and the inlet volumetric flow rate — affects organoid output, particularly the spatial variation in organoid size.

5.1 Model set-up

We study nutrient and waste metabolite transport within the CXP1 bioreactor. We distinguish two regions: a layer of culture media, in which metabolites are transported via advection and diffusion; and a layer of organoid-containing hydrogel, in which metabolite transport is governed by the homogenised hydrogel model derived in Chapter 3. We use the model for dense organoids undergoing volumetric growth. As in previous Chapters, we adopt a Cartesian coordinate system, $\boldsymbol{x} = (x, y, z)$, and t denotes time. The bioreactor is as described in Section 2.2 and we restate its key properties here for convenience. The bioreactor is cylindrical, with diameter L and total height h_M. The hydrogel layer is of thickness h_H and the media layer is of thickness $h_M - h_H$. The aspect ratio $\epsilon := h_M/L$ is small. We denote the inlet/outlet pipe radii as a (a small parameter) and the bioreactor radius as $b = L/2$. We denote the glucose and lactate concentrations in the media layer by c_M and w_M and the glucose and lactate concentrations in the organoid-hydrogel layer by c_O and w_O, respectively. We denote the media layer domain by ω_M and the homogenised organoid-hydrogel domain by ω_{HO}. The organoid radius is denoted as r, which we treat as a continuous field $r = r(\boldsymbol{x}, t)$ over ω_{HO}.

The dimensional equations are:

$$\frac{\partial c_M}{\partial t} + \boldsymbol{u}_M \cdot \nabla c_M = D_{CM} \nabla^2 c_M \qquad \text{for } \boldsymbol{x} \in \omega_M, \tag{5.1.1a}$$

$$\frac{\partial w_M}{\partial t} + \boldsymbol{u}_M \cdot \nabla w_M = D_{WM} \nabla^2 w_M \qquad \text{for } \boldsymbol{x} \in \omega_M, \tag{5.1.1b}$$

$$\frac{\partial}{\partial t} \left(\left(\|\omega_H\| K_C + \|\omega_O\| \right) c_O \right) = \nabla \cdot \left(\bar{D}_C(\boldsymbol{x}, t) \nabla c_O \right) - \|\omega_O\| \, s(c_O, w_O) \qquad \text{for } \boldsymbol{x} \in \omega_{HO}, \tag{5.1.1c}$$

$$\frac{\partial}{\partial t} \left(\left(\|\omega_H\| K_W + \|\omega_O\| \right) w_O \right) = \nabla \cdot \left(\bar{D}_W(\boldsymbol{x}, t) \nabla w_O \right) + 2 \|\omega_O\| \, s(c_O, w_O) \quad \text{for } \boldsymbol{x} \in \omega_{HO}, \tag{5.1.1d}$$

where Equations (5.1.1c) and (5.1.1d) are dervied in Chapter 3. Here, $\boldsymbol{u}_M$ is the culture media velocity determined in Chapter 4, the positive constants D_{CM} and D_{WM} are the diffusivities of glucose and lactate within the culture media, respectively, and $\bar{D}_C$ and $\bar{D}_W$ their effective diffusivities within the organoid-hydrogel region (derived in Section 3.3). In Equations (5.1.1c) and (5.1.1d), $\|\omega_O\| = (\frac{4\pi}{3}) r^3 / (\delta L)^3$ and $\|\omega_H\| = ((\delta L)^3 - (\frac{4\pi}{3}) r^3) / (\delta L)^3$.

The boundary conditions at the media-hydrogel interface are continuity of concentration and flux:

$$c_M = c_O, \qquad \hat{\mathbf{n}} \cdot \nabla \left(D_{CM} c_M \right) = \hat{\mathbf{n}} \cdot \nabla \left(\bar{D}_C c_O \right) \quad \text{on } z = h_H, \tag{5.1.2a}$$

$$w_M = w_O, \qquad \hat{\mathbf{n}} \cdot \nabla \left(D_{WM} w_M \right) = \hat{\mathbf{n}} \cdot \nabla \left(\bar{D}_W w_O \right) \quad \text{on } z = h_H, \tag{5.1.2b}$$

where $\hat{\mathbf{n}}$ is the unit normal. At the base and the top of the bioreactor, we assume no flux of metabolite,

$$\hat{\mathbf{n}} \cdot \left(\bar{D}_C \nabla c_O \right) = 0, \quad \hat{\mathbf{n}} \cdot \left(\bar{D}_W \nabla w_O \right) = 0 \qquad \text{at } z = 0, \tag{5.1.2c}$$

$$\hat{\mathbf{n}} \cdot \left(D_{CM} \nabla c_M \right) = 0, \quad \hat{\mathbf{n}} \cdot \left(D_{WM} \nabla w_M \right) = 0 \qquad \text{at } z = h_M. \tag{5.1.2d}$$

Similarly, at the bioreactor wall boundary, $\boldsymbol{x} \in \partial\omega_{\text{wall}} := \{(x, y, z) : x^2 + y^2 = b^2, z \in [0, h_M]\}$, we impose no flux boundary conditions:

$$\hat{\mathbf{n}} \cdot \left(\bar{D}_C \nabla c_O \right) = 0, \quad \hat{\mathbf{n}} \cdot \left(\bar{D}_W \nabla w_O \right) = 0 \qquad \text{for } z \in (0, h_H), \tag{5.1.2e}$$

$$\hat{\mathbf{n}} \cdot \left(D_{CM} \nabla c_M \right) = 0, \quad \hat{\mathbf{n}} \cdot \left(D_{WM} \nabla w_M \right) = 0 \qquad \text{for } z \in (h_H, h_M). \tag{5.1.2f}$$

At the inlet, the media flows into the domain through a vertical pipe (which is partially submerged within the layer of culture media), with velocity $\boldsymbol{u}_M$, glucose concentration $c_{-\infty}$, and lactate concentration 0. We denote the internal region of the inlet and outlet pipes as ω_{in} and ω_{out}, respectively, defined by

$$\begin{aligned} \omega_{\text{in}} &:= \left\{(x,y,z) : (x-x_I)^2 + (y-y_I)^2 < a^2,\ z > h_H\right\}, \\ \omega_{\text{out}} &:= \left\{(x,y,z) : (x-x_O)^2 + (y-y_O)^2 < a^2,\ z > h_H\right\}. \end{aligned} \tag{5.1.3}$$

Therefore, we write the conditions

$$\lim_{z\to\infty} \mathbf{e}_z \cdot (\boldsymbol{u}_M c_M - D_{CM}\nabla c_M) = \mathbf{e}_z \cdot (\boldsymbol{u}_M c_{-\infty}) \quad \text{for } \boldsymbol{x} \in \omega_{\text{in}}, \tag{5.1.4a}$$

$$\lim_{z\to\infty} \mathbf{e}_z \cdot (\boldsymbol{u}_M w_M - D_{WM}\nabla w_M) = \mathbf{e}_z \cdot (0 \times \boldsymbol{u}_M) = 0 \quad \text{for } \boldsymbol{x} \in \omega_{\text{in}}. \tag{5.1.4b}$$

At the outlet, we prescribe that the metabolite leaves the domain only via advection, through a partially-submerged vertical pipe. Therefore, we write

$$\lim_{z\to\infty} \mathbf{e}_z \cdot (-D_{CM}\nabla c_M) = 0 \quad \text{for } \boldsymbol{x} \in \omega_{\text{out}}, \tag{5.1.4c}$$

$$\lim_{z\to\infty} \mathbf{e}_z \cdot (-D_{WM}\nabla w_M) = 0 \quad \text{for } \boldsymbol{x} \in \omega_{\text{out}}. \tag{5.1.4d}$$

As in Chapter 4, we are only concerned with the metabolite flux into the lubrication region we consider, and therefore, instead of Equation (5.1.4), we impose the matching condition for the lubrication region as our effective boundary condition at the inlet and outlet pipe walls, $\partial\omega_{\text{in}}$ and $\partial\omega_{\text{out}}$, respectively. (See Section 4.1 for further details.) Hence, we prescribe continuity of metabolite flux at $\partial\omega_{\text{in}}$ and no diffusive flux at $\partial\omega_{\text{out}}$:

$$\hat{\mathbf{n}} \cdot (\boldsymbol{u}_M c_M - D_{CM}\nabla c_M) = \hat{\mathbf{n}} \cdot (\boldsymbol{u}_M c_{-\infty}) \quad \text{for } \boldsymbol{x} \in \partial\omega_{\text{in}}, \tag{5.1.5a}$$

$$\hat{\mathbf{n}} \cdot (\boldsymbol{u}_M w_M - D_{WM}\nabla w_M) = 0 \quad \text{for } \boldsymbol{x} \in \partial\omega_{\text{in}}, \tag{5.1.5b}$$

$$\hat{\mathbf{n}} \cdot (-d_{CM}\nabla c_M) = 0 \quad \text{for } \boldsymbol{x} \in \partial\omega_{\text{out}}, \tag{5.1.5c}$$

$$\hat{\mathbf{n}} \cdot (-d_{WM}\nabla w_M) = 0 \quad \text{for } \boldsymbol{x} \in \partial\omega_{\text{out}}, \tag{5.1.5d}$$

where $\partial\omega_{\text{in}}$ and $\partial\omega_{\text{out}}$ are defined as

$$\begin{aligned} \partial\omega_{\text{in}} &:= \left\{(x,y,z) : (x-x_I)^2 + (y-y_I)^2 = a^2,\ h_H < z < h_M\right\}, \\ \partial\omega_{\text{out}} &:= \left\{(x,y,z) : (x-x_O)^2 + (y-y_O)^2 = a^2,\ h_H < z < h_M\right\}. \end{aligned} \tag{5.1.6}$$

The initial metabolite concentrations are

$$c_M(\boldsymbol{x}, T=0) = c_{-\infty}, \quad w_M(\boldsymbol{x}, T=0) = 0 \quad \text{for } z \in (h_H, h_M),\ \boldsymbol{x} \in \omega_M, \tag{5.1.7a}$$

$$c_O(\boldsymbol{x}, T=0) = 0, \quad w_O(\boldsymbol{x}, T=0) = 0 \quad \text{for } z \in (0, h_H),\ \boldsymbol{x} \in \omega_{HO}. \tag{5.1.7b}$$

We pose a constitutive model for the reaction kinetics for glucose consumption, $s(c_O, w_O, t)$. We assume that the rate of glucose consumption is an increasing saturating function of the glucose concentration, c_O, and a decreasing function of the lactate concentration, w_O, of the form:

$$s(c_O, w_O, t) = s_V \phi \frac{c_O}{c_O + \nu_W w_O}, \tag{5.1.8}$$

where s_V is the rate of glucose consumption per unit volume of organoid biomass, with units $\mathrm{mol\,m^{-3}\,s^{-1}}$, ϕ is the cell packing density within the uptake region of organoid, *i.e.* the volume fraction of cells in an organoid, and ν_W is a dimensionless constant prescribing the sensitivity of the organoids to the inhibitory effects of lactate.

The metabolite transport model is coupled to the model derived in Chapter 3 for organoid growth:

$$\frac{\partial r}{\partial t} = \frac{p(c_O, w_O)}{3} r, \tag{5.1.9a}$$

where p is the metabolite-dependent rate of growth. We assume that the organoid growth rate is proportional to the rate of glucose consumption,

$$p(c_O, w_O) = f \frac{g_b}{\phi} s(c_O, w_O). \tag{5.1.9b}$$

We have assumed that a fraction, f, of the glucose consumed is synthesised into organoid biomass, where g_b is the volume of cells produced per mole of glucose consumed, units $\mathrm{m^3\,mol^{-1}}$. Since the bioreactor is initially seeded with single cells, we prescribe

$$r = r_c \quad \text{at } t = 0, \tag{5.1.9c}$$

where r_c is the radius of a single cell.

5.1.1 Dimensionless transport and organoid growth models

We non-dimensionalise the transport model (Equations (5.1.1), (5.1.2), (5.1.5) and (5.1.7) to (5.1.9)) using the scalings:

$$\begin{gathered}
(x, y, z) = L(X, Y, \epsilon Z), \quad (c_M, c_O, w_M, w_O) = c_{-\infty}(C_M, C_O, W_M, W_O), \\
t = [t]T, \quad \boldsymbol{u}_M = (u_M, v_M, 0) = [u_M]\boldsymbol{U}_M = \frac{q_{\text{ref}}}{\epsilon L^2}(U_M, V_M, 0), \\
r(\boldsymbol{x}, t) = \delta L R(\boldsymbol{X}, T), \quad s = s_V \phi S, \quad p = f g_b s_V P, \\
\bar{D}_C(\boldsymbol{x}, t) = D_{CH} \bar{d}_C(\boldsymbol{X}, T), \quad \bar{D}_W(\boldsymbol{x}, t) = D_{WH} \bar{d}_W(\boldsymbol{X}, T),
\end{gathered} \tag{5.1.10}$$

where q_{ref} is the volumetric flow rate for current CXP1 operating conditions (see Table 5.1) and we note that the dimensionless bioreactor radius is $B = b/L$. We

Table 5.1: Definitions of dimensional model parameters, together with typical values. Where no citation is given, parameters are taken from the CPX1 bioreactor.

Parameter	Definition	Typical value
D_{CM}	Diffusivity of glucose in culture media	6.0×10^{-10} $\mathrm{m^2\,s^{-1}}$ [83]
D_{CH}	Diffusivity of glucose in hydrogel	6.0×10^{-10} $\mathrm{m^2\,s^{-1}}$ [84]
D_{CO}	Diffusivity of glucose in organoid	1×10^{-10} $\mathrm{m^2\,s^{-1}}$ [95]
D_{WM}	Diffusivity of lactate in culture media	1.4×10^{-9} $\mathrm{m^2\,s^{-1}}$ [77]
D_{WH}	Diffusivity of lactate in hydrogel	1.2×10^{-9} $\mathrm{m^2\,s^{-1}}$ [98]
D_{WO}	Diffusivity of lactate in organoid	2.1×10^{-10} $\mathrm{m^2\,s^{-1}}$ [31]
$c_{-\infty}$	Glucose concentration in upstream reservoir	16 $\mathrm{mol\,m^{-3}}$
L	Typical lengthscale of bioreactor (diameter)	9×10^{-2} m
h_M	Typical depth of bioreactor	3×10^{-3} m
h_H	Typical depth of hydrogel layer	1×10^{-3} m
b	Typical bioreactor radius	4.5×10^{-2} m
a	Typical inlet/outlet pipe radius	2×10^{-3} m
q_{ref}	Typical volumetric inlet flux	1.736×10^{-10} $\mathrm{m^3\,s^{-1}}$
s_V	Rate of glucose consumption per volume of biomass	1.9×10^{-1} $\mathrm{mol\,m^{-3}\,s^{-1}}$
r_c	Radius of single cell	5×10^{-6} m
ϕ	Packing fraction of cells within an organoid	0.74 [81]
g_b	Volume of cells produced per glucose consumed	6.7×10^{-6} (anaerobic) to 10^{-3} $\mathrm{m^3\,mol^{-1}}$ (aerobic) [46]
K_C	Partition coefficient for nutrient	1
K_W	Partition coefficient for waste metabolite	1
ν_W	Sensitivity of cells to lactate	0.5
N_0	Number of cells seeded within hydrogel layer	$\mathcal{O}(10^6)$

define the aspect radio of the bioreactor height to diameter as $\epsilon := h_M/L \ll 1$. The dimensionless height of the hydrogel layer is $H_H := h_H/(\epsilon L)$. We denote by $\delta \ll 1$ the ratio of the organoid separation distance to the bioreactor diameter. This dimensionless parameter depends on the number of cells initially seeded within the bioreactor, and we estimate its value via

$$\delta = \frac{\sqrt[3]{\dfrac{\text{volume of organoid-hydrogel layer}}{\text{number of cells seeded}}}}{\text{lengthscale of bioreactor}} = \frac{1}{L}\sqrt[3]{\frac{\pi(\frac{L}{2})^2 h_H}{n}} = \sqrt[3]{\frac{\epsilon\pi H_H}{4n}}, \qquad (5.1.11)$$

where n is the number of cells initially seeded which evolve into organoids. We assume that only 20% of the cells initially seeded within the bioreactor (given in Table 5.1) develop into organoids, motivated by experimental observations, and assume that these viable cells are distributed uniformly within the hydrogel. We note that this simply means $n = 0.2N_0$, and therefore $n \sim \mathcal{O}(10^5 - 10^6)$. The sole effect is that

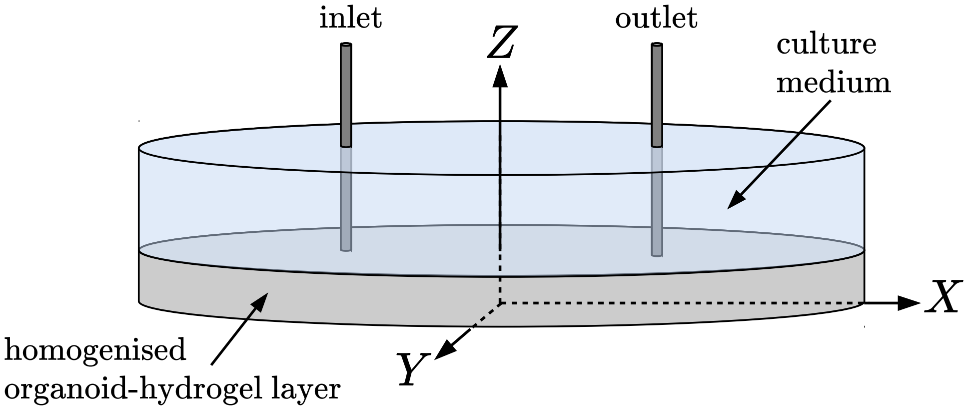

Figure 5.2: Schematic of the 3D domain in which we solve Equations (5.1.12), (5.1.13) and (5.1.15) to (5.1.17). The grey represents the homogenised organoid-hydrogel layer and the blue represents the layer of culture media.

the value of δ is $\sqrt[3]{5} \approx 1.7$ times larger than if all the cells developed into organoids. Physically, this is saying that when there are fewer organoids within the hydrogel, the more hydrogel there is per organoid (and hence, the larger the associated periodic cell, see Chapter 3).

We choose the timescale $[t]$ to be one day, $[t] = 8.64 \times 10^4$s, so that the experiment runs for $T \in [0, 7]$.

In dimensionless form, the governing equations Equation (5.1.1) are:
in the culture media ($Z \in (H_H, 1]$),

$$\frac{\partial C_M}{\partial T} + \lambda \boldsymbol{U}_M \cdot \nabla C_M = d_{CM} \left(\frac{\partial^2}{\partial X^2} + \frac{\partial^2}{\partial Y^2} + \frac{1}{\epsilon^2} \frac{\partial^2}{\partial Z^2} \right) C_M \quad \text{for } \boldsymbol{X} \in \Omega_M, \tag{5.1.12a}$$

$$\frac{\partial W_M}{\partial T} + \lambda \boldsymbol{U}_M \cdot \nabla W_M = d_{WM} \left(\frac{\partial^2}{\partial X^2} + \frac{\partial^2}{\partial Y^2} + \frac{1}{\epsilon^2} \frac{\partial^2}{\partial Z^2} \right) W_M \quad \text{for } \boldsymbol{X} \in \Omega_M; \tag{5.1.12b}$$

and in the hydrogel ($Z \in [0, H_H)$),

$$\begin{aligned} \frac{\partial}{\partial T} \left((\|\Omega_H\| K_C + \|\Omega_O\|) C_O \right) = \\ d_{CH} \left(\frac{\partial}{\partial X}, \frac{\partial}{\partial Y}, \frac{1}{\epsilon} \frac{\partial}{\partial Z} \right) \cdot \left(\bar{d}_C(X, Y, \epsilon Z, T) \left(\frac{\partial}{\partial X}, \frac{\partial}{\partial Y}, \frac{1}{\epsilon} \frac{\partial}{\partial Z} \right) C_O \right) \\ - \|\Omega_O\| \sigma_V S(C_O, W_O) \quad \text{for } \boldsymbol{X} \in \Omega_{HO}, \end{aligned} \tag{5.1.12c}$$

$$\begin{aligned} \frac{\partial}{\partial T} \left((\|\Omega_H\| K_W + \|\Omega_O\|) W_O \right) = \\ d_{WH} \left(\frac{\partial}{\partial X}, \frac{\partial}{\partial Y}, \frac{1}{\epsilon} \frac{\partial}{\partial Z} \right) \cdot \left(\bar{d}_W(X, Y, \epsilon Z, T) \left(\frac{\partial}{\partial X}, \frac{\partial}{\partial Y}, \frac{1}{\epsilon} \frac{\partial}{\partial Z} \right) W_O \right) \\ + 2 \|\Omega_O\| \sigma_V S(C_O, W_O) \quad \text{for } \boldsymbol{X} \in \Omega_{HO}, \end{aligned} \tag{5.1.12d}$$

where the dimensionless domains for the culture media and organoid-hydrogel regions are denoted by Ω_M and Ω_{HO}, respectively. The boundary conditions at the base of the hydrogel and the top of the media layer (both no flux), and media-hydrogel interface (continuity of concentration and continuity of metabolite flux) are:

$$\hat{\mathbf{n}}\cdot\left(d_{CH}\bar{d}_C\nabla C_O\right)=0,\quad \hat{\mathbf{n}}\cdot\left(d_{WH}\bar{d}_W\nabla W_O\right)=0 \quad \text{at } Z=0, \tag{5.1.13a}$$

$$\hat{\mathbf{n}}\cdot\left(d_{CM}\nabla C_M\right)=0,\quad \hat{\mathbf{n}}\cdot\left(d_{WM}\nabla W_M\right)=0 \quad \text{at } Z=1, \tag{5.1.13b}$$

$$C_M=C_O,\;\; \hat{\mathbf{n}}\cdot\nabla\left(d_{CM}C_M\right)=\hat{\mathbf{n}}\cdot\nabla\left(d_{CH}\bar{d}_C(X,Y,\epsilon Z,T)C_O\right) \quad \text{at } Z=H_H, \tag{5.1.13c}$$

$$W_M=W_O,\;\; \hat{\mathbf{n}}\cdot\nabla\left(d_{WM}W_M\right)=\hat{\mathbf{n}}\cdot\nabla\left(d_{WH}\bar{d}_W(X,Y,\epsilon Z,T)W_O\right) \quad \text{at } Z=H_H; \tag{5.1.13d}$$

and the no flux boundary conditions at the bioreactor wall boundary, $\partial\Omega_{\text{wall}}$, are

$$\hat{\mathbf{n}}\cdot\left(d_{CH}\bar{d}_C\nabla C_O\right)=0,\quad \hat{\mathbf{n}}\cdot\left(d_{WH}\bar{d}_W\nabla W_O\right)=0 \quad \text{for } Z\in[0,H_H], \tag{5.1.13e}$$

$$\hat{\mathbf{n}}\cdot\left(d_{CM}\nabla C_M\right)=0,\quad \hat{\mathbf{n}}\cdot\left(d_{WM}\nabla W_M\right)=0 \quad \text{for } Z\in[H_H,1], \tag{5.1.13f}$$

where the dimensionless bioreactor wall boundary is defined by $\boldsymbol{X}\in\partial\Omega_{\text{wall}}:=\{(X,Y,Z):X^2+Y^2=B^2,\ Z\in[0,1]\}$. The boundary conditions at the inlet pipe, $\partial\Omega_{\text{in}}$, for $Z\in(H_H,1]$ are

$$\begin{aligned}\hat{\mathbf{n}}\cdot\lambda\boldsymbol{U}_M&=\hat{\mathbf{n}}\cdot\left(\lambda\boldsymbol{U}_MC_M-d_{CM}\nabla C_M\right) \quad \text{on } \partial\Omega_{\text{in}},\\ 0&=\hat{\mathbf{n}}\cdot\left(\lambda\boldsymbol{U}_MW_M-d_{WM}\nabla W_M\right) \quad \text{on } \partial\Omega_{\text{in}},\end{aligned} \tag{5.1.13g}$$

and at the outlet pipe, $\partial\Omega_{\text{out}}$, for $Z\in(H_H,1]$,

$$0=\hat{\mathbf{n}}\cdot\left(-d_{CM}\nabla C_M\right),\quad 0=\hat{\mathbf{n}}\cdot\left(-d_{WM}\nabla W_M\right) \quad \text{on } \partial\Omega_{\text{out}}, \tag{5.1.13h}$$

where the dimensionless $\partial\Omega_{\text{in}}$ and $\partial\Omega_{\text{out}}$ are defined as

$$\begin{aligned}\partial\Omega_{\text{in}}&:=\left\{(X,Y,Z):(X-X_I)^2+(Y-Y_I)^2=A^2,\ H_H<Z\le 1\right\},\\ \partial\Omega_{\text{out}}&:=\left\{(X,Y,Z):(X-X_O)^2+(Y-Y_O)^2=A^2,\ H_H<Z\le 1\right\}.\end{aligned} \tag{5.1.14}$$

The initial conditions on the metabolite concentrations are

$$C_M=1,\quad W_M=0 \quad \text{for } Z\in(H_H,1) \;\text{ at }\; T=0, \tag{5.1.15a}$$

$$C_O=0,\quad W_O=0 \quad \text{for } Z\in(0,H_H) \;\text{ at }\; T=0. \tag{5.1.15b}$$

The dimensionless growth model is

$$\frac{\partial R}{\partial T}=\frac{\rho}{3}P(C_O,W_O)R \quad \text{with} \quad R=R_c \quad \text{at } T=0, \tag{5.1.16}$$

where the glucose consumption and proliferation rates (Equations (5.1.8) and (5.1.9b)) become:

$$S(C_O, W_O) = \frac{C_O}{C_O + \nu_W W_O}, \tag{5.1.17a}$$

$$P(C_O, W_O) = \frac{C_O}{C_O + \nu_W W_O}. \tag{5.1.17b}$$

The dimensionless parameter groupings are:

$$\begin{gathered}\{d_{CM}, d_{WM}, d_{CH}, d_{WH}\} = \frac{[t]}{L^2}\{D_{CM}, D_{WM}, D_{CH}, D_{WH}\}, \\ \lambda = \frac{[u_M][t]}{L}, \quad \sigma_V = \frac{s_V \phi [t]}{c_{-\infty}}, \quad \rho = f g_b s_V [t].\end{gathered} \tag{5.1.18}$$

The parameter values for the non-dimensional system are given in Table 5.2.

Table 5.2: Definitions of dimensionless model parameters, together with typical values. Where no citation is given, parameters are taken from the CPX1 set-up.

Parameter	Definition	Typical value
ϵ	Ratio of vertical to horizontal lengthscales	1/30
δ	Ratio of microscale 'cell' lengthscale to bioreactor lengthscale	2.44×10^{-3}
B	Radius of bioreactor	0.5
A	Radius of inlet and outlet pipe	2/90
H_H	Height of hydrogel layer	1/3
R_c	Dimensionless radius of single cell	2.27×10^{-2}
λ	Velocity scaling	0.617
d_{CM}	Diffusivity of glucose in media	6.4×10^{-3}
d_{CH}	Diffusivity of glucose in hydrogel	6.4×10^{-3}
d_{WM}	Diffusivity of lactate in media	1.49×10^{-2}
d_{WH}	Diffusivity of lactate in hydrogel	1.28×10^{-2}
σ_V	Glucose consumption rate	759
ρ	Cell proliferation rate	1.07
ν_W	Sensitivity of cell line to lactate	0.5
K_C	Organoid-hydrogel partition coefficient for glucose	1
K_W	Organoid-hydrogel partition coefficient for lactate	1

In this Section, we numerically solve the 3D problem Equations (5.1.12), (5.1.13), (5.1.16) and (5.1.17) for the 'standard' operating conditions: the culture media inlet flux is $Q = 1$ (as defined in Chapter 4), the inlet and outlet pipes positioned at $(-0.25, 0)$ and $(0.25, 0)$, respectively, and the remaining parameter values given by

Table 5.2. However, we simplify the initial conditions for glucose concentration (Equation (5.1.15)) to avoid numerical issues with zero concentration within the hydrogel, and impose instead,

$$C_M = C_O = 1 - H_H \quad \text{at } T = 0, \tag{5.1.19}$$

which we note the system under the experimental initial conditions Equation (5.1.15) will relax to over $T = \mathcal{O}(\epsilon^2/d_{CH}) \approx 4\text{h}$. Future work should consider solving this 3D model numerically with the appropriate experimental inlet condition Equation (5.1.15). We derived the numerical solutions presented in this Chapter using COMSOL Multiphysics®. Cellesce typically culture organoids to have diameters in the range of 40–85 µm — between 4 and 8.5 times their initial size. Therefore, throughout this Chapter, for ease of interpretation and comparison with desired outcome, we consider the fold increase in organoid radius:

$$\text{fold increase in organoid radius } R := \frac{R}{R_c}, \tag{5.1.20}$$

where the initial organoid radius is the dimensionless radius of a single cell, R_c. In Figure 5.3, we plot the glucose (C), lactate (W), and fold increase in organoid radius in two-dimensional cross-sections of the CXP1 bioreactor at the end of the experiment, $T = 7$. We note that we do not solve for the metabolite concentration within the pipe regions, as shown in Figure 5.3(**B**, **D**, **F**). The profiles for glucose, lactate, and organoid radius show minimal variation in depth (cf. Chapter 2). The region with most Z-variation is close to the inlet pipe, where the velocities and glucose concentration are high. There is significant variation of C, W, and R in the X- and Y-directions and high glucose concentrations are correlated with larger organoids. The lactate concentrations are very high in the bulk of the bioreactor, away from the inlet pipe, (Figure 5.3(c)), suggesting that the flow there is insufficient to remove waste from the bioreactor.

The results presented in Figure 5.3 suggest that the current operating protocol for the CXP1 bioreactor may not be optimal. Due to the significant computational expense of solving for a single experiment run ($\mathcal{O}(100\text{min})$), this motivates us to derive a reduced model, by systematically averaging in Z (cf. Chapter 2), to facilitate faster and more computationally efficient exploration of the metabolite transport and organoid growth model.

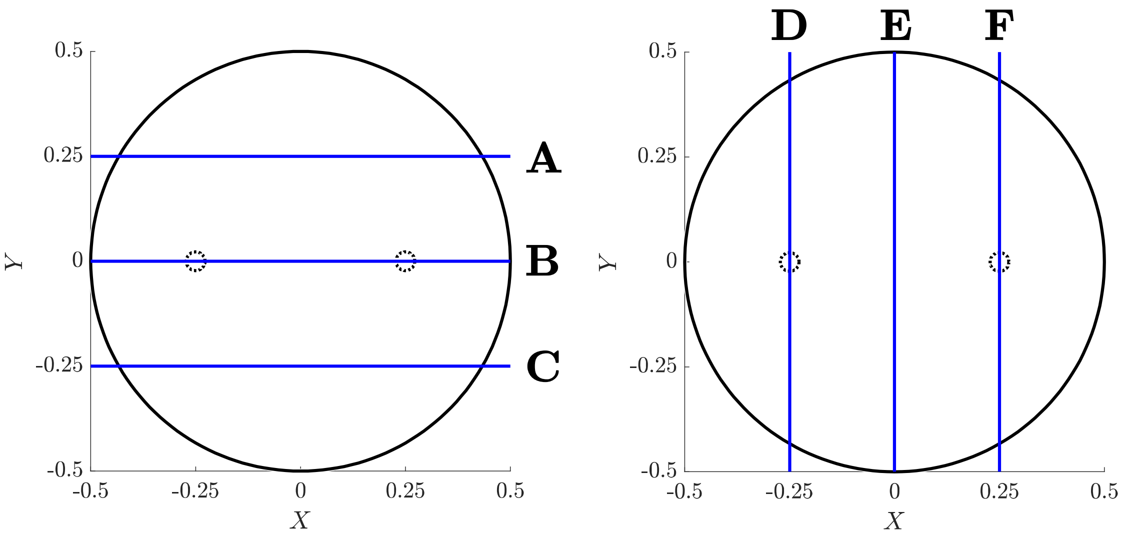

(a) Diagram depicting the cross-sections of domain considered

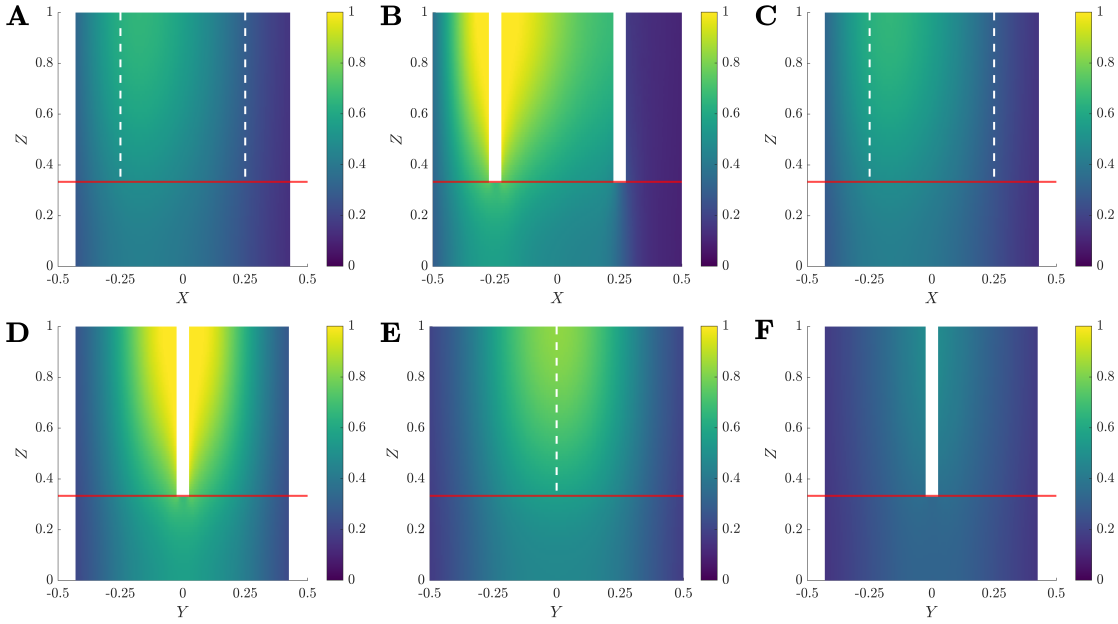

(b) glucose concentration, C

Figure 5.3: Two-dimensional cross-sections of the three-dimensional solutions of (b) glucose and (c) lactate concentrations, and (d) fold increase in organoid radius within the CXP1 bioreactor at $T = 7$. The horizontal red line at $Z = H_H$ depicts the position of the media-hydrogel interface. The cross-sections considered are shown in (a). The white dashed lines indicate the corresponding X- (**A**, **C**) and Y- (**E**) positions of the centre of the inlet/outlet pipes.

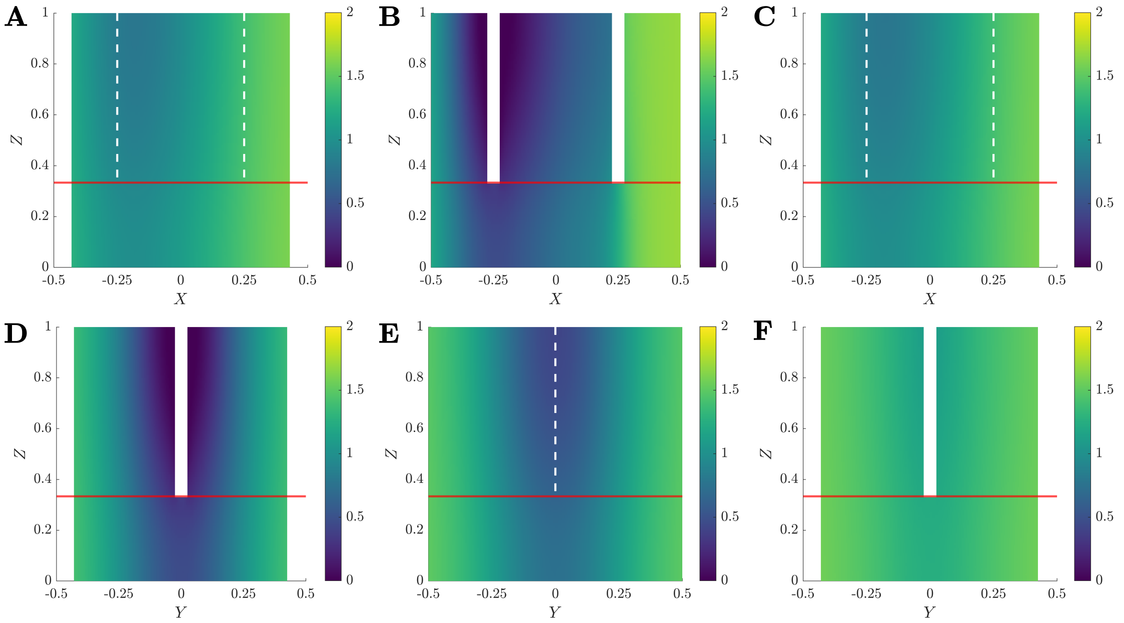

(c) lactate concentration, W

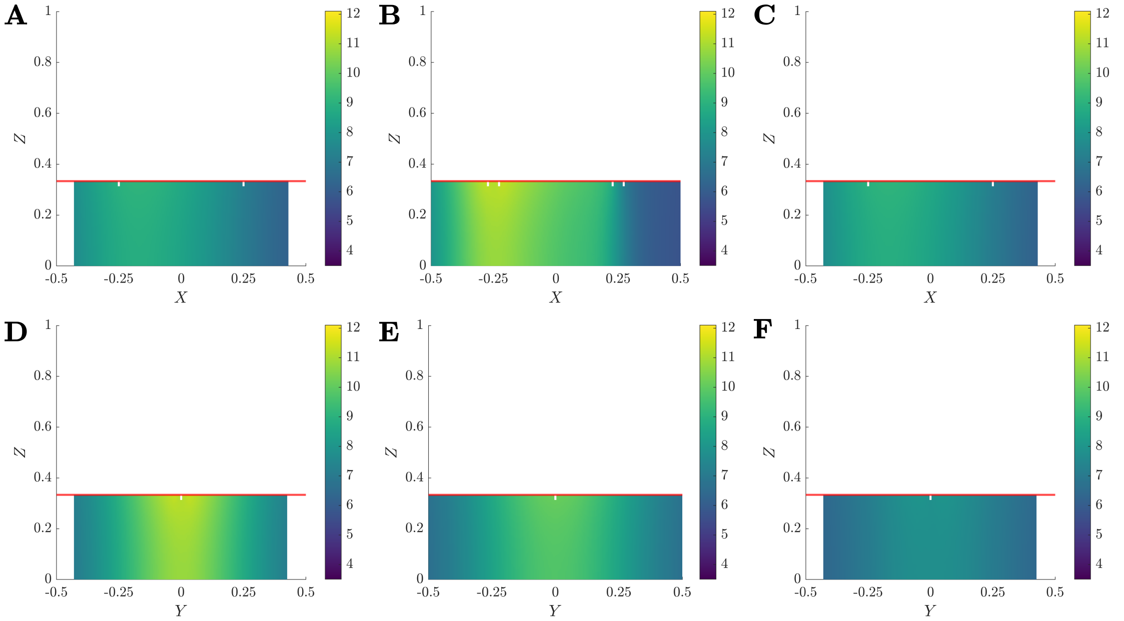

(d) fold organoid radius increase, R/R_c

Figure 5.3: Two-dimensional cross-sections of the three-dimensional solutions of (b) glucose and (c) lactate concentrations, and (d) fold increase in organoid radius within the CXP1 bioreactor at $T = 7$. The horizontal red line at $Z = H_H$ depicts the position of the media-hydrogel interface. The cross-sections considered are shown in (a). The white dashed lines indicate the corresponding X- (**A**, **C**) and Y- (**E**) positions of the centre of the inlet/outlet pipes.

5.1.2 Model reduction

We consider the metabolite transport model (Equations (5.1.12), (5.1.13) and (5.1.15) to (5.1.17)) in the limit $\epsilon \to 0$. Motivated by the parameter values in Table 5.2, we find that Z-diffusion dominates advection, which in turn dominates diffusion in the (X, Y)-plane:

$$\mathcal{O}\left(\frac{\{d_{CM}, d_{CH}, d_{WM}, d_{WH}\}}{\epsilon^2}\right) \gg \mathcal{O}\left(\lambda\right) \gg \mathcal{O}\left(\{d_{CM}, d_{CH}, d_{WM}, d_{WH}\}\right). \tag{5.1.21}$$

To proceed in our analysis, we assume $\{d_{CM}, d_{CH}, d_{WM}, d_{WH}\} \sim \mathcal{O}(\epsilon)$ and $\lambda \sim \mathcal{O}(1)$. We note that, although $\sigma_V \sim \mathcal{O}(10^2)$, the glucose consumption and lactate production terms are of size $4\pi R^3 \sigma_V/3$ and, since $R = R_c = 0.0227$ at $T = 0$, the reaction terms are initially $\mathcal{O}(10^{-2})$. Since the magnitude of this term increases over time, as the organoids grow, we assume $\|\Omega_O\|\,\sigma_V \sim \mathcal{O}(1)$. We define

$$\left\{\tilde{d}_{CM}, \tilde{d}_{CH}, \tilde{d}_{WM}, \tilde{d}_{WH}\right\} = \frac{1}{\epsilon}\left\{d_{CM}, d_{CH}, d_{WM}, d_{WH}\right\} \sim \mathcal{O}(1). \tag{5.1.22}$$

We consider the following asymptotic expansions for the dependent variables:

$$f \sim f_0 + \epsilon f_1 + \epsilon^2 f_2, \text{ as } \epsilon \to 0, \text{ where } f \in \{C_M, C_O, W_M, W_O\}. \tag{5.1.23}$$

We outline the following asymptotic analysis for glucose transport and, for brevity, omit the analysis for the waste metabolite behaviour as it follows analogously.

Multiplying the governing equations Equation (5.1.12) by ϵ^2 and using Equation (5.1.23), we obtain the governing equations for glucose:

$$\epsilon\frac{\partial}{\partial T}\left(C_{M0} + \epsilon C_{M1} + \dots\right) + \epsilon\lambda \boldsymbol{U}_M \cdot \nabla\left(C_{M0} + \epsilon C_{M1} + \dots\right)$$
$$= \tilde{d}_{CM}\left(\epsilon^2\frac{\partial^2}{\partial X^2} + \epsilon^2\frac{\partial^2}{\partial Y^2} + \frac{\partial^2}{\partial Z^2}\right)\left(C_{M0} + \epsilon C_{M1} + \dots\right), \tag{5.1.24a}$$

$$\epsilon\frac{\partial}{\partial T}\left(\left(\|\Omega_H\|\,K_C + \|\Omega_O\|\right)\left(C_{O0} + \epsilon C_{O1} + \dots\right)\right)$$
$$= \tilde{d}_{CH}\left(\epsilon\frac{\partial}{\partial X}, \epsilon\frac{\partial}{\partial Y}, \frac{\partial}{\partial Z}\right) \cdot \left(\bar{d}_C(X, Y, 0, T)\left(\epsilon\frac{\partial}{\partial X}, \epsilon\frac{\partial}{\partial Y}, \frac{\partial}{\partial Z}\right)\left(C_{O0} + \epsilon C_{O1} + \dots\right)\right)$$
$$- \epsilon\,\|\Omega_O\|\,\sigma_V S(C_{O0}, W_{O0}). \tag{5.1.24b}$$

In this lubrication approximation regime, we expand $\bar{d}_C(X, Y, \epsilon Z, T)$ about $(X, Y, 0, T)$, to find $\bar{d}_C \sim \bar{d}_C(X, Y, 0, T) + \mathcal{O}(\epsilon)$.

The leading order problem is:

$$0 = \tilde{d}_{CM}\frac{\partial^2 C_{M0}}{\partial Z^2}, \quad 0 = \tilde{d}_{CH}\bar{d}_C(X, Y, 0, T)\frac{\partial^2 C_{O0}}{\partial Z^2}, \tag{5.1.25a}$$

subject to boundary conditions

$$\tilde{d}_{CH}\bar{d}_C(X,Y,0,T)\frac{\partial C_{O0}}{\partial Z} = 0 \text{ at } Z=0, \quad \tilde{d}_{CM}\frac{\partial C_{M0}}{\partial Z} = 0 \text{ at } Z=1, \tag{5.1.25b}$$

$$C_{M0} = C_{O0}, \quad \tilde{d}_{CH}\bar{d}_C(X,Y,0,T)\frac{\partial C_{O0}}{\partial Z} = \tilde{d}_{CM}\frac{\partial C_{M0}}{\partial Z} \text{ at } Z = H_H. \tag{5.1.25c}$$

From Equation (5.1.25) we deduce that both C_{M0} and C_{O0} are independent of Z and that $C_{M0} = C_{O0}$.

Proceeding to $\mathcal{O}(\epsilon)$, Equation (5.1.24) supplies:

$$\tilde{d}_{CM}\frac{\partial^2 C_{M1}}{\partial Z^2} = \frac{\partial C_{M0}}{\partial T} + \lambda \boldsymbol{U}_M \cdot \nabla_{\boldsymbol{X}} C_{M0}, \tag{5.1.26a}$$

$$\tilde{d}_{CH}\bar{d}_C(X,Y,0,T)\frac{\partial^2 C_{O1}}{\partial Z^2} = \frac{\partial}{\partial T}\left((\|\Omega_H\| K_C + \|\Omega_O\|)C_{O0}\right) + \sigma_V \|\Omega_O\| S(C_{O0}, W_{O0}), \tag{5.1.26b}$$

subject to the boundary conditions

$$\tilde{d}_{CH}\bar{d}_C(X,Y,0,T)\frac{\partial C_{O1}}{\partial Z} = 0 \text{ at } Z=0, \quad \tilde{d}_{CM}\frac{\partial C_{M1}}{\partial Z} = 0 \text{ at } Z=1, \tag{5.1.26c}$$

$$C_{M1} = C_{O1}, \quad \tilde{d}_{CH}\bar{d}_C(X,Y,0,T)\frac{\partial C_{O1}}{\partial Z} = \tilde{d}_{CM}\frac{\partial C_{M1}}{\partial Z} \text{ at } Z = H_H. \tag{5.1.26d}$$

Integrating Equations (5.1.26a) and (5.1.26b) with respect to Z and applying the no flux conditions (Equation (5.1.26c)) yields:

$$-\tilde{d}_{CM}\left.\frac{\partial C_{M1}}{\partial Z}\right|_{Z=H_H} = (1-H_H)\left(\frac{\partial C_{M0}}{\partial T} + \lambda \bar{\boldsymbol{U}}_M \cdot \left(\frac{\partial}{\partial X}, \frac{\partial}{\partial Y}\right) C_{M0}\right), \tag{5.1.27a}$$

$$\begin{aligned}&\tilde{d}_{CH}\bar{d}_C(X,Y,0,T)\left.\frac{\partial C_{O1}}{\partial Z}\right|_{Z=H_H} \\ &\quad = H_H\left(\frac{\partial}{\partial T}\left((\|\Omega_H\| K_C + \|\Omega_O\|)C_{O0}\right) + \sigma_V \|\Omega_O\| S(C_{O0}, W_{O0})\right),\end{aligned} \tag{5.1.27b}$$

where the depth-averaged flow velocity is defined as follows,

$$\bar{\boldsymbol{U}}_M = \frac{1}{1-H_H}\int_{H_H}^{1} \boldsymbol{U}_M(X,Y,Z)\,\mathrm{d}Z, \tag{5.1.28a}$$

and, since $\boldsymbol{U}_M \sim \boldsymbol{U}G(Z) = (U(X,Y)G(Z), V(X,Y)G(Z), 0)$, derived in Section 4.1, where $G(Z)$ is as defined in Equation (4.1.19b), we have

$$\bar{\boldsymbol{U}}_M = \frac{(U,V)}{1-H_H}\int_{H_H}^{1} G(Z)\,\mathrm{d}Z = \frac{(1-H_H)^2}{3}(U,V). \tag{5.1.28b}$$

Using the continuity of flux condition (Equation (5.1.13c)) at the media-hydrogel interface, $Z = H_H$, to connect Equation (5.1.27a) and Equation (5.1.27b), we obtain:

$$\frac{\partial}{\partial T}\left(C_{M0} + \theta\left((\|\Omega_H\| K_C + \|\Omega_O\|)C_{O0}\right)\right) + \lambda \bar{\boldsymbol{U}}_M \cdot \nabla C_{M0} = -\theta \sigma_V \|\Omega_O\| S(C_{O0}, W_{O0}), \tag{5.1.29}$$

and, using the relationship $C_{M0} = C_{O0}(= \bar{C}$, say), this becomes

$$\frac{\partial}{\partial T}\left(\left(1+\theta\left(\left\|\Omega_H\right\| K_C+\left\|\Omega_O\right\|\right)\right) \bar{C}\right)+\lambda \bar{\boldsymbol{U}}_M \cdot \nabla \bar{C}=-\theta \sigma_V\left\|\Omega_O\right\| S(\bar{C}, \bar{W}), \tag{5.1.30a}$$

where we define the dimensionless parameter $\theta = H_H/(1 - H_H)$ to be the ratio between the hydrogel and media layer depths and the two-dimensional gradient is $\nabla = (\partial/\partial X, \partial/\partial Y)$.

The equivalent procedure for lactate yields

$$\frac{\partial}{\partial T}\left(\left(1+\theta\left(\left\|\Omega_H\right\| K_W+\left\|\Omega_O\right\|\right)\right) \bar{W}\right)+\lambda \bar{\boldsymbol{U}}_M \cdot \nabla \bar{W}=2\theta \sigma_V\left\|\Omega_O\right\| S(\bar{C}, \bar{W}). \tag{5.1.30b}$$

We determine the effective initial conditions by integrating the initial conditions, Equation (5.1.15), in Z to find,

$$\begin{cases} \int_0^{H_H} C_{O0} \, \mathrm{d}Z + \int_{H_H}^1 C_{M0} \, \mathrm{d}Z &= \int_0^{H_H} 0 \, \mathrm{d}Z + \int_{H_H}^1 1 \, \mathrm{d}Z, \\ \int_0^{H_H} W_{O0} \, \mathrm{d}Z + \int_{H_H}^1 W_{M0} \, \mathrm{d}Z &= \int_0^{H_H} 0 \, \mathrm{d}Z + \int_{H_H}^1 0 \, \mathrm{d}Z, \end{cases} \tag{5.1.31a}$$

$$\Rightarrow \begin{cases} H_H C_{O0} + (1-H_H) C_{M0} &= 1 - H_H, \\ H_H W_{O0} + (1-H_H) W_{M0} &= 0. \end{cases} \tag{5.1.31b}$$

Using $C_{O0} = C_{M0} = \bar{C}$ and $W_{O0} = W_{M0} = \bar{W}$, we determine

$$\bar{C} = 1 - H_H \quad \text{at } T = 0, \tag{5.1.32a}$$

$$\bar{W} = 0 \quad \text{at } T = 0. \tag{5.1.32b}$$

We note that the highest order spatial derivative in Equation (5.1.30) is now first order and, therefore, we can only impose one boundary condition. Since the information propagates downstream, we impose the depth-averaged boundary condition at the inlet. At the inlet boundary, $\boldsymbol{X} \in \partial\Omega_{\text{in}}$, we impose Equations (5.1.13g) and (5.1.13h). Expanding this in powers of ϵ, we have

$$\hat{\mathbf{n}} \cdot (\lambda \boldsymbol{U}_M) = \hat{\mathbf{n}} \cdot (\lambda \boldsymbol{U}_M (C_{M0} + \epsilon C_{M1} + \dots) - \epsilon \tilde{d}_{CM} \nabla (C_{M0} + \epsilon C_{M1} + \dots)), \tag{5.1.33a}$$

$$0 = \hat{\mathbf{n}} \cdot (\lambda \boldsymbol{U}_M (W_{M0} + \epsilon W_{M1} + \dots) - \epsilon \tilde{d}_{WM} \nabla (W_{M0} + \epsilon W_{M1} + \dots)). \tag{5.1.33b}$$

Thus, the leading-order inlet conditions are

$$\hat{\mathbf{n}} \cdot (\lambda \boldsymbol{U}_M) = \hat{\mathbf{n}} \cdot (\lambda \boldsymbol{U}_M C_{M0}) \quad \text{for } \boldsymbol{X} \in \partial\Omega_{\text{in}}, \tag{5.1.34a}$$

$$0 = \hat{\mathbf{n}} \cdot (\lambda \boldsymbol{U}_M W_{M0}) \quad \text{for } \boldsymbol{X} \in \partial\Omega_{\text{in}}. \tag{5.1.34b}$$

Integrating Equation (5.1.34) with respect to $Z \in (H_H, 1)$, we obtain

$$\hat{\mathbf{n}} \cdot (\lambda \bar{\boldsymbol{U}}_M) = \hat{\mathbf{n}} \cdot (\lambda \bar{\boldsymbol{U}}_M C_{M0}) \quad \Rightarrow \quad C_{M0} = \bar{C} = 1 \quad \text{at } (X, Y) \in \partial\Omega_{\text{in}}, \tag{5.1.35a}$$

$$0 = \hat{\mathbf{n}} \cdot (\lambda \bar{\boldsymbol{U}}_M W_{M0}) \quad \Rightarrow \quad W_{M0} = \bar{W} = 0 \quad \text{at } (X, Y) \in \partial\Omega_{\text{in}}, \tag{5.1.35b}$$

We note that the distinguished limit we have taken is singular, in that small parameters (X- and Y-diffusivities) pre-multiply the second-order spatial derivatives. As such, we no longer impose outlet boundary conditions on $\partial\Omega_{\text{out}}$. (These boundary conditions could be imposed through an appropriate boundary layer analysis near the outlet if required, though we note its effect will be weak.) Our reduced system, therefore, consists of Equations (5.1.30), (5.1.32) and (5.1.35).

5.1.3 Transforming from Cartesian to streamfunction-arclength formulation

We choose to work with coordinate system (ψ, s), where ψ is the streamfunction determined in Section 4.2 and s parameterises the streamlines (measured tangentially along the streamlines), similar to the approach taken by Cummings and Waters [13]. Without loss of generality, we suppose $0 \leq s \leq 1$, where we take $s = 0, 1$ to correspond to the inlet ($\boldsymbol{X} \in \partial\Omega_{\text{in}}$) and outlet ($\boldsymbol{X} \in \partial\Omega_{\text{out}}$), respectively. The contours of constant s are perpendicular to the streamlines at any point and parallel to lines of constant velocity potential, ϕ, as shown in Figure 5.4. We have analytic expressions for $\psi = \psi(X, Y)$ and $\phi = \phi(X, Y)$, given in Equation (4.2.8). The metrics of the transformation $(X, Y) \mapsto (\phi, \psi)$ are

$$H_\phi = \left| \frac{\partial \boldsymbol{X}}{\partial \phi} \right|, \quad H_\psi = \left| \frac{\partial \boldsymbol{X}}{\partial \psi} \right|. \tag{5.1.36}$$

We introduce the arclength along a streamline, $\mathcal{L}$, which is defined by

$$\mathcal{L}(\phi, \psi) = \int_{\psi,\phi} \hat{\mathbf{t}} \cdot \mathrm{d}\boldsymbol{X} = \int \mathbf{e}_\phi \cdot (\mathrm{d}X, \mathrm{d}Y), \tag{5.1.37a}$$

$$= \int \mathbf{e}_\phi \cdot \left(\frac{\partial \boldsymbol{X}}{\partial \psi} \, \mathrm{d}\psi + \frac{\partial \boldsymbol{X}}{\partial \phi} \, \mathrm{d}\phi \right) = \int \mathbf{e}_\phi \cdot \left(\left| \frac{\partial \boldsymbol{X}}{\partial \psi} \right| \mathbf{e}_\psi \, \mathrm{d}\psi + \left| \frac{\partial \boldsymbol{X}}{\partial \phi} \right| \mathbf{e}_\phi \, \mathrm{d}\phi \right), \tag{5.1.37b}$$

$$= \int_{-\infty}^{\phi} \left| \frac{\partial \boldsymbol{X}}{\partial \phi} \right| \, \mathrm{d}\phi, \tag{5.1.37c}$$

since the unit vectors in the ψ- ($\mathbf{e}_\psi$) and ϕ- ($\mathbf{e}_\phi$) directions are orthogonal. Therefore, taking the derivative with respect to ϕ, we find

$$\frac{\partial \mathcal{L}}{\partial \phi} = \left| \frac{\partial \boldsymbol{X}}{\partial \phi} \right| \equiv H_\phi. \tag{5.1.38}$$

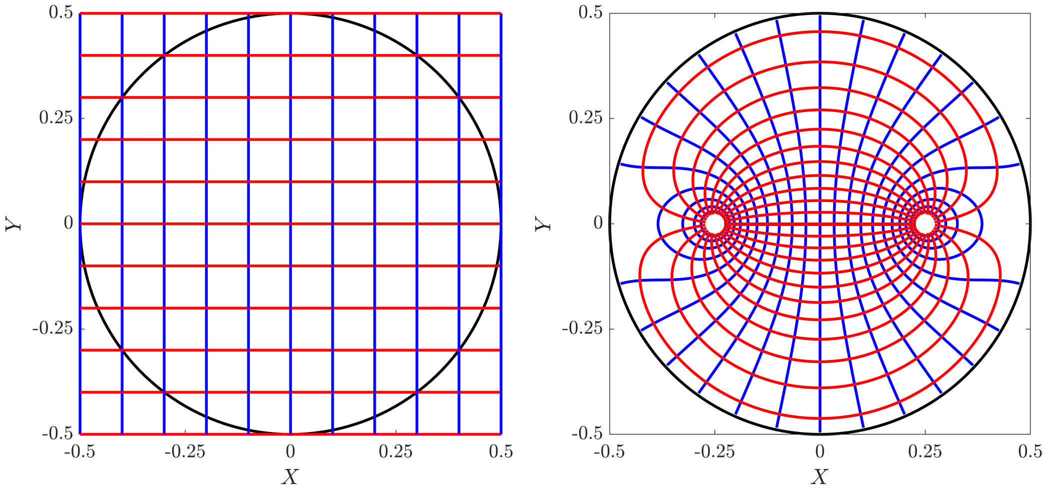

Figure 5.4: Visualisation of the change of coordinate system from Cartesian (X, Y) to streamfunction-arclength (ψ, s). The blue lines are lines of constant X (**left**) and ϕ (**right**), and red lines are lines of constant Y (**left**) and ψ (**right**).

Along a streamline, with ψ constant,

$$\mathrm{d}\mathcal{L}^2 = \mathrm{d}X^2 + \mathrm{d}Y^2, \tag{5.1.39a}$$

evaluated for constant ψ and varying ϕ. This means

$$\left(\frac{\partial \mathcal{L}}{\partial \phi}\right)^2 = \left(\frac{\partial X}{\partial \phi}\right)^2 + \left(\frac{\partial Y}{\partial \phi}\right)^2 = \left|\frac{\partial \boldsymbol{X}}{\partial \phi}\right|^2, \tag{5.1.39b}$$

$$\Rightarrow \quad \frac{\partial \mathcal{L}}{\partial \phi} = \left|\frac{\partial \boldsymbol{X}}{\partial \phi}\right|. \tag{5.1.39c}$$

We note that, $|\partial(\phi, \psi)/\partial(X, Y)|$ is known in terms of velocity components from Equations (4.2.1) and (4.2.4) and, therefore,

$$\begin{pmatrix} X_\phi & X_\psi \\ Y_\phi & Y_\psi \end{pmatrix} = \begin{pmatrix} \phi_X & \phi_Y \\ \psi_X & \psi_Y \end{pmatrix}^{-1} = \frac{1}{(\phi_X \psi_Y - \phi_Y \psi_X)} \begin{pmatrix} \psi_Y & -\phi_Y \\ -\psi_X & \phi_X \end{pmatrix} \tag{5.1.40a}$$

$$\Rightarrow \quad \begin{pmatrix} X_\phi & X_\psi \\ Y_\phi & Y_\psi \end{pmatrix} = \frac{1}{(U^2 + V^2)} \begin{pmatrix} U & -V \\ V & U \end{pmatrix}. \tag{5.1.40b}$$

Hence,

$$H_\phi \equiv \left|\frac{\partial \boldsymbol{X}}{\partial \phi}\right| = \sqrt{X_\phi^2 + Y_\phi^2} = \frac{1}{|\boldsymbol{U}|^2}\sqrt{U^2 + V^2} = \frac{1}{\tilde{U}}, \tag{5.1.41a}$$

$$H_\psi \equiv \left|\frac{\partial \boldsymbol{X}}{\partial \psi}\right| = \sqrt{X_\psi^2 + Y_\psi^2} = \frac{1}{|\boldsymbol{U}|^2}\sqrt{U^2 + V^2} = \frac{1}{\tilde{U}}, \tag{5.1.41b}$$

where $\tilde{U}$ is the fluid speed along a streamline,

$$\tilde{U}(\psi, s) = |\boldsymbol{U}| = \sqrt{U^2 + V^2}. \tag{5.1.42}$$

The depth-averaged media velocity, $\bar{\boldsymbol{U}}_M$, is related to $\tilde{U}$ by

$$\bar{\boldsymbol{U}}_M = \frac{(1-H_H)^2}{3}\left(U\mathbf{e}_X + V\mathbf{e}_Y\right) = \frac{(1-H_H)^2}{3}\tilde{U}\mathbf{e}_\phi, \tag{5.1.43}$$

and, therefore, for ease of notation, we define the depth-averaged velocity along streamlines $\tilde{U}_M$:

$$\tilde{U}_M(\phi, \psi) = \frac{(1-H_H)^2}{3}\tilde{U}. \tag{5.1.44}$$

Hence, the gradient, ∇, under the coordinate transformation $(X, Y) \mapsto (\phi, \psi)$ becomes:

$$\nabla = \mathbf{e}_X\frac{\partial}{\partial X} + \mathbf{e}_Y\frac{\partial}{\partial Y} = \mathbf{e}_\phi\frac{1}{H_\phi}\frac{\partial}{\partial \phi} + \mathbf{e}_\psi\frac{1}{H_\psi}\frac{\partial}{\partial \psi}. \tag{5.1.45}$$

Under the transformation given by the map $(X, Y) \mapsto (\phi(X, Y), \psi(X, Y))$, the governing equations for the depth-averaged metabolite transport model, Equation (5.1.30), become:

$$\frac{\partial}{\partial T}\left((1+\theta\left(\|\Omega_H\|\,K_C + \|\Omega_O\|\right))\bar{C}\right) + \lambda\frac{(1-H_H)^2}{3}\frac{\tilde{U}(\phi,\psi)}{H_\phi}\frac{\partial \bar{C}}{\partial \phi} = -\theta\sigma_V\,\|\Omega_O\|\,S(\bar{C},\bar{W}), \tag{5.1.46a}$$

$$\frac{\partial}{\partial T}\left((1+\theta\left(\|\Omega_H\|\,K_W + \|\Omega_O\|\right))\bar{W}\right) + \lambda\frac{(1-H_H)^2}{3}\frac{\tilde{U}(\phi,\psi)}{H_\phi}\frac{\partial \bar{W}}{\partial \phi} = 2\theta\sigma_V\,\|\Omega_O\|\,S(\bar{C},\bar{W}), \tag{5.1.46b}$$

where the metrics H_ϕ and H_ψ are defined by Equation (5.1.36) and $\|\Omega_O\|$ and $\|\Omega_H\|$ depend on $R = R(\phi(X,Y), \psi(X,Y), T)$, subject to boundary and initial conditions (Equation (5.1.35)).

In order for $s \in [0, 1]$, we define s as

$$s(\phi, \psi) := \frac{\mathcal{L}(\phi,\psi)}{\mathcal{L}^{\text{total}}(\psi)}, \tag{5.1.47a}$$

and, therefore, $s \in [0, 1]$ parameterises streamlines, with

$$\frac{\partial s}{\partial \phi} = \frac{1}{\mathcal{L}^{\text{total}}(\psi)}\frac{\partial \mathcal{L}}{\partial \phi} = \frac{1}{\mathcal{L}^{\text{total}}(\psi)}\frac{1}{\tilde{U}(\phi,\psi)}, \qquad \frac{\partial \mathcal{L}}{\partial s} = \mathcal{L}^{\text{total}}(\psi). \tag{5.1.47b}$$

We use the relationship

$$\frac{\partial}{\partial \phi} = \frac{\partial \mathcal{L}}{\partial \phi}\frac{\partial s}{\partial \mathcal{L}}\frac{\partial}{\partial s} = H_\phi\frac{1}{\mathcal{L}^{\text{total}}(\psi)}\frac{\partial}{\partial s}, \tag{5.1.48}$$

together with Equation (5.1.44), to transform Equation (5.1.46) into streamfunction-arclength formulation:

$$\frac{\partial}{\partial T}\left((1+\theta\left(\|\Omega_H\|\,K_C+\|\Omega_O\|\right))\bar{C}\right)+\lambda\frac{\tilde{U}_M(s,\psi)}{\mathcal{L}^{\text{total}}(\psi)}\frac{\partial\bar{C}}{\partial s}=-\theta\sigma_V\,\|\Omega_O\|\,S(\bar{C},\bar{W}), \tag{5.1.49a}$$

$$\frac{\partial}{\partial T}\left((1+\theta\left(\|\Omega_H\|\,K_W+\|\Omega_O\|\right))\bar{W}\right)+\lambda\frac{\tilde{U}_M(s,\psi)}{\mathcal{L}^{\text{total}}(\psi)}\frac{\partial\bar{W}}{\partial s}=2\theta\sigma_V\,\|\Omega_O\|\,S(\bar{C},\bar{W}), \tag{5.1.49b}$$

Since $\|\Omega_O\|+\|\Omega_H\|=1$, for the special case when $K_C=K_W=1$, the governing equations reduce to give:

$$(1+\theta)\frac{\partial\bar{C}}{\partial T}+\lambda\frac{\tilde{U}_M(s,\psi)}{\mathcal{L}^{\text{total}}(\psi)}\frac{\partial\bar{C}}{\partial s}=-\theta\sigma_V\,\|\Omega_O\|\,S(\bar{C},\bar{W}), \tag{5.1.50a}$$

$$(1+\theta)\frac{\partial\bar{W}}{\partial T}+\lambda\frac{\tilde{U}_M(s,\psi)}{\mathcal{L}^{\text{total}}(\psi)}\frac{\partial\bar{W}}{\partial s}=2\theta\sigma_V\,\|\Omega_O\|\,S(\bar{C},\bar{W}), \tag{5.1.50b}$$

with boundary and initial conditions

$$\bar{C}=1, \qquad \bar{W}=0 \quad \text{at } s=0, \tag{5.1.50c}$$

$$\bar{C}=1-H_H, \quad \bar{W}=0 \quad \text{at } T=0. \tag{5.1.50d}$$

An example of the one-dimensional streamline along which we are solving Equation (5.1.50) is shown in Figure 5.5

Transformed into streamfunction-arclength formulation, our model has spatial derivatives in the s-direction only, and has been reduced to a first-order hyperbolic PDE along streamlines. The ψ-dependence enters parametrically via the velocity $\tilde{U}_M(\psi,s)$ and the total length of streamline, $\mathcal{L}^{\text{total}}(\psi)$, both of which can be easily computed numerically *a priori* from Equations (4.2.8) and (4.2.9).

In order to obtain metabolite concentrations and organoid radius across the entire domain, we must solve the model for all values of the streamfunction ψ. However, since the inter-streamline diffusion is systematically neglected, this can be done in parallel and, hence, is significantly less computationally expensive to solve than in Cartesian coordinates. The runtime for a numerical solution of the streamfunction-arclength model is $\mathcal{O}(2\text{min})$ in MATLAB, compared to a runtime of $\mathcal{O}(10\text{min})$ or the Cartesian framework in COMSOL Multiphysics®.

We note that there are other distinguished limits for the system Equations (5.1.12), (5.1.13) and (5.1.15) to (5.1.17) which may be of interest for different parameter regimes. One such limit is the case where advection balances vertical diffusion, $\lambda\sim d_{CH}/\epsilon^2\sim\mathcal{O}(1)$, which would correspond to less extreme bioreactor geometries and/or

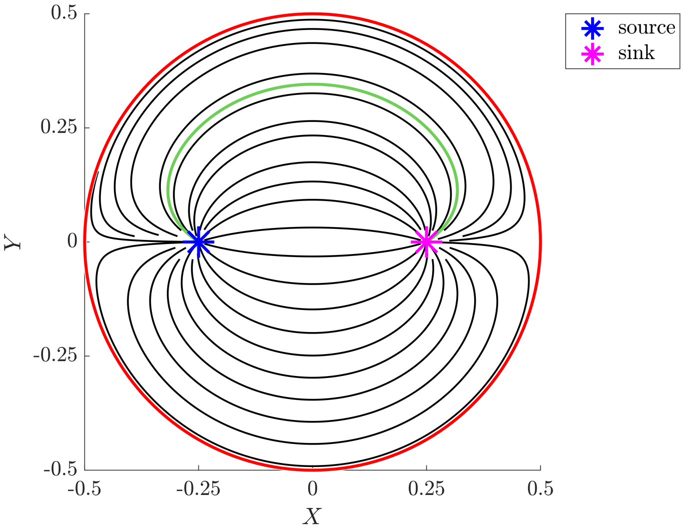

Figure 5.5: Plot to depict how one can solve along a given streamline (shown in green).

operating protocols with faster flow rates. A model reduction can still be made for this distinguished limit and we outline this in Appendix E.

5.2 Results

In Section 5.1, we derived mechanistic models to describe the transport of a nutrient (glucose, C) and a waste metabolite (lactate, W) within the media, hydrogel, and organoid regions of the CXP1 bioreactor, which we coupled to a model describing the growth of organoids. Our motivation was to understand organoid growth within the bioreactor to predict the variation of organoid size spatially across the hydrogel, and to gain insight into how changes to the operating protocol would affect the growth and variation seen during organoid expansion within the CXP1 bioreactor. The key control parameters we consider are: (1) the position of the inlet and outlet pipes; and (2) the flux of fresh culture media through the inlet pipe, Q.

In this Section, we present results for the reduced metabolite transport and organoid growth model, in Cartesian (Equations (5.1.30) and (5.1.35)) and streamfunction-arclength (Equations (5.1.35) and (5.1.46)) formulations. We anticipate from the asymptotic analysis performed in Section 5.1.2 that the error should be $\mathcal{O}(\epsilon)$ compared to solving the full 3D system, away from regions where the parameter value assumptions break down (*i.e.* near the inlet and outlet pipes).

We investigate the spatiotemporal behaviour of the metabolites and associated organoid growth within the CXP1 bioreactor. We explore how the positions of the inlet and outlet pipes, together with the inlet volumetric flux — both of which affect the culture media velocity across the domain — affect organoid growth and its variation across the hydrogel. Since Cellesce typically culture organoids until they are approximately 4 to 8.5 times their initial size, we also present results for the fold increase in organoid radius:

$$\text{fold increase in organoid radius } R := \frac{R}{R_c}, \tag{5.2.1}$$

where the initial organoid radius is that of a single cell, R_c.

5.2.1 Methods for numerical solution of metabolite transport and organoid growth models

We solve the reduced model (Equations (5.1.30) and (5.1.35)) via a finite-element method, using COMSOL Multiphysics® software. For the reduced model in streamfunction-arclength formulation, we solve the 1D system (Equations (5.1.35) and (5.1.46)) numerically using the Chebfun toolbox in MATLAB [20]. To do this, we must determine the velocity $\tilde{U}_M(\psi, s)$ and the total length, $\mathcal{L}^{\text{total}}(\psi)$, of each streamline. We determine these numerically *a priori* from Equations (4.2.8) and (4.2.9). We do this by integrating the system of ODEs

$$\frac{\partial X}{\partial \phi} = \frac{U}{U^2 + V^2}, \qquad \frac{\partial Y}{\partial \phi} = \frac{V}{U^2 + V^2}, \qquad \frac{\partial \mathcal{L}}{\partial \phi} = \frac{1}{\sqrt{U^2 + V^2}} \tag{5.2.2}$$

over a suitable range of ϕ with a Runge-Kutta method using the in-built ODE solver `ode15s` in MATLAB. The velocity potential ϕ determined in Equation (4.2.8) is defined between $-\infty$ and ∞, treating the inlet and outlet as a point source and sink, respectively. However, our metabolite transport model is only defined in a disc of radius B centred about the origin excluding the inlet and outlet pipes — both small circular regions of radius A, centred about (X_I, Y_I) and (X_O, Y_O), respectively. Therefore, for each streamline, ψ, we integrate Equation (5.2.2) between the velocity potential at the inlet and outlet pipe walls. That is, for starting position $(X, Y) = (X_I + A\cos(\theta(\psi)), Y_I + A\sin(\theta(\psi)))$, we integrate

$$\left.\begin{aligned} \frac{\partial X}{\partial \phi} &= \frac{U}{U^2 + V^2} \\ \frac{\partial Y}{\partial \phi} &= \frac{V}{U^2 + V^2} \\ \frac{\partial \mathcal{L}}{\partial \phi} &= \frac{1}{\sqrt{U^2 + V^2}} \end{aligned}\right\} \text{ subject to } \left\{\begin{aligned} X(\phi_I^*) &= X_I + A\cos(\theta(\psi)) \\ Y(\phi_I^*) &= Y_I + A\sin(\theta(\psi)) \\ \mathcal{L}(\phi_I^*) &= 0, \end{aligned}\right\} \text{ for } \phi \in [\phi_I^*,\ \phi_O^*]\,, \tag{5.2.3a}$$

where the velocity potentials for the streamline ψ at the inlet and outlet walls are given by ϕ_I^* and ϕ_O^*, respectively, where

$$\phi_I^* = \phi(X_I + A\cos(\theta(\psi)), Y_I + A\sin(\theta(\psi))), \tag{5.2.3b}$$

$$\phi_O^* = \phi(X_O + A\cos(\theta(\psi)), Y_O + A\sin(\theta(\psi))). \tag{5.2.3c}$$

Computationally, there is significant difference between the runtimes of the numerical solvers we implement for each of the models derived in this Chapter. On a standard desktop, the full 3D model is solved in $\mathcal{O}$(100min); the reduced 2D model in Cartesian coordinates in $\mathcal{O}$(10min); and the reduced 2D model in streamfunction-arclength formulation is solved in $\mathcal{O}$(2min). This gives a speed up of ≈ 10 between the 3D and 2D models. Transforming coordinate system from (X, Y) to (ψ, s) further reduces the computational time by a fifth. We also note that for the streamfunction-arclength formulation, we could consider only the shortest and longest streamlines, to capture the range of behaviour and potential variation while reducing post-processing of the data.

For each numerical approach, the results were shown to be mesh convergent (results not shown). The mesh used for the 2D reduced model within COMSOL consists of 9164 domain elements and 456 boundary elements with a maximum and minimum element size of 0.008 and 2×10^{-5}, respectively, with maximum element growth rate 1.1 and curvature factor 0.2. The relative tolerance was set to 0.005 (physics controlled). For the streamfunction-arclength formulation, we use a tolerance of 10^{-5} using the '`Eps`' option within the `pdeset` command. For the numerical solutions of all models, we use the parameter values stated in Table 5.2.

5.2.2 Current operating protocol

We first consider the reduced 2D model, given by Equations (5.1.30) and (5.1.35), under the operating conditions given in Table 5.2, which we refer to as the 'standard' operating conditions. The 'standard' inlet and outlet positions are at $(X, Y) = (X_I, Y_I) = (-0.25, 0)$ and $(X, Y) = (X_O, Y_O) = (0.25, 0)$, respectively.

In Figure 5.6, we present the glucose and lactate concentrations and the fold increase in organoid radius at the end of the experiment, $T = 7$. We observe that the glucose concentration is high near the inlet pipe, where fresh culture media enters the domain with $C = 1$ (and $W = 0$). The glucose concentration decreases with increasing distance from the inlet. The lactate concentration is low at the inlet and increases towards the outlet. Similar to observations made in Chapter 3, the organoid radius R behaves in a similar manner to glucose concentration C; regions exposed to higher glucose concentrations contain larger organoids. In a small region close to the stagnation point at $(B, 0)$, $X > X_O$ close to $Y = 0$, the velocities are sufficiently slow that they no longer dominate horizontal diffusion: in this region, the assumption Equation (5.1.21) breaks down, and the (X, Y)-diffusion terms are no longer negligible in the region near the stagnation point.

In Figure 5.7, we plot the Z-averaged solutions (a,b,c) and standard deviations (d,e,f) of the metabolite concentrations and fold increase in organoid radius of the full 3D model, Equations (5.1.12), (5.1.13) and (5.1.15) to (5.1.17). As expected, based on the 3D results shown in Figure 5.3, the most pronounced Z-variation is in the region close to the inlet pipe — where the velocity of the culture media is maximal.

In the reduced 2D model, we do not consider the organoid-hydrogel region directly below the inlet and outlet pipes. We assume that vertical diffusion is instantaneous and, therefore, the metabolite concentrations in the media and organoid-hydrogel layers are the same. However, in the 3D model (and experimental set-up), organoid-containing hydrogel lies below the inlet and outlet pipes and, therefore, glucose is consumed and lactate is produced in these regions. In practice, there is a small boundary layer region around the inlet and outlet pipes in the media layer, in which the glucose and lactate concentrations relax to the Z-independent forms predicted by our asymptotic analysis and observed in Figure 5.3. This accounts for the variation in glucose and lactate concentrations at the inlet pipe between Figure 5.6 and Figure 5.7.

We find that in the Z-averaged 3D data (Figure 5.7), 62% of the domain contains organoids whose radii show a 4 to 8.5 fold increase at $T = 7$: the mean and standard deviation of fold increase in organoid radius are 8.12 and 1.32, respectively, and the smallest organoid has radius $R = 5.7R_c$. For the reduced model, Figure 5.6(c), the mean fold increase in organoid radius is 5.66 with standard deviation 1.57, and 91% of the domain contains organoids in the ideal size range. In the bulk, away from the inlet pipe, the 2D reduced model is in good agreement with the depth-averaged data from the 3D model. We also note that, if anything, we overestimate the variation in organoid radius, and we would expect that the experimental results that Cellesce obtain/from the 3D model will not be worse than those predicted from the reduced model.

Growth is negatively impacted both by decreasing glucose concentrations and also by rising lactate levels. In our reduced model, we find $2C + W$ is a constant, and, therefore, glucose is a good proxy for lactate concentrations. Hence, our focus is primarily on the glucose concentration and organoid radius.

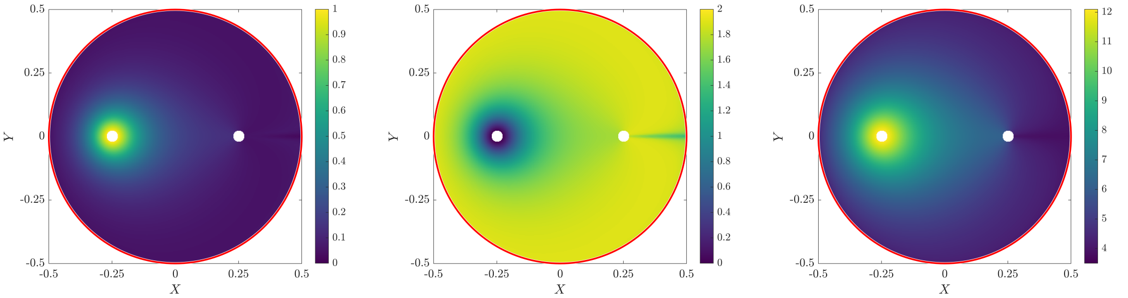

(a) glucose concentration (b) lactate concentration (c) fold increase in organoid radius

Figure 5.6: Profiles in the (X, Y)-plane of the (a) glucose, (b) lactate, and (c) fold increase in organoid radius for the 2D reduced model derived in Section 5.1.2 (Equations (5.1.30) and (5.1.35)) under the standard operating conditions given in Table 5.2.

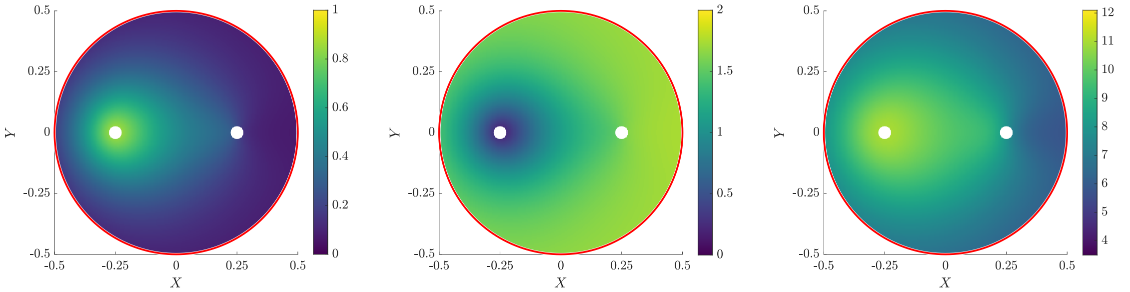

(a) depth-averaged glucose concentration (b) depth-averaged lactate concentration (c) fold increase in organoid radius

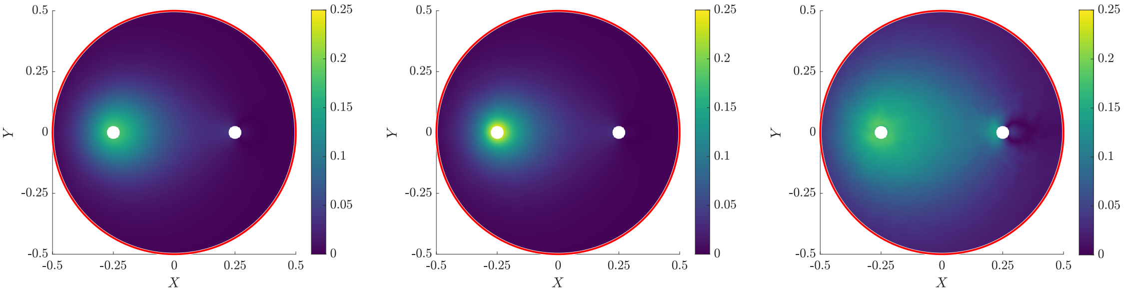

(d) standard deviation in depth of C (e) standard deviation in depth of W (f) standard deviation in depth of R/R_c

Figure 5.7: Depth-averaged concentrations and fold increase organoid radius with the corresponding standard deviation computed from the 3D metabolite transport model (Equations (5.1.12), (5.1.13) and (5.1.15) to (5.1.17)) under standard operating conditions given in Table 5.2.

5.2.3 Changing inlet and outlet position

One simple alteration to the operation of the CXP1 bioreactor is to change the position of the inlet and outlet pipes. In this subsection, we consider the impact of this.

5.2.3.1 Changing distance between inlet and outlet pipes

We consider a CXP1 geometry with inlet pipe at position $(X, Y) = (-X_O, 0)$ and an outlet pipe at position $(X, Y) = (X_O, 0)$, retaining the symmetry in the line $Y = 0$ of the typical CXP1 set-up. We consider the effect of changing the distance between the inlet and outlet port, by varying X_O at intervals of 0.05 between 0.05 and 0.45 — representing 10% and 90% of the diameter of the bioreactor. All other model parameters are fixed at the default values (see Table 5.2).

In Figure 5.8 we present the (X, Y)-profiles of the fold increase of organoid radius at the end of the experiment ($T = 7$) for different inlet and outlet pipe positions. We observe that increasing X_O increases the mean organoid radius. We note that increasing X_O corresponds to moving the inlet and outlet pipes towards the bioreactor wall, which we observed in Section 4.3 also corresponds to streamlines of more uniform length (Figures 4.5(b), 4.6(a) and 4.6(b)). For all cases considered, organoids closer to the inlet pipe experience high glucose concentrations and, as a results, are larger than organoids at distance from the inlet. At the inlet, the organoids increase to approximately 12 times their initial size. Although this is larger than the organoid size that Cellesce aim to culture, it shows that the current experimental run time is sufficient to produce organoids of the required size, if they are exposed to sufficient nutrient. For inlet and outlet pipes close together (Figure 5.8(a)), advection due to flow fails to provide adequate glucose to facilitate organoid growth. The average growth observed, approximately 3.5 times the initial organoid size, is due to the initial presence of glucose in the bioreactor at the start of the experiment. For $X_O = 0.25$ (Figure 5.8(b)), the standard operation pipe position, the organoids receive more glucose than for $X_O = 0.05$, however organoids near the wall $\|\boldsymbol{X}\| = B$ are significantly smaller than those in the region between the inlet and outlet pipe, $\|\boldsymbol{X}\| \leq X_O$. Moving the inlet and outlet further apart (to $X_O = 0.45$; Figure 5.8(c)), reduces the variation in organoid size. However, organoids near the outlet only increase in size by a factor of approximately 4.5. This suggests that insufficient nutrient propagates downstream by the end of the experiment.

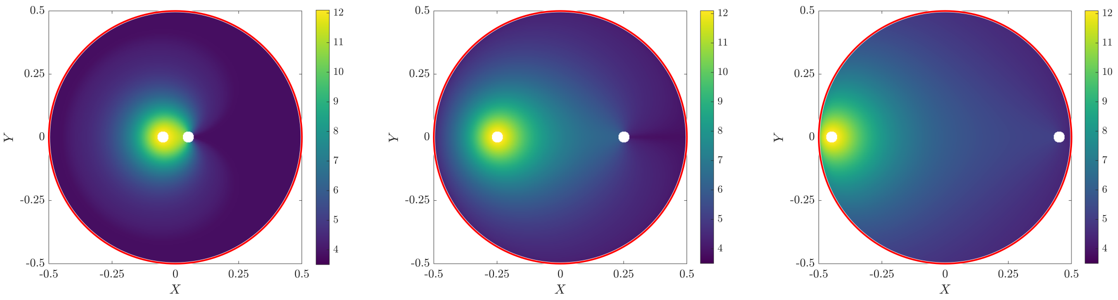

(a) $X_O = 0.05$ (b) $X_O = 0.25$ (c) $X_O = 0.45$

Figure 5.8: Mean fold increase of organoid radius, R/R_c, at $T = 7$, for different inlet and outlet positions. The parameter values used are given in Table 5.2.

We consider the time evolution of the fold increase in organoid radius in Figure 5.9. We plot the mean (Figure 5.9(a)) and standard deviation (Figure 5.9(b)) over the duration of the experiment for nine different inlet positions, $X_O \in \{0.05, 0.1, 0.15, \ldots, 0.45\}$. Both the mean and standard deviation increase monotonically over time. At early times, $T \lesssim 2 - 3$, there is negligible difference in mean and variation in organoid size for the different X_O. During this time, the organoids consume the glucose initially present in the bioreactor (the delivery of glucose via advection is unimportant). At later times, increasing X_O increases the mean fold increase in organoid radius, albeit with diminishing returns. The rate of increase in organoid growth decreases after three to four days, when glucose concentrations start to decrease (Figure 5.10(a)). This suggests there is insufficient glucose to support a sustained rate of increase in organoid radius. Further, increasing X_O from 0.05 to 0.1 increases the variation in organoid size. This is because for $X_O = 0.05$ all organoids (excluding a small region around the inlet pipe) experience similar, low glucose concentrations. Increasing X_O above 0.15 decreases the standard deviation in organoid size, with the standard deviation for $X_O = 0.45$ being lower than $X_O = 0.05$ for all times.

We compare the mean and standard deviation of fold increase in organoid radius for the 'best' ($X_O = 0.45$) and 'worst' ($X_O = 0.05$) inlet and outlet positions in Figure 5.9(c). When $X_O = 0.45$, one standard deviation either side of the mean fold increase in organoid radius (representing $\sim$ 68% of the organoids) are within the ideal range of organoid size ($4 - 8.5$ times a single cell). Using the data in Figure 5.8, we can determine the proportion of the domain which produces organoids in the ideal range. Further, Table 5.3 shows when $X_O = 0.25$ or $X_O = 0.45$ over 90% of the organoids attain the desired radius. However, even when $X_O = 0.45$, the variation is significant, with the standard deviation tripling from $T = 5$ to $T = 7$. This suggests

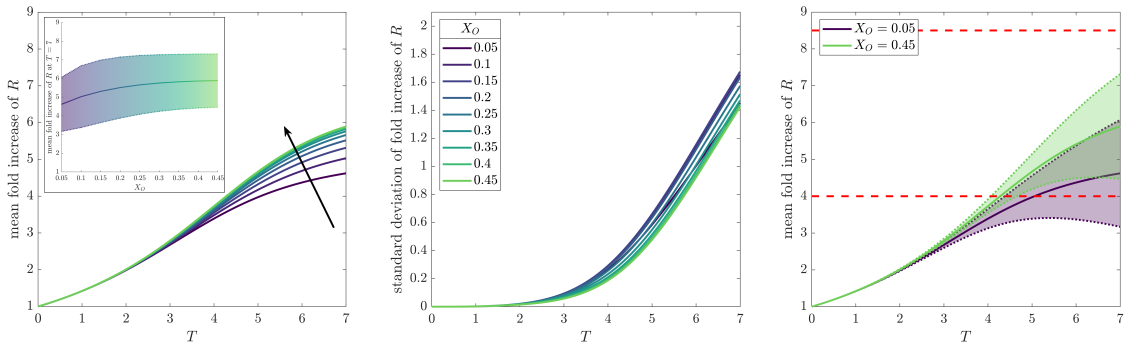

(a) (**main**) mean R/R_c; (**inset**) mean and standard deviation of R/R_c at $T = 7$ vs X_O

(b) standard deviation of R/R_c

(c) mean and standard deviation of R/R_c for $X_O \in \{0.05, 0.45\}$

Figure 5.9: Series of plots showing how the mean and standard deviation of fold increase of organoid radius, R/R_c, evolve over time as the positions of the inlet and outlet pipes vary. The inlet and outlet are at $(-X_O,\ 0)$ and $(X_O, 0)$, respectively, where $X_O \in \{0.05, 0.1, \ldots, 0.45\}$. Arrow direction indicates increasing X_O. The parameter values used are given in Table 5.2.

that there is insufficient nutrient delivery for the number of cells present at these later times.

We investigate this further in Figure 5.10, where we plot the mean and standard deviation of glucose concentration. The mean glucose concentration increases over the first two days and then it decreases. The mean glucose concentration for $X_O = 0.05$ does not increase significantly above its initial value $C = (1 - H_H)$, and as X_O increases, the maximum value of the mean glucose concentration increases. As the organoids increase in size, they require more glucose to sustain themselves and proliferate and, therefore, eventually the glucose concentration starts to decrease because insufficient nutrient is being delivered via the culture media to sustain the earlier growth rates. Figure 5.10(a) confirms that at later times, the glucose concentration within the domain is low for all X_O and insufficient nutrient is delivered to organoids away from the inlet pipe. The standard deviation of the glucose concentration is non-monotonic (Figure 5.10(b)). In all cases, the initial concentration of glucose is uniform across the CXP1 bioreactor. It takes approximately two days for the culture media to advect across the bioreactor. We see this most clearly when $X_O = 0.45$, where the streamlines have similar length which are approximately the diameter of the bioreactor, where the variation in glucose reaches a minima around two to three days. At later times ($3 \lessapprox T \lessapprox 5$), the variation of glucose concentration increases before decreasing again to low levels ($C < 0.3$).

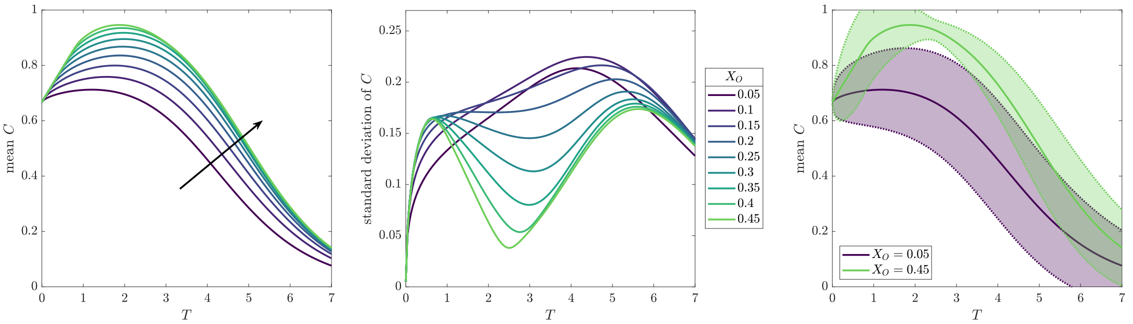

(a) mean glucose

(b) standard deviation of glucose

(c) mean and standard deviation of glucose for $X_O \in \{0.05, 0.45\}$

Figure 5.10: Series of plots showing how the mean and standard deviation of glucose concentration, C, evolve over time as the positions of the inlet and outlet pipes vary. Inlet and outlet are at $(-X_O, 0)$ and $(X_O, 0)$, respectively, where $X_O \in \{0.05, 0.1, \dots, 0.45\}$. Arrow direction indicates increasing X_O. The parameter values used are given in Table 5.2.

Table 5.3: Proportion of domain in which the fold increase in organoid radius is smaller than, in, or larger than the desired range for the 'one inlet, one outlet' set-up after 7 days. The parameter values used are given in Table 5.2.

Outlet position, X_O	Inlet flux, Q	Proportion of domain in which fold increase in organoid radius lies within a specific range		
		$R/R_c < 4$	$4 < R/R_c < 8.5$	$R/R_c > 8.5$
0.05	1	0.493	0.467	0.0406
0.25	1	0.0169	0.913	0.0696
0.45	1	0	0.931	0.0695

5.2.3.2 Changing number of inlets

In Section 5.2.3.1, we observed that the organoids close to the inlet grew larger than those at distance away from the inlet. This motivates us to consider the behaviour of a CXP1 set-up with multiple inlets. One might expect that more of the domain is exposed to fresh culture media, and therefore this could provide better organoid growth in more of the domain. In this Section, we consider three inlets and a single outlet. We distribute the inlets uniformly on a disc of radius r_I, and place the single outlet at the origin. We maintain the *total* volumetric flux entering the domain and, therefore, each inlet acts as a source with strength $Q = 1/3$. The coordinates of the inlets and outlet are denoted by (X_{Ij}, Y_{Ij}), for $j \in \{1, 2, 3\}$, and (X_O, Y_O), respectively, where

$$(X_{Ij}, Y_{Ij}) = r_I \left(\cos\left(\frac{\pi}{6} + \frac{2\pi(j-1)}{3} \right), \ \sin\left(\frac{\pi}{6} + \frac{2\pi(j-1)}{3} \right) \right) \ \text{for } j \in \{1, 2, 3\}, \tag{5.2.4a}$$

$$(X_O, Y_O) = (0, 0). \tag{5.2.4b}$$

The complex potential, $W(\zeta)$, for this set-up (cf. Equation (4.2.6d)) is:

$$W(\zeta) = \frac{3Q}{2\pi(1-H_H)^2} \left[\frac{1}{3} \sum_{j=1}^{3} \left(\log(\zeta - \zeta_{Ij}) + \log\left(\zeta - \frac{B^2}{\bar{\zeta}_{Ij}} \right) \right) - \log(B^2) \right], \tag{5.2.5a}$$

$$\Rightarrow \quad \frac{\mathrm{d}W}{\mathrm{d}\zeta} = \frac{3Q}{2\pi(1-H_H)^2} \left[\frac{1}{3} \sum_{j=1}^{3} \left(\frac{1}{\zeta - \zeta_{Ij}} + \frac{1}{\zeta - \frac{B^2}{\bar{\zeta}_{Ij}}} \right) \right], \tag{5.2.5b}$$

where we denote the position of inlet j in the complex plane by $\zeta_{Ij} = X_{Ij} + iY_{Ij}$, for $j \in \{1, 2, 3\}$, with associated depth-averaged velocity $\bar{\boldsymbol{U}}_M = (\bar{U}_M, \bar{V}_M)$:

$$\bar{U}_M = \frac{(1-H_H)^2}{3} \operatorname{Re}\left(\frac{\mathrm{d}W}{\mathrm{d}\zeta} \right), \qquad \bar{V}_M = -\frac{(1-H_H)^2}{3} \operatorname{Im}\left(\frac{\mathrm{d}W}{\mathrm{d}\zeta} \right). \tag{5.2.5c}$$

We consider nine different values of r_I, the distance of the inlets from the origin, $r_I \in \{0.05, 0.1, \ldots, 0.45\}$.

Figure 5.11 shows the (X, Y)-profiles of the fold increase in organoid radius for $r_I = 0.05$ (Figure 5.11(a)), $r_I = 0.25$ (Figure 5.11(b)), and $r_I = 0.45$ (Figure 5.11(c)). As for the 'one inlet, one outlet' case explored in Section 5.2.3.1, increasing the distance between the inlet and the outlet (equivalently, moving the inlets closer to the bioreactor wall) increases the mean organoid size within the bioreactor. Since there are three inlets, there are now six stagnation points (see Figure 4.6(d)) and regions with very slow media velocities, where (X, Y)-diffusion becomes an significant transport mechanism.

Figure 5.12 depicts the time evolution of the mean and standard deviation fold increase in organoid radius, and we see that these increase monotonically over time. Increasing r_I increases the mean organoid size. As for the 'one inlet, one outlet' case, increasing the distance between the inlet and outlet in the range $0.05 \leq r_I \leq 0.25$ increases the variation in organoid radius. However, for $r_I > 0.25$, the standard deviation decreases. While this may seem significantly larger than the threshold of $X_O = 0.15$, the distance between the inlet and the outlet for the 'one inlet, one outlet' set-up is now $2X_O$, and therefore our observations are consistent with the earlier result. The maximum distance between the inlet and the outlet in the 'three

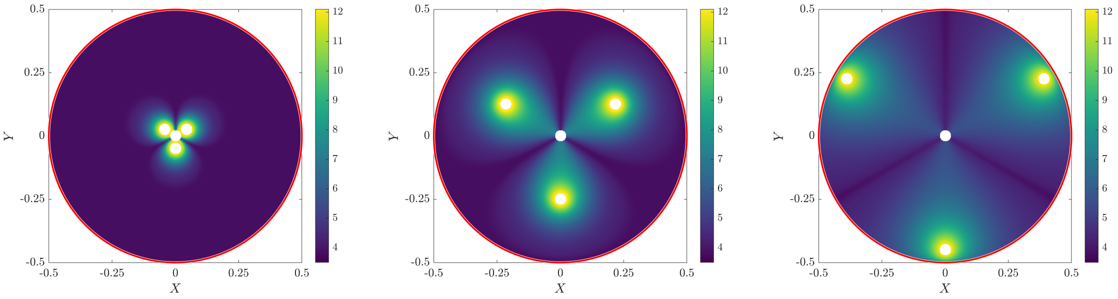

(a) $r_I = 0.05$ (b) $r_I = 0.25$ (c) $r_I = 0.45$

Figure 5.11: Mean fold increase of organoid radius, R/R_c, at $T = 7$, for 3 inlets and 1 outlet for different inlet positions. The inlets and outlet are at positions given in Equation (5.2.4). The parameter values used are given in Table 5.2.

inlets, one outlet' set-up, $r_I = B - A \approx 0.48$, is half the maximum distance for the 'one inlet, one outlet' case. Further increasing r_I, even for $r_I = 0.45$, yields organoids with greater variation than for $r_I = 0.05$. We note, however, that in this case, around 89% of the bioreactor contains organoids of radius $3.8R_c$, which is below the required size (Table 5.4). For $r_I = 0.25$, this decreases to 29% and for $r_I = 0.45$ it decreases further to approximately 1.4%. Comparing the 'best' and 'worst' choices of r_I considered, in terms of fold increase in mean organoid radius, in Figure 5.14, we see that moving the inlet pipes close to the bioreactor wall significantly improves organoid growth overall.

Table 5.4: Proportion of domain with organoids of fold increase in radius which are smaller, in, or larger than the desired range for 'three inlets, one outlet' set-up after 7 days. The parameter values used are given in Table 5.2.

Inlet position, r_I	Inlet flux, Q	Proportion of domain in which fold increase in organoid radius lies within a specific range		
		$R/R_c < 4$	$4 < R/R_c < 8.5$	$R/R_c > 8.5$
0.05	1	0.891	0.0937	0.0153
0.25	1	0.288	0.643	0.0690
0.45	1	0.0148	0.916	0.0696

We consider the mean and standard deviation in glucose concentration for this set-up in Figure 5.13. We find that for small values of r_I, the glucose concentration does not increase significantly above its initial value and starts to decrease after two days. Changes in the standard deviation in glucose concentration are similar to those for the 'one inlet, one outlet' set-up, although we only observe a trough in standard deviation for $r_I \geq 0.35$, as opposed to $X_O \geq 0.2$.

In Figure 5.14(a) we compare the standard operating conditions to the 'three inlets, one outlet' case with $r_I = 0.45$. The 'three inlets, one outlet' case slightly outperforms the standard operating conditions, with a larger mean fold increase and smaller variation. However, when we compare the 'best' inlet and outlet position for the 'one inlet, one outlet' and 'three inlets, one outlet' cases, $X_O = 0.45$ and $r_I = 0.45$, respectively, we find that the single inlet and outlet performs slightly better. This counter-intuitive result can be explained by considering the velocity profiles (Figure 5.15): for 'three inlets, one outlet' (Figure 5.15(a)), there are six regions with very slow flow, each larger than the two slow flow regions of the standard operating conditions (cf. Figure 5.15(b)). Further, the equivalent slow flow regions in the 'one inlet, one outlet' case with $X_O = 0.45$ are significantly smaller in terms of area. The slow flow regions are particularly detrimental for two reasons: first, little glucose reaching these slow flow regions; second, any glucose that enters does not propagate downstream and is instead consumed by organoids in the slow flow regions. A notable difference between the 'three inlets, one outlet' case compared to the 'one inlet, one outlet' case, is that when slow flow regions occur, they are typically halfway along a streamline rather than at the start. It is preferable to have slow flow regions as far down the streamlines as possible, since more of organoids along the streamline experience higher levels of glucose. Since the media velocity is the most spatially uniform when $X_O = 0.45$, with much smaller regions of slow flow, we conclude that it is the best domain set-up considered for nutrient delivery that is practically attainable.

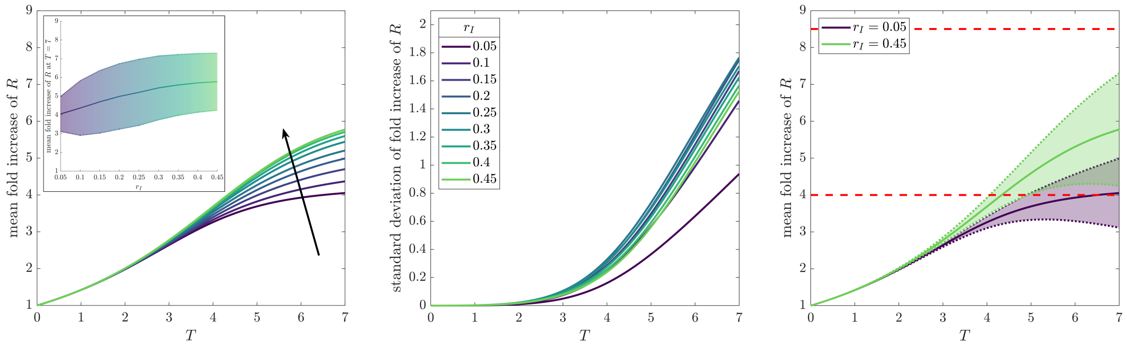

(a) (**main**) mean R/R_c; (**inset**) mean and standard deviation of R/R_c at $T = 7$ vs r_I

(b) standard deviation of R/R_c

(c) mean and standard deviation of R/R_c for $X_O \in \{0.05, 0.45\}$

Figure 5.12: Series of plots showing how the mean and standard deviation of fold increase of organoid radius, R/R_c, evolve over time as the position of the inlet pipes vary. The inlets and outlet are at positions given in Equation (5.2.4). Arrow direction indicates increasing r_I. The parameter values used are given in Table 5.2.

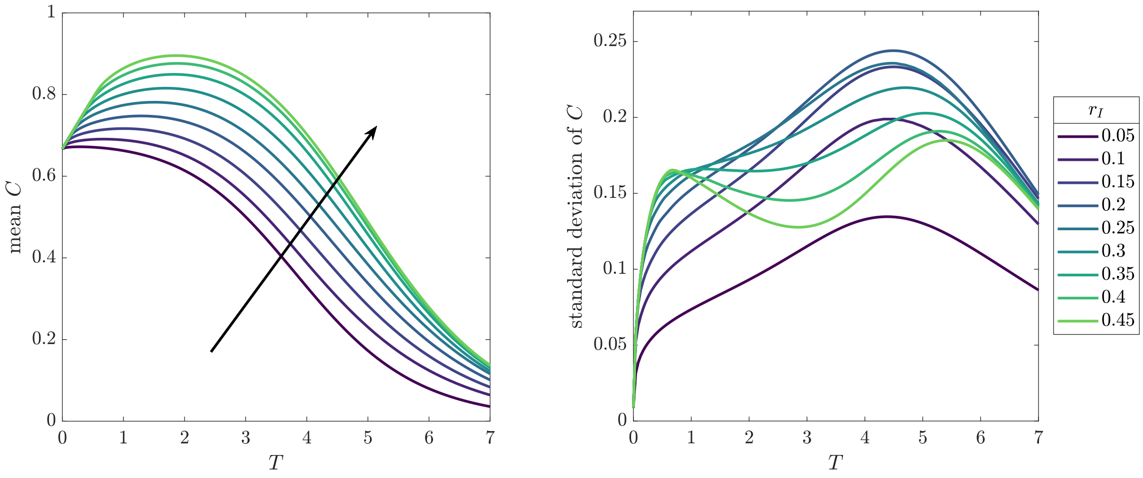

(a) mean glucose

(b) standard deviation of glucose

Figure 5.13: Series of plots showing how the mean and standard deviation of glucose concentration, C, evolve over time as the position of the inlet pipes vary. The inlets and outlet are at positions given in Equation (5.2.4). Arrow direction indicates increasing r_I. The parameter values used are given in Table 5.2.

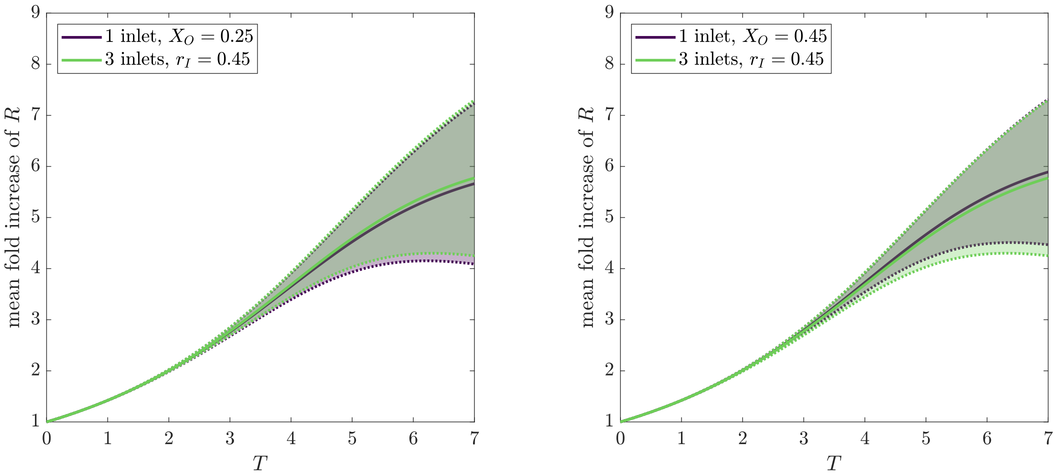

(a) Comparing 1 vs 3 inlets for $X_O = 0.5$ and $r_I = 0.9$

(b) Comparing 1 vs 3 inlets for $X_O = 0.9$ and $r_I = 0.9$

Figure 5.14: Comparing the mean and standard deviation of fold increase of organoid radius, R/R_c, evolving in time for two different set-ups; 'one inlet, one outlet', and 'three inlets, 1 outlet'. For the 1 inlet case, the inlet and outlet are at $(-X_O, 0)$ and $(X_O, 0)$, respectively. For the 3 inlets case, the inlets and outlet are at positions given in Equation (5.2.4). The parameter values used are given in Table 5.2.

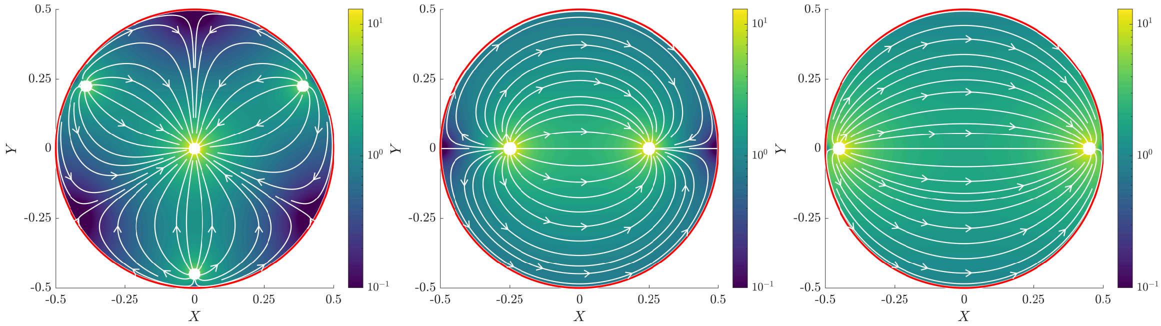

(a) $r_I = 0.45$

(b) $X_O = 0.25$

(c) $X_O = 0.45$

Figure 5.15: Velocity magnitude profile with streamlines for (b) 3 inlet and 1 outlet with $r_I = 0.45$; (b) 1 inlet and 1 outlet with $X_O = 0.25$; and (c) 1 inlet and 1 outlet with $X_O = 0.45$. The parameter values used are given in Table 5.2.

5.2.4 Changing inlet flux

We now consider the effect of varying the prescribed volumetric flow rate, Q. In Section 5.2.3, we found that after around four days, even if we improved organoid growth and reduced spatial variation by increasing the distance between the inlet and outlet ports, the rate of organoid radius increase decreases over time. This suggests that nutrient delivery for constant volumetric flux $Q = 1$ is insufficient for larger organoids and this cannot be overcome by improved inlet and outlet pipe positioning alone. Lower inlet fluxes correspond to: (1) less culture media required for bioreactor operation, which saves resources; and (2) reduced risk of damage to the hydrogel surface due to shear forces. Therefore, it is important to understand the extent to which the inlet flux affects organoid growth.

5.2.4.1 Changing inlet flux

We consider nine different values for the culture media inlet fluxes Q, that span two orders of magnitude:

$$Q = 10^k \quad \text{for} \quad k \in \{-1, -0.75, -0.5, -0.25, 0, 0.25, 0.5, 0.75, 1\}. \tag{5.2.6}$$

For now, the inlet and outlet pipes are fixed at $(-0.25, 0)$ and $(0.25, 0)$, respectively. All other parameter values are fixed at the values for the standard operating protocol (see Table 5.2).

In Figure 5.16 we present 2D spatial profiles of the fold increase of organoid radius at the end of the experiment, $T = 7$, for the flux values $Q = 0.1$, $Q = 1$, and $Q = 10$. We indicate the proportion of the domain with the ideal organoid radius range, 4 to 8.5 fold increase, in Table 5.5. When $Q = 0.1$ (Figure 5.16(a)), organoids in only 38% of the domain have grown more than 3.8 times their initial size. Further, only organoids very close to the inlet pipe have grown significantly larger than this. This set-up is even worse than inducing slow media flow in the bulk of the domain by placing the inlet and outlet pipes close together (X_O small), Section 5.2.3.1. This is expected, as even though the velocity within the reactor is more uniform than for Figure 5.8(a), its magnitude is ten times smaller. A lower inlet flux leads to slower flow and, hence, advection occurring over a longer timescale, but also less glucose entering the domain. Both of these effects negatively impact organoid growth. When the flow is increased to ten times the standard operating amount ($Q = 10$, Figure 5.16(c)), the organoids are significantly larger throughout the whole domain and the minimum increase in organoid radius is 5.1 fold. However, approximately half the domain has organoids

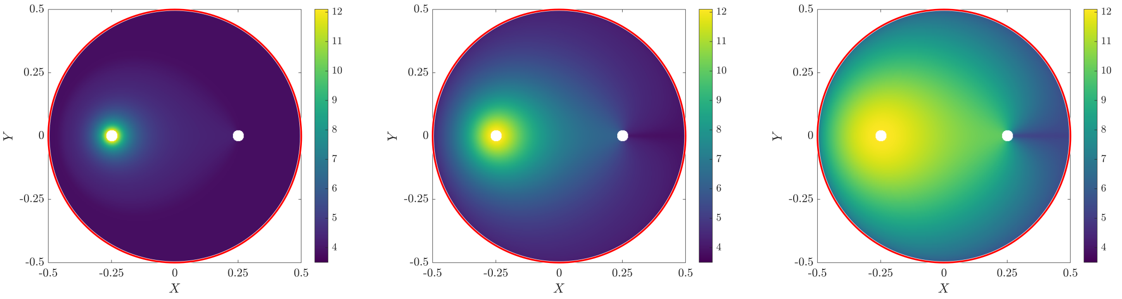

(a) $Q = 0.1$ (b) $Q = 1$ (c) $Q = 10$

Figure 5.16: Mean fold increase of organoid radius, R/R_c, at $T = 7$, for different inlet fluxes, Q. The parameter values used are given in Table 5.2.

which grow larger than the 8.5 fold increase desired by Cellesce. This suggests, that for an inlet flux of $Q = 10$, the experiment run time of 7 days is too long and a shorter run time would yield more organoids within the ideal size range.

We investigate the temporal evolution of mean and standard deviation of fold increase of organoid radius in Figure 5.17. We find, as expected, that organoid size is monotonically increasing in time. We observe that there is an initial transient period of approximately two days, where the organoids consume the glucose which is initially supplied in the bioreactor (cf. Section 5.2.3), and the mean organoid size has negligible variation with inlet flux. With increasing Q, the time when the rate of organoid radius increase begins to decrease occurs later in the experiment. When $Q = 0.1$ this occurs at $T \approx 3$; for $Q = 1$, this increases to $T \approx 4$; and for $Q = 10$, this occurs at $T \approx 5.5$. For the higher inlet fluxes, the mean organoid size is perhaps too large for requirements. For, *e.g.* $Q = 10$, it would be more beneficial to stop the experiment at $T = 5$, since the mean fold increase in organoid size is 5.5 and the standard deviation is 0.36. By $T = 6$, the organoids have grown to 7.1 times their initial size, but, more crucially, the standard deviation is 0.91 — a 2.5 fold increase.

Table 5.5: Proportion of domain with organoids of fold increase in radius which are smaller, in, or larger than the desired range for 'one inlet, one outlet' set-up with varying inlet flux Q after 7 days. The parameter values used are given in Table 5.2.

Outlet position, X_O	Inlet flux, Q	Proportion of domain in which fold increase in organoid radius lies within a specific range		
		$R/R_c < 4$	$4 < R/R_c < 8.5$	$R/R_c > 8.5$
0.25	0.1	0.617	0.376	0.00699
0.25	1	0.0169	0.913	0.0696
0.25	10	0	0.486	0.514

In Figure 5.17(a)(**inset**), we plot the mean and standard deviation of the fold increase of organoid radius at $T = 7$, which highlights that *by the end of the experiment*, the variation in organoid size increases with increasing flux. In Figure 5.17(b), we see that the variation in organoid radius increases with increasing time. After an initial period of low variation, the variation suddenly increases. As Q increases, the standard deviation increases at later times but also at a greater rate. In Figure 5.17(c), we see that there is a significant difference in organoid size by increasing the flux, and hence culture media velocity, by two orders of magnitude. The behaviours diverge for $T \geq 2$. However, the relationship is nonlinear, since increasing Q by 100 does not increase in organoid radius by 100 fold.

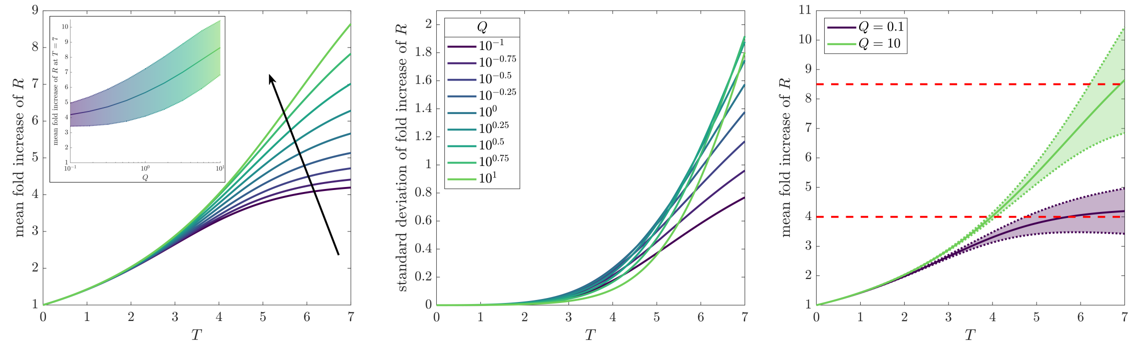

(a) (**main**) mean R/R_c; (**inset**) mean and standard deviation of R/R_c at $T = 7$ vs Q

(b) standard deviation of R/R_c

(c) mean and standard deviation of R/R_c for $Q \in \{0.1, 10\}$

Figure 5.17: Series of plots showing how the mean and standard deviation of fold increase of organoid radius, R/R_c, evolve over time as the inlet flux, Q, varies. Inlet flux values are $Q = 10^k$, for $k \in \{-1, -0.75, -0.5, 0.25, 0, 0.25, 0.5, 0.75, 1\}$. Arrow direction indicates increasing flux. The parameter values used are given in Table 5.2.

We consider the behaviour of the glucose concentration over time in Figure 5.18. We see that increasing Q corresponds to higher glucose concentrations over time. For earlier times ($T < 5$), this is also associated with lower variation in glucose. The results indicate that large, consistent glucose concentration leads to uniform growth.

These results suggest that the standard inlet flux of $Q = 1$ may be too low for the desired organoid output and that a flux of $Q = 10$ may be too large for a 7 day experimental run time and also inefficient in terms of resource usage. We anticipate that an intermediate value of Q may be optimal.

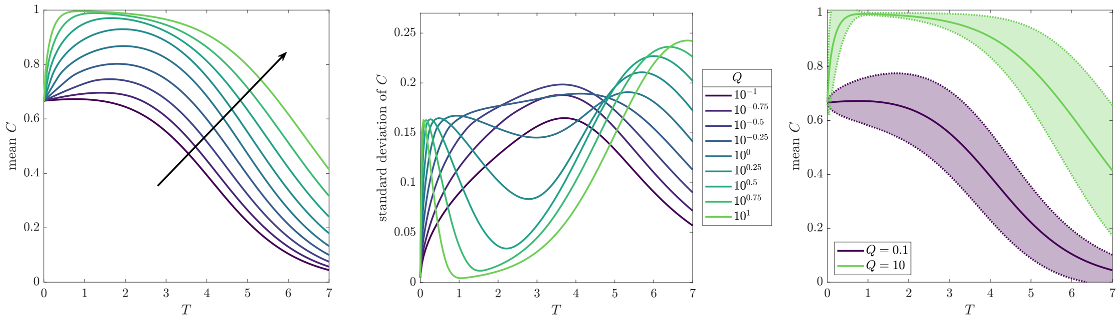

(a) mean glucose

(b) standard deviation of glucose

(c) mean and standard deviation of glucose for $Q = 0.1, 10$

Figure 5.18: Series of plots showing how the mean and standard deviation of glucose concentration, C, evolve over time as the inlet flux, Q, varies. Inlet flux values are $Q = 10^k$, for $k \in \{-1, -0.75, -0.5, 0.25, 0, 0.25, 0.5, 0.75, 1\}$. Arrow direction indicates increasing flux. The parameter values used are given in Table 5.2.

5.2.4.2 Cost-effective volumetric inlet flux

The model exploration in Section 5.2.4.1 suggests that the amount of glucose required within the CXP1 bioreactor is not constant. Rather, it increases in time and depends on the size of the organoids. Therefore, we propose that a better operating protocol, that simultaneously reduces resource wastage while also improving organoid growth and minimising spatial variation, would be to vary the inlet flux over time. To test this hypothesis, we consider a piecewise constant flux $Q = Q_{CE}(T)$ of the form:

$$Q_{CE}(T;\tau) = \begin{cases} \dfrac{1}{3} & \text{for } 0 \leq T \leq \tau, \\ 2 & \text{for } \tau < T \leq 7, \end{cases} \tag{5.2.7}$$

where the control parameter τ determines the time at which we increase the flux. We assume that the jump in flux, and associated increase in culture media velocity, happens instantaneously at $T = \tau$.

We plot the mean and standard deviation of the fold increase in organoid radius in Figure 5.19. We observe that the earlier the flux increases (the smaller τ is), the larger the organoids. As expected, the rate of increase in organoid size increases significantly when the flux increases. We compare this inlet flux protocol, Equation (5.2.7), to the standard operating protocol, and find that for $\tau \leq 5$, the time-dependent flux protocol produces organoids with a greater mean radius. The standard deviations for all τ and for $Q = 1$ are similar for the first 5 days (Figure 5.19(b)). After $\tau = 7$ (corresponding to a constant inlet flux of $Q = 1/3$) has the lowest spatial variation. However, this does not mean that $\tau = 7$ is the best choice for CXP1 operation — we saw in Section 5.2.4.1 that low fluxes give rise to much poorer metabolite environment for organoid growth and, therefore, a significant proportion of the organoids cultured will be smaller than the minimum 4 fold increase required.

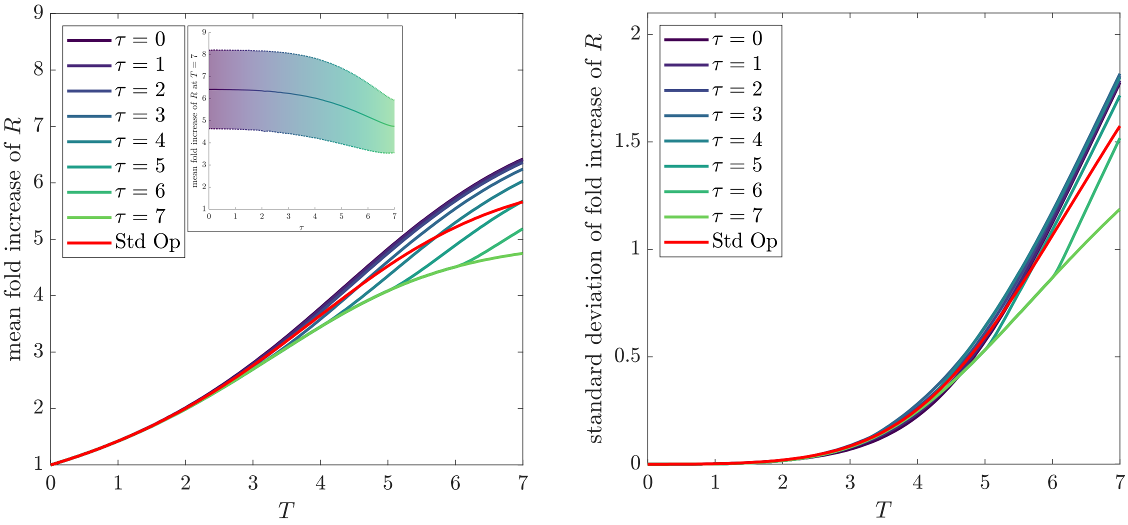

(a) (**main**) mean R/R_c; (**inset**) mean and standard deviation of R/R_c at $T = 7$ vs τ

(b) standard deviation of R/R_c

Figure 5.19: Mean and standard deviation of fold increase of organoid radius, R/R_c, evolving in time for different functional form of fluxes, $Q = Q_{CE}(T;\tau)$. The parameter values used are given in Table 5.2.

In Figure 5.20, we plot the mean and standard deviation of the mean fold increase of organoid radius at $T = 7$. We note that the total volume of culture media required for operation varies with τ. For $\tau > 4.2$, the time-dependent flux protocol uses less culture media than the standard operating conditions with constant flux $Q = 1$. We find that for $\tau \in (4.2, 5.03)$, using $Q = Q_{CE}(T;\tau)$ produces a mean fold increase in organoid radius greater than taking $Q = 1$, while also using less culture media. Although the standard deviation of organoid radius for $Q_{CE}(T = 7, \tau \in (4.2, 5.03))$ is larger than for constant flux, the increase is only approximately 10%. In Figure 5.20(a)(**inset**), the proportion of culture media that can be saved by using inlet flux $Q_{CE}(T;\tau)$ is plotted against $\tau \in (4.2, 5.03)$. We can save up to 19% of the total volume of culture media by changing from a constant inlet flux $Q = 1$ to a time-dependent flux, $Q = Q_{CE}(T;\tau)$. This shows that varying the inlet flux to take into account the organoid size and glucose requirements is a more cost-effective approach. It also shows how our mathematical model can be used to identify ways to improve operating protocol, though we note that a more complex procedure would be required to fully optimise protocol.

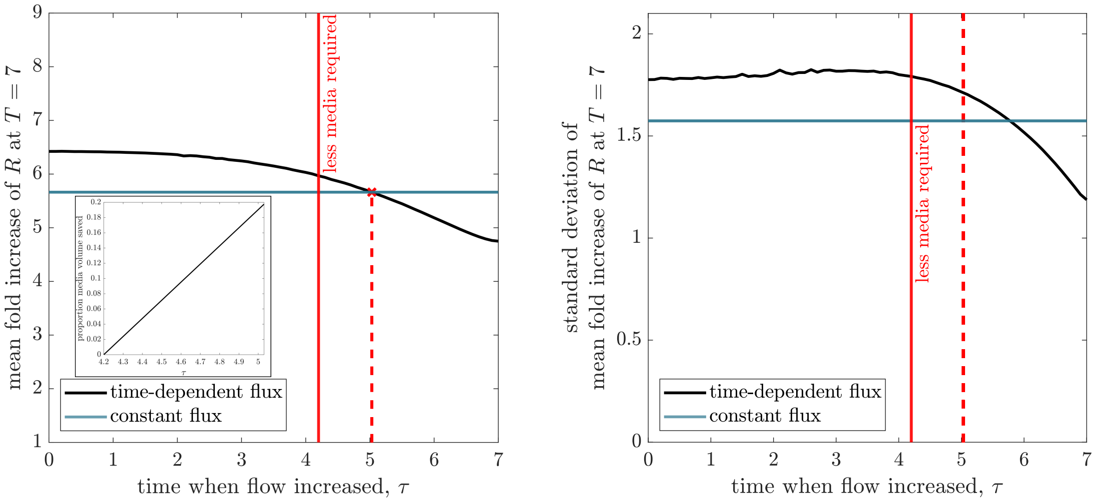

(a) (**main**) mean R/R_c at $T = 7$; (**inset**) proportion of culture media volume saved vs τ

(b) standard deviation of R/R_c at $T = 7$

Figure 5.20: Mean and standard deviation of fold increase of organoid radius, R/R_c, at $T = 7$ for different functional form of fluxes, $Q = Q_{CE}(T; \tau)$, as a function of τ. Solid red line indicates the time at which the total volume of culture media used is the same as the current operating protocol. The dashed red line indicates the time at which the time-dependent flux performs the same as the current operating protocol. The parameter values used are given in Table 5.2.

5.2.5 Streamfunction-arclength formulation

We have gained valuable insight by investigating the reduced model in Cartesian coordinates (Equations (5.1.30) and (5.1.35)) in Sections 5.2.3 and 5.2.4. Now, we explore the reduced model in streamfunction-arclength formulation. In this coordinate system, we can better understand the behaviour along a streamline and how the upstream metabolic environment affects organoid growth downstream.

5.2.5.1 Solving the metabolite transport model along streamlines

In this Section, we solve the reduced model in streamfunction-arclength formulation for the standard operating conditions of CXP1 (see Equation (5.1.50) derived in Section 5.1.3 and associated parameter values in Table 5.2). We solve the model for nine streamlines, uniformly spaced with $\psi \in [-Q/(2(1-H_H)), -0.01Q/(2(1-H_H))]$, defined by

$$\psi = \psi_j^* \quad \text{for } j = 1, \ldots, 9, \tag{5.2.8a}$$

$$\text{where} \qquad \psi_j^* = -\frac{Q}{2(1-H_H)} + \frac{(j-1)}{9}\frac{0.99Q}{2(1-H_H)}, \tag{5.2.8b}$$

and standard operation protocol uses a volumetric inlet flux of $Q = 1$.

The initial and boundary conditions in Equation (5.1.50) for glucose are inconsistent. Furthermore, since we have neglected diffusion along streamlines, a shock could form. Indeed, in Section 2.4.2, we observed a shock solution for a similar system, but were able to determine analytic solutions in each of the regions either side of the shock. To avoid issues with numerically solving for shock solutions, instead we impose impose $\bar{C} = 1$ at $T = 0$, for consistency with the boundary condition. We note that this initial condition is not consistent with the physical system we have thus far considered. This is equivalent to increasing the initial supply of glucose within the bioreactor by a half. Although we cannot quantitatively compare the metabolite concentrations to those computed from the Cartesian formulation of the model considered in Sections 5.2.2 to 5.2.4, the results are still qualitatively similar and are informative. At later times, we expect the organoids to have consumed the initial glucose supply and to be reliant on glucose entering through the inlet pipe and transported via advection. Future work would be to consider solution of the experimental initial conditions Equation (5.1.50).

We show the (X, Y)-coordinates of these 9 streamlines in Figure 5.21(a) and the velocity along these, parameterised by s (defined in Equation (5.1.47)), in Figure 5.21(b), where each colour in Figures 5.21(a) and 5.21(b) represents a streamline $\psi = \psi_j^*$ defined in Equation (5.2.8). We also plot the velocity as a colourmap on the (X, Y)-coordinates of each streamline in Figure 5.21(c). Comparison of Figure 5.21(c) to Figure 5.21(b) reveals that the minima in media velocity occur when streamlines turn a corner. We see that as $|\psi|$ decreases, s becomes more stretched across the domain.

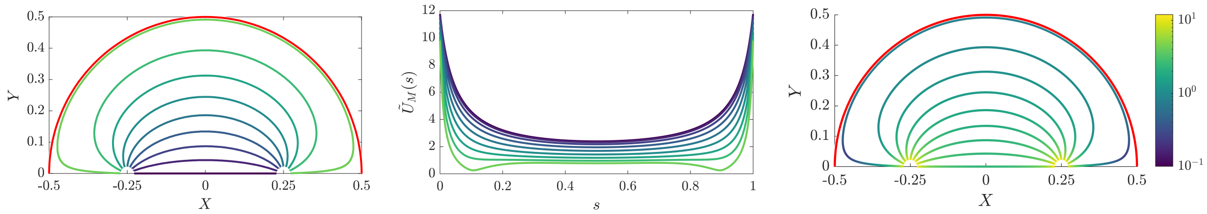

(a) Position in (X, Y)-plane of streamlines considered

(b) Velocity along streamline

(c) Velocity along streamline in (X, Y)-plane

Figure 5.21: The behaviour of the 9 streamlines considered in Section 5.2.5.1.

We plot the concentrations of glucose and lactate and fold increase in organoid radius at the end of the experiment, $C(\psi, s, T = 7)$ and $W(\psi, s, T = 7)$, and $R(\psi, s, T = 7)/R_c$, respectively, in Figure 5.22. In the top figures, we plot C, W, and R/R_c against the arclength parameter s, where $s \in [0, 1]$, and in the bottom figures, we plot C, W, and R/R_c against the arclength $\mathcal{L}$, where $\mathcal{L} \in [0, \mathcal{L}^{\text{total}}(\psi)]$. We see that the glucose concentrations increase and the lactate concentrations decrease at all points along the streamline for increasing $|\psi|$. Correspondingly, the fold increase in organoid radius is higher for higher glucose levels and lower lactate levels, *i.e.* the behaviour of the fold increase in organoid radius is qualitatively similar to the glucose concentration. By plotting the glucose, lactate, and fold increase in organoid radius against the distance travelled along the streamline $\mathcal{L}$, we see that not only are the organoids along the streamline exposed to lower glucose and higher lactate concentrations, but many more organoids are on these longer streamlines. Therefore, the domain has worse metabolite conditions than one may expect from inspection of the top figures in Figure 5.22.

Our observations suggest that to reduce variation along a single streamline, we should reduce streamline length. Combining this with our previous observation that less variation in streamline length reduces variation of organoid radius between streamlines, we deduce that the optimal regime would be one that minimises both length of streamlines and the variation in their length across the CXP1 bioreactor (which we observed in Section 5.2.3 when varying the inlet and outlet positions $|X_O|$).

We now consider the temporal evolution of the metabolite concentrations and organoid radius. We consider three streamlines, corresponding to the (X, Y)- coordinates and streamline velocity shown in Figure 5.23, described by $\psi = \psi_j^*$ for $j = 1, 5, 9$, where we define ψ_j^* in Equation (5.2.8). We refer to ψ_1^* as *short*, ψ_5^* as *mid*, and ψ_9^* as *long*, to emphasise that there is a significant difference in $\mathcal{L}^{\text{total}}$ for these streamlines ($\mathcal{L}^{\text{total}}(\psi_1^*) = 0.456$; $\mathcal{L}^{\text{total}}(\psi_5^*) = 0.649$; $\mathcal{L}^{\text{total}}(\psi_9^*) = 1.86$). In Figure 5.24, we present the glucose (top), lactate (middle), and fold increase of organoid radius (bottom) for the three different streamlines every day throughout the experiment ($T = 0, 1, 2, \ldots, 7$). We see that over time, the rate at which glucose concentration decreases from the inlet value ($C = 1$) increases for all streamlines. For the *long* streamline, the rate of decrease of glucose is fast and then plateaus, with only small variation of glucose concentration for $s > 0.2$. This plateau begins at around $s \approx 0.1$, and corresponds to where the streamline rounds a corner (see Figure 5.23(b)). This indicates that these 'slow flow' regions adversely impact downstream nutrient transport and enable the lactate levels to accumulate before they are advected downstream, where they inhibit organoid growth.

In Figure 5.25(bottom), the flow of media from the inlet pipe only starts making a significant impact after about 4 days. The rate of organoid increase is greater towards the inlet $s = 0$, where glucose levels are high. By 15% of the way along

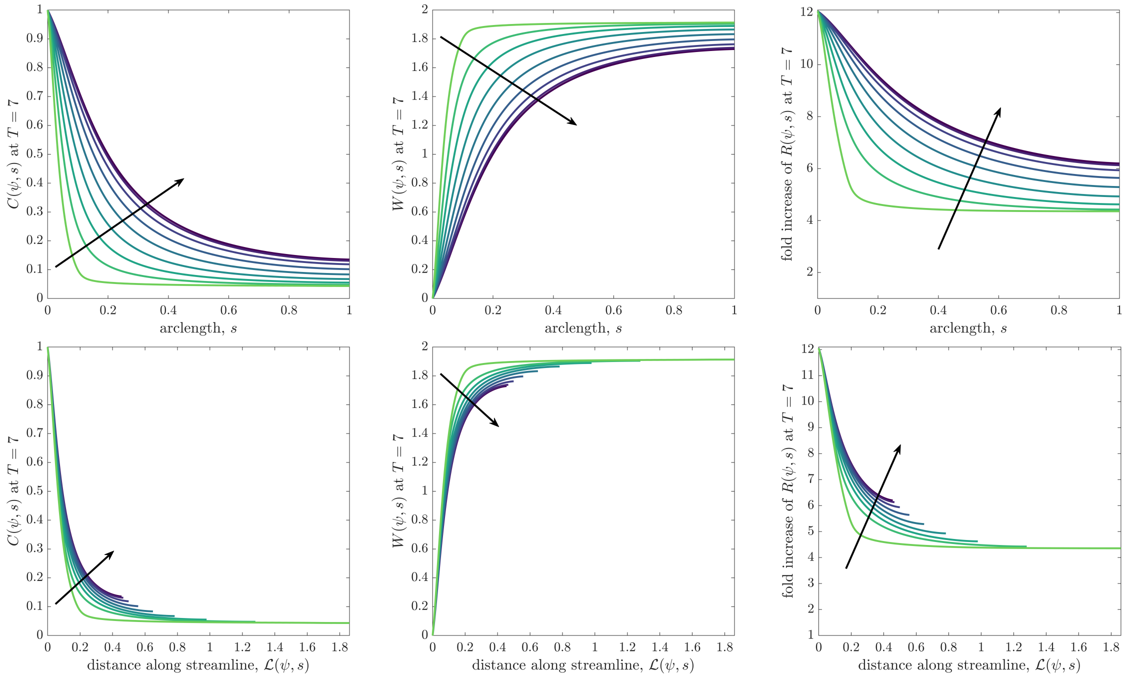

(a) glucose (b) lactate (c) fold increase of organoid radius

Figure 5.22: Glucose, C, and lactate, W, concentrations and fold increase of organoid radius along streamline at $T = 7$: (**top**) plotted against parameterisation of streamline s; (**bottom**) plotted against distance travelled along streamline $\mathcal{L}(\psi, s)$. Arrow direction indicates increasing $|\psi|$. The parameter values used are given in Table 5.2.

the *long* streamline, insufficient glucose is supplied via advection to enable organoid growth at days 6 and 7. This suggests Cellesce should halt the experiment by day 6, since the organoids in $s \in (0.2, 1]$ are roughly the same size, and with less spatial variation, as for day 7, since the maximum organoid radius increase is approximately 8 fold, rather than 12. These organoids are slightly larger than the minimum 4-fold increase required by Cellesce.

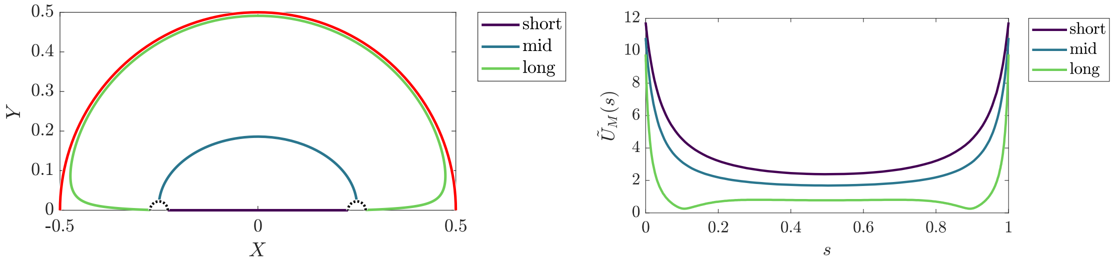

(a) Position of streamlines (b) Velocity along streamlines

Figure 5.23: Position in (X, Y)-plane of and velocity along three streamlines of different lengths.

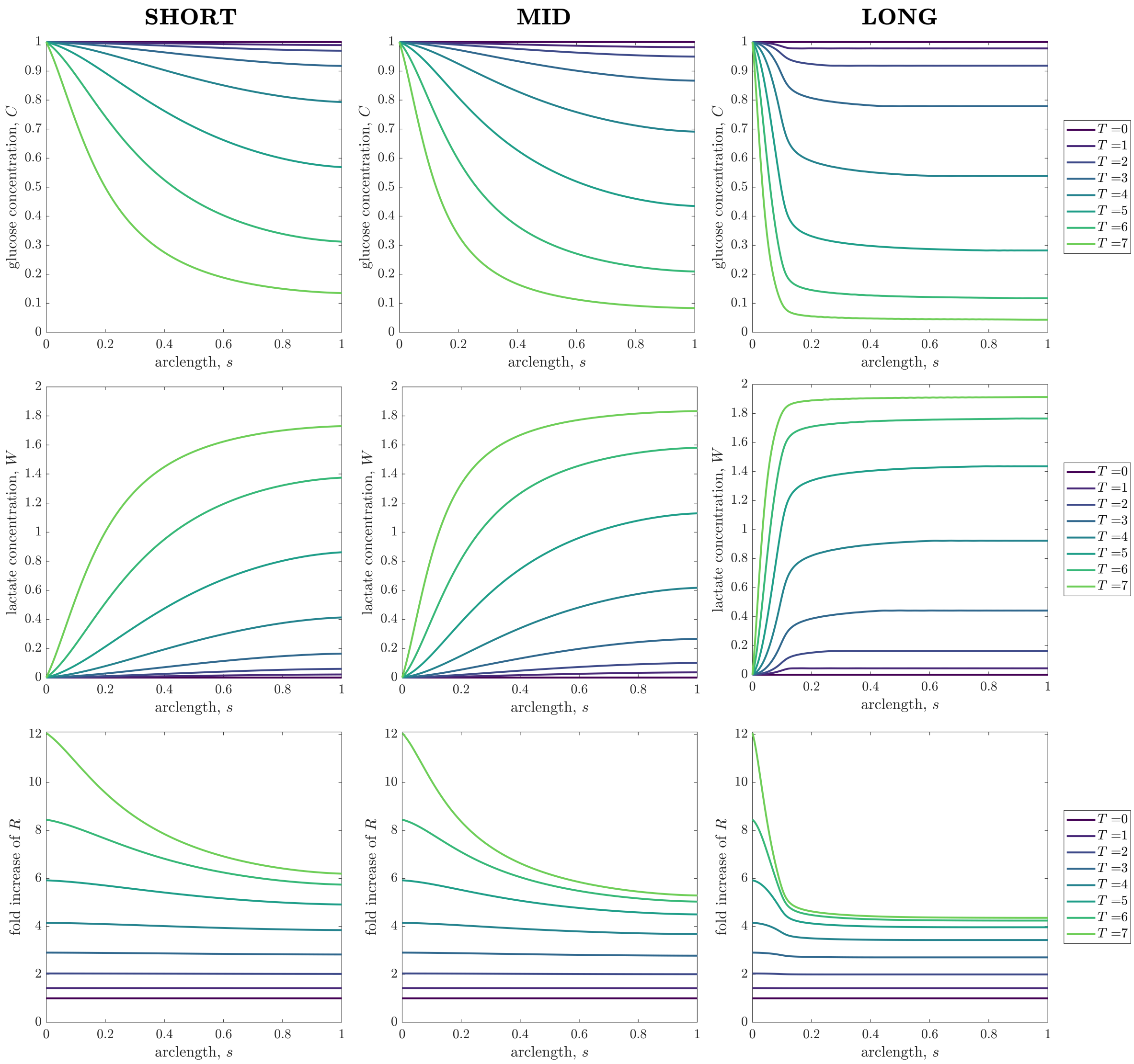

Figure 5.24: Series of plots showing the glucose (**top**) and lactate (**middle**) concentrations and fold increase in organoid radius (**bottom**) along three different streamlines, plotted at daily intervals. The parameter values used are given in Table 5.2.

We can also plot the metabolite concentrations and fold organoid radius increase along these three streamlines ($\psi = \psi_j^*$ for $j = 1, 5, 9$) as continuous functions in time, Figure 5.25. Most of the spatial variation in fold increase in organoid radius is masked by the larger variation in organoid radius in time. Since the glucose and lactate concentrations always range between $[0, 1]$ and $[0, 2]$, respectively, it is easier to see the variation in s. As we noted earlier, $(2C + W)$ is a conserved quantity and we can see this clearly in Figure 5.25.

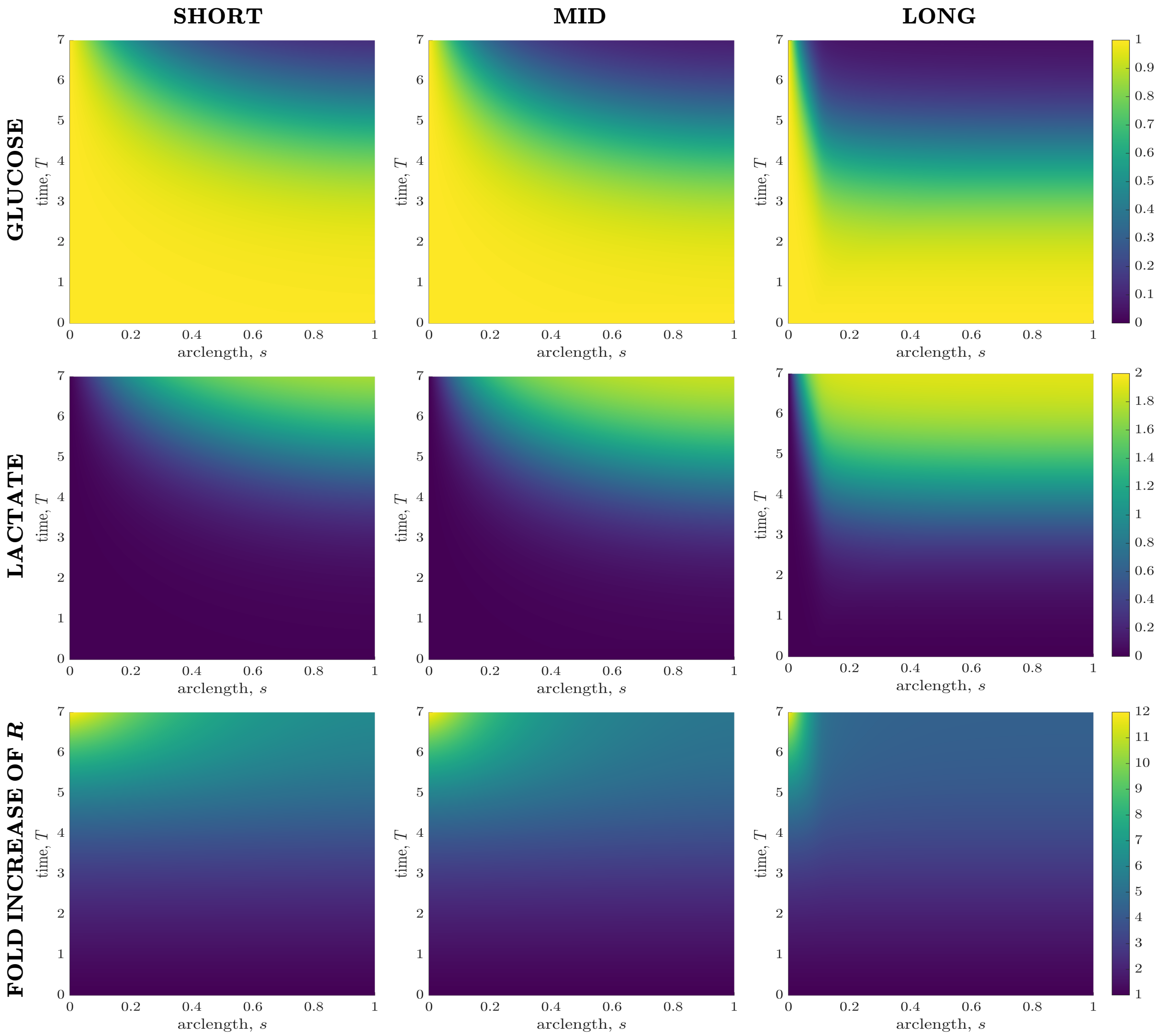

Figure 5.25: Series of plots showing the metabolite concentrations and fold increase in organoid radius along three different streamlines evolving in time throughout the duration of the experiment. The parameter values used are given in Table 5.2.

5.3 Discussion

We have presented an unsteady 3D model for metabolite transport throughout the CXP1 bioreactor, which we coupled to a model for organoid growth. We used asymptotic analysis to reduce the dimensionality of the model, by exploiting the extreme spatial and temporal parameter ratios in our system. We combined the approaches from Chapter 2 and Chapter 3 to develop a continuum macroscale model based on relevant microscale level information, coupled to the flow model in Chapter 4. Our model predicts the spatiotemporal distribution of the metabolic environment within the bioreactor and how organoids cultured under these conditions would grow and influence the local metabolite concentrations. This information is infeasible to gain from experiments alone. The flexibility of our model has enabled us to explore the influence of key parameters of the CXP1 operating protocol — such as inlet and outlet pipe positions and culture media inlet flux — on the glucose and lactate concentrations and the associated organoid growth.

Our reduced model consists of a coupled reaction-advection system for glucose and lactate transport, and a growth model for the evolution of the organoid radius. Through careful consideration of the media flow field, we transformed the coordinate system from Cartesian (X, Y) to streamfunction-arclength (ψ, s), and showed how this allows further model simplification from 2D to 1D. We derived a system of 1D reaction-advection PDEs for glucose and lactate, which describes the transport of metabolite along a streamline. Each choice of coordinate system has its own advantages. In a Cartesian frame, it is intuitive to understand the spatial variation in metabolite and organoid size across the whole bioreactor — in particular, *between* streamlines — and how the positioning of the inlet and outlet pipes affects nutrient delivery and waste removal. The streamfunction-arclength formulation is convenient to understand how the metabolite levels and organoid size vary *along* a streamline. It is less computationally expensive to solve, and allows us to solve only 'extremes' of streamlines to predict the best and worst case scenarios possible for a given operational set-up.

Our reduced model enabled us to efficiently explore a range of operating conditions for the CXP1 bioreactor. We found that changing the position of the inlet and outlet pipes affects the flow of culture media and hence the metabolite transport, since the dominant transport mechanism is advection. We found that increasing the distance between the pipes gives less spatial variation in metabolite levels and organoid radius, corresponding to a flow with less variation in streamline length. However, after the first couple of days, there was always spatial variation in metabolite levels and organoid size. We investigated the behaviour of a set-up with multiple (three) uniformly spaced inlet pipes and a single outlet at the origin. Since more of the domain was exposed to the fresh culture media entering through the inlet pipe and the average streamline length is shorter than in the 'one inlet, one outlet' case, we expected this to perform better. However, the multiple inlets gave rise to more stagnation points and slow flow regions, and therefore increasing the number of inlets is not necessarily the ideal operating protocol. Our results indicate that we can optimise the position (and number) of the pipes to reduce the spatial variation between streamlines within the bioreactor by minimising the variation in streamline length. However, only limited progress can be made to reduce spatial variation, due to: (1) the insufficient glucose levels within CXP1 at later times, and (2) the inherent spatial variation along each streamline. These factors are due to the large nutrient requirement for the size of organoid that exist by the later stages of culture.

We also considered the effect of varying the inlet flux. Increasing inlet flux corresponds to faster flow of culture media and an increase in organoid size everywhere. Small organoids (those which exist at early times) require less glucose and can manage with lower levels of inlet flux, however large organoids require more glucose and therefore require higher inlet fluxes to maintain the same rate of proliferation. Our results suggest that under the current operating conditions of a constant inlet flux, that we are initially oversupplying glucose and by later times are significantly undersupplying glucose. When we increased the inlet flux by an order of magnitude, we found that there was still spatial variation. Furthermore, over half of the organoids were larger than the ideal range of 40µm to 85µm and, since this protocol requires ten times the volume of culture media without a highly significant improvement in organoid output, it is wasteful and an inefficient use of resources. We note that even when considering the case $Q = 10$ for a run time of 5 days, this utilises 7 times the volume of culture media (as well as increasing the risk of damage of the hydrogel surface due to increased shear stress from the higher velocities of the culture media), suggesting this is not optimal. To this end, we considered a simple 'cost-effective' approach, where we allowed our inlet flux to no longer be constant in time, but a step-function. For an initial period, we prescribed a third of the current inlet flux, and then we increased it (instantaneously) to double the current inlet flux. We found that this protocol produces organoids with the same, or larger, mean fold increase in radius (with only slightly more spatial variation) than the current operating procedure using nearly 20% less culture media. We note that this is a simple, first approach to determining a more optimal inlet flux for organoid growth. Our 2D reduced model is computationally cheap enough to solve that performing more elaborate optimisation approaches is feasible. Varying inlet flux has a significant impact on the spatial variation along a streamline. It is clear that only varying a time-independent inlet flux (within a experimentally feasible upperbound) is insufficient to vastly reduce the spatial variation within CXP1 due to the variation between streamlines (their length and associated velocities). One should consider varying things such as experimental run-time and exploring a time-dependent inlet flux to improve organoid output and reduce running costs.

We used the streamline-arclength formulation to deepen our understanding of the model behaviour along streamlines; how this evolves in time and for different streamlines and, consequently, streamline lengths. We found that near stagnation points, when the flow turns a corner, there are sharp decreases in the culture media velocity. This is bad for nutrient delivery, as less glucose is transported downstream as the organoids consume significant levels of glucose locally while the media only slowly advects the metabolite. The lactate levels also build in these regions, since the media flow is insufficient for clearance at the rate of lactate production, and these high lactate levels are then exposed to the organoids downstream of the slow flow regions. We observed that the metabolite concentrations experienced by the organoids are heavily dependent on (1) which streamline they lie on and (2) how far along the streamline they are, since the organoids at the outlet receive a lot less glucose. This dependence only increases in time.

The mathematical modelling approach taken in this Chapter has given us a framework in which to derive a reduced 2D model to predict metabolite transport and organoid growth within the CXP1 bioreactor. Model validation was not performed due to the extremely limited data currently provided by Cellesce, however the metabolite concentrations and organoid sizes predicted are within the regime (and order of magnitude) of what is typically observed experimentally. We have explored our model to show that by varying the inlet and outlet pipe positions and the inlet flux that it is possible to reduce the spatial variation in organoid radius. Changing inlet and outlet position allows us to alter the flow of culture media, the associated streamlines, and the variation in streamline length, and this, in turn, reduces variation between streamlines. Changing the inlet flux allows us more control over the glucose concentrations along a streamline and an avenue for minimising variation along a streamline. The existence of this 2D reduced model for the CXP1 bioreactor means that it is feasible to optimise over a range of a large space of operating protocol variables, which we have shown to have influence over the organoid output.

Chapter 6

Conclusions and future work

The work contained in this thesis was motivated by the culture of organoids within a bioreactor, specifically developing mathematical models to describe the interplay between metabolite transport and organoid growth. The goal was to determine spatiotemporal information concerning glucose and lactate concentrations and organoid size within the CXP1 bioreactor. This information is required to optimise the bioreactor operating conditions and we take a mathematical modelling approach, because this information is infeasible to obtain experimentally. In this Chapter, we summarise the work covered in the thesis and its implications, and highlight avenues for future work.

6.1 Summary of work

In Chapter 2, we considered a 2D representation of the bioreactor system, as a simple idealised model that retains the key biological features but can be probed analytically. We developed an unsteady model for the transport of two metabolites — glucose and lactate — within the culture media and hydrogel layers. The effect of the organoids on metabolite levels was modelled via a volumetric (bulk) reaction term in the hydrogel, and the organoids were assumed to grow exponentially, at a rate independent of local metabolite concentrations. Motivated by the extreme parameter ratios in the system (firstly, the aspect ratio of the bioreactor depth to lengthscale and, secondly, the separation of timescales between the metabolite transport and reaction mechanisms) and the observation that there is minimal depth variation in the numerical simulations, we utilised asymptotic analysis to systematically reduce the spatial dimension of the model from 2D to 1D. We used a lubrication scaling to derive the *longwave approximation*, a coupled system of reaction-advection-diffusion equations (second-order 1D parabolic PDEs). The asymptotic analysis enabled us to identify the dominant transport mechanisms on our timescale of interest — on the order of days, since the experiment occurs over 7 days. We found that vertical diffusion occurs on the timescale of hours; growth and metabolite consumption/production occur on the timescale of days; and horizontal diffusion occurs on the timescale of months. We also exploited the separation of timescales for the transport mechanisms to obtain the *sublimit approximation*, a reaction-advection system (first-order 1D hyperbolic PDEs). A strength of the sublimit approximation is its analytic tractability; we obtained explicit solutions via the method of characteristics, which revealed the spatiotemporal-dependence of the metabolite concentrations, as well as their dependence on bioreactor control parameters, such as the media flow rate. We found that the sublimit approximation can give rise to discontinuous shock solutions if the initial and boundary conditions are inconsistent. The solution has two distinct regions, either side of the dividing characteristic (the 'shock'): an *unreplenished region*, in which the organoids subsist on the initial glucose within the bioreactor; and a *replenished region*, in which fresh culture media shapes the spatial distribution of the metabolites. We showed that the reduced models serve as excellent approximations of the full 2D system averaged in depth for physically relevant parameter regimes. When varying the flow rate, we found that there were two regimes for the bioreactor operation: (1) *transport-limited*, where there was insufficient nutrient delivery/waste removal (for flow rates lower than a threshold value); and (2) *proliferation-limited*, where the rate of cell growth set the timescale at which lactate is produced (for flow rates above this threshold value). We identified a trade-off between promoting high glucose conversion (to minimise resource wastage and operating costs), ensuring high glucose levels (for consistent, high levels of cell proliferation), and keeping lactate within tolerable levels. Our model allows efficient calculation of these quantities.

In Chapter 3, we focused on accurately capturing the microscale behaviour of the organoids within the hydrogel and how to model individual organoids suspended within the hydrogel as an effective continuum. We presented a 3D model for glucose and lactate transport coupled to organoid growth within a hydrogel. The organoids are modelled as spherical regions with time-varying radius, in which metabolites diffuse, glucose is consumed, and lactate is produced. We consider both *dense* organoids, which are dense clusters of cells (with packing space) and exhibit volumetric metabolite consumption/production, and *shell* organoids, which comprise a single layer of cells with metabolite consumption/production localised to the organoid-hydrogel interface. The metabolites diffuse in the hydrogel region. At the (moving) interfaces between the organoids and hydrogel region, we imposed continuity of metabolite concentration and flux. Since it is computationally challenging to resolve the full problem (due to the multiply connected 3D domain involving millions of moving boundaries between the organoid and hydrogel regions), we employed mathematical homogenisation (via the method of multiple scales) to derive the effective macroscale behaviour of metabolite transport across the entire 'organoid-hydrogel' region. The resulting homogenised model consists of a coupled reaction-diffusion system for metabolite transport, where the effective diffusion and reaction terms depend on the microscale structure. The effective diffusivity of metabolites is determined via solution of the 'cell problem'. This is a quasi-steady problem within each periodic 'cell', consisting of Laplace's equation in the organoid and hydrogel regions, coupled with a partition condition and discontinuous flux condition at the organoid-hydrogel interface and periodicity conditions at the cell boundary. The uptake terms scale with the volume of the organoids for dense (volumetric uptake) organoids and with the surface area for shell (surface uptake) organoids, as might be expected on physical grounds. Although the cell problem is quasi-static, it is coupled to the evolving organoid microstructure. Therefore, we reformulated the cell problem so that it could be solved *a priori* to the coupled macroscale metabolite transport and organoid growth models, reducing the computational expense further.

Through consideration of idealised problems representing static and flowing culture media conditions, we determined how the organoid radius depends explicitly on the local metabolite concentrations, as well as the characteristics of the cell lines used to generate the organoids (*e.g.* glucose requirements, sensitivity to lactate, organoid structure). We considered modified Michaelis-Menten glucose consumption/lactate production reaction kinetics, and assumed that cell proliferation is proportional to the rate of glucose consumption. The sensitivity of a cell line to lactate was incorporated by modifying the Michaelis constant (concentration at which the reaction rate is half the maximum rate achievable) to depend on the local lactate concentration. As a result, the optimal flow rate is unique to each organoid line and must be determined for each hydrogel (macroscale) geometry and organoid line. With a homogenised metabolite transport model, it is possible to determine the influence of the organoid behaviour at the microscale on the macroscale metabolite environment and organoid output and, in this way, identify optimal flow rates for different organoid lines.

In Chapter 4, we developed a model for the flow of culture media within the CXP1 bioreactor, motivated by the advection-dominated nature of metabolite transport within the layer of culture media. We modelled the flow using incompressible

Navier-Stokes and continuity equations. Using a lubrication scaling, we showed that the depth-dependence of the flow decouples and, therefore, the problem can be formulated as a two-dimensional problem (with Laplace's equation governing the pressure) in the horizontal plane, with a point source and a point sink, representing the in/out-flux of culture media through the inlet and outlet pipes, respectively. The flow profile in depth is half-Poiseuille flow. We derived analytical expressions for the velocity potential and streamfunction, and related these to the velocity profile within the bioreactor. We showed that the flow is fundamentally driven by, and therefore qualitatively dependent on, the number and position of inlet and outlet pipes. We found that varying the inlet and outlet pipe positions significantly influences glucose delivery and lactate removal and, ultimately, organoid growth.

In Chapter 5, we combined the approaches from Chapter 2 and Chapter 3, and incorporated the media flow model derived in Chapter 4, to derive a model for unsteady 3D metabolite transport and organoid growth within the CXP1 bioreactor. An important feature of this macroscale model is that it systematically retains information about the evolving microstructure within the hydrogel. Our model predicts not only the spatiotemporal distribution of the metabolites within the bioreactor and the growth of organoids cultured under these conditions, but also the way in which the organoids locally influence metabolite levels. The flexibility of our model has enabled us to explore the influence of key parameters of the CXP1 operating protocol — such as inlet and outlet pipe positions and culture media inlet flux — on the metabolite concentrations and organoid growth in a straightforward manner. We used asymptotic analysis to systematically reduce the full 3D model to a more tractable 2D model by averaging in depth (analogous to the systematic reduction of a 2D representative region of the bioreactor to a 1D problem via depth-averaging in Chapter 2), and this reduced model consists of a coupled reaction-advection system for metabolite transport and an organoid growth model. We neglected diffusive transport in the horizontal directions, as this occurs on a slower timescale of months compared to advection and reaction, which occurs on the timescale of days. We showed that a judicious change of coordinate system from Cartesian to a streamfunction-arclength formulation reduces the dimensionality of the system further. Using information about the streamfunction (from the media flow model in Chapter 4), we note that the culture media velocity has only one component in this coordinate system — that is, the culture media flows only in the direction along the streamline, and not perpendicular to the streamline (essentially, by definition). Therefore, we change the coordinate system from Cartesian to one in the direction of (and orthogonal to) streamlines, which we refer to as the ‘streamfunction-arclength’ formulation. Each streamline is described by a constant value of streamfunction and a parameterisation for (normalised) distance along the streamline, which we refer to as the arclength. In this ‘streamfunction-arclength’ formulation, our model reduces to a reaction-advection problem along streamlines. The model can be related back to the model from Chapter 2 if we view the system in Chapter 2 as a transport problem for metabolites along a streamline, where the the horizontal spatial variable is interpreted as the arclength. However, we note that the work in Chapter 2 does not account for the variation in flow strength along a streamline. We showed in Section 5.2 that any ‘slow flow’ regions (near stagnation points) hinder nutrient delivery and that waste accumulates in these regions, and therefore bioreactor geometry should be chosen to minimise the number of ‘slow flow’ regions. We found that moving the inlet and outlet pipes further apart reduces the spatial variation in metabolite concentration and organoid size, and this corresponds to minimising the variation in streamline length across the bioreactor. The mean glucose levels are higher and the mean lactate levels are lower the further apart the inlet and outlet pipes. However, there is inherent spatial variation along each streamline, which becomes more pronounced the longer the streamline. This suggests that one should decrease the length of streamlines, to minimise spatial variation along streamlines. When we varied the inlet media flux, we found that under the current operating regime, the organoids receive an excess of nutrients at early times and a deficit at later times (*i.e.* at the end of the experiment). This led us to propose a ‘cost-effective’ piecewise constant flow rate, which achieves similar results to the current culture conditions with markedly reduced media requirements.

Throughout this thesis, we have developed models to answer questions that we initially posed — *are the glucose concentrations sufficiently high and the lactate levels sufficiently low within CXP1?*, and *can we alter the operating parameters to ensure spatially uniform metabolite concentrations?*. We have determined the spatiotemporal glucose and lactate concentrations and shown that, depending on the positioning of the inlet and outlet pipes, regions in which the organoids do not receive sufficient nutrients may form. These regions coincide with areas of high lactate concentrations, which may be intolerable to the organoids (depending on the sensitivity of the organoid line to lactate levels). We explored different operating conditions, characterised by different flow regimes and inlet/outlet positions, to understand their influence on spatial variation in both metabolite distributions and organoid size. Our recommendation to Cellesce, as a simple first step to improving CXP1 operation, is to incorporate a time-dependent flow rate. We observed that, for a constant flow rate, while the organoids are initially oversupplied with nutrient, by the end of the experiment there is insufficient glucose and high lactate build-up within the system. We demonstrated that even having a simple piece-wise constant flow rate — with a slower initial flow rate which then increases later in the experiment (around 4/5 days) — has the benefits of maintaining (or even improving) organoid output while requiring less culture media, therefore decreasing operating costs. We found that, while we can improve on the current operational protocol in terms of reducing spatial variation in metabolite concentration and organoid size, there is limited scope for improvement when only a single control parameter is varied.

We have shown that the bioreactor operating conditions can have a significant impact on the distribution of organoid size within the bioreactor. However, we have shown that altering operating conditions with a sole focus on improving homogeneity in organoid size can have undesirable consequences in terms of introducing significant resource wastage. Therefore, one needs to understand the constraints on the input resources and desired operational outcomes (organoid output), and prioritise accordingly, since the operating parameters and bioreactor outputs have been shown to be interdependent.

The 2D reduced model we derived and analysed in Chapter 5 for the CXP1 bioreactor enables identification of key operating parameters. Importantly, it also means that identification of optimal operating conditions for the bioreactor (its geometry, set-up, and operating conditions) is now feasible, due to the reduced computational costs of a 2D model compared to a 3D model.

6.2 Future work

While we have made significant progress in understanding the fluid flow, metabolite transport, and organoid growth within the CXP1 bioreactor, several avenues for future work naturally lead on from the work contained in this thesis. These are interesting both from a mathematical viewpoint and also for experimentalists, those at Cellesce in particular.

A natural next step is model validation through comparison to experimental data. For example, can we accurately predict metrics such as the mean and standard deviation of organoid size? Although Cellesce do not have spatial data (due to the challenges associated with obtaining such experimental data), they can quantify the number of organoids within the bioreactor at the end of an experiment and determine the organoid size distributions within a representative sample. In the future, Cellesce aim to collect real-time measurements of the metabolite concentrations at the outlet pipe(s). These data could be used to calibrate and validate our model and to compare the dynamics of different organoid lines. To validate our model, we can compare the model-predicted and experimental mean metabolite concentrations at the outlet and also cumulative glucose conversion (Equation (2.5.3)) within CXP1. Ideally, we would obtain data for the organoid size distributions for a series experiments run under the same operating conditions (and same cell line), for different run times (*e.g.* daily, $T = 1, \ldots, 7$). This would allow us to compare the agreement of the mean and standard deviation of organoid size at regular intervals throughout the duration of the experiment. We could use experimental metrics such as cumulative glucose consumption and the initial and final number of cells within the bioreactor to help parameterise the cell line characteristics required for our model — namely, the glucose consumption and cell proliferation rates. It would also be of interest to explore mathematical and experimental agreement of metabolite concentrations and organoid size distributions as the flux of culture media into the bioreactor varies. This would enable us to establish the physical relevance of any mathematically optimised model to the (real-world) CXP1 system. As the mathematical models introduced in this thesis are further developed, it will always be prudent to perform experimental validation. The overarching goal of this research is to develop a framework that accurately captures the organoid growth and metabolite transport within CXP1, and then exploit it to efficiently optimise the CXP1 operating protocol and improve organoid output. Establishing what metrics should be used to identify an ‘ideal organoid output’ remains an open question and requires further discussion with Cellesce.

There are several model extensions that would improve the physiological relevance of the homogenised organoid-hydrogel model. Given the mechanical stimuli experienced by a cell affects its behaviour (*e.g.* proliferation, differentiation) via *mechanotransduction* [19, 42], it would be useful to be able to predict these conditions within the bioreactor. A promising approach involves viewing the hydrogel and organoids as poroelastic materials (see *e.g.* [11] for such an approach), through which culture media can flow while metabolites diffuse and are consumed/produced. By considering the poroelastic behaviour of the hydrogel and organoid regions — in particular, the stresses present at the interfaces between the organoid and hydrogel regions — it would be possible to predict the local biomechanical environment experienced by the organoids. This information could be incorporated into our organoid growth model, enabling consideration of biochemical and biomechanical stimuli on organoid growth.

Other model extensions include a relaxation of the assumption that the organoids are spherical and also variation in the separation distance between organoids. Although it is relatively simple to homogenise our transport model with non-spherical organoids, there is some nuance with how to model radially asymmetric growth. In the regime described in Chapter 3, the metabolite concentrations are uniform across a single organoid, and therefore, under our current growth model, the organoid material proliferates uniformly and the initial organoid shape is retained throughout the experiment. Hence, a more complicated growth model is required, to capture further physiological effects which induce non-uniform organoid growth. The latter extension — variation in organoid separation distance — would be mathematically challenging, although we could consider an approach such as that used in Auton et al. [2], where solute transport within a spatially heterogeneous porous medium with arbitrary obstacle shape and spatially varying anisotropic 'periodic cell' is considered. Such an approach would be of particular interest if the stresses (due to (elastic) deformation of the hydrogel as a result of organoid growth) vary on the organoid-scale and induce/inhibit growth in a particular direction.

Since only 20% of the single cells seeded within the CXP1 bioreactor develop into organoids, the distribution of organoids within the hydrogel is not necessarily uniform. Therefore, it would be of interest to compare the homogenised organoid-hydrogel model from Chapter 3 to a stochastic model, where the organoids are randomly distributed across the hydrogel, rather than the uniform cubic lattice considered in this thesis — a comparison similar to that performed by Bruna and Chapman [5]. Reassuringly, the authors found good agreement between the two approaches, as long as the inclusions were not too dense, and, therefore, we anticipate similar good agreement in the case of our homogenised model.

While in this thesis we have considered steady flows, it would be straightforward to extend our framework to study time-dependent flows, including oscillating flows (as long as the timescale of oscillations is not very fast). As we recommend the introduction of a piecewise-constant inlet flux into the CXP1 operating protocol, we could also consider transitions between these flow regimes, by exploring a time-dependent boundary layer during this relaxation period (a period of time during which the flow is time-dependent as it transitions from one steady state to another). The consideration of unsteady flows will be particularly important when attempting to limit resource wastage while minimising spatial variation in metabolite concentrations across the bioreactor. We anticipate this due to our observations in Chapter 2 that steady flows which facilitate little spatial variation in metabolite concentration also have very low glucose conversion, and therefore are very inefficient in terms of resource usage. The predictions of our mathematical model can be exploited to inform candidate scenarios, *e.g.* differing flow regimes, bioreactor design, and operation. These can be simulated in advance of engineering the prototype bioreactors and, hence, our approach has the potential to streamline the bioreactor development process. Cellesce is currently developing their next generation bioreactor, CXP2, a fluidised bed bioreactor, which has significantly different fluid dynamics to the current CXP1 bioreactor. Future mathematical modelling work in collaboration with Cellesce will be to predict the metabolite transport and organoid growth within CXP2. We anticipate that a fruitful approach would be to utilise the homogenised-organoid hydrogel model derived in Chapter 3 in CXP2-relevant geometry, and couple this to the appropriate flow problem for a fluidised bed, though this will come with additional mathematical challenges.

A key area of future work is the optimisation of the CXP1 operating conditions, using the models developed in Chapter 5. To implement this, we could consider *e.g.* an optimal control approach [53]. Such an approach has been used successfully for optimisation of other bioreactor operations, see *e.g.* [8, 64, 69]. As we have highlighted through this thesis, there are numerous parameters which we have shown influence metabolite concentrations and organoid size across the CXP1 bioreactor. Potential parameters to consider in our optimisation are: number of inlet and outlet pipes; position of inlet and outlet pipes; volumetric inlet flux; experimental runtime; initial cell seeding density; and even bioreactor geometry (such as thickness of organoid-hydrogel layer and length of bioreactor). In this thesis, we have introduced and considered a wide range metrics, such as: *glucose conversion*; *minimum glucose concentration*; *maximum lactate concentration*; *proportion of uninhabitable domain*; *turn-off time*; *mean organoid radius*; *standard deviation in organoid radius*; and *proportion of domain in which organoid radius lies within a specified range.* The specification of an appropriate cost function for the optimisation requires consideration of the desired outcomes and their relative importance for each individual organoid line. For example, benign tissue is significantly more sensitive to lactate than cancerous tissue, which motivates weighting the minimisation of the lactate concentration more strongly for benign organoid lines compared to cancer organoids. The optimal operating conditions are likely to change during the course of the experiment due to organoid growth. Future modelling work could predict how and when operating conditions should change to account for this growth. We anticipate that incorporating the flexibility of a piecewise-constant volumetric inlet flux, with tunable transition times, into an optimisation protocol will be an interesting mathematical problem and improve organoid output. An exciting future development is to create a model which uses real-time data from metabolite concentrations to predict how the inlet flux should be adjusted to yield optimal organoid output, creating a real-time feedback loop.

6.3 Concluding remarks

In conclusion, we have developed a series of mathematical models for coupled metabolite transport and organoid transport within the CXP1 bioreactor. Our models allow us to efficiently predict the spatiotemporal distributions of glucose and lactate, as well as organoid size, across the bioreactor, and to determine how these quantities depend on the bioreactor operating conditions and biological parameters (*e.g.* glucose uptake) — data that is infeasible to obtain experimentally. We have shown the power of asymptotic analysis and mathematical homogenisation techniques to derive accurate reduced-order models. The models developed in this thesis represent important steps towards optimisation of the CXP1 bioreactor operating conditions, and have the potential to improve the quality and reproducibility of bioreactor-expanded organoid output. In future work, our theoretical framework could be used to guide scale-up in the production of viable organoids and, in doing so, contribute to advancing organoid technology, enabling organoids to be exploited as powerful tools for accelerating drug discovery and testing.

Appendix A

Derivation of analytic solution to the sublimit approximation

We consider the sublimit approximation discussed in Section 2.4.2,

$$\alpha\frac{\partial C}{\partial T}+\beta\frac{\partial C}{\partial X}=-\gamma C\exp(PT), \tag{A.0.1a}$$

$$\alpha\frac{\partial W}{\partial T}+\beta\frac{\partial W}{\partial X}=2\gamma C\exp(PT), \tag{A.0.1b}$$

with boundary and initial conditions

$$C=1,\quad W=0\quad \text{at } X=0, \tag{A.0.2a}$$

$$C=\frac{1}{\alpha},\quad W=0\quad \text{at } T=0. \tag{A.0.2b}$$

We can make progress analytically via the method of characteristics.

A.1 Solution for glucose concentration

We begin by considering the glucose concentration, since Equation (A.0.1a) is decoupled from Equation (A.0.1b), and introduce our coordinates in characteristic space, (ξ,τ), where we define

$$\xi=\alpha X-\beta T, \tag{A.1.1}$$

noting that ξ is a constant along each characteristic curve, and τ parameterises the characteristics. Each characteristic curve for Equation (A.0.1a) will satisfy:

$$\frac{\mathrm{d}T}{\mathrm{d}\tau}=\alpha, \tag{A.1.2a}$$

$$\frac{\mathrm{d}X}{\mathrm{d}\tau}=\beta, \tag{A.1.2b}$$

$$\frac{\mathrm{d}C}{\mathrm{d}\tau}=-\gamma Ce^{PT}, \tag{A.1.2c}$$

with our initial data curve, $\Gamma(\xi) = (T(\xi), X(\xi), C(\xi))$ at $\tau = 0$,

$$\Gamma(\xi) = \begin{cases} \left(0,\ \dfrac{\xi}{\alpha},\ \dfrac{1}{\alpha}\right) & \text{for } \ \xi > 0, & \text{(A.1.3a)} \\ \left(-\dfrac{\xi}{\beta},\ 0,\ 1\right) & \text{for } \ \xi < 0. & \text{(A.1.3b)} \end{cases}$$

Solving Equations (A.1.2a) and (A.1.2b) subject to the initial data Equation (A.1.3) gives the coordinate transformations,

$$\text{for } \xi > 0: \begin{cases} T = \alpha\tau, \\ X = \beta\tau + \dfrac{\xi}{\alpha}, \end{cases} \quad \text{and for } \xi < 0: \begin{cases} T = \alpha\tau - \dfrac{\xi}{\beta}, \\ X = \beta\tau. \end{cases} \tag{A.1.4}$$

Region 1, $\boldsymbol{\xi > 0}$:

The governing equation for C, Equation (A.1.2c), becomes

$$\frac{\mathrm{d}C}{\mathrm{d}\tau} = -\gamma C e^{P\alpha\tau}, \tag{A.1.5}$$

which we integrate to obtain

$$C = D(\xi) \exp\left(-\frac{\gamma}{P\alpha} e^{P\alpha\tau}\right), \tag{A.1.6}$$

where $D(\xi)$ is an arbitrary function of ξ to be determined from the initial condition $C(\xi, \tau = 0) = 1/\alpha$ from Equation (A.1.3a). We obtain

$$C(\xi, \tau) = \frac{1}{\alpha} \exp\left(\frac{\gamma}{P\alpha}\right) \exp\left(-\frac{\gamma}{P\alpha} e^{P\alpha\tau}\right) \quad \text{for } \xi > 0, \tag{A.1.7}$$

which we can rewrite in Cartesian coordinates as:

$$C(T, X) = \frac{1}{\alpha} \exp\left(\frac{\gamma}{\alpha P}\left(1 - e^{PT}\right)\right), \quad \text{which holds for } \alpha X - \beta T > 0. \tag{A.1.8}$$

Region 2, $\boldsymbol{\xi < 0}$:

The governing equation for C, Equation (A.1.2c), becomes

$$\frac{\mathrm{d}C}{\mathrm{d}\tau} = -\gamma C e^{P\left(\alpha\tau - \frac{\xi}{\beta}\right)}, \tag{A.1.9}$$

which we integrate to obtain

$$C = E(\xi) \exp\left(-\frac{\gamma}{P\alpha} e^{P\left(\alpha\tau - \frac{\xi}{\beta}\right)}\right), \tag{A.1.10}$$

where $E(\xi)$ is an arbitrary function of ξ to be determined from the boundary condition, $C(\xi, \tau = 0) = 1$. We obtain

$$C(\xi, \tau) = \exp\left(\frac{\gamma}{P\alpha} e^{-P\frac{\xi}{\beta}}\right) \exp\left(-\frac{\gamma}{P\alpha} e^{P\left(\alpha\tau - \frac{\xi}{\beta}\right)}\right) \quad \text{for } \xi < 0, \tag{A.1.11}$$

which we can rewrite in Cartesian coordinates as:

$$C(T, X) = \exp\left(\frac{\gamma}{\alpha P}\left(e^{-P\left(\frac{\alpha}{\beta}X - T\right)} - e^{PT}\right)\right), \text{ which holds for } \alpha X - \beta T < 0. \tag{A.1.12}$$

A.2 Solution for lactate concentration

In a similar manner, we can use the method of characteristics to make analytic progress for the lactate concentration, W. We introduce our characteristic coordinates ξ and τ again, and the governing equation, Equation (A.0.1b), satisfies:

$$\frac{\mathrm{d}T}{\mathrm{d}\tau} = \alpha, \quad \frac{\mathrm{d}X}{\mathrm{d}\tau} = \beta, \quad \frac{\mathrm{d}W}{\mathrm{d}\tau} = 2\gamma C e^{PT}, \tag{A.2.1}$$

with initial data, $\tilde{\Gamma}(\xi) = (T(\xi), X(\xi), W(\xi))$ at $\tau = 0$:

$$\tilde{\Gamma}(\xi) = \begin{cases} \left(0,\ \dfrac{\xi}{\alpha},\ 0\right) & \text{for} \ \ \xi > 0, \quad \text{(A.2.2a)} \\ \left(-\dfrac{\xi}{\beta},\ 0,\ 0\right) & \text{for} \ \ \xi < 0. \quad \text{(A.2.2b)} \end{cases}$$

We have the same coordinate transformation for Regions 1 and 2 as for C, Equation (A.1.4). Hence, we can write the governing equation for W as an explicit integral of known functions:

$$W(\xi,\tau) = \int_0^{\tau} 2\gamma C\left(T(\xi,\tau), X(\xi,\tau)\right) e^{PT(\xi,\tau)}\ \mathrm{d}\tau, \tag{A.2.3a}$$

$$\text{subject to} \quad W = 0 \quad \text{at } \tau = 0, \tag{A.2.3b}$$

where ξ is treated as a constant and C is defined in Equations (A.1.7) and (A.1.11).

Region 1, $\boldsymbol{\xi > 0}$:

For Region 1 ($\xi > 0$), Equation (A.2.1) becomes,

$$\frac{\mathrm{d}W}{\mathrm{d}\tau} = 2\gamma\frac{1}{\alpha}\exp\left(\frac{\gamma}{P\alpha}\right)\exp\left(-\frac{\gamma}{P\alpha}e^{P\alpha\tau}\right)e^{P\alpha\tau}, \tag{A.2.4}$$

We integrate to solve this explicitly, to find

$$W = -\frac{2}{\alpha}\exp\left(\frac{\gamma}{P\alpha}\right)\exp\left(-\frac{\gamma}{P\alpha}e^{P\alpha\tau}\right) + F(\xi), \tag{A.2.5}$$

where the arbitrary function $F(\xi)$ is determined by the boundary condition $W = 0$ at $\tau = 0$ to give $F = 2/\alpha$, and so

$$W(\xi,\tau) = \frac{2}{\alpha}\left(1 - \exp\left(\frac{\gamma}{P\alpha}\right)\exp\left(-\frac{\gamma}{P\alpha}e^{P\alpha\tau}\right)\right), \tag{A.2.6}$$

which we can rewrite in Cartesian coordinates as:

$$W(T,X) = \frac{2}{\alpha}\left(1 - \exp\left(\frac{\gamma}{P\alpha}\left(1 - e^{PT}\right)\right)\right). \tag{A.2.7}$$

Region 2, $\boldsymbol{\xi < 0}$:

For Region 2 ($\xi < 0$), Equation (A.2.1) becomes,

$$\frac{\mathrm{d}W}{\mathrm{d}\tau} = 2\gamma \exp\left(\frac{\gamma}{P\alpha} e^{-P\frac{\xi}{\beta}}\right) \exp\left(-\frac{\gamma}{P\alpha} e^{P\left(\alpha\tau - \frac{\xi}{\beta}\right)}\right) e^{P\left(\alpha\tau - \frac{\xi}{\beta}\right)}. \tag{A.2.8}$$

Similary, we integrate this to find

$$W = -2 \exp\left(\frac{\gamma}{P\alpha} e^{-\frac{P\xi}{\beta}}\right) \exp\left(-\frac{\gamma}{P\alpha} e^{P\left(\alpha\tau - \frac{\xi}{\beta}\right)}\right) + G(\xi), \tag{A.2.9}$$

where the arbitrary function $G(\xi)$ is determined by the boundary condition $W = 0$ at $\tau = 0$ to give $G = 2$, and so:

$$W(\xi, \tau) = 2\left(1 - \exp\left(\frac{\gamma}{P\alpha}\left(e^{-P\frac{\xi}{\beta}} - e^{P\left(\alpha\tau - \frac{\xi}{\beta}\right)}\right)\right)\right), \tag{A.2.10}$$

which we can rewrite in Cartesian coordinates as:

$$W(T, X) = 2\left(1 - \exp\left(\frac{\gamma}{P\alpha}\left(e^{-P\left(\frac{\alpha}{\beta}X - T\right)} - e^{PT}\right)\right)\right). \tag{A.2.11}$$

Appendix B

Derivation of cell problem boundary condition

We derive the boundary condition on $\boldsymbol{Y} \in \partial\Omega_O$ for the cell problem, Equation (3.3.18). Using the ansatz Equations (3.3.17a) and (3.3.17b), the boundary condition Equation (3.3.16a) becomes:

$$\begin{aligned}&\left[\left(\mathbf{n}_{\boldsymbol{Y}} \cdot \left(\nabla_{\boldsymbol{Y}}(-\psi_1)\right) \partial_{X_1} + \mathbf{n}_{\boldsymbol{Y}} \cdot \left(\nabla_{\boldsymbol{Y}}(-\psi_2)\right) \partial_{X_2} + \mathbf{n}_{\boldsymbol{Y}} \cdot \left(\nabla_{\boldsymbol{Y}}(-\psi_3)\right) \partial_{X_3}\right) + \mathbf{n}_{\boldsymbol{Y}} \cdot \nabla_{\boldsymbol{X}}\right] C_{H0} \\ &= d_{CO}\left[\left(\mathbf{n}_{\boldsymbol{Y}} \cdot \left(\nabla_{\boldsymbol{Y}}(-\Psi_1)\right) \partial_{X_1} + \mathbf{n}_{\boldsymbol{Y}} \cdot \left(\nabla_{\boldsymbol{Y}}(-\Psi_2)\right) \partial_{X_2} + \mathbf{n}_{\boldsymbol{Y}} \cdot \left(\nabla_{\boldsymbol{Y}}(-\Psi_3)\right) \partial_{X_3}\right) + \mathbf{n}_{\boldsymbol{Y}} \cdot \nabla_{\boldsymbol{X}}\right] C_{O0}.\end{aligned} \tag{B.1}$$

We rearrange and impose the partition condition $K_C C_{O0} = C_{H0}$ for all $\boldsymbol{Y}$ to obtain,

$$\begin{aligned}&K_C\left[\left(\mathbf{n}_{\boldsymbol{Y}} \cdot \left(\nabla_{\boldsymbol{Y}}(-\psi_1)\right) \partial_{X_1} + \mathbf{n}_{\boldsymbol{Y}} \cdot \left(\nabla_{\boldsymbol{Y}}(-\psi_2)\right) \partial_{X_2} + \mathbf{n}_{\boldsymbol{Y}} \cdot \left(\nabla_{\boldsymbol{Y}}(-\psi_3)\right) \partial_{X_3}\right)\right] C_{O0} \\ &- d_{CO}\left[\left(\mathbf{n}_{\boldsymbol{Y}} \cdot \left(\nabla_{\boldsymbol{Y}}(-\Psi_1)\right) \partial_{X_1} + \mathbf{n}_{\boldsymbol{Y}} \cdot \left(\nabla_{\boldsymbol{Y}}(-\Psi_2)\right) \partial_{X_2} + \mathbf{n}_{\boldsymbol{Y}} \cdot \left(\nabla_{\boldsymbol{Y}}(-\Psi_3)\right) \partial_{X_3}\right)\right] C_{O0} \\ &= d_{CO}\mathbf{n}_{\boldsymbol{Y}} \cdot \nabla_{\boldsymbol{X}}(C_{O0}) - \mathbf{n}_{\boldsymbol{Y}} \cdot \nabla_{\boldsymbol{X}}(K_C C_{O0}).\end{aligned} \tag{B.2}$$

Since the parameters d_{CO} and K_C are constant (and therefore independent of $\boldsymbol{Y}$), we can rewrite this as

$$\begin{aligned}&\mathbf{n}_{\boldsymbol{Y}} \cdot \nabla_{\boldsymbol{Y}}\left(-K_C\psi_1 + d_{CO}\Psi_1\right)\partial_{X_1}C_{O0} + \mathbf{n}_{\boldsymbol{Y}} \cdot \nabla_{\boldsymbol{Y}}\left(-K_C\psi_2 + d_{CO}\Psi_2\right)\partial_{X_2}C_{O0} \\ &+ \mathbf{n}_{\boldsymbol{Y}} \cdot \nabla_{\boldsymbol{Y}}\left(-K_C\psi_3 + d_{CO}\Psi_3\right)\partial_{X_3}C_{O0} = d_{CO}\mathbf{n}_{\boldsymbol{Y}} \cdot \nabla_{\boldsymbol{X}}(C_{O0}) - K_C\mathbf{n}_{\boldsymbol{Y}} \cdot \nabla_{\boldsymbol{X}}(C_{O0}),\end{aligned} \tag{B.3}$$

which we can rewrite as,

$$\begin{pmatrix}\mathbf{n}_{\boldsymbol{Y}} \cdot \nabla_{\boldsymbol{Y}}\left(-K_C\psi_1 + d_{CO}\Psi_1\right) \\ \mathbf{n}_{\boldsymbol{Y}} \cdot \nabla_{\boldsymbol{Y}}\left(-K_C\psi_2 + d_{CO}\Psi_2\right) \\ \mathbf{n}_{\boldsymbol{Y}} \cdot \nabla_{\boldsymbol{Y}}\left(-K_C\psi_3 + d_{CO}\Psi_3\right)\end{pmatrix} \cdot \nabla_{\boldsymbol{X}}C_{O0} = -\left(K_C - d_{CO}\right)\mathbf{n}_{\boldsymbol{Y}} \cdot \nabla_{\boldsymbol{X}}C_{O0}. \tag{B.4}$$

By dotting Equation (B.4) by $\boldsymbol{e}_i$, to compare coefficients of $\partial_{X_i}C_{O0}$, we find the boundary condition on $\boldsymbol{Y} \in \partial\Omega_O$ in component form:

$$\mathbf{n}_{\boldsymbol{Y}} \cdot \left(K_C\nabla_{\boldsymbol{Y}}\psi_i - d_{CO}\nabla_{\boldsymbol{Y}}\Psi_i\right) = \left(K_C - d_{CO}\right)\mathbf{n}_{\boldsymbol{Y}} \cdot \boldsymbol{e}_i. \tag{B.5}$$

Similarly, for the lactate problem, the boundary condition on $\boldsymbol{Y} \in \partial\Omega_O$ in component form is

$$\mathbf{n}_{\boldsymbol{Y}} \cdot \left(K_W\nabla_{\boldsymbol{Y}}\gamma_i - \frac{d_{WO}}{d_{WH}}\nabla_{\boldsymbol{Y}}\Gamma_i\right) = \left(K_W - \frac{d_{WO}}{d_{WH}}\right)\mathbf{n}_{\boldsymbol{Y}} \cdot \boldsymbol{e}_i. \tag{B.6}$$

Appendix C

Derivation of proxy flow boundary condition

A similar *proxy* flow boundary condition to the one considered in this Appendix is derived in the Supplementary Information of [17] .

In the media layer above the hydrogel, we have Stokes flow and the glucose and lactate concentrations are $c_M = c_{-\infty}$ and $w_M = 0$, respectively. The governing behaviour is

$$\frac{\partial c_M}{\partial t} = \nabla \cdot \left(D_{CM} \nabla c_M - \boldsymbol{u} c_M \right), \tag{C.1a}$$

$$\frac{\partial w_M}{\partial t} = \nabla \cdot \left(D_{WM} \nabla w_M - \boldsymbol{u} w_M \right). \tag{C.1b}$$

We have continuity of concentration and continuity of flux at the interface $z = h_H$:

$$\bar{c} = c_M, \quad \boldsymbol{n} \cdot \left(\bar{D}_C \nabla \bar{c} \right) = \boldsymbol{n} \cdot \left(D_{CM} \nabla c_M \right), \tag{C.2a}$$

$$\bar{w} = w_M, \quad \boldsymbol{n} \cdot \left(\bar{D}_W \nabla \bar{w} \right) = \boldsymbol{n} \cdot \left(D_{WM} \nabla w_M \right), \tag{C.2b}$$

with

$$\boldsymbol{u} \cdot \boldsymbol{n} = 0 \text{ (no slip)}, \tag{C.2c}$$

where $\bar{D}_C$ and $\bar{D}_W$ are the dimensional effective diffusivities of glucose and lactate in the homogenised hydrogel. We consider the system after an initial transient boundary layer in time, when it has relaxed to a quasi-steady state.

We non-dimensionalise using the scalings:

$$(\bar{c},\ c_M,\ \bar{w},\ w_M) = c_{-\infty}(\bar{C},\ C_M,\ \bar{W}, W_M), \tag{C.3}$$

$$\boldsymbol{u} = [u]\boldsymbol{U}, \quad \boldsymbol{x} = L\boldsymbol{X}, \quad t = \frac{L^2}{D_{CH}} T, \tag{C.4}$$

where $\dot{\gamma}$ is the shear rate, but $[u] = \dot{\gamma} L$ is the typical velocity of the fluid, and the interface is at $Z = H = h_H/L$ We obtain the following system for metabolite within the media (C_M, W_M), in $Z > H$ and homogenised hydrogel ($\bar{C}$, $\bar{W}$), $0 < Z < H$, layers:

$$\frac{\partial C_M}{\partial T} = \nabla \cdot \left(d_{CM} \nabla C_M - \mathrm{Pe} \boldsymbol{U} C_M \right), \tag{C.5a}$$

$$\frac{\partial W_M}{\partial T} = \nabla \cdot \left(d_{WM} \nabla W_M - \mathrm{Pe} \boldsymbol{U} W_M \right), \tag{C.5b}$$

$$\frac{\partial \bar{C}}{\partial T} = \nabla \cdot \big(\bar{d}_C(\boldsymbol{X}, T) \nabla \bar{C} \big) - \sigma_V S(\bar{C}, \bar{W}), \tag{C.5c}$$

$$\frac{\partial \bar{W}}{\partial T} = \nabla \cdot \big(\bar{d}_W(\boldsymbol{X}, T) \nabla \bar{W} \big) + 2\sigma_V S(\bar{C}, \bar{W}), \tag{C.5d}$$

where we define the dimensionless parameters:

$$(d_{CM},\ d_{WM}) = \frac{1}{D_{CH}} (D_{CM}, D_{WM}) \quad \text{and} \quad \mathrm{Pe} = \frac{\dot{\gamma} L^2}{D_{CH}}, \tag{C.6}$$

where Pe is the Péclet number.

The flow near the hydrogel layer can be well approximated by a shear flow within the mass transfer boundary layer. This is because we consider a flow where the Schmidt number (the ratio of the kinematic viscosity μ to the mass diffusivity, $\mathrm{Sc} = \mu/\rho D_{iM}$) is large, so the hydrodynamic boundary layer is much thicker than the mass transfer boundary layer. (We note that the Schmidt number is generally large for mass transport in water.) We choose that the flow is in the positive X-axis direction and the positive Z-direction points towards the culture media from the hydrogel, with the hydrogel interface at $Z = H$, $\boldsymbol{U} \sim (Z - H)\boldsymbol{e}_X$.

Considering a thin layer of culture media near the hydrogel-media boundary, and noting that $\mathrm{Pe} \gg 1$ and $d_{CM} \sim \mathcal{O}(1)$, we rescale in Z and take $Z = H + (d_{CM}/\mathrm{Pe})^{1/3} \hat{Z}$, The leading-order version of the governing equations in the media are then:

$$0 = \frac{\partial^2 C_M}{\partial \hat{Z}^2} - \hat{Z} \frac{\partial C_M}{\partial X}, \tag{C.7a}$$

$$0 = \frac{d_{CM}}{d_{WM}} \frac{\partial^2 W_M}{\partial \hat{Z}^2} - \hat{Z} \frac{\partial W_M}{\partial X}, \tag{C.7b}$$

with far-field condition:

$$C_M \to 1, \qquad W_M \to 0 \quad \text{as} \quad \hat{Z} \to \infty. \tag{C.8}$$

The interfacial conditions at $\hat{Z} = 0$ are:

$$\bar{C} = C_M \quad \text{and} \quad \bar{W} = W_M, \tag{C.9a}$$

$$\bar{d}_C \frac{\partial \bar{C}}{\partial \hat{Z}} = d_{CM} \frac{\partial C_M}{\partial \hat{Z}} \quad \text{and} \quad \bar{d}_W \frac{\partial \bar{W}}{\partial \hat{Z}} = d_{WM} \frac{\partial W_M}{\partial \hat{Z}}. \tag{C.9b}$$

We seek similarity solutions for C_M and W_M of the form

$$C_M = f(\zeta) \quad \text{where } \zeta = \left(\frac{1}{X}\right)^{1/3} \hat{Z}, \tag{C.10a}$$

$$W_M = g(\xi) \quad \text{where } \xi = \left(\frac{d_{CM}}{d_{WM} X}\right)^{1/3} \hat{Z}, \tag{C.10b}$$

and we note that the following partial derivatives take the form:

$$\frac{\partial \zeta}{\partial X} = -\frac{\zeta}{3X}, \qquad \frac{\partial \zeta}{\partial \hat{Z}} = X^{-1/3} = \frac{\zeta}{\hat{Z}}, \tag{C.11a}$$

$$\frac{\partial \xi}{\partial X} = -\frac{\xi}{3X}, \quad \frac{\partial \xi}{\partial \hat{Z}} = \left(\frac{\mathrm{Pe}}{d_{WM} X}\right)^{1/3} = \frac{\xi}{\hat{Z}}. \tag{C.11b}$$

Therefore, the derivatives of C_M and W_M become:

$$\frac{\partial C_M}{\partial X} = -\frac{\zeta}{3X} f', \quad \frac{\partial C_M}{\partial \hat{Z}} = \frac{\zeta}{\hat{Z}} f', \quad \frac{\partial^2 C_M}{\partial \hat{Z}^2} = \frac{\zeta^2}{\hat{Z}^2} f'', \tag{C.12a}$$

$$\frac{\partial W_M}{\partial X} = -\frac{\xi}{3X} g', \quad \frac{\partial W_M}{\partial \hat{Z}} = \frac{\xi}{\hat{Z}} g', \quad \frac{\partial^2 W_M}{\partial \hat{Z}^2} = \frac{\xi^2}{\hat{Z}^2} g''. \tag{C.12b}$$

The quasi-steady behaviour of Equations (C.7a) and (C.7b) can then be written in terms of the similarity solutions ζ and ξ as

$$0 = f'' + \frac{\zeta^2}{3} f', \tag{C.13a}$$

$$0 = g'' + \frac{\xi^2}{3} g'; \tag{C.13b}$$

with boundary conditions (from Equation (C.8)):

$$C_M = 1 \text{ as } \zeta \to \infty, \ \textit{i.e.} \ \ f(\infty) = 1, \tag{C.13c}$$

$$W_M = 0 \text{ as } \xi \to \infty, \ \textit{i.e.} \ \ g(\infty) = 0. \tag{C.13d}$$

Writing Equations (C.13a) and (C.13b) as total derivatives,

$$0 = \left(f' \exp\left(\frac{\zeta^3}{9}\right)\right)' \quad \Rightarrow \quad f' = A \exp\left(-\frac{\zeta^3}{9}\right), \tag{C.14a}$$

$$0 = \left(g' \exp\left(\frac{\xi^3}{9}\right)\right)' \quad \Rightarrow \quad g' = B \exp\left(-\frac{\xi^3}{9}\right), \tag{C.14b}$$

where we find $A = f'(0)$ and $B = g'(0)$. Therefore, using $f(\infty) = 1$ and $g(\infty) = 0$, we find an expression for f and g,

$$f = A \int_{\infty}^{\zeta} \exp\left(-\frac{s^3}{9}\right) \, \mathrm{d}s + 1, \tag{C.15a}$$

$$g = B \int_{\infty}^{\xi} \exp\left(-\frac{s^3}{9}\right) \, \mathrm{d}s. \tag{C.15b}$$

Evaluating Equation (C.15) at $\zeta = 0$ and $\xi = 0$, respectively, we find

$$f(0) = 1 + A\int_{\infty}^{0} \exp\left(-\frac{\zeta^3}{9}\right)\, \mathrm{d}\zeta, \tag{C.16a}$$

$$g(0) = B\int_{\infty}^{0} \exp\left(-\frac{\xi^3}{9}\right)\, \mathrm{d}\xi, \tag{C.16b}$$

which we can rearrange and substitute for A and B to give:

$$f(0) + f'(0)\int_{0}^{\infty} \exp\left(-\frac{\zeta^3}{9}\right)\, \mathrm{d}\zeta = 1, \tag{C.17a}$$

$$g(0) + g'(0)\int_{0}^{\infty} \exp\left(-\frac{\xi^3}{9}\right)\, \mathrm{d}\xi = 0, \tag{C.17b}$$

where

$$\int_{0}^{\infty} \exp\left(-\frac{\zeta^3}{9}\right)\, \mathrm{d}\zeta = \int_{0}^{\infty} \exp\left(-\frac{\xi^3}{9}\right)\, \mathrm{d}\xi = 3^{-\frac{1}{3}}\Gamma\left(\frac{1}{3}\right) \approx 1.86. \tag{C.17c}$$

Since we posed similarity solutions $C_M(\boldsymbol{X}) = f(\zeta)$ and $W_M(\boldsymbol{X}) = g(\xi)$, and therefore

$$\frac{\partial C_M}{\partial \hat{Z}} = \left(\frac{1}{X}\right)^{1/3} f'(\zeta), \tag{C.18a}$$

$$\frac{\partial W_M}{\partial \hat{Z}} = \left(\frac{d_{CM}}{d_{WM}X}\right)^{1/3} g'(\xi), \tag{C.18b}$$

which we can evaluate at $\hat{Z} = 0$, that is $Z = H$, *i.e.* $\zeta = 0$ and $\xi = 0$, to find

$$f(0) = C_M\Big|_{\hat{Z}=0}, \quad f'(0) = X^{1/3}\,\frac{\partial C_M}{\partial \hat{Z}}\Big|_{\hat{Z}=0} \tag{C.19a}$$

$$g(0) = W_M\Big|_{\hat{Z}=0}, \quad g'(0) = \left(\frac{d_{WM}X}{d_{CM}}\right)^{1/3}\,\frac{\partial W_M}{\partial \hat{Z}}\Big|_{\hat{Z}=0}. \tag{C.19b}$$

Substituting Equation (C.19) into Equation (C.17), we obtain a relationship for the behaviour of C_M and W_M at the hydrogel-media interface, $\hat{Z} = 0$:

$$C_M + 3^{-\frac{1}{3}}\Gamma\left(\frac{1}{3}\right) X^{1/3}\frac{\partial C_M}{\partial \hat{Z}} = 1, \tag{C.20a}$$

$$W_M + 3^{-\frac{1}{3}}\Gamma\left(\frac{1}{3}\right)\left(\frac{d_{WM}X}{d_{CM}}\right)^{1/3}\frac{\partial W_M}{\partial \hat{Z}} = 0, \tag{C.20b}$$

which we can write in terms of the metabolite concentrations within the homogenised hydrogel layer, using the continuity of concentration and continuity of flux conditions, Equation (C.9), and find at $\hat{Z} = 0$:

$$\bar{C} + 3^{-\frac{1}{3}}\Gamma\left(\frac{1}{3}\right) X^{1/3} \frac{\bar{d}_C(\boldsymbol{X}, T)}{d_{CM}} \frac{\partial \bar{C}}{\partial \hat{Z}} = 1, \tag{C.21a}$$

$$\bar{W} + 3^{-\frac{1}{3}}\Gamma\left(\frac{1}{3}\right) \left(\frac{d_{WM} X}{d_{CM}}\right)^{1/3} \frac{\bar{d}_W(\boldsymbol{X}, T)}{d_{WM}} \frac{\partial \bar{W}}{\partial \hat{Z}} = 0. \tag{C.21b}$$

We scale back out of the boundary layer in the culture media near the media-hydrogel interface $Z = H$, and rewrite Equation (C.21) in terms of Z,

$$\bar{C} + 3^{-\frac{1}{3}}\Gamma\left(\frac{1}{3}\right) \left(\frac{d_{CM} X}{\mathrm{Pe}}\right)^{1/3} \frac{\bar{d}_C(\boldsymbol{X}, T)}{d_{CM}} \frac{\partial \bar{C}}{\partial Z} = 1, \tag{C.22a}$$

$$\bar{W} + 3^{-\frac{1}{3}}\Gamma\left(\frac{1}{3}\right) \left(\frac{d_{WM} X}{\mathrm{Pe}}\right)^{1/3} \frac{\bar{d}_W(\boldsymbol{X}, T)}{d_{WM}} \frac{\partial \bar{W}}{\partial Z} = 0. \tag{C.22b}$$

We define the dimensionless parameters α_C and α_W as

$$\alpha_C = \frac{3^{1/3}\mathrm{Pe}^{1/3} {d_{CM}}^{2/3}}{\Gamma\left(\frac{1}{3}\right)} \tag{C.23}$$

$$\alpha_W = \frac{3^{1/3}\mathrm{Pe}^{1/3} {d_{WM}}^{2/3}}{\Gamma\left(\frac{1}{3}\right)} = \alpha_C \left(\frac{d_{CM}}{d_{WM}}\right)^{2/3} \approx 0.57\alpha_C, \tag{C.24}$$

and rewrite Equation (C.21) to obtain *effective boundary conditions* for $\bar{C}$ and $\bar{W}$, which are consistent and closed, at the hydrogel-media interface, $Z = H$:

$$\bar{d}_C(\boldsymbol{X}, T)\frac{\partial \bar{C}}{\partial Z} + \frac{\alpha_C}{X^{1/3}}(\bar{C} - 1) = 0, \tag{C.25a}$$

$$\bar{d}_W(\boldsymbol{X}, T)\frac{\partial \bar{W}}{\partial Z} + \frac{\alpha_W}{X^{1/3}}\bar{W} = 0. \tag{C.25b}$$

where we note α_C and α_W are effective Péclet numbers, and increasing α_C and α_W correspond to increasing the flow rate in the culture media. We note that this this boundary condition does not apply strictly in the case of no advection, however, Dalwadi and Pearce [17] show that this type of effective boundary condition is valid even for moderately sized Péclet numbers.

Appendix D

Small organoid and strong uptake distinguished limit

Now, we consider a different distinguished limit of our model, given by Equations (3.3.5) and (3.3.6), which corresponds to a hydrogel embedded with small organoids with strong metabolite uptake/production. Instead of scaling as in Equation (3.3.7), we now consider the distinguished limit:

$$\begin{gathered} d_{CO} \sim d_{WO} \sim d_{WH} \sim \mathcal{O}(1), \quad R \sim \mathcal{O}(\delta^2), \quad \sigma_V \sim \mathcal{O}(\delta^{-6}), \\ \boldsymbol{U}_O \sim \boldsymbol{U}_H \sim \boldsymbol{U}_{\partial\Omega_O} \sim \mathcal{O}(\delta^2), \end{gathered} \tag{D.0.1}$$

where we note that since the velocity scaling is chosen to balance the rate of organoid growth (see Section 3.2.2), the velocity terms $\boldsymbol{U}_O$, $\boldsymbol{U}_H$, and $\boldsymbol{U}_{\partial\Omega_O}$ must be of the same asymptotic order as the organoid radius R. Therefore, in this distinguished limit $\boldsymbol{U}_O \sim \boldsymbol{U}_H \sim \boldsymbol{U}_{\partial\Omega_O} \sim \mathcal{O}(\delta^2)$.

We rescale the organoid radius, glucose uptake strength, and velocities as:

$$R = \delta^2 \tilde{R}, \quad \sigma_V = \frac{\tilde{\sigma}_V}{\delta^6} \quad \{\boldsymbol{U}_O, \boldsymbol{U}_H, \boldsymbol{U}_{\partial\Omega_O}\} = \delta^2 \{\tilde{\boldsymbol{U}}_O, \tilde{\boldsymbol{U}}_H, \tilde{\boldsymbol{U}}_{\partial\Omega_O}\}, \tag{D.0.2}$$

where the variables $\tilde{R}$ and $\{\tilde{\boldsymbol{U}}_O,\ \tilde{\boldsymbol{U}}_H,\ \tilde{\boldsymbol{U}}_{\partial\Omega_O}\}$, and parameter $\tilde{\sigma}_V$ are order 1. The governing equation for glucose transport for becomes:

$$\begin{aligned} &\delta^2 \frac{\partial C_H}{\partial T} + \delta^4 \left(\nabla_{\boldsymbol{Y}} + \delta \nabla_{\boldsymbol{X}}\right) \cdot \left(\tilde{\boldsymbol{U}}_H C_H\right) \\ &\quad = \left(\nabla_{\boldsymbol{Y}} + \delta \nabla_{\boldsymbol{X}}\right) \cdot \left(\nabla_{\boldsymbol{Y}} + \delta \nabla_{\boldsymbol{X}}\right) C_H \quad \text{for } \|\boldsymbol{Y}\| > \delta^2 \tilde{R} \text{ and } \|\boldsymbol{Y}\|_\infty < \frac{1}{2}, \end{aligned} \tag{D.0.3a}$$

$$\begin{aligned} &\delta^2 \frac{\partial C_O}{\partial T} + \delta^4 \left(\nabla_{\boldsymbol{Y}} + \delta \nabla_{\boldsymbol{X}}\right) \cdot \left(\tilde{\boldsymbol{U}}_O C_O\right) \\ &\quad = d_{CO} \left(\nabla_{\boldsymbol{Y}} + \delta \nabla_{\boldsymbol{X}}\right) \cdot \left(\nabla_{\boldsymbol{Y}} + \delta \nabla_{\boldsymbol{X}}\right) C_O - \delta^{-4} \tilde{\sigma}_V S(C_O, W_O) \text{ for } \|\boldsymbol{Y}\| < \delta^2 \tilde{R}, \end{aligned} \tag{D.0.3b}$$

with boundary conditions on $\|Y\| = \delta^2 \tilde{R}$ (*i.e.* on $\boldsymbol{Y} \in \partial\Omega_O(\boldsymbol{X}, T)$):

$$K_C C_O = C_H, \qquad K_W W_O = W_H, \tag{D.0.4a}$$

$$\begin{aligned}&\left(\mathbf{n}_{\boldsymbol{Y}} - \delta^3 \nabla_{\boldsymbol{X}} \tilde{R}\right) \cdot \left(\left(\nabla_{\boldsymbol{Y}} + \delta \nabla_{\boldsymbol{X}}\right) C_H + \delta^4 C_H \left(\tilde{\boldsymbol{U}}_{\partial\Omega_O} - \tilde{\boldsymbol{U}}_H\right) \left\|\mathbf{n}_{\boldsymbol{Y}} - \delta^3 \nabla_{\boldsymbol{X}} \tilde{R}\right\|\right) \\ &= \left(\mathbf{n}_{\boldsymbol{Y}} - \delta^3 \nabla_{\boldsymbol{X}} \tilde{R}\right) \cdot \left(d_{CO} \left(\nabla_{\boldsymbol{Y}} + \delta \nabla_{\boldsymbol{X}}\right) C_O + \delta^4 C_O \left(\tilde{\boldsymbol{U}}_{\partial\Omega_O} - \tilde{\boldsymbol{U}}_O\right) \left\|\mathbf{n}_{\boldsymbol{Y}} - \delta^3 \nabla_{\boldsymbol{X}} \tilde{R}\right\|\right), \end{aligned} \tag{D.0.4b}$$

and periodicity of C_H and W_H in $\boldsymbol{Y}$ on the unit cell boundary, $\boldsymbol{Y} \in \partial\Omega$, that is $\|\boldsymbol{Y}\|_\infty = 1/2$. The solution for C_O is dependent on the parameter δ, which is problematic. Therefore, we seek an inner solution, close to the organoid at the origin, where $\|Y\| = \mathcal{O}(\delta^2)$.

D.1 Investigating inner problem

To explore this inner solution, we rescale $\boldsymbol{Y} = \delta^2 \tilde{\boldsymbol{Y}}$, where $\tilde{\boldsymbol{Y}} \in \mathbb{R}^3$, and define the inner region as $\Omega_{\text{in}}(\boldsymbol{X}, T)$, where the dependence on $\boldsymbol{X}$ and T comes from the organoid radius. We denote the radial spatial variable in the inner region as ϱ. Then, our governing equations, Equations (D.0.3) and (D.0.4) become:

$$\begin{aligned}&\delta^6 \frac{\partial C_H}{\partial T} + \delta^6 \left(\nabla_{\tilde{\boldsymbol{Y}}} + \delta^3 \nabla_{\boldsymbol{X}}\right) \cdot \left(\tilde{\boldsymbol{U}}_H C_H\right) \\ &\qquad = \left(\nabla_{\tilde{\boldsymbol{Y}}} + \delta^3 \nabla_{\boldsymbol{X}}\right) \cdot \left(\nabla_{\tilde{\boldsymbol{Y}}} + \delta^3 \nabla_{\boldsymbol{X}}\right) C_H \qquad \text{for } \varrho > \tilde{R}(\boldsymbol{X}, T),\end{aligned} \tag{D.1.1a}$$

$$\begin{aligned}&\delta^6 \frac{\partial C_O}{\partial T} + \delta^6 \left(\nabla_{\tilde{\boldsymbol{Y}}} + \delta^3 \nabla_{\boldsymbol{X}}\right) \cdot \left(\tilde{\boldsymbol{U}}_O C_O\right) \\ &= d_{CO} \left(\nabla_{\tilde{\boldsymbol{Y}}} + \delta^3 \nabla_{\boldsymbol{X}}\right) \cdot \left(\nabla_{\tilde{\boldsymbol{Y}}} + \delta^3 \nabla_{\boldsymbol{X}}\right) C_O - \tilde{\sigma}_V S(C_O, W_O) \text{ for } \varrho < \tilde{R}(\boldsymbol{X}, T),\end{aligned} \tag{D.1.1b}$$

with boundary condition on $\varrho = \tilde{R}(\boldsymbol{X}, T)$:

$$K_C C_O = C_H, \qquad K_W W_O = W_H, \tag{D.1.2a}$$

$$\begin{aligned}&\left(\mathbf{n}_{\tilde{\boldsymbol{Y}}} - \delta^3 \nabla_{\boldsymbol{X}} \tilde{R}\right) \cdot \left(\left(\nabla_{\tilde{\boldsymbol{Y}}} + \delta^3 \nabla_{\boldsymbol{X}}\right) C_H + \delta^4 C_H \left(\tilde{\boldsymbol{U}}_{\partial\Omega_O} - \tilde{\boldsymbol{U}}_H\right) \left\|\mathbf{n}_{\tilde{\boldsymbol{Y}}} - \delta^3 \nabla_{\boldsymbol{X}} \tilde{R}\right\|\right) \\ &= \left(\mathbf{n}_{\tilde{\boldsymbol{Y}}} - \delta^3 \nabla_{\boldsymbol{X}} \tilde{R}\right) \cdot \left(d_{CO} \left(\nabla_{\tilde{\boldsymbol{Y}}} + \delta^3 \nabla_{\boldsymbol{X}}\right) C_O + \delta^6 C_O \left(\tilde{\boldsymbol{U}}_{\partial\Omega_O} - \tilde{\boldsymbol{U}}_O\right) \left\|\mathbf{n}_{\tilde{\boldsymbol{Y}}} - \delta^3 \nabla_{\boldsymbol{X}} \tilde{R}\right\|\right), \end{aligned} \tag{D.1.2b}$$

Therefore, the glucose transport model for the 'small organoid, high uptake' distinguished limit is

$$\mathcal{O}(\delta^3) = \nabla^2_{\tilde{\boldsymbol{Y}}} C_H \qquad \text{for } \varrho > \tilde{R}(\boldsymbol{X}, T), \tag{D.1.3a}$$

$$\mathcal{O}(\delta^3) = d_{CO} \nabla^2_{\tilde{\boldsymbol{Y}}} C_O - \tilde{\sigma}_V S(C_O, W_O) \qquad \text{for } \varrho < \tilde{R}(\boldsymbol{X}, T), \tag{D.1.3b}$$

with boundary conditions

$$K_C C_O = C_H, \quad \frac{\partial C_H}{\partial \varrho} = d_{CO} \frac{\partial C_O}{\partial \varrho} + \mathcal{O}(\delta^3) \qquad \text{for } \varrho = \tilde{R}(\boldsymbol{X}, T). \tag{D.1.3c}$$

Therefore, we seek an inner solution, $\{C_{O\text{in}}, C_{H\text{in}}\}$, to the leading-order problem:

$$0 = \nabla^2_{\tilde{\mathbf{Y}}} C_{H\text{in}} \qquad \text{for } \varrho > \tilde{R}(\boldsymbol{X}, T), \tag{D.1.4a}$$

$$0 = d_{CO} \nabla^2_{\tilde{\mathbf{Y}}} C_{O\text{in}} - \tilde{\sigma}_V S(C_{O\text{in}}, W_{O\text{in}}) \qquad \text{for } \varrho < \tilde{R}(\boldsymbol{X}, T), \tag{D.1.4b}$$

with boundary condition at the organoid-hydrogel interface

$$K_C C_{O\text{in}} = C_{H\text{in}}, \quad \frac{\partial C_{H\text{in}}}{\partial \varrho} = d_{CO} \frac{\partial C_{O\text{in}}}{\partial \varrho} \qquad \text{for } \varrho = \tilde{R}(\boldsymbol{X}, T), \tag{D.1.4c}$$

where we impose the far-field matching condition $C_{H\text{in}} \to C_{H0}(\boldsymbol{X}, T)$ as $\varrho \to \infty$ (by Van Dyke's matching rule [87]), where C_{H0} is the leading-order solution to the outer problem, yet to be determined. To make analytical progress, we consider linear uptake (*i.e.* $S(C_{O\text{in}}, W_{O\text{in}}) = C_{O\text{in}}$), and for ease of notation, we define $\tilde{\lambda} = \tilde{\sigma}_V / d_{CO}$. We seek a radially symmetric solution, $C_{O\text{in}} = C_{O\text{in}}(\varrho, T)$ and $C_{H\text{in}} = C_{H\text{in}}(\varrho, T)$. We impose vanishing concentration flux at the origin

$$\frac{\partial C_{O\text{in}}}{\partial \varrho} = 0 \quad \text{at} \quad \varrho = 0, \tag{D.1.4d}$$

to ensure boundedness. Therefore, our system, Equation (D.1.4), becomes:

$$0 = \frac{1}{\varrho^2} \frac{\partial}{\partial \varrho} \left(\varrho^2 \frac{\partial C_{H\text{in}}}{\partial \varrho} \right) \qquad \text{for } \varrho > \tilde{R}, \tag{D.1.5a}$$

$$0 = \frac{1}{\varrho^2} \frac{\partial}{\partial \varrho} \left(\varrho^2 \frac{\partial C_{O\text{in}}}{\partial \varrho} \right) - \tilde{\lambda} C_{O\text{in}} \qquad \text{for } \varrho < \tilde{R}, \tag{D.1.5b}$$

with

$$\frac{\partial C_{O\text{in}}}{\partial \varrho} = 0 \qquad \text{at } \varrho = 0, \tag{D.1.5c}$$

$$K_C C_{O\text{in}} = C_{H\text{in}}, \quad \frac{\partial C_{H\text{in}}}{\partial \varrho} = d_{CO} \frac{\partial C_{O\text{in}}}{\partial \varrho} \qquad \text{at } \varrho = \tilde{R}, \tag{D.1.5d}$$

$$C_{H\text{in}} \to C_{H0}(\boldsymbol{X}, T) \qquad \text{as } \varrho \to \infty. \tag{D.1.5e}$$

We integrate Equation (D.1.5a) with respect to ϱ and impose the far-field boundary condition, Equation (D.1.5e), to obtain

$$C_{H\text{in}} = C_{H0}(\boldsymbol{X}, T) \left(1 - \frac{A}{\varrho} \right), \tag{D.1.6}$$

where $A = A(\boldsymbol{X}, T)$ is a function independent of ϱ to be determined. The general solution to Equation (D.1.5b) is

$$C_{O\text{in}} = \tilde{A} \frac{\cosh(\sqrt{\tilde{\lambda}} \varrho)}{\varrho} + B \frac{\sinh(\sqrt{\tilde{\lambda}} \varrho)}{\varrho}, \tag{D.1.7}$$

where $\tilde{A}$ and B are functions independent of ϱ to be determined. We note that near $\varrho = 0$, $C_{O\text{in}}$ behaves like

$$C_{O\text{in}} \sim \frac{\tilde{A}}{\varrho} + B\frac{\sinh(\sqrt{\tilde{\lambda}}\varrho)}{\varrho}, \tag{D.1.8}$$

where the second term is bounded and has zero derivative at $\varrho = 0$. Therefore, using the boundedness at origin condition, Equation (D.1.5c), we find

$$C_{O\text{in}} = B\frac{\sinh(\sqrt{\tilde{\lambda}}\varrho)}{\varrho}. \tag{D.1.9}$$

We determine A and B using the interfacial conditions at $\varrho = \tilde{R}$. Using the partition condition, we find

$$K_C C_{O\text{in}} = C_{H\text{in}} \quad \Rightarrow \quad B = \frac{\tilde{R}C_{H0}(\boldsymbol{X}, T)}{K_C \sinh(\sqrt{\tilde{\lambda}}\tilde{R})}\left(1 - \frac{A}{\tilde{R}}\right), \tag{D.1.10a}$$

and using the continuity of diffusive flux condition, we obtain

$$\frac{\partial C_{H\text{in}}}{\partial \varrho} = d_{CO}\frac{\partial C_{O\text{in}}}{\partial \varrho} \quad \Rightarrow \quad \frac{AC_{H0}}{\tilde{R}^2} = d_{CO}B\left(\frac{\sqrt{\tilde{\lambda}}\cosh(\sqrt{\tilde{\lambda}}\tilde{R})}{\tilde{R}} - \frac{1}{\tilde{R}^2}\sinh(\sqrt{\tilde{\lambda}}\tilde{R})\right). \tag{D.1.10b}$$

We solve Equation (D.1.10) simultaneously to determine A and B are:

$$A = \frac{d_{CO}}{K_C}\tilde{R}\frac{\sqrt{\tilde{\lambda}}\tilde{R}\coth(\sqrt{\tilde{\lambda}}\tilde{R}) - 1}{1 + \frac{d_{CO}}{K_C}\left(\sqrt{\tilde{\lambda}}\tilde{R}\coth(\sqrt{\tilde{\lambda}}\tilde{R}) - 1\right)}; \tag{D.1.11a}$$

$$B = \frac{\tilde{R}C_{H0}}{(K_C - d_{CO})\sinh(\sqrt{\tilde{\lambda}}\tilde{R}) + d_{CO}\sqrt{\tilde{\lambda}}\tilde{R}\cosh(\sqrt{\tilde{\lambda}}\tilde{R})}. \tag{D.1.11b}$$

Substituting Equation (D.1.11) into the expressions for $C_{H\text{in}}$ and $C_{O\text{in}}$, Equations (D.1.6) and (D.1.9), we obtain

$$C_{H\text{in}} = C_{H0}(\boldsymbol{X}, T)\left(1 - \frac{d_{CO}\tilde{R}}{\varrho}\frac{\sqrt{\tilde{\lambda}}\tilde{R}\coth(\sqrt{\tilde{\lambda}}\tilde{R}) - 1}{K_C + d_{CO}\left(\sqrt{\tilde{\lambda}}\tilde{R}\coth(\sqrt{\tilde{\lambda}}\tilde{R}) - 1\right)}\right), \tag{D.1.12}$$

$$C_{O\text{in}} = \frac{C_{H0}(\boldsymbol{X}, T)\tilde{R}\sinh(\sqrt{\tilde{\lambda}}\varrho)}{\varrho\left((K_C - d_{CO})\sinh(\sqrt{\tilde{\lambda}}\tilde{R}) + d_{CO}\sqrt{\tilde{\lambda}}\tilde{R}\cosh(\sqrt{\tilde{\lambda}}\tilde{R})\right)}. \tag{D.1.13}$$

In a similar manner, we seek an inner solution, $\{W_{O\text{in}}, W_{H\text{in}}\}$, to the leading-order lactate transport problem in the ‘small organoid, high uptake’ distinguished limit:

$$0 = \nabla^2_{\mathbf{Y}} W_{H\text{in}} \qquad \text{for } \varrho > \tilde{R}(\boldsymbol{X}, T), \tag{D.1.14a}$$

$$0 = d_{WO}\nabla^2_{\mathbf{Y}} W_{O\text{in}} + 2\tilde{\sigma}_V S(C_{O\text{in}}, W_{O\text{in}}) \qquad \text{for } \varrho < \tilde{R}(\boldsymbol{X}, T), \tag{D.1.14b}$$

with boundary conditions at the organoid-hydrogel interface

$$K_W W_{O\text{in}} = W_{H\text{in}}, \quad d_{WH}\frac{\partial W_{H\text{in}}}{\partial \varrho} = d_{WO}\frac{\partial W_{O\text{in}}}{\partial \varrho} \quad \text{for } \varrho = \tilde{R}(\boldsymbol{X}, T), \tag{D.1.14c}$$

where we impose the far-field matching condition $W_{H\text{in}} \to W_{H0}(\boldsymbol{X}, T)$ as $\varrho \to \infty$ (by Van Dyke's matching rule), where W_{H0} is the leading-order solution to the outer problem, yet to be determined. We consider linear glucose consumption $S = C_{O\text{in}}$, and determined $C_{O\text{in}}$ (Equation (D.1.13)) is

$$C_{O\text{in}} = \frac{C_{H0}(\boldsymbol{X}, T)\tilde{R}\sinh(\sqrt{\tilde{\lambda}}\varrho)}{\varrho\left((K_C - d_{CO})\sinh(\sqrt{\tilde{\lambda}}\tilde{R}) + d_{CO}\sqrt{\tilde{\lambda}}\tilde{R}\cosh(\sqrt{\tilde{\lambda}}\tilde{R})\right)}. \tag{D.1.15}$$

We seek a radially symmetric solution, $W_{O\text{in}} = W_{O\text{in}}(\varrho, T)$ and $W_{H\text{in}} = W_{H\text{in}}(\varrho, T)$, and we impose vanishing concentration flux at the origin

$$\frac{\partial W_{O\text{in}}}{\partial \varrho} = 0 \quad \text{at} \quad \varrho = 0, \tag{D.1.16}$$

to ensure boundedness.

Solving for $W_{O\text{in}}$ and $W_{H\text{in}}$, we find that the solutions are of the form:

$$W_{O\text{in}} = -\frac{2\tilde{\sigma}_V B}{d_{WO}}\frac{\sinh(\sqrt{\tilde{\lambda}}\varrho)}{\tilde{\lambda}\varrho} + M, \tag{D.1.17a}$$

$$W_{H\text{in}} = W_{H0}(\boldsymbol{X}, T)\left(1 - \frac{N}{\varrho}\right), \tag{D.1.17b}$$

where B as defined in Equation (D.1.11b), and M and N are functions independent of ϱ to be determined. From the organoid-hydrogel interfacial boundary conditions, Equation (D.1.14c), we determine that M and N are:

$$M = \frac{W_{H0}}{K_W} - \frac{2\tilde{\sigma}_V B}{K_W d_{WH}}\left(\frac{\sinh(\sqrt{\tilde{\lambda}}\tilde{R})}{\tilde{\lambda}\tilde{R}} - \frac{\cosh(\sqrt{\tilde{\lambda}}\tilde{R})}{\sqrt{\tilde{\lambda}}}\right) + \frac{2\tilde{\sigma}_V B}{d_{WO}}\frac{\sinh(\sqrt{\tilde{\lambda}}\tilde{R})}{\tilde{\lambda}\tilde{R}}, \tag{D.1.18a}$$

$$N = \frac{2\tilde{\sigma}_V B}{d_{WH} W_{H0}}\left(\frac{\sinh(\sqrt{\tilde{\lambda}}\tilde{R})}{\tilde{\lambda}} - \frac{\tilde{R}\cosh(\sqrt{\tilde{\lambda}}\tilde{R})}{\sqrt{\tilde{\lambda}}}\right). \tag{D.1.18b}$$

Using the definitions of B and N, (Equations (D.1.11b) and (D.1.18b), respectively), then $W_{H\text{in}}$ is given by

$$\begin{aligned} W_{H\text{in}} =& W_{H0}(\boldsymbol{X}, T) \\ &+ \frac{C_{H0}(\boldsymbol{X}, T)}{\varrho}\left(\frac{2\tilde{\sigma}_V \tilde{R}\left(\sqrt{\tilde{\lambda}}\tilde{R}\cosh(\sqrt{\tilde{\lambda}}\tilde{R}) - \sinh(\sqrt{\tilde{\lambda}}\tilde{R})\right)}{d_{WH}\tilde{\lambda}\left((K_C - d_{CO})\sinh(\sqrt{\tilde{\lambda}}\tilde{R}) + d_{CO}\sqrt{\tilde{\lambda}}\tilde{R}\cosh(\sqrt{\tilde{\lambda}}\tilde{R})\right)}\right). \end{aligned} \tag{D.1.19}$$

To match into the 'periodic cell region', we write the $\mathcal{O}(1)$ solution in the inner region (Equations (D.1.12) and (D.1.19)) in terms of the 'periodic cell region' variables $(\boldsymbol{X}, \boldsymbol{Y})$ and expand to $\mathcal{O}(\delta^2)$. Noting that $\varrho = \left\|\tilde{\boldsymbol{Y}}\right\| \Rightarrow \varrho = \|\boldsymbol{Y}\|/\delta^2$, we find

$$C_{H\text{in}} \sim C_{H0}(\boldsymbol{X}, T) - \delta^2 \frac{\mu_C}{\|4\pi\boldsymbol{Y}\|} C_{H0}(\boldsymbol{X}, T), \tag{D.1.20a}$$

$$W_{H\text{in}} \sim W_{H0}(\boldsymbol{X}, T) + \delta^2 \frac{\mu_W}{\|4\pi\boldsymbol{Y}\|} C_{H0}(\boldsymbol{X}, T), \tag{D.1.20b}$$

where we define $\mu_C(\tilde{R})$ and $\mu_W(\tilde{R})$ as

$$\mu_C = 4\pi \frac{d_{CO}\tilde{R}\left(\sqrt{\tilde{\lambda}}\tilde{R}\coth(\sqrt{\tilde{\lambda}}\tilde{R}) - 1\right)}{K_C + d_{CO}\left(\sqrt{\tilde{\lambda}}\tilde{R}\coth(\sqrt{\tilde{\lambda}}\tilde{R}) - 1\right)}, \tag{D.1.20c}$$

$$\mu_W = 8\pi \frac{d_{CO}\tilde{R}\left(\sqrt{\tilde{\lambda}}\tilde{R}\coth(\sqrt{\tilde{\lambda}}\tilde{R}) - 1\right)}{d_{WH}\left(K_C + d_{CO}\left[\sqrt{\tilde{\lambda}}\tilde{R}\coth(\sqrt{\tilde{\lambda}}\tilde{R}) - 1\right]\right)}. \tag{D.1.20d}$$

The form of the matching condition (Equation (D.1.20)) at $\mathcal{O}(\delta^2)$ implies that the outer problem in the 'periodic cell region' (Equation (D.0.3a)) with a boundary at $\|\boldsymbol{Y}\| = \delta^2\tilde{R}$ can be replaced by an effective outer problem in the 'periodic cell region', replacing the small organoid boundary region in the models for C_H and W_H with a Dirac delta function at the origin of strengths $-\delta^2\mu_C C_{H0}$ and $+\delta^2\mu_W C_{H0}$, respectively.

D.2 Investigating the outer problem

We now introduce the Dirac delta function formulation of the 'periodic cell' region problem:

$$\delta^2 \frac{\partial C_H}{\partial T} = (\nabla_{\boldsymbol{Y}} + \delta\nabla_{\boldsymbol{X}}) \cdot (\nabla_{\boldsymbol{Y}} + \delta\nabla_{\boldsymbol{X}}) C_H - \tilde{\delta}(\boldsymbol{Y})\delta^2\mu_C C_H \quad \text{for } \boldsymbol{Y} \in \Omega, \tag{D.2.1a}$$

$$\delta^2 \frac{\partial W_H}{\partial T} = d_{WH} (\nabla_{\boldsymbol{Y}} + \delta\nabla_{\boldsymbol{X}}) \cdot (\nabla_{\boldsymbol{Y}} + \delta\nabla_{\boldsymbol{X}}) W_H + \tilde{\delta}(\boldsymbol{Y})\delta^2\mu_W C_H \quad \text{for } \boldsymbol{Y} \in \Omega, \tag{D.2.1b}$$

where $\tilde{\delta}$ is the Dirac delta function, and with $\{C_H, W_H\}$ periodic for $\boldsymbol{Y} \in \partial\Omega$, and we expand $f \sim f_0 + \delta f_1 + \delta^2 f_2 + \dots$, where $f \in \{C_H, W_H\}$. We proceed by considering the model for glucose transport, and note that the analysis for lactate transport is analogous.

Noting that the leading-order problem gives C_{H0} and C_{H1} independent of $\boldsymbol{Y}$, we find that the $\mathcal{O}(\delta^2)$ problem is:

$$\frac{\partial C_{H0}}{\partial T} = \nabla_{\boldsymbol{Y}}^2 C_{H2} + \nabla_{\boldsymbol{X}}^2 C_{H0} - \tilde{\delta}(\boldsymbol{Y})\mu_C C_{H0} \quad \text{for } \boldsymbol{Y} \in \Omega, \tag{D.2.2}$$

with C_{H0} periodic for $\boldsymbol{Y} \in \partial\Omega$. Integrating Equation (D.2.2) over the cell Ω,

$$\int_{\Omega(\boldsymbol{X},T)} \frac{\partial C_{H0}}{\partial T} \, \mathrm{d}\boldsymbol{Y} = \int_{\Omega(\boldsymbol{X},T)} \underbrace{\nabla_{\boldsymbol{Y}}^2 C_{H2}}_{\textcircled{\dagger_1}} + \nabla_{\boldsymbol{X}}^2 C_{H0} - \tilde{\delta}(\boldsymbol{Y})\mu_C C_{H0} \, \mathrm{d}\boldsymbol{Y}, \tag{D.2.3}$$

we use Reynolds' transport theorem on the LHS, and use the divergence theorem on $\textcircled{\dagger_1}$:

$$\begin{aligned} &\frac{\partial}{\partial T}\left(\int_\Omega C_{H0} \, \mathrm{d}\boldsymbol{Y}\right) - \int_{\partial\Omega}\left(\mathbf{n}_{\boldsymbol{Y}} \cdot \frac{\partial \boldsymbol{Y}^{\mathrm{bdy}}}{\partial T}\right) C_{H0} \, \mathrm{d}A \\ &\qquad = \underbrace{\int_{\partial\Omega} \mathbf{n}_{\boldsymbol{Y}} \cdot \left(\nabla_{\boldsymbol{Y}} C_{H2}\right) \, \mathrm{d}A}_{=0 \text{ by periodic BC}} + \underbrace{\int_\Omega \nabla_{\boldsymbol{X}}^2 C_{H0} \, \mathrm{d}\boldsymbol{Y}}_{\textcircled{\dagger_2}} - \mu_C C_{H0}, \end{aligned} \tag{D.2.4}$$

where we note that all velocities within the system are $\mathcal{O}(\delta^2)$ in this distinguished limit and, therefore, the term $\partial(\boldsymbol{Y}^{\mathrm{bdy}})/\partial T$, representing the velocity of the periodic cell boundary is $\mathcal{O}(\delta^2)$ relative to the other terms in the equation and so we neglect it. We use Reynolds' transport theorem component-wise (twice) (Equation (3.3.26)) on $\textcircled{\dagger_2}$ and note that we have no contribution from the surface integral (twice), giving

$$\frac{\partial}{\partial T}\left(\int_\Omega C_{H0} \, \mathrm{d}\boldsymbol{Y}\right) = \nabla_{\boldsymbol{X}}^2 \left(\int_\Omega C_{H0} \, \mathrm{d}\boldsymbol{Y}\right) - \mu_C C_{H0}. \tag{D.2.5}$$

We define the *intrinsic-averaged* glucose concentration in the hydrogel as

$$\check{C}_H(\boldsymbol{X},T) = \frac{1}{\|\Omega_H(\boldsymbol{X},T)\|} \int_{\Omega_H} C_H(\boldsymbol{X},\boldsymbol{Y},T) \, \mathrm{d}\boldsymbol{Y}, \tag{D.2.6}$$

and note that, since $C_H \sim C_{H0} + \mathcal{O}(\delta)$, at leading order

$$\check{C}_H \sim C_{H0}. \tag{D.2.7}$$

Therefore, the effective equation for the intrinstic-averaged glucose concentration is

$$\frac{\partial \check{C}_H}{\partial T} = \nabla_{\boldsymbol{X}}^2 \check{C}_H - \mu_C \check{C}_H, \tag{D.2.8a}$$

where $\mu_C(\tilde{R})$ is as defined in Equation (D.1.20c), and subject to the initial condition

$$\check{C}_H(\boldsymbol{X}, T=0) = C_{H\mathrm{init}}(\boldsymbol{X}). \tag{D.2.8b}$$

The effective diffusion coefficient is unity, which we can see is a sublimit (small organoid radius) of the effective diffusivity for the distinguished limit considered in Section 3.3.1, and the effective uptake is $\mathcal{O}(1)$.

Similarly, the effective equation for the intrinsic-averaged lactate concentration is

$$\frac{\partial \check{W}_H}{\partial T} = d_{WH} \nabla^2_{\boldsymbol{X}} \check{W}_H + \mu_W \check{C}_H, \tag{D.2.9a}$$

subject to

$$\check{W}_H(\boldsymbol{X}, T = 0) = W_{H\text{init}}(\boldsymbol{X}), \tag{D.2.9b}$$

where $\mu_W(\tilde{R})$ is given by Equation (D.1.20d).

Moreover, we note that since the organoids are small, that is $\|\Omega_O\| = \mathcal{O}(\delta^2)$, the *volumetric-averaged* glucose and lactate concentrations, which we define as

$$\bar{C}_H(\boldsymbol{X}, T) = \frac{1}{\|\Omega\|} \left(\int_{\Omega_H} C_H \, \mathrm{d}\boldsymbol{Y} + \int_{\Omega_O} C_O \, \mathrm{d}\boldsymbol{Y} \right), \tag{D.2.10}$$

$$\bar{W}_H(\boldsymbol{X}, T) = \frac{1}{\|\Omega\|} \left(\int_{\Omega_H} W_H \, \mathrm{d}\boldsymbol{Y} + \int_{\Omega_O} W_O \, \mathrm{d}\boldsymbol{Y} \right), \tag{D.2.11}$$

respectively, behave as

$$\bar{C}_H \sim \check{C}_H, \quad \bar{W}_H \sim \check{W}_H, \tag{D.2.12}$$

and, therefore, Equation (D.2.8) and Equation (D.2.9) are also the homogenised transport models for $\bar{C}_H$ and $\bar{W}_H$, respectively.

D.3 Effective behaviour in thin layer of hydrogel

We consider the glucose and lactate transport within a thin layer of organoid-seeded hydrogel with a layer of culture media flowing slowly (Stokes flow) across the top. We denote the volumetric-averaged concentrations of glucose and lactate as $\bar{C}_H$ and $\bar{W}_H$, respectively. Using Appendix C, we consider the transport within the homogenised-hydrogel region with the proxy flow boundary condition Equation (C.25). We are specifically interested in the timescale of organoid growth. We note that for a thin layer of hydrogel, the vertical diffusion will be on a significantly faster timescale than organoid growth. We consider a regime where the nutrient uptake balances the vertical diffusion. Therefore, we can treat the leading-order metabolite transport problem as quasi-steady. The behaviour is governed by the following system of equations:

$$0 = \frac{\partial^2 \bar{C}_H}{\partial Z^2} - \mu_C \bar{C}_H \qquad \text{for } 0 < Z < H, \tag{D.3.1a}$$

$$0 = d_{WH} \frac{\partial^2 \bar{W}_H}{\partial Z^2} + \mu_W \bar{C}_H \quad \text{for } 0 < Z < H, \tag{D.3.1b}$$

with boundary conditions:

$$\frac{\partial \bar{C}_H}{\partial Z} = 0, \quad \frac{\partial \bar{W}_H}{\partial Z} = 0 \qquad \text{at } Z = 0, \tag{D.3.1c}$$

$$\bar{C}_H + \frac{X^{\frac{1}{3}}}{\alpha_C}\frac{\partial \bar{C}_H}{\partial Z} = 1, \quad \bar{W}_H + \frac{X^{\frac{1}{3}}}{\alpha_W} d_{WH}\frac{\partial \bar{W}_H}{\partial Z} = 0 \quad \text{at } Z = H. \tag{D.3.1d}$$

and organoid growth model

$$\frac{\partial \tilde{R}}{\partial T} = \frac{\rho}{3} P\left(\frac{\bar{C}_H}{K_C}, \frac{\bar{W}_H}{K_W}\right)\tilde{R}, \quad \text{with} \quad \tilde{R} = \tilde{R}_{\text{init}} \quad \text{at} \quad T = 0, \tag{D.3.1e}$$

where the media-hydrogel interface is at $Z = H$ and the glucose consumption and lactate production strengths, μ_C and μ_W, respectively, depend on the organoid radius $\tilde{R}$ and are as defined in Equation (D.1.20c) and Equation (D.1.20d), respectively. In the following analysis, we treat X as a parameter of the system.

We first consider the glucose concentration $\bar{C}_H$, as this decouples from the lactate concentration, $\bar{W}_H$. We integrate Equation (D.3.1a) with respect to Z, to find the general solution of the form

$$\bar{C}_H = A\cosh(\sqrt{\mu_C}Z) + B\sinh(\sqrt{\mu_C}Z), \tag{D.3.2}$$

where A and B are arbitrary functions independent of Z, to be determined from the boundary conditions Equations (D.3.1c) and (D.3.1d). From the no flux condition at the base of the hydrogel, Equation (D.3.1c), we determine that $B = 0$. Using Equation (D.3.1d) at $Z = H$, we determine that A is

$$A = \left(\frac{X^{1/3}}{\alpha_C}\sinh(\sqrt{\mu_C}H) + \cosh(\sqrt{\mu_C}H)\right)^{-1}. \tag{D.3.3}$$

Therefore, the glucose concentration is given by:

$$\bar{C}_H = \frac{\alpha_C\cosh(\sqrt{\mu_C}Z)}{X^{1/3}\sinh(\sqrt{\mu_C}H) + \alpha_C\cosh(\sqrt{\mu_C}H)} := \beta_C\cosh(\sqrt{\mu_C}Z), \tag{D.3.4}$$

where we introduce the parameter β_C (where $\beta_C = A$) for notational convenience.

The governing equation for lactate, using the analytic form for glucose Equation (D.3.4), becomes

$$0 = d_{WH}\frac{\partial^2 \bar{W}_H}{\partial Z^2} + \mu_W\beta_C\cosh(\sqrt{\mu_C}Z). \tag{D.3.5}$$

Integrating Equation (D.3.5) with respect to Z, we obtain

$$\frac{\partial \bar{W}_H}{\partial Z} = -\frac{\mu_W\beta_C}{\sqrt{\mu_C}d_{WH}}\sinh(\sqrt{\mu_C}Z) + \tilde{A}, \tag{D.3.6}$$

where we find the arbitrary function $\tilde{A} = 0$ from the boundary condition at $Z = 0$ (Equation (D.3.1c)). We integrate with respect to Z again and find

$$\bar{W}_H = \frac{\mu_W \beta_C}{\mu_C d_{WH}} \cosh(\sqrt{\mu_C} Z) + \tilde{B}, \tag{D.3.7}$$

where we must determine the arbitrary function $\tilde{B}$ from the *proxy* flow boundary condition at $Z = H$. We find that $\tilde{B}$ is

$$\tilde{B} = \frac{\mu_W \beta_C}{\mu_C d_{WH} \alpha_W} \left(d_{WH} \sqrt{\mu_C} X^{1/3} \sinh\left(\sqrt{\mu_C} H\right) + \alpha_W \cosh\left(\sqrt{\mu_C} H\right) \right). \tag{D.3.8}$$

Therefore, the lactate concentration is given by

$$\bar{W}_H = \frac{\mu_W \beta_C}{\mu_C d_{WH} \alpha_W} \left(d_{WH} \sqrt{\mu_C} X^{1/3} \sinh(\sqrt{\mu_C} H) + \alpha_W (\cosh(\sqrt{\mu_C} H) - \cosh\left(\sqrt{\mu_C} Z\right)) \right), \tag{D.3.9}$$

which we can rewrite as

$$\bar{W}_H = \frac{\mu_W \alpha_C}{\mu_C \alpha_W d_{WH}} \left(\frac{d_{WH} \sqrt{\mu_C} X^{1/3} \sinh(\sqrt{\mu_C} H) + \alpha_W (\cosh(\sqrt{\mu_C} H) - \cosh\left(\sqrt{\mu_C} Z\right))}{X^{1/3} \sinh(\sqrt{\mu_C} H) + \alpha_C \cosh(\sqrt{\mu_C} H)} \right). \tag{D.3.10}$$

We note that μ_C and μ_W are dependent on organoid radius $\tilde{R}$.

We have determined the glucose, $\bar{C}_H$, and lactate, $\bar{W}_H$, concentrations as a function of position, $\boldsymbol{X}$, and organoid radius, $\tilde{R}$, and these are given by Equation (D.3.4) and Equation (D.3.10), respectively. We note that the metabolite concentrations are implicitly dependent on time, since they are dependent on $\mu_C(\tilde{R})$ and $\mu_W(\tilde{R})$, which is time-dependent. We can substitute the metabolite concentration into the organoid growth model Equation (D.3.1e) (derived in Section 3.2.1.2), for dense organoids:

$$\frac{\partial \tilde{R}}{\partial T} = \frac{\rho}{3} P \left(\frac{\bar{C}_H}{K_C}, \frac{\bar{W}_H}{K_W} \right) \tilde{R}. \tag{D.3.11}$$

We can solve this numerically for $\tilde{R} = \tilde{R}(T; \boldsymbol{X})$. Therefore, our system has reduced to solving an ODE in time at each spatial position in the domain.

Appendix E

Another distinguished limit for metabolite transport along streamlines: advection balancing vertical diffusion

We note that there are other distinguished limits for the 3D system considered in Chapter 5 (Equations (5.1.12), (5.1.13) and (5.1.15) to (5.1.17)) which may be of interest for different parameter regimes. One such limit is the case where advection balances vertical diffusion, $\lambda \sim d_{CH}/\epsilon^2 \sim \mathcal{O}(1)$. This distinguished limit would correspond to less extreme bioreactor geometries and/or operating protocols with faster flow rates. In this case, since advection balances vertical diffusion, we are unable to depth-average the model straightforwardly. However, since vertical diffusion and advection always dominate horizontal diffusion (away from 'slow flow' regions near stagnation points), we can still systematically reduce our model. We now outline how to reduce the model via transformation into streamfunction-arclength formulation.

In the case $\lambda \sim d_{CM}/\epsilon^2 \sim \mathcal{O}(1)$, the leading-order equations become

$$\frac{\partial C_{M0}}{\partial T} + \lambda \boldsymbol{U}_M \cdot \nabla_{\boldsymbol{X}} C_{M0} = \frac{d_{CM}}{\epsilon^2} \frac{\partial^2 C_{M0}}{\partial Z^2}, \tag{E.1a}$$

$$\frac{\partial W_{M0}}{\partial T} + \lambda \boldsymbol{U}_M \cdot \nabla_{\boldsymbol{X}} W_{M0} = \frac{d_{WM}}{\epsilon^2} \frac{\partial^2 W_{M0}}{\partial Z^2}, \tag{E.1b}$$

$$\frac{\partial}{\partial T}\left(\left(\|\Omega_H\| K_C + \|\Omega_O\|\right) C_{O0}\right) = \frac{d_{CH}}{\epsilon^2} \bar{d}_C(X,Y,0,T) \frac{\partial^2 C_{O0}}{\partial Z^2} - \sigma_V \|\Omega_O\| S(C_{O0}, W_{O0}), \tag{E.1c}$$

$$\frac{\partial}{\partial T}\left(\left(\|\Omega_H\| K_W + \|\Omega_O\|\right) W_{O0}\right) = \frac{d_{WH}}{\epsilon^2} \bar{d}_W(X,Y,0,T) \frac{\partial^2 W_{O0}}{\partial Z^2} + 2\sigma_V \|\Omega_O\| S(C_{O0}, W_{O0}), \tag{E.1d}$$

subject to

$$d_{CH} \bar{d}_C(X,Y,0,T) \frac{\partial C_{O0}}{\partial Z} = 0, \quad d_{WH} \bar{d}_W(X,Y,0,T) \frac{\partial W_{O0}}{\partial Z} = 0 \quad \text{at } Z = 0, \tag{E.2a}$$

$$d_{CM}\frac{\partial C_{M0}}{\partial Z} = 0, \quad d_{WM}\frac{\partial W_{M0}}{\partial Z} = 0 \quad \text{at } Z = 1, \tag{E.2b}$$

$$C_M = C_O, \qquad d_{CH}\bar{d}_C(X,Y,0,T)\frac{\partial C_{O0}}{\partial Z} = d_{CM}\frac{\partial C_{M0}}{\partial Z} \quad \text{at } Z = H_H, \tag{E.2c}$$

$$W_M = W_O, \qquad d_{WM}\frac{\partial W_{M0}}{\partial Z} = d_{WH}\bar{d}_W(X,Y,0,T)\frac{\partial W_{O0}}{\partial Z} \quad \text{at } Z = H_H. \tag{E.2d}$$

As before, since there is no (X,Y)-diffusion at leading order, we impose the boundary condition at the inlet, $\boldsymbol{X} \in \partial\Omega_{\text{in}}$:

$$\hat{\mathbf{n}} \cdot (\lambda \boldsymbol{U}_M) = \hat{\mathbf{n}} \cdot (\lambda \boldsymbol{U}_M C_{M0}) \quad \Rightarrow \quad C_{M0} = 1 \quad \text{for } Z \in (H_H, 1], \tag{E.2e}$$

$$0 = \hat{\mathbf{n}} \cdot (\lambda \boldsymbol{U}_M W_{M0}) \quad \Rightarrow \quad W_{M0} = 0 \quad \text{for } Z \in (H_H, 1]. \tag{E.2f}$$

We use the transformation $(X,Y,Z) \mapsto (\psi, s, Z)$ defined by Equations (4.2.8) and (5.1.47) and outlined in Section 5.1.3, where we note that the streamlines lie in the (X,Y)-plane since there is no velocity in the Z-direction. This yields the system:

$$\frac{\partial C_{M0}}{\partial T} + \lambda\frac{\tilde{U}(s,\psi)G(Z)}{\mathcal{L}^{\text{total}}(\psi)}\frac{\partial C_{M0}}{\partial s} = \frac{d_{CM}}{\epsilon^2}\frac{\partial^2 C_{M0}}{\partial Z^2}, \tag{E.3a}$$

$$\frac{\partial W_{M0}}{\partial T} + \lambda\frac{\tilde{U}(s,\psi)G(Z)}{\mathcal{L}^{\text{total}}(\psi)}\frac{\partial W_{M0}}{\partial s} = \frac{d_{WM}}{\epsilon^2}\frac{\partial^2 W_{M0}}{\partial Z^2}, \tag{E.3b}$$

$$\frac{\partial C_{O0}}{\partial T} = \frac{d_{CH}}{\epsilon^2}\bar{d}_C(X,Y,0,T)\frac{\partial^2 C_{O0}}{\partial Z^2} - \sigma_V \left\|\Omega_O\right\| S(C_{O0}, W_{O0}), \tag{E.3c}$$

$$\frac{\partial W_{O0}}{\partial T} = \frac{d_{WH}}{\epsilon^2}\bar{d}_W(X,Y,0,T)\frac{\partial^2 W_{O0}}{\partial Z^2} + 2\sigma_V \left\|\Omega_O\right\| S(C_{O0}, W_{O0}), \tag{E.3d}$$

where we fix $K_C = K_W = 1$ for simplicity, and the media velocity along streamlines is

$$\boldsymbol{U}_M(s,\psi,Z) = |\boldsymbol{U}_M|\mathbf{e}_s = G(Z)|\boldsymbol{U}|\mathbf{e}_s = \tilde{U}(\psi,s)G(Z)\mathbf{e}_s. \tag{E.4}$$

The governing equations are subject to boundary conditions Equation (E.2) (noting the effective diffusivities now depend on $(\psi(X,Y), s(X,Y), Z)$), and the appropriate inlet boundary and initial conditions are:

$$C_{M0} = 1, \quad W_{M0} = 0 \quad \text{at } s = 0 \text{ for } Z \in (H_H, 1], \tag{E.5a}$$

$$C_{M0} = 1, \quad W_{M0} = 0, \quad C_{O0} = 0, \quad W_{O0} = 0 \quad \text{at } T = 0. \tag{E.5b}$$

The streamfunction-arclength formulation of the model is easier to work with, as there are now spatial derivatives in only two, not three, dimensions. This reduces the computational expense. We can solve for all streamlines in parallel, or focus on, for example, the shortest and longest streamlines — to understand the range of behaviours exhibited by the model.

References

[1] D. J. Acheson. Elementary fluid dynamics. Acoustical Society of America. 1991.

[2] L. Auton, S. Pramanik, M. Dalwadi, C. MacMinn, and I. Griffiths. A homogenised model for flow, transport and sorption in a heterogeneous porous medium. *Journal of Fluid Mechanics* 932 (2022), A34. DOI: `10.1017/jfm.2021.938`.

[3] C. Batchelor and G. Batchelor. An introduction to fluid dynamics. Cambridge University Press. 2000.

[4] C. Bock, M. Boutros, J. G. Camp, L. Clarke, H. Clevers, J. A. Knoblich, P. Liberali, A. Regev, A. C. Rios, O. Stegle, et al. The Organoid Cell Atlas. *Nature Biotechnology* (2020), pp. 1–5. DOI: `https://doi.org/10.1038/s41587-020-00762-x`.

[5] M. Bruna and S. J. Chapman. Diffusion in spatially varying porous media. *SIAM Journal on Applied Mathematics* 75.4 (2015), pp. 1648–1674.

[6] D. Caccavo. An overview on the mathematical modeling of hydrogels' behavior for drug delivery systems. *International Journal of Pharmaceutics* 560 (2019), pp. 175–190.

[7] D. Caccavo, S. Cascone, G. Lamberti, and A. Barba. Hydrogels: experimental characterization and mathematical modelling of their mechanical and diffusive behaviour. *Chemical Society Reviews* 47.7 (2018), pp. 2357–2373.

[8] F. Cacik, R. G. Dondo, and D. Marqués. Optimal control of a batch bioreactor for the production of xanthan gum. *Computers & Chemical Engineering* 25.2-3 (2001), pp. 409–418.

[9] L. A. Chapman, R. J. Shipley, J. P. Whiteley, M. J. Ellis, H. M. Byrne, and S. L. Waters. Optimising cell aggregate expansion in a perfused hollow fibre bioreactor via mathematical modelling. *PLoS ONE* 9.8 (2014). DOI: `10.1371/journal.pone.0105813`.

[10] L. A. Chapman, J. P. Whiteley, H. M. Byrne, S. L. Waters, and R. J. Shipley. Mathematical modelling of cell layer growth in a hollow fibre bioreactor. *Journal of Theoretical Biology* 418.August 2016 (2017), pp. 36–56. DOI: `10.1016/j.jtbi.2017.01.016`.

[11] M. Chen, L. Kimpton, J. Whiteley, M. Castilho, J. Malda, C. Please, S. Waters, and H. Byrne. Multiscale modelling and homogenisation of fibre-reinforced hydrogels for tissue engineering. *European Journal of Applied Mathematics* 31.1 (2020), pp. 143–171.

[12] I. L. Chernyavsky, L. Leach, I. L. Dryden, and O. E. Jensen. Transport in the placenta: homogenizing haemodynamics in a disordered medium. *Philosophical Transactions of the Royal Society A: Mathematical, Physical and Engineering Sciences* 369.1954 (2011), pp. 4162–4182.

[13] L. J. Cummings and S. L. Waters. Tissue growth in a rotating bioreactor. Part II: Fluid flow and nutrient transport problems. *Mathematical Medicine and Biology* 24.2 (2007), pp. 169–208. DOI: `10.1093/imammb/dql024`.

[14] M. P. Dalwadi. Flow and nutrient transport problems in rotating bioreactor systems. PhD thesis. 2014.

[15] M. P. Dalwadi, M. Bruna, and I. M. Griffiths. A multiscale method to calculate filter blockage. *Journal of Fluid Mechanics* 809 (2016), pp. 264–289.

[16] M. P. Dalwadi and J. R. King. A Systematic Upscaling of Nonlinear Chemical Uptake Within a Biofilm. *SIAM Journal on Applied Mathematics* 80.4 (2020), pp. 1723–1750. DOI: `10.1137/19M130220X`.

[17] M. P. Dalwadi and P. Pearce. Emergent robustness of bacterial quorum sensing in fluid flow. *Proceedings of the National Academy of Sciences* 118.10 (2021).

[18] M. P. Dalwadi, Y. Wang, J. R. King, and N. P. Minton. Upscaling diffusion through first-order volumetric sinks: A homogenization of bacterial nutrient uptake. *SIAM Journal on Applied Mathematics* 78.3 (2018), pp. 1300–1329. DOI: `10.1137/17M1138625`.

[19] P. F. Davies. Flow-Mediated Mechanotransduction. *Physiological Reviews* 75.3 (1995).

[20] T. A. Driscoll, N. Hale, and L. N. Trefethen. Chebfun guide. 2014.

[21] J. Drost and H. Clevers. Organoids in cancer research. *Nature Reviews Cancer* 18.7 (2018), pp. 407–418. DOI: `10.1038/s41568-018-0007-6`.

[22] S. J. Duncan, K. R. Daly, D. M. McKay Fletcher, S. Ruiz, P. Sweeney, and T. Roose. Multiple scale homogenisation of nutrient movement and crop growth in partially saturated soil. *Bulletin of Mathematical Biology* 81.10 (2019), pp. 3778–3802.

[23] R. Eibl, D. Eibl, R. Pörtner, G. Catapano, and P. Czermak. Cell and tissue reaction engineering. Springer Science & Business Media. 2008.

[24] M. Eisenstein. Organoids: the body builders. *Nature Methods* 15.1 (2018), pp. 19–23. DOI: `10.1038/nmeth.4538`.

[25] M. J. Ellis, J. Chaudhuri, and T. C. Dale. Methods for culturing organoids. U.S. Patent Application No. 16/316,573. Washington, DC: U.S. Patent and Trademark Office (2019).

[26] M. A. Ellis, M. P. Dalwadi, M. J. Ellis, H. M. Byrne, and S. L. Waters. A systematically reduced mathematical model for organoid expansion. *Frontiers in Bioengineering and Biotechnology* 9 (2021), p. 446.

[27] Y.-G. Fang and B. Li. Multiscale problems and analysis of soil mechanics. *Mechanics of Materials* 103 (2016), pp. 55–67.

[28] A. French. Mechanotransduction. *Annual Review of Physiology* 54.1 (1992), pp. 135–152.

[29] C. J. Galban and B. R. Locke. Analysis of cell growth kinetics and substrate diffusion in a polymer scaffold. *Biotechnology and Bioengineering* 65.2 (1999), pp. 121–132. DOI: `https://doi.org/10.1002/(SICI)1097-0290(19991020)65:2<121::AID-BIT1>3.0.CO;2-6`.

[30] C. J. Galban and B. R. Locke. Effects of spatial variation of cells and nutrient and product concentrations coupled with product inhibition on cell growth in a polymer scaffold. *Biotechnology and Bioengineering* 64.6 (1999), pp. 633–643. DOI: `10.1002/(SICI)1097-0290(19990920)64:6<633::AID-BIT1>3.0.CO;2-6`.

[31] A. I. Garciá-Pérez, E. A. López-Beltrán, P. Klüner, J. Luque, P. Ballesteros, and S. Cerdán. Molecular crowding and viscosity as determinants of translational diffusion of metabolites in subcellular organelles. *Archives of Biochemistry and Biophysics* 362.2 (1999), pp. 329–338.

[32] F. Gòdia and C. Solà. Fluidized-Bed Bioreactors. *Biotechnology Progress* 11.5 (1995), pp. 479–497. DOI: `10.1021/bp00035a001`.

[33] T. E. Gorochowski. Agent-based modelling in synthetic biology. *Essays in Biochemistry* 60.4 (Nov. 2016), pp. 325–336. DOI: `10.1042/EBC20160037`.

[34] T. C. Hales. A proof of the Kepler conjecture. *Annals of Mathematics* (2005), pp. 1065–1185.

[35] E. J. Hinch. Perturbation Methods. Cambridge Texts in Applied Mathematics. Cambridge University Press. 1991. DOI: `10.1017/CBO9781139172189`.

[36] E. C. Holden, J. Collis, B. S. Brook, and R. D. O'Dea. A multiphase multiscale model for nutrient limited tissue growth. *The ANZIAM Journal* 59.4 (2018), pp. 499–532.

[37] M. Horner, W. M. Miller, J. Ottino, and E. T. Papoutsakis. Transport in a grooved perfusion flat-bed bioreactor for cell therapy applications. *Biotechnology Progress* 14.5 (1998), pp. 689–698.

[38] U. Hornung. Homogenization and porous media. Vol. 6. Springer Science & Business Media. 1996.

[39] U. Hornung and W. Jäger. Diffusion, convection, adsorption, and reaction of chemicals in porous media. *Journal of Differential Equations* 92.2 (1991), pp. 199–225.

[40] U. Hornung, W. Jäger, and A. Mikelić. Reactive transport through an array of cells with semi-permeable membranes. *ESAIM: Mathematical Modelling and Numerical Analysis* 28.1 (1994), pp. 59–94.

[41] P. Howell, G. Kozyreff, and J. Ockendon. More general theories. In: *Applied Solid Mechanics*. Cambridge Texts in Applied Mathematics. Cambridge University Press. 2008, pp. 378–425. DOI: `10.1017/CBO9780511611605.010`.

[42] G. Huang, L. Wang, S. Wang, Y. Han, J. Wu, Q. Zhang, F. Xu, and T. J. Lu. Engineering three-dimensional cell mechanical microenvironment with hydrogels. *Biofabrication* 4.4 (2012). DOI: `10.1088/1758-5082/4/4/042001`.

[43] L. Hyndman, S. McKee, N. J. Mottram, B. Singh, S. D. Webb, and S. McGinty. Mathematical modelling of fluid flow and solute transport to define operating parameters for in vitro perfusion cell culture systems. *Interface Focus* 10.2 (2020). DOI: `10.1098/rsfs.2019.0045`.

[44] J. M. Jepson, N. T. Fadai, and R. D. O'Dea. Travelling-wave and asymptotic analysis of a multiphase moving boundary model for engineered tissue growth. *Bulletin of Mathematical Biology* 84.8 (2022), pp. 1–19.

[45] M. Jove, J. A. Spencer, M. E. Hubbard, E. C. Holden, R. D. O'Dea, B. S. Brook, R. M. Phillips, S. W. Smye, P. M. Loadman, and C. J. Twelves. Cellular uptake and efflux of palbociclib in vitro in single cell and spheroid models. *Journal of Pharmacology and Experimental Therapeutics* 370.2 (2019), pp. 242–251.

[46] D. Kilburn, M. Lilly, and F. Webb. The energetics of mammalian cell growth. *Journal of Cell Science* 4.3 (1969), pp. 645–654.

[47] J. Kondo and M. Inoue. Application of Cancer Organoid Model for Drug Screening and Personalized Therapy. *Cells* 8.5 (2019). DOI: `10.3390/cells8050470`.

[48] K. J. Lampe, R. M. Namba, T. R. Silverman, K. B. Bjugstad, and M. J. Mahoney. Impact of lactic acid on cell proliferation and free radical induced cell death in monolayer cultures of neural precursor cells. *Biotechnology and Bioengineering* 103.6 (2009), pp. 1214–1223.

[49] M. Lappa. Organic Tissues in Rotating Bioreactors: Fluid-Mechanical Aspects, Dynamic Growth Models, and Morphological Evolution. *Biotechnology and Bioengineering* 84.5 (2003), pp. 518–532. DOI: `10.1002/bit.10821`.

[50] G. Lemon, J. R. King, H. M. Byrne, O. E. Jensen, and K. M. Shakesheff. Mathematical modelling of engineered tissue growth using a multiphase porous flow mixture theory. *Journal of Mathematical Biology* 52.5 (2006), pp. 571–594. DOI: `10.1007/s00285-005-0363-1`.

[51] M. V. Liberti and J. W. Locasale. The Warburg Effect: How Does it Benefit Cancer Cells? (vol 41, pg 211, 2016). *Trends in Biochemical Sciences* 41.3, SI (2016), p. 287. DOI: `10.1016/j.tibs.2016.01.004`.

[52] E. Luckins, C. Breward, I. Griffiths, and Z. Wilmott. Homogenisation problems in reactive decontamination. *European Journal of Applied Mathematics* 31.5 (2020), pp. 782–805.

[53] J. Macki and A. Strauss. Introduction to optimal control theory. Springer Science & Business Media. 2012.

[54] P. Macklin, M. E. Edgerton, V. Cristini, and J. Lowengrub. Discrete cell modeling. In: *Multiscale Modeling of Cancer: An Integrated Experimental and Mathematical Modeling Approach.* Cambridge University Press. 2010, pp. 88–122. DOI: `10.1017/CBO9780511781452.007`.

[55] I. Martin, D. Wendt, and M. Heberer. The role of bioreactors in tissue engineering. *Trends in Biotechnology* 22.2 (2004), pp. 80–86. DOI: `10.1016/j.tibtech.2003.12.001`.

[56] J. Metzcar, Y. Wang, R. Heiland, and P. Macklin. A review of cell-based computational modeling in cancer biology. *JCO Clinical Cancer Informatics* 2 (2019), pp. 1–13.

[57] F. Meuwly, P.-A. Ruffieux, A. Kadouri, and U. Von Stockar. Packed-bed bioreactors for mammalian cell culture: bioprocess and biomedical applications. *Biotechnology Advances* 25.1 (2007), pp. 45–56.

[58] Y. Nahmias, F. Berthiaume, and M. L. Yarmush. Integration of technologies for hepatic tissue engineering. *Tissue Engineering II* (2006), pp. 309–329.

[59] T. L. van Noorden and A. Muntean. Homogenisation of a locally periodic medium with areas of low and high diffusivity. *European Journal of Applied Mathematics* 22.5 (2011), pp. 493–516.

[60] R. D. O'Dea, S. L. Waters, and H. M. Byrne. A multiphase model for tissue construct growth in a perfusion bioreactor. *Mathematical Medicine and Biology* 27.2 (2009), pp. 95–127. DOI: `10.1093/imammb/dqp003`.

[61] R. O'Dea, H. Byrne, and S. Waters. Continuum modelling of in vitro tissue engineering: a review. *Computational Modeling in Tissue Engineering* (2012), pp. 229–266.

[62] P. Pathi, T. Ma, and B. R. Locke. Role of nutrient supply on cell growth in bioreactor design for tissue engineering of hematopoietic cells. *Biotechnology and Bioengineering* 89.7 (2005), pp. 743–758.

[63] N. C. Pearson, R. J. Shipley, S. L. Waters, and J. M. Oliver. Multiphase modelling of the influence of fluid flow and chemical concentration on tissue growth in a hollow fibre membrane bioreactor. *Mathematical Medicine and Biology* 31.4 (2014), pp. 393–430. DOI: `10.1093/imammb/dqt015`.

[64] C. V. Peroni, N. S. Kaisare, and J. H. Lee. Optimal control of a fed-batch bioreactor using simulation-based approximate dynamic programming. *IEEE Transactions on Control Systems Technology* 13.5 (2005), pp. 786–790.

[65] M. R. Placzek, I.-M. Chung, H. M. Macedo, S. Ismail, T. Mortera Blanco, M. Lim, J. Min Cha, I. Fauzi, Y. Kang, D. C. Yeo, et al. Stem cell bioprocessing: fundamentals and principles. *Journal of the Royal Society Interface* 6.32 (2009), pp. 209–232.

[66] C. Poon. Measuring the density and viscosity of culture media for optimized computational fluid dynamics analysis of in vitro devices. *Journal of the Mechanical Behavior of Biomedical Materials* 126 (2022), p. 105024.

[67] R. Pörtner and C. Giese. An Overview on Bioreactor Design, Prototyping and Process Control for Reproducible Three-Dimensional Tissue Culture. *Drug Testing in vitro: Breakthroughs and Trends in Cell Culture Technology* 3 (2006), pp. 53–78. DOI: `10.1002/9783527609611.ch2`.

[68] R. Pörtner, S. Nagel-Heyer, C. Goepfert, P. Adamietz, and N. M. Meenen. Bioreactor design for tissue engineering. *Journal of Bioscience and Bioengineering* 100.3 (2005), pp. 235–245. DOI: `10.1263/jbb.100.235`.

[69] C. A. Riascos and J. M. Pinto. Optimal control of bioreactors: a simultaneous approach for complex systems. *Chemical Engineering Journal* 99.1 (2004), pp. 23–34.

[70] G. Richardson, G. Denuault, and C. Please. Multiscale modelling and analysis of lithium-ion battery charge and discharge. *Journal of Engineering Mathematics* 72.1 (2012), pp. 41–72.

[71] S. Romero-Garcia, M. M. B. Moreno-Altamirano, H. Prado-Garcia, and F. J. Sánchez-García. Lactate contribution to the tumor microenvironment: Mechanisms, effects on immune cells and therapeutic relevance. *Frontiers in Immunology* 7.FEB (2016). DOI: `10.3389/fimmu.2016.00052`.

[72] J. A. Sánchez Pérez, E. M. Rodríguez Porcel, J. L. Casas López, J. M. Fernández Sevilla, and Y. Chisti. Shear rate in stirred tank and bubble column bioreactors. *Chemical Engineering Journal* 124.1-3 (2006), pp. 1–5. DOI: `10.1016/j.cej.2006.07.002`.

[73] G. L. Sanford, D. Ellerson, C. Melhado-Gardner, A. E. Sroufe, and S. Harris-Hooker. Three-dimensional growth of endothelial cells in the microgravity-based rotating wall vessel bioreactor. *In Vitro Cellular and Developmental Biology - Animal* 38.9 (2002), pp. 493–504. DOI: `10.1290/1071-2690(2002)038<0493:TGOECI>2.0.CO;2`.

[74] J. A. Sanz-Herrera, J. M. Garcia-Aznar, and M. Doblare. A mathematical model for bone tissue regeneration inside a specific type of scaffold. *Biomechanics and Modeling in Mechanobiology* 7.5 (2008), pp. 355–366. DOI: `10.1007/s10237-007-0089-7`.

[75] J. Schmid, S. Schwarz, R. Meier-Staude, S. Sudhop, H. Clausen-Schaumann, M. Schieker, and R. Huber. A Perfusion Bioreactor System for Cell Seeding and Oxygen-Controlled Cultivation of Three-Dimensional Cell Cultures. *Tissue Engineering Part C: Methods* 24.10 (2018), pp. 585–595.

[76] K. Schügerl, J. Lücke, and U. Oels. Bubble column bioreactors. In: *Advances in Biochemical Engineering, Volume 7.* Springer. 1977, pp. 1–84.

[77] R. J. Shipley, A. J. Davidson, K. Chan, J. B. Chaudhuri, S. L. Waters, and M. J. Ellis. A strategy to determine operating parameters in tissue engineering hollow fiber bioreactors. *Biotechnology and Bioengineering* 108.6 (2011), pp. 1450–1461. DOI: `10.1002/bit.23062`.

[78] R. J. Shipley, G. W. Jones, R. J. Dyson, B. G. Sengers, C. L. Bailey, C. J. Catt, C. P. Please, and J. Malda. Design criteria for a printed tissue engineering construct: A mathematical homogenization approach. *Journal of Theoretical Biology* 259.3 (2009), pp. 489–502. DOI: `10.1016/j.jtbi.2009.03.037`.

[79] R. J. Shipley and S. J. Chapman. Multiscale modelling of fluid and drug transport in vascular tumours. *Bulletin of Mathematical Biology* 72.6 (2010), pp. 1464–1491.

[80] R. J. Shipley and S. L. Waters. Fluid and mass transport modelling to drive the design of cell-packed hollow fibre bioreactors for tissue engineering applications. *Mathematical Medicine and Biology* 29.4 (2012), pp. 329–359. DOI: `10.1093/imammb/dqr025`.

[81] N. Sloane. The proof of the packing. *Nature* 425.6954 (2003), pp. 126–127.

[82] N. de Souza. Organoids. *Nature Methods* 15.1 (2018), pp. 23–24. DOI: `https://doi.org/10.1038/nmeth.4576`.

[83] H. Suhaimi and D. Das. Glucose diffusion in tissue engineering membranes and scaffolds. *Reviews in Chemical Engineering* 32.6 (2016), pp. 629–650. DOI: `10.1515/revce-2015-0021`.

[84] H. Suhaimi, S. Wang, and D. B. Das. Glucose diffusivity in cell culture medium. *Chemical Engineering Journal* 269 (2015), pp. 323–327. DOI: `10.1016/j.cej.2015.01.130`.

[85] A. W. Tilles, H. Baskaran, P. Roy, M. L. Yarmush, and M. Toner. Effects of oxygenation and flow on the viability and function of rat hepatocytes cocultured in a microchannel flat-plate bioreactor. *Biotechnology and Bioengineering* 73.5 (2001), pp. 379–389.

[86] D. Tuveson and H. Clevers. Cancer modeling meets human organoid technology. *Science* 364.6444 (2019), pp. 952–955. DOI: `10.1126/science.aaw6985`.

[87] M. Van Dyke. Perturbation methods in fluid mechanics. Annotated ed. Parabolic Press. Stanford, Calif. 1975.

[88] M. G. Vander Heiden, L. C. Cantley, and C. B. Thompson. Understanding the Warburg effect: the metabolic requirements of cell proliferation. *Science* 324.5930 (2009), pp. 1029–1033.

[89] T.-Y. Wang and J. D. Wu. A Continuous Perfusion Bioreactor for Long-Term Bone Marrow Culture. *Annals of the New York Academy of Sciences* 665.1 (1992), pp. 274–284.

[90] S. L. Waters, L. J. Cummings, K. M. Shakesheff, and F. R. Rose. Tissue growth in a rotating bioreactor. Part I: Mechanical stability. *Mathematical Medicine and Biology* 23.4 (2006), pp. 311–337. DOI: `10.1093/imammb/dql013`.

[91] D. Wendt, S. A. Riboldi, M. Cioffi, and I. Martin. Potential and bottlenecks of bioreactors in 3D cell culture and tissue manufacturing. *Advanced Materials* 21.32-33 (2009), pp. 3352–3367. DOI: `10.1002/adma.200802748`.

[92] S. Whitaker. The method of volume averaging. Vol. 13. Springer Science & Business Media. 2013.

[93] X. Yan, D. J. Bergstrom, and X. B. Chen. Modeling of cell cultures in perfusion bioreactors. *IEEE Transactions on Biomedical Engineering* 59.9 (2012), pp. 2568–2575. DOI: `10.1109/TBME.2012.2206077`.

[94] M. Young and K. R. Reed. Organoids as a model for colorectal cancer. *Current Colorectal Cancer Reports* 12.5 (2016), pp. 281–287. DOI: `10.1007/s11888-016-0335-4`.

[95] T. Zeuthen, E. Zeuthen, and N. MacAulay. Water transport by GLUT2 expressed in Xenopus laevis oocytes. *The Journal of Physiology* 579.2 (2007), pp. 345–361.

[96] F. Zhao and T. Ma. Perfusion bioreactor system for human mesenchymal stem cell tissue engineering: Dynamic cell seeding and construct development. *Biotechnology and Bioengineering* 91.4 (2005), pp. 482–493. DOI: `10.1002/bit.20532`.

[97] Z. Zhao, C. Vizetto-Duarte, Z. K. Moay, M. I. Setyawati, M. Rakshit, M. H. Kathawala, and K. W. Ng. Composite hydrogels in three-dimensional in vitro models. *Frontiers in Bioengineering and Biotechnology* 8 (2020), p. 611.

[98] S. Zhou, Z. Cui, and J. P. Urban. Nutrient gradients in engineered cartilage: Metabolic kinetics measurement and mass transfer modelings. *Biotechnology and Bioengineering* 101.2 (2008), pp. 408–421. DOI: `10.1002/bit.21887`.